Modeling and numerical simulation for the planning of percutaneous transluminal angioplasty

Bernard Al Helou

UNIVERSITÉ DE RENNES 1

THESE DE DOCTORAT DE

L'UNIVERSITE DE RENNES 1

ECOLE DOCTORALE N° 601
Mathématiques et Sciences et Technologies de l'Information et de la Communication
Spécialité : *Signal, Image, Vision*

Par
Bernard AL HELOU

Modeling and numerical simulation for the planning of percutaneous transluminal angioplasty

Thèse présentée et soutenue à Rennes, le 12 juillet 2021
Unité de recherche : LTSI, UMR Inserm 1099, Laboratoire Traitement du Signal et de l'image
Thèse N° :

Rapporteurs avant soutenance :

Yohan PAYAN	DR CNRS, TIMC-IMAG, Univ. Grenoble Alpes - CNRS UMR 5525. La Tronche, France.
Giancarlo PENNATI	PR, LaBS, Politecnico di Milano. Milan, Italie.

Composition du Jury :

Président :		
Examinateurs :	Yohan PAYAN	DR CNRS, TIMC-IMAG, Univ. Grenoble Alpes. La Tronche, France.
	Giancarlo PENNATI	PR, LaBS, Politecnico di Milano. Milan, Italie.
	Laurent SARRY	PR, Institut Pascal, Université Clermont Auvergne. Aubière, France.
	Adrien KALADJI	MCU-PH, LTSI, Université de Rennes 1. Rennes, France.
Dir. de thèse :	Pascal HAIGRON	PR, LTSI, Université de Rennes 1. Rennes, France.
Co-dir. de thèse :	Aline BEL-BRUNON	MC HDR, LaMCoS, INSA de Lyon. Villeurbanne France.

Invité(s)

Michel ROCHETTE	Directeur technique, ANSYS France, Villeurbanne, France.
Claudio SILVESTRO	Engineering Program Manager, MEDTRONIC. Santa Rosa, CA, USA.

ACKNOWLEDGEMENTS

Aware of the work that this represents, I would first like to thank Mr. Yohan Payan and Mr. Giancarlo Pennati who agreed to report on this thesis. I equally thank Mr. Laurent Sarry and all the defense jury members for their devoted time in evaluating this PhD work. I am much honored. I would like to thank them for their expertise, advices and comments, in addition to their interest in our work.

Besides, I owe my deepest gratitude to Mr. Pascal Haigron and Ms. Aline Bel-Brunon, the directors of this thesis. Their expertise and guidance have been highly precious to me. I would really like to thank them for their kindness, patience, continuous support and their confidence in my work. Thanks for being cool and professional simultaneously ☺.

I would also like to express my special thanks to all whom I had the chance to collaborate or discuss with during this thesis, enriching the work with their expertise, and making these three years interesting and rich on an intellectual and human level. Thanks to Dr. Antoine Lucas and Dr. Adrien Kaladji (CHU de Rennes); to Mr. Michel Rochette and Mr. Wenfeng Ye (Ansys, France); to Mr. Claudio Silvestro (Medtronic, USA); and to Ms. Claire Dupont and Mr. Miguel Castro (LTSI, Rennes).

Moreover I would like to thank Mr. Lotfi Senhadji for welcoming me in LTSI and the secretaries Soizic, Patricia and Muriel for their logistical support and kindness.

Many thanks go to my friends and colleagues in LTSI and CHU de Rennes for the memorable moments shared during these years.

Finally, it is also a privilege to express my sincere appreciation to my parents, my sister Marianne, and my brother Richard for their unconditional love, sacrifices, and endless support through ups and downs. Words will never be enough to express how grateful I am to them; thanks for just being there...

"*We are so often caught up in our destination that we forget to appreciate the journey, especially the goodness of the people we met on the way. Gratitude is part of success, don't overlook it…*"

TABLE OF CONTENTS

LIST OF FIGURES

CHAPTER 2 - STATE OF THE ART AND PROPOSED METHODOLOGY

CHAPTER 3 - PTA BALLOON MODELING

CHAPTER 4 - SIMULATION OF BALLOON ANGIOPLASTY IN A GENERIC MODEL

CHAPTER 5 - PLAQUE AND ARTERY MATERIAL MODELS CALIBRATION

CHAPTER 6 - PATIENT SPECIFIC GEOMETRIC MODELING OF A DISEASED ARTERY

CHAPTER 7 - PATIENT-SPECIFIC FINITE ELEMENT ANALYSIS OF PTA IN FEMORAL ARTERIES

APPENDIXES

LIST OF TABLES

RÉSUMÉ EN FRANÇAIS

L'athérosclérose est l'une des pathologies vasculaires les plus courantes dans le monde, avec un taux de mortalité élevé. Sa pathogenèse est globalement complexe. De façon simplifiée, elle pourrait être décrite comme l'accumulation d'abord de cellules inflammatoires et de lipides au niveau de la paroi interne de l'artère, suivie de la croissance de la plaque, formant une structure plus rigide composée de tissus conjonctifs, de fibres de collagène et de calcifications. La plaque peut devenir stable ou instable (plus susceptible de se rompre).

Les plaques obstruent partiellement ou totalement la lumière artériel, ce qui affecte la circulation sanguine normale et peut avoir des conséquences graves sur les organes perfusés [Figure - I]. La formation et la rupture de plaques d'athérome dans les artères coronaires et carotides sont directement associées aux cardiopathies ischémiques et aux accidents vasculaires cérébraux, respectivement, qui sont les deux principales causes de décès depuis 15 ans. Dans les artères périphériques, en particulier les artères fémorales, elles sont la principale cause de claudication et d'ischémie critique des membres (douleur ischémique au repos).

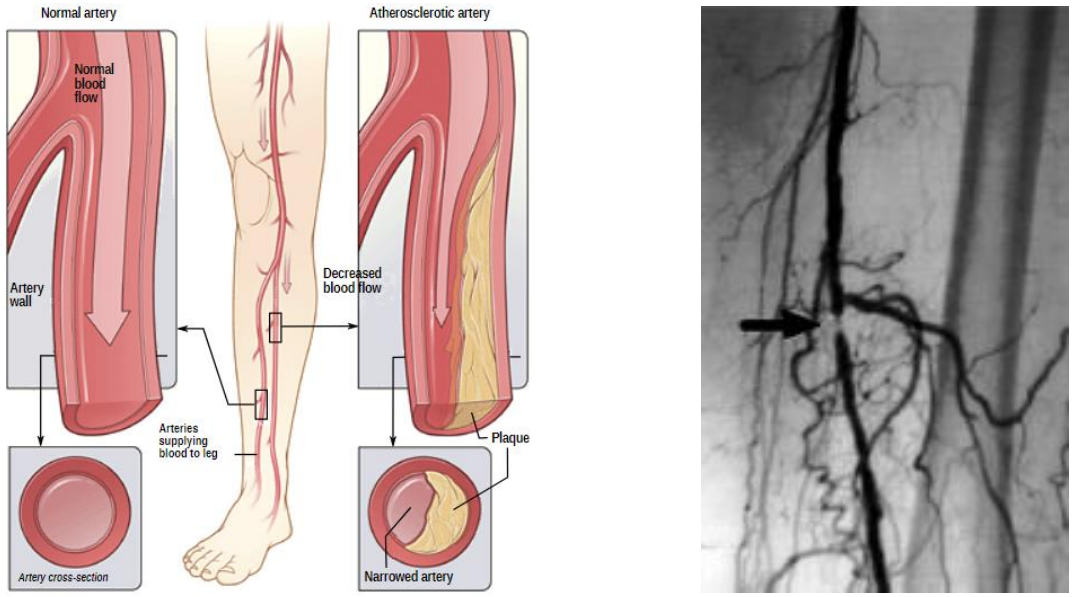

Figure - I: (A) Athérosclérose dans une artère périphérique [www. upload.wikimedia.org] ; et (B) Artériographie présentant un cas réel de sténose de l'artère fémorale superficielle [Jaff et al. (2005)].

Plusieurs techniques de traitement de l'athérosclérose sont cliniquement pratiquées, certaines chirurgicales et d'autres endovasculaires. Pour les maladies artérielles périphériques, même si cela doit encore être confirmé par des publications cliniques, les traitements endovasculaires, moins invasifs,

sont généralement l'alternative privilégiée aux traitements invasifs afin d'éviter les complications rencontrées avec les chirurgies conventionnelles, en particulier pour les patients présentant des risques plus élevés de morbidité et de mortalité chirurgicales. Il existe aujourd'hui plusieurs techniques endovasculaires pour traiter les sténoses artérielles, notamment l'angioplastie par ballonnet standard, les ballonnets enduits d'agents médicamenteux, les stents, les stents à élution médicamenteuse, l'athérectomie, etc. Chaque technique possédant ses propres avantages et limites, le choix de l'option de revascularisation optimale reste une question ouverte.

Notre intérêt principal étant les artères périphériques des membres inférieurs, ce travail se concentre sur la technique standard d'angioplastie transluminale percutanée (ATP), sans implantation de stent, car d'une part, il s'agit de l'approche de revascularisation initiale habituelle et d'autre part, le développement de ballons enduits permet d'envisager la conservation d'une dilatation suffisante de l'artère sans stent.

Le traitement par ATP consiste à insérer par voie percutanée un cathéter à ballonnet dans le vaisseau malade, puis à gonfler le ballonnet afin de comprimer et dégrader la plaque et d'élargir la lumière du vaisseau [Figure - II]. Le succès de l'ATP à court terme est évalué en terme de lumière résiduelle obtenue immédiatement après le traitement endovasculaire. Outre la compression/dégradation de la plaque, une déformation permanente se produit également dans les artères (appelée cliniquement "lésion contrôlée du vaisseau"). La déformation résultante est généralement évaluée soit par le taux de perméabilité, soit par le taux de retour élastique (*Elastic Recoil Ratio* - ERR) mesuré dans la région de sténose maximale après l'ATP. L'ERR caractérise l'ampleur du retour de cette section sténosée après dégonflement du ballonnet. L'anticipation précise des résultats cliniques (déformations résiduelles, retour élastique...) après une angioplastie par ballonnet est d'une importance capitale pour l'évaluation du succès du traitement, qui peut influencer les décisions thérapeutiques ultérieures. Bien que l'angioplastie par ballonnet soit une technique de traitement fréquemment utilisée, le choix du ballonnet optimal (type et taille) pour un patient sténosé spécifique, qui minimiserait le retour élastique, maximiserait la dilatation de la lumière, sans endommager la paroi artérielle, reste un défi de nos jours selon les fabricants et les cliniciens.

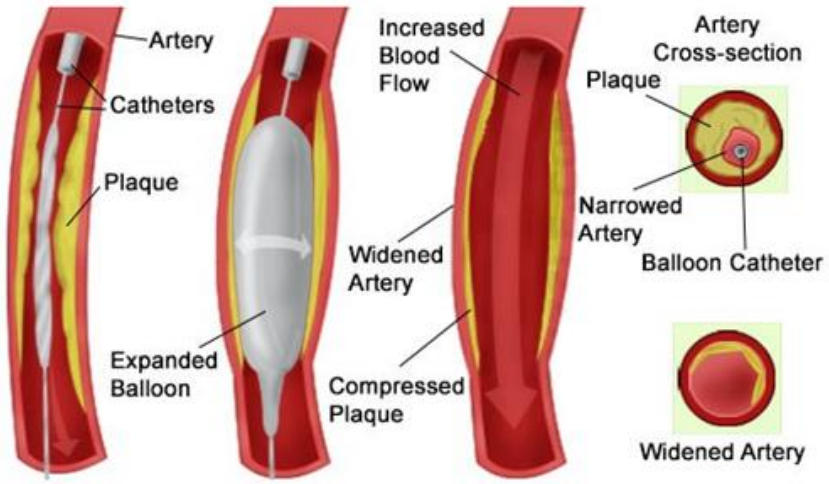

Figure - II: La procédure d'angioplastie transluminale percutanée (ATP) [www.healthhearty.com].

Plusieurs études dans la littérature ont rapporté le développement de modèles pour simuler l'ATP dans des artères sténosées en utilisant la méthode des éléments finis (MEF). Différentes combinaisons de géométries, de lois constitutives et de conditions de chargement ont été mises en œuvre, conduisant à une variabilité des résultats obtenus. En général, un facteur clé permettant ou non aux études par MEF d'évaluer les résultats d'une ATP immédiatement après le traitement est le modèle de matériau sélectionné pour modéliser l'artère malade. Les études par MEF actuelles se concentrent principalement sur les données expérimentales *in vitro* afin de développer leurs lois constitutives. Cependant, parmi le nombre limité d'études expérimentales disponibles, très peu ont considéré la quantification des déformations résiduelles dans les tissus athérosclérotiques humains et l'évaluation de leur comportement inélastique à des charges supra-physiologiques. En conséquence, la majorité des études par MEF n'ont pas inclus de déformations résiduelles dans leurs modèles de matériaux, et se sont donc limitées à la modélisation de l'ATP jusqu'à l'état gonflé du ballon, sans explorer le dégonflage du ballon. Même les quelques études par MEF modélisant des lois constitutives inélastiques (incluant la plasticité) sont limitées en termes de données présentées à court terme après l'ATP seule. En outre, les études reportées dans la littérature se focalisent sur un seul type de ballon d'un unique diamètre dans une unique composition de plaque. En général, très peu d'études par MEF ont confronté les résultats de leur simulation aux résultats cliniques.

Dans le but de progresser dans le domaine de la chirurgie assistée par ordinateur, ce travail vise à mettre en œuvre la MEF pour élaborer un outil d'aide à la décision en fournissant des informations augmentées aux chirurgiens pour une meilleure planification de l'ATP. D'un point de vue clinique, cet outil pourrait être utilisé pour anticiper et éviter les complications intra et post-opératoires (associées spécifiquement au comportement des tissus mous), de réduire la morbidité et de sécuriser les scénarii d'intervention. Ceci pourrait permettre d'étendre les indications de ces traitements mini-invasifs.

En conséquence, l'objectif de cette thèse est de proposer une approche de modélisation utilisant l'analyse par EF implicite pour simuler l'ATP (d'abord dans un modèle générique, puis pour des cas spécifiques de patients), et d'évaluer l'influence de différentes combinaisons de caractéristiques du ballon et de la plaque (type de ballon, composition de la plaque, taille du ballon) sur les résultats post-opératoires juste après l'ATP, sans implantation de stent. La méthodologie proposée peut servir d'étape vers un système d'aide à la décision clinique pour améliorer la sélection, avant la chirurgie, du ballon d'angioplastie optimal, en fonction de la sténose du patient considéré.

La [Figure - III] synthétise la méthodologie de modélisation que nous proposons en vue d'une analyse par éléments finis de l'angioplastie par ballonnet spécifique au patient.

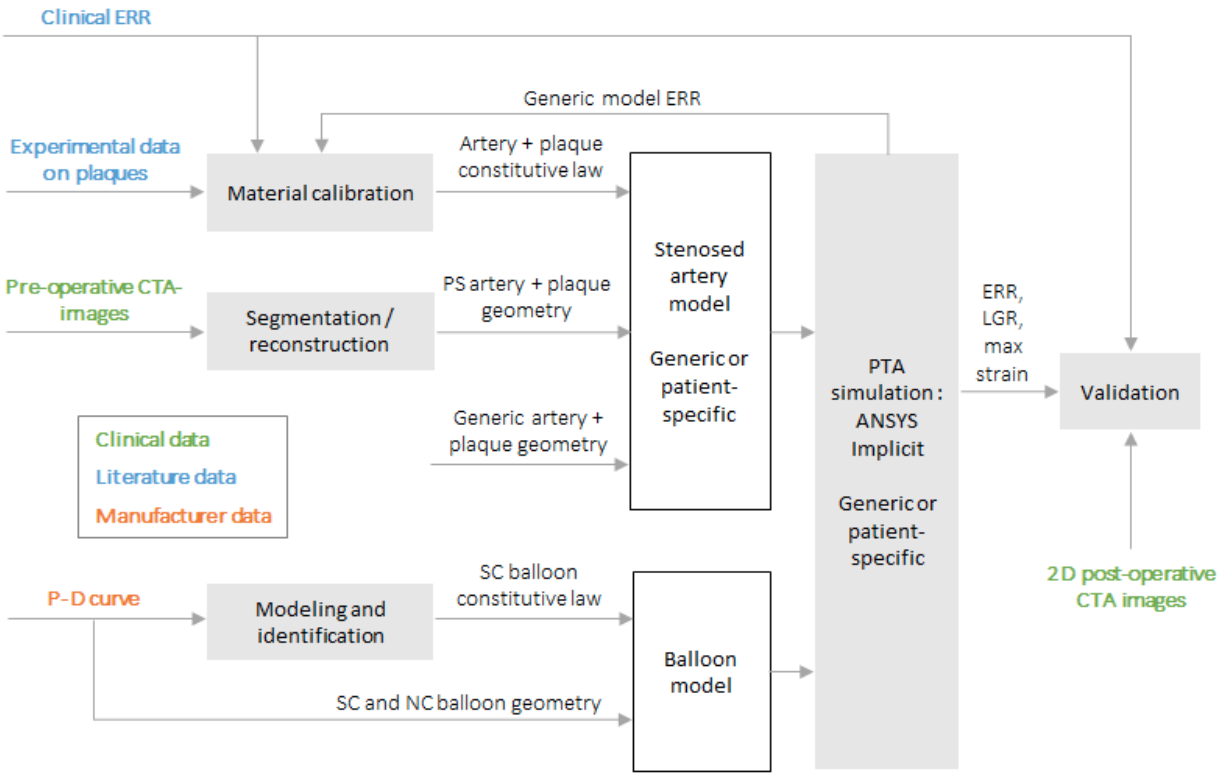

Figure - III: Approche proposée pour l'analyse par éléments finis de l'angioplastie par ballonnet spécifique au patient. Avec (CTA), (ERR), (LGR), (SC), (NC), et (PTA) représentant respectivement : angiographie par tomographie assistée par ordinateur, taux de retour élastique, taux de dilatation de la lumière, semi-compliant, non-compliant et angioplastie transluminale percutanée.

❖ MODÉLISATION DES BALLONS D'ATP

L'un des composants de base du processus de simulation de l'ATP est la modélisation du ballon d'angioplastie lui-même. En fonction de son matériau et de l'épaisseur de sa paroi, chaque ballon d'ATP haute pression possède un tableau de compliance fourni par le fabricant, qui décrit son évolution pression-diamètre. En réalité, les ballons PTA sont comprimés dans un cathéter pendant la fabrication, afin de faciliter leur insertion dans le système vasculaire du patient. Leur processus de

déploiement peut alors être divisé en deux phases : la phase de dépliage et la phase d'inflation. Ces dispositifs ont été modélisés à différents niveaux de sophistication dans la littérature : de la substitution du ballon par une pression de surface, à la modélisation détaillée du pliage du ballon. Comme ce travail vise à évaluer les résultats de la simulation immédiatement après une angioplastie par ballonnet seul (sans implantation de stent), nous nous sommes principalement intéressés à l'évaluation du comportement du ballonnet et de l'artère sténosée à trois états critiques pendant l'ATP : avant le gonflement, à gonflement maximal et après son dégonflement. Nous nous sommes donc moins intéressés à la prédiction de la déformation du dispositif au cours de son déploiement. Par conséquent, pour réduire les coûts de calcul importants associés à la modélisation des plis du ballon (voir par exemple Geith et al. (2019)), un cylindre non plié est considéré ici. Nous avons d'abord proposé une relation pour catégoriser les ballons en fonction de leurs données de compliance en deux grandes familles : les ballons semi-compliants et les ballons non-compliants. Ensuite, deux modèles différents ont été proposés en utilisant le solveur implicite d'Ansys en fonction des caractéristiques de chaque famille, dans le but d'optimiser à la fois la vitesse/le coût de la simulation et sa précision pour différentes tailles de ballons dans leurs plages de travail. Le type *semi-compliant* a été modélisé avec un pilotage en pression interne, tandis que le type *non-compliant* est piloté en déplacement.

- **SIMULATION DE L'ANGIOPLASTIE PAR BALLONNET DANS UN MODÈLE D'ARTERE GÉNÉRIQUE**

Après avoir été modélisés et validés en dehors des artères, les ballons d'angioplastie doivent être simulés dans des vaisseaux sténosés. En conséquence, nous avons proposé une stratégie de modélisation générique de l'ATP en utilisant un solveur MEF implicite pour évaluer les résultats post-opératoires. Un modèle générique représentant une artère sténosée a été créé à cette fin. À l'aide de ce modèle, nous avons réalisé une étude paramétrique basée sur le type de ballon, la composition de la plaque, la distribution des matériaux de la plaque et la taille du ballon, qui quantifie leur influence sur l'ERR et le taux de dilatation de la lumière (*Lumen Gain Ratio* - LGR) obtenus juste après l'ATP. Les valeurs d'ERR et de LGR ne semblent pas influencees par le type de balloon, malgré les différences observées dans leur profil à gonflement maximal. De plus, le LGR et l'ERR varient inversement à l'augmentation du niveau de calcification au sein de la plaque, le LGR le plus important étant obtenu lorsque la sténose était entièrement lipidique. D'une manière différente, les plaques avec des compositions matérielles similaires mais des distributions spatiales de calcifications différentes ont montré des influences mineures sur l'ERR et le LGR, mais de fortes variations dans la répartition de leurs déformations plastiques. En outre, les résultats ont montré une corrélation directe entre la taille du ballon et le LGR et l'ERR, avec des variations nettement plus élevées pour le LGR. Les résultats de la simulation illustrent que, contrairement à son type, la taille du ballon a un impact significatif sur la dilatation de la lumière obtenue après l'ATP, mais pourrait également augmenter le risque de lésion

artérielle. La méthodologie proposée ouvre la voie à l'évaluation des ballons d'angioplastie en vue de l'optimisation des procédures cliniques par une sélection optimale du ballon.

- **CALIBRATION DES MODÈLES DE MATÉRIAU DE LA PLAQUE ET DE L'ARTÈRE**

Une étape essentielle pour générer un modèle fiable est de valider les lois constitutives utilisées. Une méthode de calibration pour définir les modèles de matériau de la plaque et de l'artère avant de réaliser des simulations d'ATP a été proposée dans ce travail. Les données expérimentales in vitro sur le comportement inélastique des plaques sous compression obtenues par Maher et al. (2011) ont été prises en compte dans notre modèle afin d'identifier les paramètres des lois constitutives des plaques, considérées élasto-plastiques bilinéaires. Ensuite, les modèles de matériaux artériels, eux-mêmes supposés élasto-plastiques bilinéaires, ont été ajustés en tension pour satisfaire les valeurs moyennes d'ERR obtenues cliniquement après dégonflement du ballon. Les paramètres matériaux obtenus sont ceux implémentés dans les simulations génériques et patient-spécifiques d'ATP présentés dans cette thèse.

- **MODÉLISATION GÉOMÉTRIQUE SPÉCIFIQUE AU PATIENT D'UNE ARTÈRE MALADE**

Une autre étape importante d'un processus visant à modéliser l'ATP de cas patients est la génération du modèle géométrique patient-spécifique. Dans ce travail, nous présentons une méthode pour générer des géométries 3D spécifiques au patient pour des artères périphériques sténosées à partir de scanners CTA préopératoires. Dans le but de développer un outil pouvant être intégré dans la routine clinique sans imagerie supplémentaire, seuls les scanners CTA ont été considérés dans ce travail. Le processus de segmentation et de génération de modèles surfaciques est dans un premier temps décrit sur une section d'aorte abdominale sténosée par une plaque de composition mixte (lipidique et calcifiée). Il a ensuite été appliqué à deux artères fémorales superficielles sténosées présentant chacune une constitution de plaque différente : plaque calcifiée et plaque lipidique. Enfin, les géométries patient-spécifiques ont été générées à partir des régions segmentées et préparées pour les simulations par MEF.

- **ANALYSE PAR ÉLÉMENTS FINIS SPÉCIFIQUE AU PATIENT DE L'ATP DANS LES ARTÈRES FÉMORALES**

Après avoir élaborées toutes les étapes nécessaires à la simulation patient-spécifique de l'angioplastie par ballonnet, nous avons finalement appliqué le processus complet aux cas patients, au niveau des

artères périphériques. Plusieurs tailles de ballons ont été testées. Comme nous nous intéressons à l'influence de la taille du ballon sur les résultats post-opératoires, outre l'analyse des déformations principales de la paroi artérielle, les résultats ont été évalués principalement en termes d'ERR (caractérisant le retour élastique) et de LGR (caractérisant la dilatation résiduelle) le long de la ligne centrale de l'artère sténosée, en comparant les géométries avant et après traitement pour chaque taille de ballon. Les résultats obtenus confirment l'expérience du clinicien, à savoir qu'il est nécessaire de trouver un compromis entre la maximisation de la dilatation et la prévention de la rupture de la paroi artérielle ; un tel modèle peut aider à quantifier ce compromis et guider les chirurgiens dans la phase de dimensionnement préopératoire. Enfin, une comparaison qualitative est présentée entre les résultats cliniques obtenus à partir d'images médicales 2D postopératoires et les résultats des simulations afin d'évaluer la validité du processus proposé.

Malgré les limites de notre modèle, principalement dans les modèles de matériau choisis, il a généralement montré des résultats cohérents par rapport aux résultats cliniques rapportés dans la littérature. Il semble être un outil prometteur pour l'évaluation des résultats à court terme après une ATP. En outre, une comparaison qualitative entre l'ATP simulée et les résultats cliniques correspondants a montré des résultats encourageants dans les cas patient-spécifiques également.

Compte tenu de son potentiel, une validation plus poussée des paramètres de notre modèle (à l'aide de données cliniques pré et postopératoires sur plusieurs cas de dimensions artérielles, de gravité et de composition de plaque différentes) devrait être la prochaine étape en vue d'une introduction dans la routine clinique en tant qu'outil d'aide à la décision pour les chirurgiens avant l'intervention.

Pour conclure, nous avons élaboré une méthodologie complète de modélisation spécifique au patient permettant de simuler l'ATP et d'évaluer les résultats post-opératoires à court terme après le dégonflement du ballon de dilatation. L'approche originale proposée s'appuie sur la combinaison de l'analyse par éléments finis structurels implicites, de l'identification de la loi matériau et du traitement d'images médicales.

Les contributions principales de cette thèse peuvent être résumées de la manière suivante: (i) la modélisation du ballon d'angioplastie en fonction de son type, (ii) la définition des lois de comportement de l'artère et de la plaque d'athérome incluant la plasticité et la représentation de la déformation résiduelle, (iii) l'utilisation d'un solveur implicite pour un meilleur contrôle des paramètres du modèle, (iv) une étude paramétrique (type de ballon, composition et distribution du matériau de la plaque, dimensionnement du ballon) permettant d'évaluer l'influence des paramètres en termes de retour élastique (ERR) et de dilatation (LGR), (v) la segmentation et génération de modèles pour obtenir des géométries 3D patients-spécifiques adaptées aux simulations FE, pour les artères périphériques sténosées à partir d'images CTA préopératoires, et (vi) l'application de l'approche de

simulation patient spécifique proposée sur deux cas afin d'évaluer son intérêt pour prédire l'influence du dimensionnement du ballon d'angioplastie en phase de planning interventionnel.

GENERAL INTRODUCTION

Atherosclerosis is one of the most common vascular pathologies in the world, with high mortality rates. This pathogenesis is complex in general. In a simplified description, it could be defined as the accumulation first of inflammatory cells and lipids at the arterial inner wall, followed by the growth of the plaque with time forming a stiffer structure composed of connective tissues, collagen fibers, and calcifications. The plaque can either become stable or unstable (more prone to rupture).

Plaques partly or totally occlude the arterial lumen, affecting normal blood circulation, and can lead to severe consequences on perfused organs. Atherosclerotic plaque formation and rupture within the coronary and the carotid arteries are directly associated with ischaemic heart diseases and strokes respectively: the two primary causes of death for the last 15 year. Similarly, in femoral peripheral arteries for example, they are the main cause leading to claudication and critical limb ischemia (ischemic rest pain). High numbers of hospitalized cases with relatively long stays are being reported every year as a result of atherosclerosis in lower-extremity arteries.

Several treatment techniques are clinically available for atherosclerosis, some are surgical while others endovascular. For peripheral arterial diseases, even though not yet explicitly published, being the minimally-invasive option, endovascular treatments are usually a favored alternative to invasive treatments in order to avoid complications experienced with conventional surgeries, specifically for patients at higher risks of surgical morbidity and mortality. Several endovascular techniques exist nowadays that can be used to treat arterial stenosis, including: standard balloon angioplasty, drug-coated balloons, stents, drug-eluting stents, atherectomy, etc. With each technique possessing its own advantages and limitations, deciding on the optimal revascularization option remains an open question.

Our primary interest being peripheral lower extremity arteries, this work is focused on the standard percutaneous transluminal angioplasty (PTA) technique, without stent implantation, because first, it is the usual initial revascularization approach and second, the development of drug-coated balloons makes it even more possible to retain sufficient dilation without stent.

Treatment via PTA consists of inserting percutaneously a balloon catheter within the diseased vessel region, followed by inflating the balloon in order to compress/damage the plaque and enlarge the vessel lumen. Even though it is a frequently performed treatment technique, choosing the optimal balloon (design and sizing) for the specific stenosed patient that would minimize the elastic recoil, maximize lumen gain, but at the same time not damage the arterial wall is still challenging nowadays according to manufacturers and clinicians.

In the recent decades, computational studies have made it possible to model and simulate complex nonlinear problems in several fields of engineering science (e.g. automotive, energy, civil constructions etc.). In general, besides reducing design costs and increasing safety, numerical simulations also allowed optimizing the performance in several applications by better understanding the considered systems. While still relatively less applied in the medical field (mainly due to evident challenges in correctly representing the large varieties present among different patients' bodies), numerical simulations are gaining more interest with the late evolution in medical technology for diagnosis and treatment. Numerical simulations such as finite element methods (FEM) can help simulate and more appropriately assess the interactions between the deployed device and the stenosed artery that cannot be fully characterized by routine clinical methods.

Towards more progress in the computer-assisted surgery field, this work aims at implementing FEM to develop a tool that can provide valuable information to surgeons for a better planning of PTA. From a clinical point of view, these tools can be used in the objective of avoiding intra and post-operative complications (associated specifically with soft tissues behavior), reducing morbidity, and securing the intervention scenarios. This should accordingly increase the number of patients benefiting from these minimally invasive treatments.

Following previous joined work between the same partners in endovascular surgery simulation, this work has been performed in collaboration between LTSI (Laboratoire Traitement du Signal et de l'Image), LaMCoS (Laboratoire de Mécanique des Contacts et des Structures), Ansys France, and the University Hospital of Rennes, with the support of Labex CAMI (Computer Assisted Medical Interventions).

Accordingly, in this thesis we propose a modeling method using implicit FE analysis for simulating PTA (first within a generic model, then for patient-specific cases), and evaluating the influence of different combinations of balloon-plaque features (balloon type, plaque composition, balloon sizing) on acute post-procedural outcomes right after PTA, without stent implantation. After presenting the clinical context and the positioning of our work with respect to the state of the art, we develop in the following of the document a balloon model, a generic simulation of PTA, and a material model calibration method for the artery and plaque. Patient-specific geometric modeling and FE analysis of PTA in femoral arteries are then presented to show how the proposed approach is a step towards a clinical decision support system.

CHAPTER 1

CLINICAL CONTEXT

This first chapter presents the clinical context for treatments of atherosclerosis disease, in particular on the procedure of balloon angioplasty within stenosed peripheral arteries. A description of this vascular pathology is initially introduced, followed by the typical possible therapeutic options, with specific attention on percutaneous transluminal angioplasty (PTA) technique, on which this thesis focuses.

OUTLINE

1 DESCRIPTION OF THE PATHOLOGY

1.1 ANATOMY OF A HEALTHY ARTERY

Even though a precise structure of an artery might depend on its location, the arterial wall basic components are similar at all sites within the arterial tree. A healthy artery mainly consists of three layers: the tunica externa (adventitia), tunica media (media), and the tunica intima (intima) [Figure 1.1]. The intima, the inner most layer, mainly consists of endothelial cells, a thin basal membrane and a subendothelial layer. It is the layer in direct contact with the lumen and hence the blood flow [1]. The arterial flow of blood is usually regulated through vasoconstriction (the narrowing of luminal diameter), and vasodilatation (the growth in lumen diameter). Above the intima lies the internal elastic lamina separating the intima from the media. The media is composed of a network of elastic and collagen fibrils, and smooth muscle cells; it is the thickest layer in the artery. Covering the media, the external elastic lamina separates it from the adventitia, the outermost layer in an artery which comprises mainly collagen.

In general, arteries can be divided into two large categories: elastic and muscular arteries [2]. Elastic arteries are characterized by large amount of elastin in their media; they generally have large diameters and are located near the heart (e.g. aorta). Differently, muscular arteries have relatively thicker media containing more smooth muscles rather than elastin or collagen fibers. They are of smaller diameter in general and are usually located further away from the heart (e.g. peripheral artery).

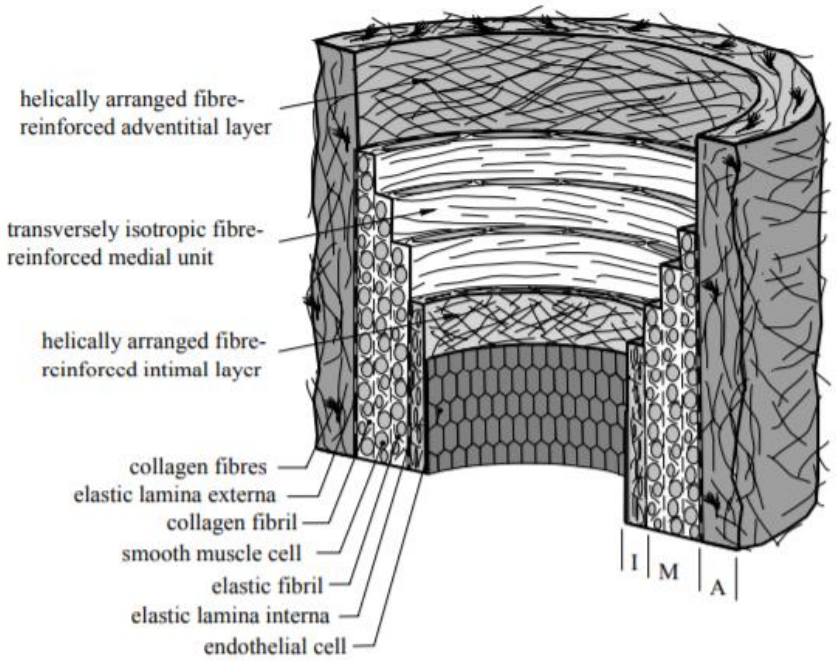

Figure 1.1: A schematic illustration of a healthy arterial structure presenting the adventitia (A), media (M) and intima (I) layers along with their compositions [3].

1.2 PATHOLOGY OF ATHEROSCLEROSIS

Atherosclerosis is one of the most common vascular pathologies in the world, with high mortality rates [4]–[6]. In 2016, ischaemic heart disease and stroke were shown to be the two leading causes of death worldwide [Figure 1.2]. These diseases have been the primary death causes for the last 15 years. Ischaemic heart disease and stroke are associated with atherosclerosis development and atherosclerotic plaque rupture occurring in coronary and carotid arteries respectively [7]–[9]. Furthermore, peripheral arteries are also of the most vulnerable vascular locations for the occurrence of atherosclerosis. The development of this pathology in femoral (peripheral) vessels is the main cause leading to claudication and critical limb ischemia (ischemic rest pain) [10], [11].

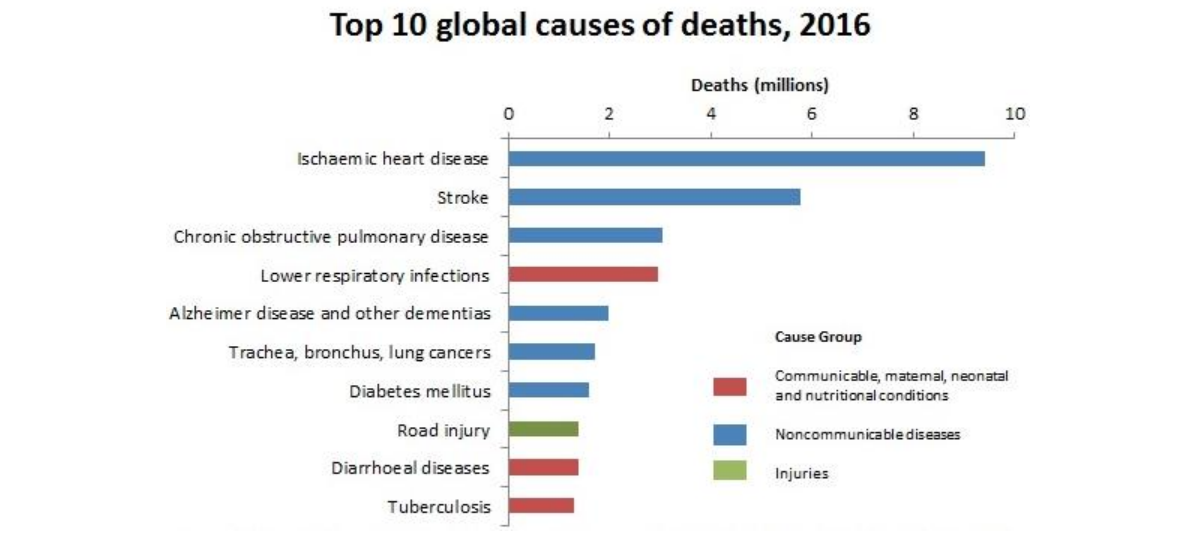

Figure 1.2: The 10 global causes of death in the world in 2016, with ischaemic heart disease and stoke being the two leading ones [12].

Atherosclerosis results in the narrowing of vessel diameter by the accumulation of lipids, calcium and collagen on its inner wall. It consists in the formation of a plaque within the arterial wall, known by atheroma or atherosclerotic plaque [Figure 1.3]. In most cases, atherosclerotic plaque development occurs during a long period of time (more than 40 years), with its primary stages (known by the fatty streaks) initiating at early ages (age of 11-12) [13]. Plaque depositions partly or totally block the lumen, affect normal blood circulation, and might even lead to severe implications on perfused organs (brain, heart, legs, etc). This decrease in blood supply (insufficient oxygen supply) would trigger thickening of the arterial wall [14], [15], which in turn would cause the change in mechanical properties [16], [17].

From one side, atherosclerosis leads to two mechanisms of vascular changes: functional stiffening and morphological thickening of the arterial wall [18]. The arterial wall stiffening process also drives the progression of atherosclerosis in its turn as well, progressively stiffening more the diseased segment

[19], [20]. Atherosclerosis involves elasticity reduction in addition to thickening in arterial walls, thus causing hardening and blood flow blocking in arteries.

Nevertheless, occlusions and elasticity alterations in arteries are not the only consequences of the formation of atherosclerotic plaque. Atherosclerosis is also an inflammatory response to an endothelial dysfunction injury [21]. Blood pressure generating concentrated circumferential tensile stress at certain regions of the plaque surface can cause rupture in the plaque, thus leading to more severe pathologies. Within the fractured plaque, circulating blood would be in direct contact with the cholesterol in the artery. Thromboses (or clot) would therefore form by the coagulation mechanism, preventing normal blood flow, and resulting in a sudden growth in the plaque. Any further portion splitting from the generated plaque would circulate within the blood until reaching smaller blood vessels where it can totally block them, causing perfused organs damage or even death (heart attack, stroke, claudication...). This observation occurs most of the time without any warning beforehand [22], [23]. Small atheroma lesions are usually widely present within populations; they can form in almost any artery in the body. However, only a small amount of these diseased cases cruelly evolve and start showing sharp symptoms; others remaining asymptomatic, augments the sudden risks of this disease (atherosclerosis).

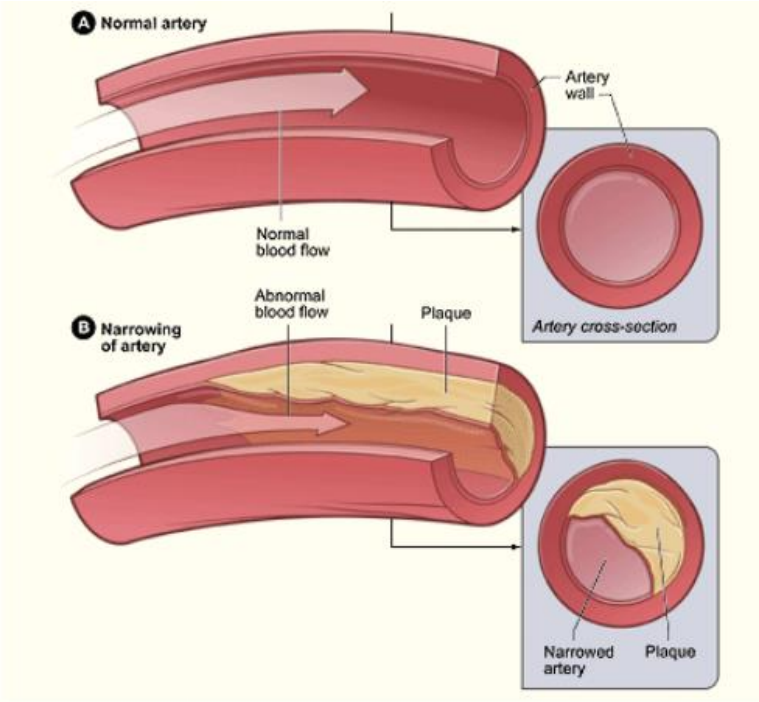

Figure 1.3: Diagram illustrating a healthy artery with normal blood flow (A) and an artery with an atherosclerotic plaque buildup narrowing the arterial lumen (B) [www.lafeber.com].

Atherosclerosis pathogenesis is complex in general. A simplified description for this process could be: first the accumulation of lipids (mainly cholesterol) at the arterial inner wall followed by the growth of the plaque with time forming a stiffer structure composed of connective tissues and collagen fibers.

The resulting deposition occludes the arterial lumen, what is known by stenosis [21]. A more detailed description of the devolvement of atherosclerotic plaque was summarized by Libby (1995) [24] and Sommer (2008) [25] as follows: first low density lipoproteins (LDL) accumulate at lesion prone sites due to an imbalance in their concentration in the tissue in comparison to the plasma; thus lipids are trapped in the extracellular matrix of the intima. An increased number of leukocytes adhere to the endothelial surface, accompanied by specific adhesion molecules. This indicates the initiation of the inflammatory response. Accordingly, monocytes enter the arterial wall, differentiate first into macrophages, and then transform into foam cell after feasting the lipoproteins. Foam cells favor some additional factors which in their turn accelerates atherogenesis process. T-cells also enter the arterial wall, and together with the foam cells start to accumulate forming what is known as the 'fatty streaks' which is the earliest stage of an atherosclerotic plaque [Figure 1.4]. The plaque continues its growth due to the existing inflammatory molecules; then smooth muscle cells migrate from the media to the intima, produce large amounts of connective tissues, and form the plaque fibrous cap over the lipid pool (which comprises necrotic core and microscopic calcium nodules). At its final stage of development, the atherosclerotic plaque described above would either become stable and reduce blood flow only, or it would become unstable and be at risk of rupture and thrombose formation.

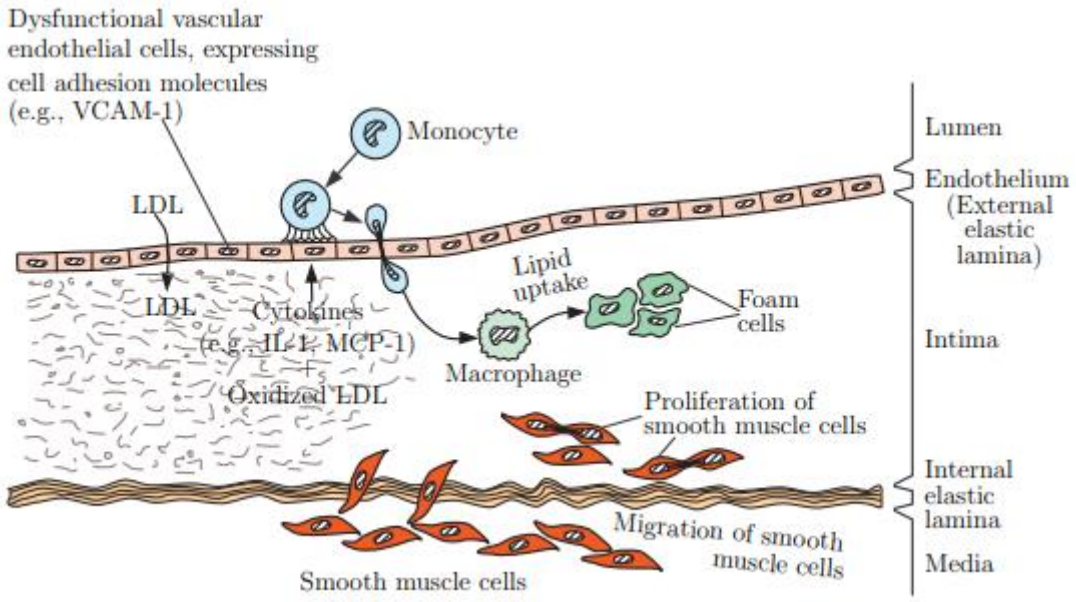

Figure 1.4: Development of the atherosclerotic plaque, initiating at dysfunctional vascular endothelial cells [25].

1.3 FOCUS ON THE LOWER EXTREMITIES

1.3.1 Pelvic and lower extremities anatomy

The distal abdominal aorta bifurcates into the common iliac arteries (CIAs) [Figure 1.5 (A)] which in turn divide at the lumbosacral junction into: 1. the internal iliac arteries (IIAs) that continue posteriorly and medially, and 2. the external iliac arteries (EIAs) that take off anteriorly and laterally reaching the pelvis (at the position just posterior to the inguinal ligament) where they become the common femoral arteries (CFAs). The common femoral artery (CFA) then splits into the deep femoral artery (DFA) posterolaterally and the superficial femoral artery (SFA) anteromedially [Figure 1.5 (B)]. CFA bifurcations usually occur at the lower portion of the femoral head. The superficial femoral artery then crosses the anteromedial thigh becoming the popliteal artery (running posterior to the femur) as it dives through the adductor (Hunter) canal [Figure 1.5 (C)]. The popliteal artery branches laterally into the anterior tibial artery (AT), and continues straight into the tibioperoneal trunk (TPT) which in turn splits into the peroneal (PER) and posterior tibial (PT) arteries [Figure 1.5 (D)]. Finally, both the anterior artery (AT) (which continues as the dorsalis pedis artery (DP) beyond the ankle), and the posterior tibial (PT) (which gives off the plantar branches), would continue branching into smaller arteries in the lower foot [Figure 1.5 (E)].

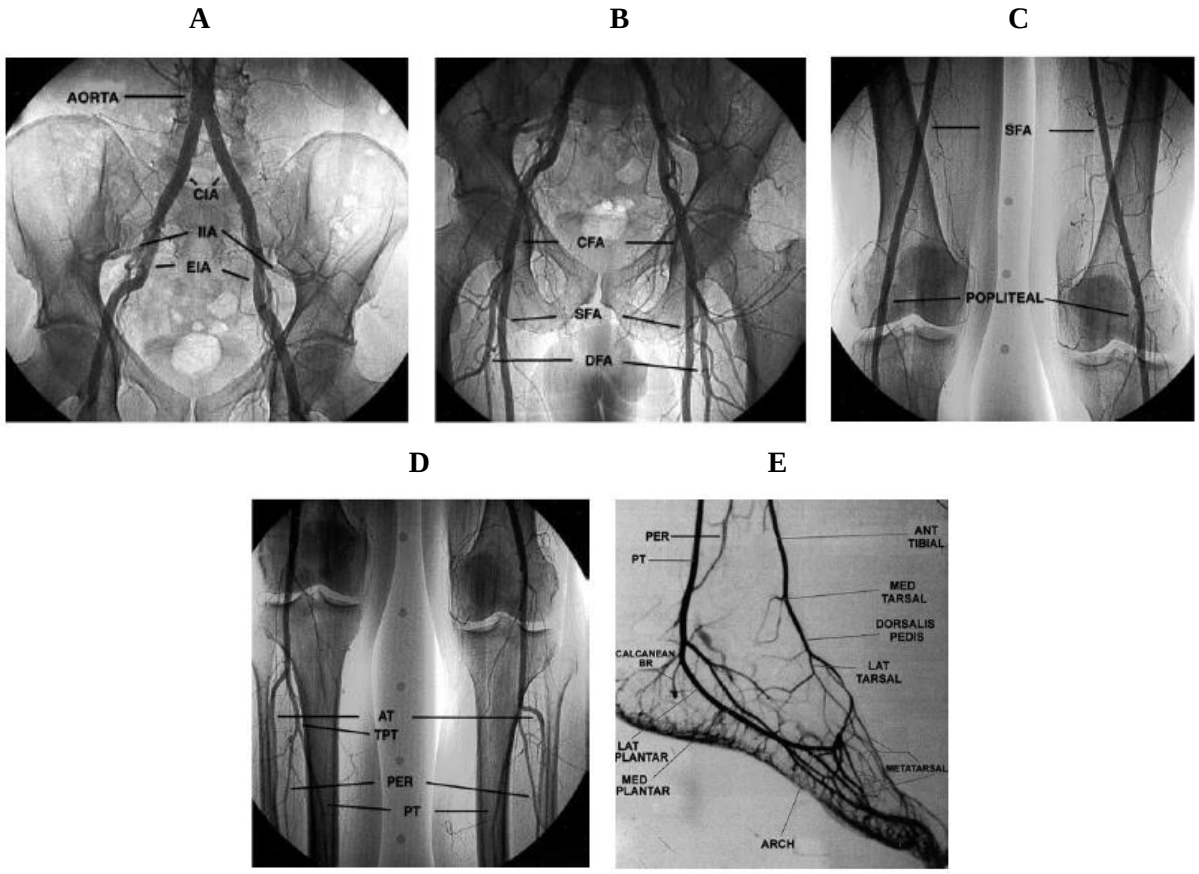

Figure 1.5: Arteriogram showing the pelvic and lower-extremity anatomy [26].

1.3.2 Lower-extremities atherosclerotic plaque

Morbidity and mortality due to peripheral arterial occlusive disease is one of the principle health problems in the Western hemisphere [27]. Likewise, the United States National Institutes of Health reports that atherosclerosis in lower-extremity arteries causes over 60,000 hospitalized cases every year, with each stay lasting more than 11 days on average [28]. Nevertheless, it is always difficult to assess the exact rate of occurrences of Peripheral Arterial Disease (PAD) among populations. The main reason is because a significant part of people with PAD would show no symptoms of the disorder, making it hard to evaluate the exact prevalence in the population. In most cases, patients suffering from PAD would first develop intermittent claudication, a symptom that describes muscle pain on mild effort which occurs during exercise (such as walking), and is relieved after a short period of rest. It is classically associated to early stages of PAD. Unless treated or its risk factors (causing the disease) are modified, intermittent claudication can progress into more advanced stages of PAD: critical limb ischemia, rest pain or even gangrene (tissue death) [Figure 1.6]. Even though intermittent claudication are more frequently seen in men at any age, PAD physical examination findings occur with matching prevalence between females and males [29]. Superficial femoral arteries (SFA) are among the most susceptible arterial locations for atherosclerosis to form [10].

It is important also to mention that it is widely accepted that the presence of PAD increases the likelihood of the patient to also suffer from myocardial infraction, renovascular disease, stroke, and even cardiovascular mortality [30]. A patient with intermittent claudication show a 5-year survival of 70%, with 75% of these deaths being associated to cardiovascular events [31]. Some studies also suggested that patients with asymptomatic PAD have similar risks of cardiovascular morbidity and mortality as their symptomatic counterparts [32].

The accepted methods for determining PAD presence currently comprises physical examination, patient symptoms historical review and atherosclerosis risk factors, in addition to other mini-invasive vascular tests, e.g. ankle-brachial index (ABI). The ABI is a noninvasive test that measures blood pressure in the ankles and then compares it with the pressure of the blood in the arms at rest and after exercise. Imaging tests such as magnetic resonance angiography (MRA), ultrasound and computed tomography angiography (CTA) might also be used for diagnosing peripheral arterial diseases [33], see Chapter 2.

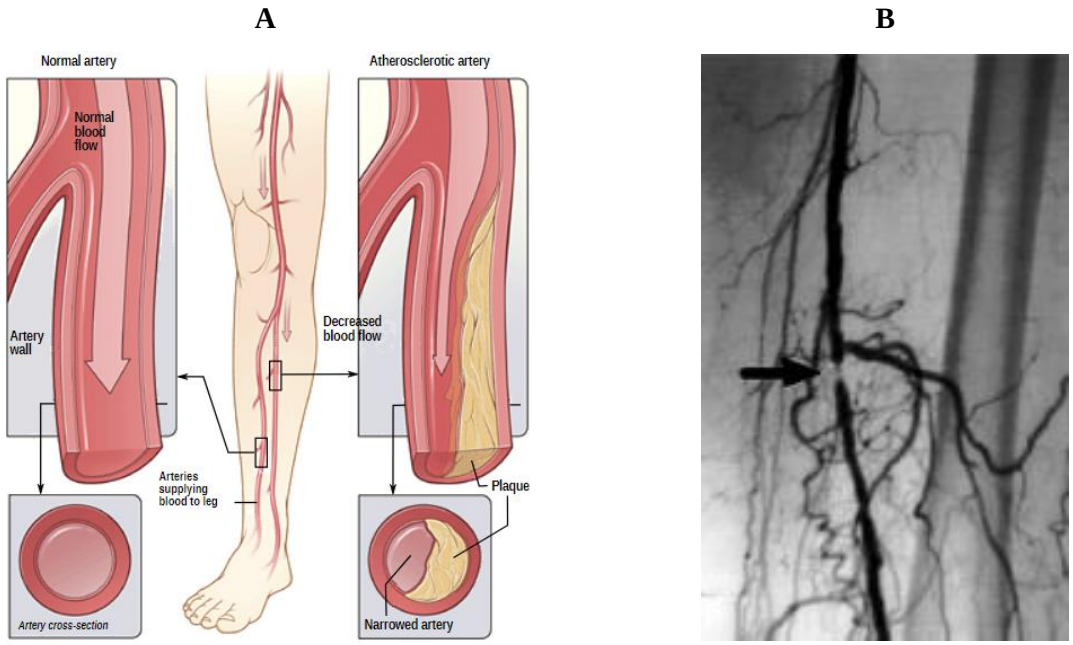

Figure 1.6: (A) Atherosclerosis in peripheral artery [www. upload.wikimedia.org]*; and (B) Arteriogram presenting a real case stenosis in superficial femoral artery (PAD)* [26].

2 THERAPEUTIC OPTIONS FOR ATHEROSCLEROSIS

Lifetime changes (healthy diet, exercising...) are often the most recommended first line treatments for atherosclerosis. Furthermore, medications such as drugs for high cholesterol and high blood pressure can also be appropriate for preventing atherosclerosis from worsening and for reducing its risks (heart attacks, strokes...). However, whenever symptoms are crucial, or if perfused tissues and organs are endangered, surgical interventions would be required. Two families of these interventions are commonly possible nowadays: the open surgeries and the endovascular treatments [11], [34].

2.1 OPEN SURGERIES

2.1.1 Bypass surgery

Bypass surgery involves surgically creating a new path for the blood to divert around and overcome the narrowed or blocked region. The graft is used in order to bypass the obstructed part of the artery [Figure 2.1]. This graft might be either a synthetic tube or a healthy blood vessel taken from the same patient body during the operation. This surgery can be performed in several arteries within the arterial tree: coronary, iliac, carotid, femoral, popliteal… It is most commonly known as a treatment for occlusions in the coronary arteries (coronary artery bypass grafting) where blood flow is re-routed (flowing around the blocked portion) in order to reach the heart. This procedure is considered as very invasive as it requires median sternotomy, incision of the pericardium, in addition to the use of a heart-lung machine for extra corporal circulation as the patient's heart would be stopped during the surgery.

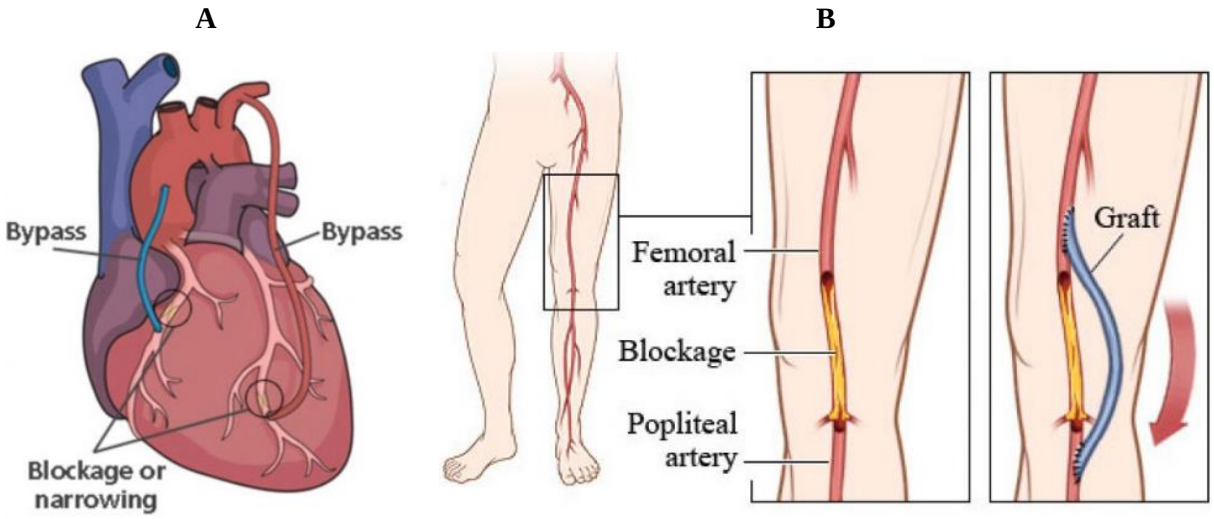

Figure 2.1: Bypass surgery (A) in a coronary artery [www. phg.eu], *and (B) in a peripheral artery* [www.bcm.edu].

2.1.2 Endarterectomy

Endarterectomy is an operation that consists of removing the atherosclerotic plaque from the occluded artery in order to improve blood flow and circulation. It is usually performed on arteries that are close to the skin surface (carotid, femoral); hence it is considered not as invasive as the bypass surgery. Endarterectomy consists of making first an incision in the skin until reaching the diseases artery. Subsequently, the affected artery is cut, and the plaque is removed (also by cutting it) from the arterial lumen. A temporary flexible tube might be inserted to maintain an adequate blood flow during the surgery (especially to the brain in the carotid endarterectomy case). Finally, and after removing the plaque, the surgeon closes the artery and the skin incisions with stitches [Figure 2.2].

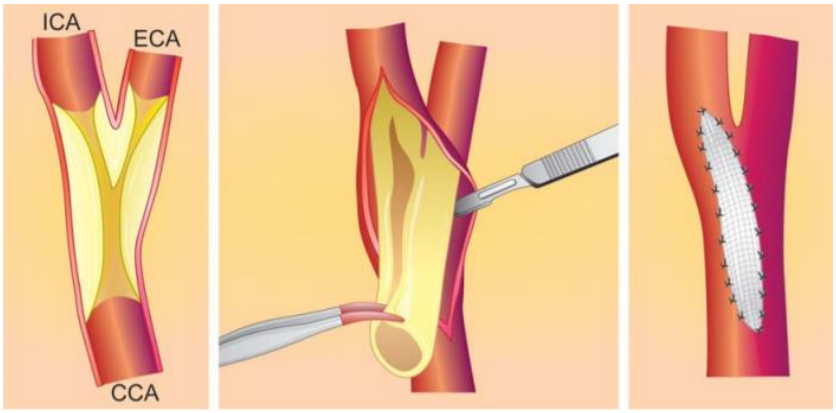

Figure 2.2: Carotid endarterectomy technique. The atherosclerotic plaque involving the common carotid artery (CCA), the internal carotid artery (ICA) and the external carotid artery (ECA) [35].

2.2 ENDOVASCULAR TREATMENTS

2.2.1 Percutaneous transluminal angioplasty (PTA)

2.2.1.1 Percutaneous transluminal angioplasty alone

Percutaneous transluminal angioplasty (PTA) is a minimally invasive procedure for treating atherosclerosis by re-opening occluded vessels. Using specific imaging techniques (i.e., angiography), a balloon catheter is percutaneously inserted and guided to the exact site of the lesion. The PTA balloon located at the tip of the catheter is then inflated in order to compress the plaque against the arterial walls, enlarge the vessel inner lumen and recover an adequate arterial blood flow [36], [37]. Once the artery opens successfully, the angioplasty balloon catheter is then deflated and removed. A detailed description of this endovascular treatment is presented in Section 2.4 of this chapter.

2.2.1.2 Percutaneous transluminal angioplasty with stent implantation

Stent implantation can generally be divided into two categories: balloon-expandable-stents and the self-expandable-stents, based on the embedding approach.

Concerning the balloon-expandable-stent class, the same PTA procedure described in Section 2.2.1.1 is first applied, after which a stent (a tiny expandable metallic scaffold) would be inserted and placed within the newly-opened arterial area in order to support the arterial wall and prevent its re-closure. Deployed by the balloon inflation, the stent would hence remain expanded keeping the vessel open.

Differently, in general self-expandable-stents are deployed without balloons positioned within them initially. Instead they usually expand by themselves after being gradually released from catheters inside the stenosed region, due to their mechanical properties. However, and in most cases (especially when the plaque is calcified and hard to compress), the post-dilatation of the stent with a balloon catheter would also be required to achieve a satisfactory expansion of the deployed stent [Figure 2.3].

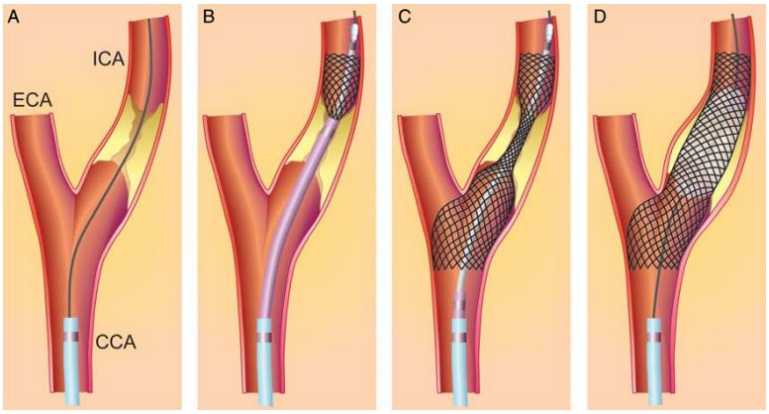

Figure 2.3: Self-expandable-stenting procedure in a carotid artery. (CCA), (ICA) and (ECA) are the common, the internal and the external carotid arteries respectively. After introducing the guiding catheter and wire (A), the self-expanding stent is deployed (B and C). Finally a balloon post-inflation is performed to achieve the required expansion of the stent (D) [35].

2.2.1.3 Drug-coated percutaneous balloon angioplasty/ Drug-eluting stents

Due to recent medical device innovations including catheters with an "active" mode of action, drug-coated balloons and drug-eluting stents are also being lately introduced as minimally-invasive endovascular treatments for stenosed arteries. The deployment of drug-coated balloons and stents are similar to normal implantation procedures described in Sections 2.2.1.1 and 2.2.1.2 respectively for standard PTA balloons and stents. These devices use drug substances: i.e. paclitaxel (initially coated on their folded surfaces during manufacturing) that would be released towards the vessel wall during deployment as an anti-restenotic therapy for atherosclerosis. Drug-eluting stents generally have the advantage of showing better consistency in drug delivery over balloons; however, drug-coated balloons with higher drug surface area in contact with the diseased region, provide more drug tissue bioavailability in comparison to stents [38].

2.2.2 Atherectomy

Besides percutaneous balloon angioplasty and stents which consists of compressing and pushing the plaque into the vessel wall, there exist also other minimally-invasive procedures for treating stenosed arteries. These procedures can generally be joined under the name 'Atherectomy', an endovascular surgery technique that consists of cutting and removing the plaque from the vessel wall. There are in general four types of atherectomy devices: orbital, rotational, laser and directional. The rotational atherectomy for example comprises a rotary device cutting tool (an oval-shaped burr encrusted with microscopic diamond mounted on a catheter) that would break up the plaque blocking the vessel by its high speed revolutions. The main reason for using atherectomy device is usually to treat tortuous and totally occluded arteries that would be difficult to navigate directly using the balloon angioplasty guide wire alone. Surgeons sometimes perform angioplasty preceded by atherectomy; reducing arterial walls stretch injury, dissection and elastic recoil, the two endovascular treatments performing successively might reduce restenosis rates while restoring the healthy vessel lumen [39], [40].

2.3 COMPARISON OF THE DIFFERENT THERAPEUTIC OPTIONS FOR PERIPHERAL ARTERIES

2.3.1 Open surgery vs. endovascular treatment

The common femoral endarterectomy (open surgery) has been the standard treatment for atherosclerosis occlusive disease of the femoral arteries since 1950s [41]. Several studies evaluating the 5 year patency rates of this procedure reported values ranging between 68% and 98% [42]–[44]. However despite the relatively high efficiency of this open surgery treatment, due to its invasive nature, endarterectomy is still associated with high morbidity rates (10%-20%) [45]. A recent review also reported a combined morbidity/mortality of 15% in addition to more than 60% of complications occurring after the femoral endarterectomy [46]. Significant secondary complications can also result

from this surgical revascularization technique. Kuy et al. in 2014 reported possible wound infection rates of around 31%, and hematoma and seromas in 22% of the cases [47]. Moreover, some patients may encounter surgical site infections after their surgery, hence requiring blood transfusion, longer stays at the hospitals, and higher reoperation rates [47]. Hence, for patients who are at high risk for surgical morbidity and mortality, endovascular techniques (i.e. PTA) are favored as alternative treatments [45].

Endovascular treatments are generally less invasive compared to surgical procedures. Their advantage comprises the quicker and less painful recovery of the patients. Unlike surgical procedures that may require several weeks for complete recuperation, endovascular interventions are performed in a much faster time, and treated patients would only have to stay for few days in the hospital, after which they can return home for a small healing period.

Since the publication of the TransAtlantic Inter-Society Consensus for the Management of Peripheral Arterial Disease (TASC II) document in 2007, a large number of observational reports and scientific publications have been using regional and national databases in order to document the prompt adoption of endovascular therapy as a primary approach for treating peripheral arterial diseases (PAD) [48], [49]. This clinical practice fast shift generally appeared due to the continuous technology evolution in the manufactured devices used within endovascular treatments of PAD (i.e. catheters, balloons, stents…). In addition, the improvement attained in the vascular imaging techniques field, and the rising skill levels of endovascular specialists also significantly contributed to this shift in treatment strategy. This lead to an increase in adoption of endovascular treatments compared to surgical therapies even in most complex anatomies (i.e. TASC D category, which represented the most complex revascularization scenario among the four classified categories (from A through D) in the aortoiliac and femoropopliteal territories) [50]. However, this shift was not clearly reported in TASC II; instead it was re-questioned and criticized. But since studies assessing endovascular surgery in relation to other surgical treatments are not common yet and hard to perform, up to our knowledge there is still no clear evidence to support or favor one treatment technique over the other [51]. With the remaining lack in well controlled randomized clinical trials on treatment decision making, whether selecting a surgical revascularization or an endovascular treatment remains an open question.

One main concern when using the endovascular intervention compared to the surgical treatment is usually the lumen patency achieved. Open surgeries have higher primary patency rates in general (durability of patency before any repeated intervention) [51], [52]. According to the recent review study of Wong et al. (2019), it can be seen that there is still a deficiency in evidence for deciding on one treatment strategy within the common femoral artery. Very limited studies with randomized controlled trials compare outcomes at long-term between endovascular and surgical therapies, hence further studies would be required to clarify the effect of each procedure on these (long-term) outcome.

Yet at short-terms, the endovascular interventions showed acceptable acute outcomes for the treated common femoral arteries in comparison to the standard endarterectomy therapies, while limiting procedural complications [53]. Differently, and in practical terms, the initial revascularization strategy (first-line therapy) for atherosclerosis in aortoiliac and other femoropopliteal systems have commonly become an endovascular intervention, despite the limited available level of proof [51], [52]. Arterial tortuosities and atherosclerotic plaque anatomies (length, thickness, stiffness…) can also always interfere in the treatment strategy decisions [51].

2.3.2 Percutaneous transluminal angioplasty alone vs. with stent implantation

As mentioned in Section 2.3.1, endovascular treatments are less invasive compared to surgical interventions. Beside their high procedural success rates, they are relatively easier to perform too. Among endovascular treatments, percutaneous transluminal angioplasty (PTA) has been the most commonly accepted technique for treating atherosclerotic diseases in arteries, and in peripheral ones specifically. Followed by a stent implantation when needed, PTA is the most widely used modality for the treatment of femoropopliteal arterial occlusions for example. Therefore the advantages and the disadvantages of PTA performed alone vs. combined with a stent implantation in peripheral arteries are discussed in this section.

To start with, studies reported primary patency rates in common femoral arteries (CFA) ranging between 59% and 88% at 1 year, and 83% at 2 years after PTA alone [54]–[59]. At longer terms available data are more limited, but primary patency rates reported after PTA were 66% at 4 years, and 60% at 5 years [55], [60], [61]. It is important to mention that provisional stenting, (i.e. conditional implantation of stents when no optimal patency results could be obtained after balloon angioplasty alone), were used in 37% of these studies which might have somehow overestimated the attained primary patency rates presented after PTA alone. On the other hand, primary patency rates found after PTA with primary stent implantation were between 80% and 92.3% at 1 year [62], [63], 92.5% at 2 years [64], and 72.5% at 5-years [65]. Upon comparing results obtained after PTA alone vs. after PTA with stent implantation, it can be noted that stenting seems to enhance patency results with respect to PTA alone. Balloon angioplasty endovascular treatment (alone) is usually associated to *restenosis* in two forms: 1) Elastic recoil of the arterial wall which usually happens immediately after PTA, and 2) A healing response (known by the ‘negative remodeling’ mechanism) that might naturally occur in vessels after being exposed to excessive inflations. This process can cause again the narrowing of the treated vessel by losing its attained lumen within an intermediate-term after the treatment. Surgeons tend to limit these two restricting forms of restenosis after PTA alone by introducing stents; these devices would help keeping an artery open by mechanically supporting its wall.

However, stent implantation after PTA also has its own drawbacks. The major complications associated to stents are their possibility of forming thrombogenicity and in-stent restenosis (ISR).

Thrombogenicity is the tendency of a material in contact with the blood to produce a thrombus, or what is known as a clot. Stent expansion can also cause lesions within the arterial wall with damages that usually cross the intima reaching the media layer. This phenomenon tends to increase platelet accumulation that would already be initiated by the thrombogenicity of the metallic surface of the stent.

Despite their role in supporting arterial tissues open and their aim in reducing restenosis rates, stenting techniques do not always substantially improve primary patency [27], [66], [67]. Stent deployment is still associated with high rates of in-stent restenosis (ISR): 20–40% of patients at 2 years in femoral arteries [68], [69]. ISR is the resulting combination of three main phenomena: 1) elastic recoil immediately after vessel stretching, 2) negative arterial remodeling, and 3) excessive neointimal hyperplasia (a vessel injury caused by the stent that triggers smooth muscle cells in the media to proliferate and migrate into the intima layer where they generate extracellular matrix and collagen [70]). The likelihood of ISR occurring after stent implantations is even higher when stents are deployed within small vessels of long stenosis (i.e. peripheral arteries…), or in diabetic patients [71]. Even though many techniques and inorganic coatings were tested in the aim of reducing ISR, they all ended up failing. The only method that was promising towards ISR reduction was the use of anti-proliferative drugs within the diseased region, which opened the way for drug-eluting stents.

Besides thrombogenicity and ISR, permanent metallic implants like stents also have other drawbacks on long terms. These limitations include: delayed re-endothelialization, endothelial dysfunction, chronic inflammatory local reactions and permanent physical irritations. Despite all the innovations in manufactured stents and their implantation approaches, vascular injuries associated to their deployment are still present. In addition, mechanical behavior mismatches (vasomotion) between non-stented and stented vessel regions and inabilities to adapt to growth would be encountered too. Implanting stents is moreover related to concerns of restricting future revascularizations (surgical or endovascular) or access options [72]–[74]. Finally and specifically in peripheral arteries, small arterial dimensions and complex kinematics [75] (flexions and repetitive stresses) [53] favor the mechanical fracture of stents, calling for specific decisions for their usage.

In summary, two main reasons explain our interest in focusing on PTA technique without stent implantation in this work:

- For certain arteries within the arterial tree such as the femoropopliteal for example, a policy of conventional plain balloon angioplasty appears to be the reasonable initial treatment, with other adjunctive techniques (such as stenting and local drug delivery) reserved to when angioplasty results are suboptimal or when restenosis occurs [76]. This means that, even though it is still not explicitly stated within international publications covering consensus for peripheral arterial disease management (i.e. TASC II), in most lower extremity arteries, PTA is usually the initial

revascularization approach for atherosclerosis [51], [52]. Moreover, it continues to be the technique all other endovascular treatment modalities are compared against [40].

- Due to recent medical device innovations including catheters with an "active" mode of action, drug-coated balloons (DCBs) are being lately introduced as minimally-invasive endovascular treatments for stenosed arteries as well. DCBs combine standard balloon angioplasty and anti-proliferative drug technology. These devices use drug substances such as paclitaxel that would be released towards the vessel wall during deployment. With their possible advantage in reducing restenosis rates, not leaving foreign object behind in the body (e.g. stent), and their ability to be used in anatomy where stent implantation might not be feasible (e.g., across the knee joint) [40], the interest in studying the balloon angioplasty treatment with the lumen gains and elastic recoils associated to it is back on track, as is the case in our hospital center.

The success of PTA at short term is assessed by the residual lumen gained immediately after the endovascular treatment. Besides the compression/damage within the plaques, non-recoverable deformation also occurs in the arteries (clinically termed "controlled vessel injury" [77]). The resulting deformation is usually evaluated by either the patency rate or the elastic recoil ratio (ERR) measured at the maximum stenosed region after PTA. The ERR characterizes how much this stenosed section recoils after balloon deflation. Acting as permanent implants, stents generally reduce the diseased artery recoil by supporting its inner tissue; but the main lumen gain itself is caused by the balloon being inflated. Therefore anticipating acute clinical outcome (residual deformations, elastic recoils...) after balloon angioplasty is of pivotal importance for the evaluation of the treatment success which can influence further treatment decisions.

2.4 A FOCUS ON PERCUTANEOUS TRANSLUMINAL ANGIOPLASTY

2.4.1 PTA procedure

The first clinical application of transluminal angioplasty was described and reported by Dotter and Judkins in 1964 [78]. However, it was only after the procedural enhancement performed by Gruentzig in 1976 [79] on Dotter et al. original technique that PTA method started gaining popularity. Gruentzig's double-lumen balloon catheter with the pre-shaped balloon provided both a reduced size catheter and an efficient dilating implement; this development re-opened the way and encouraged PTA further trials. Since then, balloon angioplasty dilatations have been reported in several arterial locations within the arterial tree: initially in arteries of the lower limb [79], [80]; then after few years in coronary [81] and renal arteries [82], [83]; and later in carotid arteries [37]. Its minimally invasive nature in addition to continuous technical developments in its procedure, have established PTA as a promising possible alternative to the invasive conventional surgery. As mentioned in Section 2.3.2, even though it is still not explicitly stated within international publications covering consensus for

peripheral arterial disease management [51], in practical terms, PTA have commonly become the initial revascularization approach for atherosclerosis in most lower extremity arteries [52].

The endovascular treatment by balloon angioplasty is relatively considered a simple technique. [Figure 2.4] illustrates the PTA method. The procedure which is usually performed in catheterization laboratories consists of the several steps as described below:

- First a small incision is made in the skin through which the Teflon-coated guiding catheter is inserted and threaded towards the diseased artery. The insertion can usually be performed via the femoral, the brachial or the radial arteries.
- A special harmless dye is injected through the thin tube catheter into the bloodstream. Using an X-ray monitor, angiogram (blood vessel imaging technique) allows the surgeon to detect the size and the location of the atherosclerotic plaque.
- A flexible, thin guidewire is then threaded in the guiding catheter and advanced beyond the diseased section.
- A balloon-tipped dilatation catheter is then slipped over the guidewire towards the blockage where it is precisely positioned.
- Once accurately located, the balloon is inflated within the stenosed region. The expanding balloon compresses and/or ruptures the plaque and overstretches the artery, widening the final vessel lumen.
- Once an adequate arterial lumen and blood flow are restored, the balloon is deflated and then removed with each of the guidewire and the catheter. Generally, the resulting vessel lumen is enlarged after PTA.

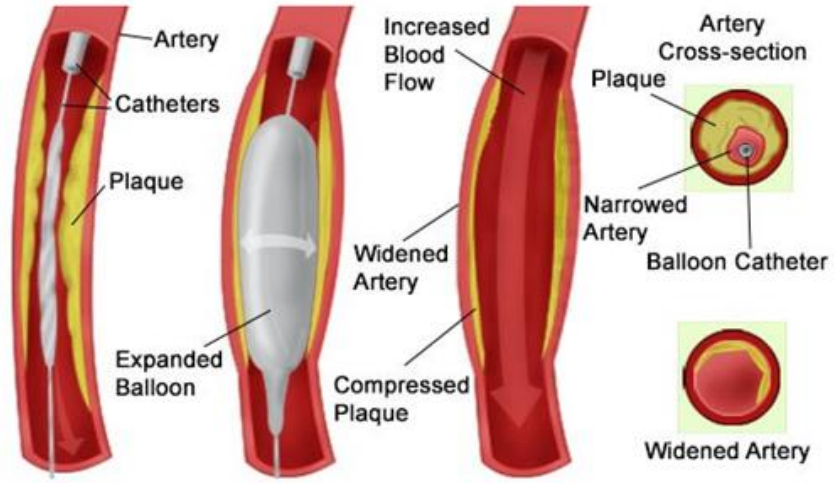

Figure 2.4: Percutaneous transluminal angioplasty (PTA) procedure [www.healthhearty.com].

The exact mechanism by which the dilatation of a balloon angioplasty leads to a successful luminal widening is still not definitively established. Some studies reported that this enlargement in vessel

lumen is due to the compression and the redistribution of the atherosclerotic plaque to adjacent locations within the arterial wall [80]. Other studies associated a successful PTA procedure to overstretching and vessel wall ruptures [84]. Then some others reported intima layer splitting near the edges of the plaque or the rupture of the plaque itself to be related to lumen opening [85]. Finally lesion embolization was also described as a result of PTA intervention [86]. Table 1 presents a brief review of the literature providing some data on the proposed mechanisms in association to the achieved arterial dilatation after PTA. However, consensus on the exact contribution of each mechanism in the lumen enlargement process is still not totally clear. One major reason for this limitation is that these mechanisms are usually highly patient-specific and depend on the selected treatment components too: from the artery being treated (location, thickness, elasticity…), to the plaque (length, thickness, stiffness…) and then to the balloon angioplasty selected (type, length, inflation pressure...).

Table 1: Suggested mechanisms explaining arterial dilatation attained by PTA [87]

Investigator	Year	Compression and redistribution of plaque	Stretching of medial layer	Rupture of wall (tunica muscularis, vessel layer)	Detachment of plaque edges from media (dissection)	Plaque rupture	Embolization of lesion
Dotter et al	1964	X					
Grüntzig et al	1974	X					
Freudenberg et al	1978			X	X	X	
Castaneda et al	1980		X	X			
Block et al	1980, 1984		X	X	X	X	X
Isner et al	1983		X	X			
Chin et al	1984	X		X	X		
Lyon et al	1987		X	X	X		
Faxon et al	1987		X	X			X
Ebner et al	1989				X		

2.4.2 PTA balloons characteristics

As mentioned in Section 2.4.1, the balloon angioplasty system is composed of three basic components: a guiding catheter, a leading guidewire, and a balloon-tipped dilatation catheter. Both the guiding catheter and the guidewire usually have specific features providing a stable access and a conduit for the progression of the dilatation equipment. [Figure 2.5] displays an example of a PTA dilatation catheter and its components.

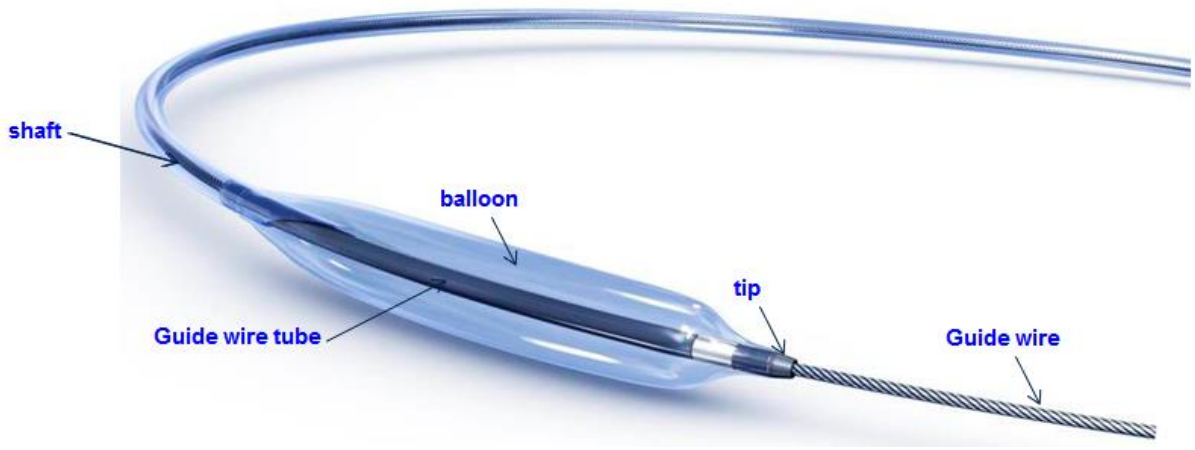

Figure 2.5: Angioplasty balloon dilatation catheter [www.indiamart.com].

In general, dilatation catheters have several crucial features that can influence their performances. To start with, the smallest opening diameter through which the balloon in its deflated configuration can be passed is important. This feature is known by the balloon *profile*. Theoretically, the smaller its initial profile, the easier the balloon can pass through the same lesion. In order to provide better balloon profiles, balloons usually undertake 'negative' (vacuum) preparations during manufacturing reducing their profiles. Thus PTA balloons are commonly crimped onto the body of the catheter so to facilitate insertion into the vasculature of the patient. Any 'positive' inflation applied to the balloon prior to its insertion within the stenosed region should be avoided as it makes it lose its crossing profile ability. This issue is usually observed when clinicians tend to re-use a previously inflated balloon to cross another lesion, and realizes that its secondary profile (after the first usage) is much less satisfactory in comparison to its primary profile (before any inflation).

Besides its profile, *trackability* and *pushability* are also important balloon catheter features. Trackability is the balloon ability to bend so as to facilitate its advancement through tortuous vascular sections. Pushability is the dilatation catheter stiffness which allows it to drive itself through the stenosis. Balloon delivery is usually also helped by the integration of a friction-resistance coating (polyethylene oxide or silicone…) to enhance the surface lubricity [88].

Beyond the mentioned features, the most significant balloon catheter characteristic is its ability to precisely inflate up to a predefined diameter when applying its corresponding inflation pressure, even at considerably high pressures (i.e. 10 to 18 atm). This feature is known by the balloon *compliance*. With the early balloons that were manufactured from polyvinyl chloride (PVC) this phenomenon was still not possible. Balloons compliance led to their oversizing and rupture at relatively low pressures (i.e. 6 atm). Luckily more suitable performances with higher accuracies are recently being attained using balloons manufactured from polyethylene terephthalate (PET), high-density polyethylene, or nylon, despite their law balloon wall thickness (i.e. 0.0076 to 0.0127 mm).

Based on its material and wall thickness, each balloon has an individual *compliance chart* provided by the manufacturer reflecting the pressure at which the balloon reaches its nominal diameter, in addition to its diameter change with increasing pressure. Hence, according to clinicians and manufacturers, PTA balloons can be classified into three main categories in general: compliant, semi-compliant, and noncompliant balloons:

- Compliant balloons tend to reach their nominal (rated) diameters at relatively low pressures (~6 atm), and then continue to significantly inflate with any further small pressure increase; they grow by around 20% above their nominal sizes before reaching their rated burst pressures.
- Semi-compliant balloons such as nylon, high density polyethylene, or polyolefin copolymer (POC) are stiffer than compliant balloons, and usually grow by around 10% over their working pressure ranges (i.e. between their nominal and rated burst inflation pressures). Special care is required when inflating compliant or semi-compliant balloons to pressures above nominal values to avoid over-distending the adjacent normal vessel.
- Non-compliant balloons such as polyethylene terephthalate balloons (PET) are made of very stiff materials that can retain their defined diameters up to very high pressures (~20 atm), allowing them to reduce their growth and experience negligible changes in profile during inflation [36], [88], [89].

Lately, there has been some debate on what type of balloon material is optimal for PTA: some retrospective observational studies suggest differences in angiographic results for different balloon materials; others do not [36].

In all cases, and independent on which balloon type is being used, it is always important to inflate the balloon within its *working range* (prescribed in its compliance chart), and not to exceed its *rated burst pressure*: a threshold pressure a balloon is designed to accept without any rupture.

2.5 SUMMARY

Several minimally-invasive endovascular techniques are clinically available nowadays for the treatment of arterial stenosis. With each technique possessing its own advantages and limitations, deciding on the optimal revascularization option remains an open question. Our primary interest being peripheral lower extremity arteries, this work is focused on the standard percutaneous transluminal angioplasty (PTA) technique, without stent implantation, because first, it is the usual initial revascularization approach and second, the development of drug-coated balloons makes it even more possible to retain sufficient dilation without stent. Even though PTA is a frequently performed treatment technique, choosing the optimum balloon (design and sizing) for the corresponding stenosed patient that would minimize the elastic recoil, maximize lumen gain, but at the same time not damage

the arterial wall is still challenging nowadays according to clinicians and manufacturers. Numerical simulation can be a tool to help design medical devices and/or choose the optimum ones for a specific treatment. The next chapter will therefore present a review of studies modeling PTA using finite element method, and the positioning of our work with respect to the state-of-the-art towards the methodology we propose in this thesis.

CHAPTER 2

STATE OF THE ART AND PROPOSED METHODOLOGY

In this chapter we describe first the varied imaging modalities associated with PTA treatment, which can feed computational studies with different levels of data on the structure and composition of diseased vessels. Then a review of studies modeling this endovascular treatment technique within atherosclerotic vessels using finite element method is presented with some of their advantages and limitations. Finally, towards improving clinical decision support systems, the aim of the thesis is described, and the proposed methodology is introduced.

OUTLINE

1 IMAGING TECHNIQUES

The clinical standard to identify arterial narrowing and to guide endovascular (catheter-based) interventions is angiography as previously illustrated in [Figure 1.5] and [Figure 1.6] in Chapter 1. It consists in using radiography (X-rays) in order to observe the vessel lumen after its injection with a radio-opaque fluid. Angiography provides satisfactory and accurate images concerning the vessel lumen, but is very limited in terms of providing data about the diseased artery and its atherosclerotic plaque. Hence, other *in vivo* imaging tools can be used to provide supplementary data on the structure and geometry of the diseased vessels and on the therapeutic intervention mechanism, in the aim of developing patient-specific geometries for computational analysis purposes.

In this section, different imaging modalities are presented with their varying degrees of accuracy, patient safety and/or cost. Deciding whether one imaging technique is more suitable than another is challenging in general, knowing that each method has its own advantages and limitations [90], [91] depending on the targeted application.

[Figure 1.1] presents images resulting from different modalities described in the following section.

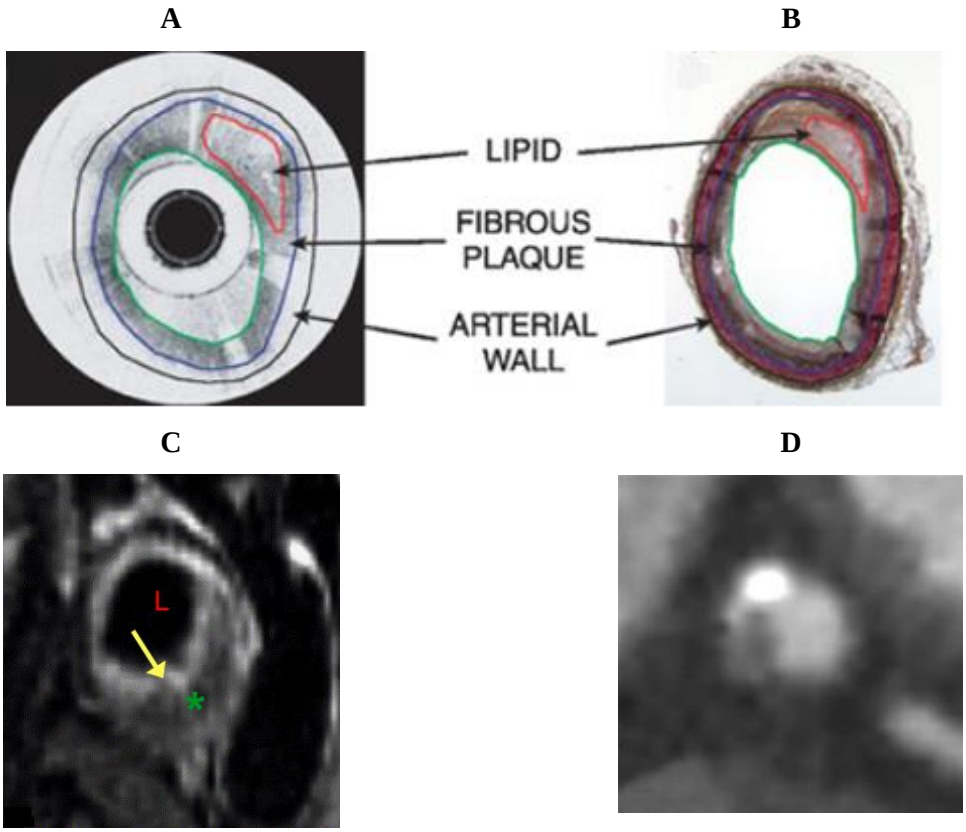

Figure 1.1: Images corresponding to different acquisition methods reported in this section: Segmented (A) optical coherence tomography (OCT) image and (B) histology image for a lipid rich coronary plaque cross-section [92]*; (C) in vivo carotid magnetic resonance (MRI) image (with L: lumen; yellow arrow: fibrous cap; green star (*): lipid pool)* [22]*; and (D) computed tomography angiography (CTA) image for a mixed coronary plaque cross-section (with the lumen seen in light grey, the lipid plaque in dark gray/black, while the calcifications in bright white)*[93].

1.1 HISTOLOGY

Histology imaging technique played an essential role in the development of the primary patient-specific finite element studies with geometry acquisitions. They were available prior to other imaging modalities recently used. Histology is the study of microscopic anatomy of biological tissues. The advantage of using histology consists in providing a large level of details regarding geometric features. In addition, it can also provide a detailed identification of the atherosclerotic plaque components in general, see for instance Ohayon et al. (2007) [94].

However, histology is limited to *in-vitro* analysis. Geometries resulting from histology are in 2D and slicing the tissue may distort its structure.

1.2 INTERVENTIONAL ULTRASOUND

These acquisition techniques use ultrasound sound waves to produce images of the inside of the body. With images usually captured in real time, they can show internal body organs movements as well as blood circulating within blood vessels. Unlike X-rays imaging, no ionizing radiation exposure is associated with ultrasounds. Elastography is one example of the interventional ultrasound imaging modalities. It consists of measuring the propagation speed of a low frequency shear wave into a tissue using ultrasound to measure its stiffness. Up to date it is still most commonly used to evaluate the liver and to diagnose/evaluate conditions in other organs and tissues such as the breast, prostate, muscles etc. However, noninvasive vascular ultrasound elastography (NIVE) are recently being introduced to assess strains or stiffness of peripheral vessel walls (e.g. carotid arteries). With further innovation on this imaging method, it might have the potential to provide a unique approach for the characterization of vascular stiffness [95].

Intravascular ultrasound (IVUS) imaging technique is another type of interventional ultrasound that uses reflected sound waves of high frequencies in order to visualize the arterial wall in a 2D format similar to a histologic cross section. Several research works have been reported as well to perform *in vivo* 3D reconstruction of the artery using IVUS when combined with other imaging modalities.

Concerning its disadvantages, first IVUS requires catheterization thus increasing the risk on patient safety. It also necessitates a pull-back technique which, and because of the pulsatility of the artery, would boost catheter movements generating further risks. This phenomenon mostly occurs within coronary arteries. Furthermore, IVUS is limited in its capability of differentiating the diseased arterial wall and plaque tissue components, thus decreasing the accuracy of their corresponding geometries. Nevertheless, a recent study emphasized that when used in conjunction with a radiofrequency spectral processing system, IVUS would be able to distinguish between the different plaque tissue components (lipid, calcified, fibrous…) [96]. Even though IVUS has provided interesting mechanical understandings to PTA, its usage is still limited to 5 or 10 % of global routine clinical cases [88]. This

is mainly due to the augmentation it causes on the procedure time and expense. Although IVUS acquisition can relatively be considered inexpensive compared other techniques (such as the magnetic resonance imaging), it is still expensive with respect to the traditional angiography.

1.3 OPTICAL COHERENCE TOMOGRAPHY

Optical coherence tomography (OCT) is an imaging modality that generates real-time tomographic images from infrared light backscattered reflections. OCT can be viewed as the optical equivalent for IVUS. The major advantage of OCT over conventional ultrasound-based approaches is its considerably higher resolution (10 times or more) [97]. Thus OCT is an *in vivo* imaging method that allows the generation of arterial 3D models too. Some studies emphasized the ability of OCT in providing more detailed information about plaque constituents in comparison to conventional ultrasound techniques like IVUS [98]. However others reported the inability of this imaging acquisition in differentiating neither between lipid pools and calcium deposits, nor between heterogeneous plaque constituents [99]. In addition, besides being expensive, OCT also requires catheterization and a pull-back practice (similar to IVUS) that would augment the risk to the safety of the patient.

1.4 SPECTROSCOPY

Spectroscopy is a catheter-based imaging tool which determines the chemical compositions of plaque materials. This is usually performed based on the analyses of spectra induced by the interaction of light (or electromagnetic radiation) with the plaque materials. Several forms of spectroscopy are currently available for the characterization of atherosclerotic plaques. One example is the diffuse reflectance near infrared (NIR) form. When a light beam containing a broad spectrum of wavelengths is projected on a certain tissue, the molecules within the illuminated tissue would absorb certain wavelengths from the original spectrum. Thus the resulting spectrum (crossing the tissue) would be missing the wavelengths absorbed by the tissue itself. Then the diffused reflectance NIR spectroscopy would interpret within the NIR window, the absorption amount as a function of wavelengths. Showing promising *ex vivo* results, spectroscopy is under active examination for *in vivo* applications [91].

However, spectroscopy is considered as a limited technique in term of its relatively long acquisition time, which results also in significant motion artifact when performed in clinical settings. Furthermore, it is unable to provide anatomical information by itself. Consequently, it must be combined with another imaging modality (e.g. OCT or IVUS) should any anatomical information be required besides chemical composition.

1.5 MAGNETIC RESONANCE IMAGING

Magnetic resonance imaging (MRI) has the ability of providing simultaneously both compositional and anatomical information on soft tissues, making it unique among other imaging modalities. In general, it can identify and categorize atherosclerotic plaques in human and animal models; it is a non-invasive imaging technique that may be applied *in vivo* for acquiring a 3D image of diseased arteries. Thus it is able to generate a detailed 3D image of the geometry in addition to the composition of a stenosed region [22], [100].

However, this imaging modality is not always available or easily accessible at all clinical sites. It is an expensive technique that would also highly enlarge the procedure time. Besides, MRI is forbidden in patients with metal implants and heart pacemakers. Moreover, Nieuwstadt et al. (2013b) reported that conventional MRI modalities are still limited in terms of correctly evaluating thin fibrous caps, thus reducing MRI capabilities in evaluating plaque rupture risks when related to fibrous caps [101].

A specific branch of the MRI family is the high-resolution magnetic resonance imaging (HRMRI). HRMRI can deliver higher signal-to-noise ratios thus producing images of better quality. It can accurately determine the structure and composition (distribution of tissue types) of a diseased artery. However, besides being more expensive, high-resolution MRI require even longer acquisition times [102]. Therefore HRMRI *in vivo* usage is usually limited to certain applications. Differently, some other studies (such as computational modeling ones) focused on *ex vivo* application of this imaging modality for the sake of obtaining higher levels of anatomical details. One clear example is the work of Holzapfel et al. in 2002 and 2006, which by using the *ex vivo* based HRMRI, presents a promising technique towards a representative patient-specific computational modeling of diseased arteries [103], [104].

1.6 COMPUTED TOMOGRAPHY

Computed tomography (CT) is a 3D imaging technique that uses X-rays to visualize the internal structure of a solid. Emitted X-rays that are transmitted and attenuated according to the tissue density are recorded by the X-ray detector as 2D projection images. The series of 2D planar (projection) images is then reconstructed into 2D cross-sectional slices, which in turn can be further processed into 3D models. Computed tomography angiography (CTA) is a type of imaging modality that combines normal CT scan with an intravenous injection of a special dye (also known as contrast agent) in order to produce ‘illuminated’ scans of blood vessels. This technique can identify mainly the injected vessel lumen in addition to plaque components that have comparably high absorption levels for X-rays such as calcifications.

However, a disadvantage associated with CTA imaging technique is its limitation in distinguishing between other components such as lipidic and fibrous plaques. Lately, several studies highlighted the

ability of high-resolution micro CT scans in establishing images with more details and of higher qualities for diseased arteries [105], [106]. But the majority of these studies were performed in *in vitro* environments. An *in vivo* application of high-resolution micro CT method is still considered relatively more expensive, applies on much smaller scales, and is not always available at all clinical locations.

1.7 SUMMARY

In general, different acquisition methods are currently available to determine patient-specific geometries *in vivo* for computational analysis purposes, with varying levels of accuracy, cost, acquisition time, and patient safety. Accordingly, deciding whether one imaging technique would be more appropriate than another is still challenging to suggest. This is mainly due to the fact that each method has its own advantages and limitations, depending on the intended application. Nevertheless, one of the very few imaging modalities generally present in most hospital protocols and being performed for the majority of patients prior to PTA treatment (specifically in peripheral arteries) is the pre-operative CTA scans. Besides, CTA also presents a satisfactory compromise with a fair cost, acceptable acquisition time, low risk on patient safety, and at the same time it provides a relatively sufficient data in terms of the diseased artery characterization. For this reason, CTA technique will be considered as the only source of patient images in this work, as it is already part of the clinical routine.

2 COMPUTATIONAL ANALYSIS OF PTA

In recent decades, computational modeling studies have been showing significant improvements giving the opportunity for both the academic and industrial sectors to simulate complex nonlinear problems in several engineering science aspects. These numerical studies are based on what is known as Finite Element Method (FEM). One main example of FEM applications is the simulation of PTA deployments within vessels stenosed by atherosclerotic plaques. Due to difficulties in reproducing and experimentally validating the mechanical behavior of atherosclerotic plaques *in vivo*, in addition to limitations for *in vitro* mechanical testing of human tissues, studies use FEM towards evaluating endovascular treatment techniques. This consists of using computational analysis in order to mimic the available *in vivo* systems by reconstructing their geometries, material compositions, loading and boundary conditions [90]. FEMs can help simulate the biomechanical interactions between deployed devices (balloons, stents...) and stenosed arteries; these interactions cannot be fully characterized by routine clinical methods [107]. Moreover, FEMs became a valuable and an essential component of the deployed device design process. Allowing for several fundamental assessments of different PTA system parameters (plaque material composition, device type, device sizing…), computational analysis is shifting towards addressing clinical decision support issues, and more specifically towards clinical pre-operative planning.

2.1 MODELING OF A DISEASED ARTERY

2.1.1 Geometry: generic vs. patient-specific

A certain number of FEM studies are based on plain strain analysis of diseased arteries; few others presented the diseased arteries using 3D models. For both types of analysis (2D and 3D), geometries were either idealized (i.e. generically generated), or created using patient-specific data. Recently, and with simulations showing high sensitivity in results to small geometric and material properties changes [103], [108] FEM studies are shifting more to patient-specific simulations.

2.1.1.1 2D models

Histology was the imaging modality initially used for generating patient-specific geometries for FEM studies. It is also one of the most available techniques implemented for the creation of 2D models. Patel et al. (2003), Ohayon et al. (2007), and Speelman et al. (2011) modeled their 2D patient-specific geometries based on histology as imaging modality [94], [109], [110]. [Figure 2.1] presents a histological cross-section of a diseased coronary artery and its corresponding segmentations for the finite element model from the study of Speelman et al. (2011) [109]. Besides histology, Li et al. (2006), Gasser and Holzapfel (2007b) and Balzani et al. (2012) used high-resolution magnetic resonance (hr-MRI) imaging in order to model respectively the carotid [22] and iliac geometries [111], [112] with an accurate distribution of tissue types. Multi-sequence of hr-MRI data extracted from Li et al. (2006) [22] was conducted as seen in [Figure 2.2]. Differently, in Ohayon et al. (2008) work, two kinds of computations were performed for each patient respectively using: the plaque morphology acquired by IVUS technique (cross-sectional images), and its associated idealized model [113] [Figure 2.3]. Versluis et al. (2006) generated idealized geometric (2D) models for the stenosed carotid artery and asymmetrical plaque [114]. Even though plain strain models are somehow useful in determining some key factors, these models are profoundly limited in terms of finite element analysis accuracy due to the plain strain assumption, in addition to the high sensitivity of the stress distribution to minor variations in geometries [103].

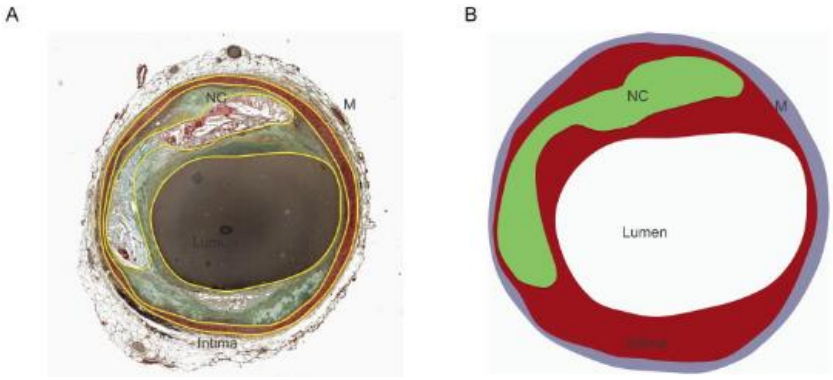

Figure 2.1: (A) Histological cross-section of the coronary artery with corresponding manual delineations of the lumen, necrotic core (NC), intima and media (M.). (B) Matching segmentations used in the finite element model [109].

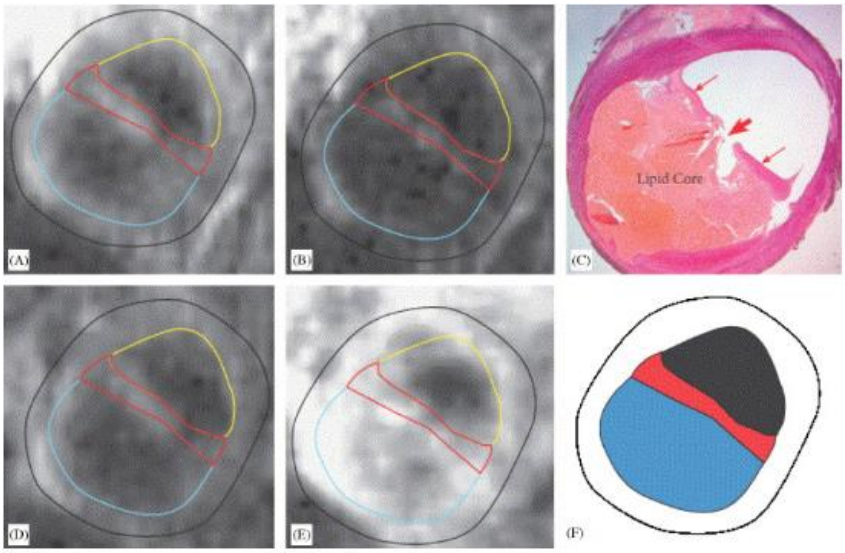

Figure 2.2: Plaque segmentation based on multi sequence in vivo MRI: (A&B) intermediate T2 weighted imaging with short and long TEs respectively; (D) intermediate T2 weighted with fat sat; and (E) T1 weighted black blood imaging. (C) Histology showing region of rupture (large red arrow) in the fibrous cap (small red arrows) in addition to hemorrhage. (F) Reconstructed geometry with lumen in black, lipid core in blue, and fibrous cap in red [22].

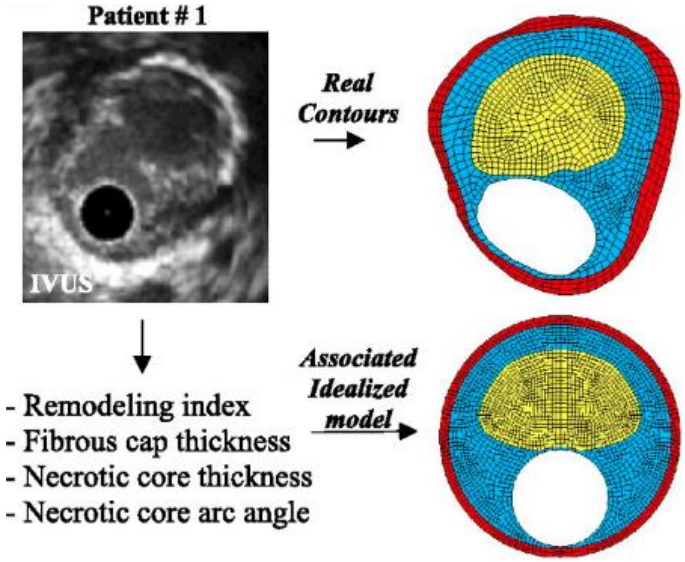

Figure 2.3: Plaque morphology acquired by IVUS technique and its associated idealized model. Red, blue and yellow colors correspond to the arterial wall, fibrosis, and the necrotic core respectively [113].

2.1.1.2 3D models

Other FE studies were based on 3D analysis of diseased arteries. Most of these 3D FE studies were performed within idealized geometries. Lally et al. (2005), Gasser and Holzapfel (2007a), Pericevic et al. (2009), and Karimi et al. (2013) performed FE simulations within generically stenosed geometries corresponding to coronary arteries [5], [115]–[117]. [Figure 2.4] presents the generic model of the diseased artery simulated by Lally et al. (2005) [116]. Similarly, Liang et al. (2005), Bedoya et al. (2006), Timmins et al. (2008), Li et al. (2012) and Conway et al (2017) also performed their simulations within 3D generalized stenotic vessels, each with particular dimensions corresponding to

the diseased artery anatomy being modeled in their work [107], [118]–[121]. Iannaccone et al. (2017) modeled a population-based generic model of the left anterior descending coronary bifurcation with its first diagonal branch [122] [Figure 2.5].

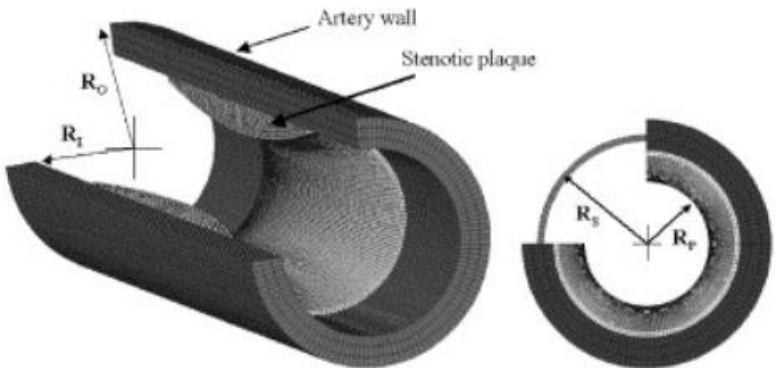

Figure 2.4: Generic geometry of the stenosed coronary artery as modeled by Lally et al. (2005) [116].

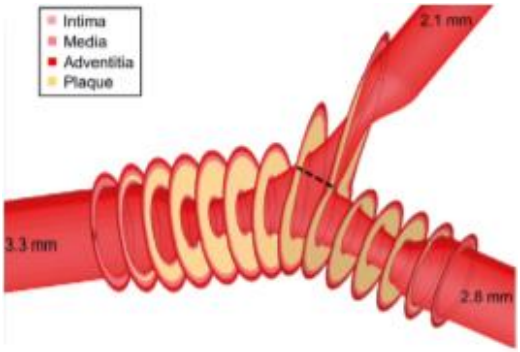

Figure 2.5: 3D view of the coronary bifurcation model with overlaid sections at the plaque location [122].

With results showing high sensitivities to small geometric changes [103], [108], some FE studies are currently using patient-specific models within their simulations. Different levels of details in the diseased artery constituents can be delivered depending on the imaging modality used. Holzapfel et al. (2002, 2005b) used high-resolution magnetic resonance imaging in addition to histology on a postmortem specimen of a human iliac artery for the creation of a full 3D geometrical model with a stenosis [103], [123], see [Figure 2.6]. Similarly, Kiousis et al. (2009) also used the same imaging techniques on an *ex vivo* human diseased carotid bifurcation in order to generate a 3D patient-specific geometry of four different tissue components for the simulations [124], see [Figure 2.7]. In Kiousis et al. (2007), the 3D geometry of the diseased iliac arterial wall was outlined by means of hrMRI, and then reconstructed by the non-uniform rational B-splines (NURBS) [125], see [Figure 2.8]. Ferrara et al. (2008) generated a 3D patient-specific model using *in vitro* magnetic resonance images of a damaged artery [126]. It should be noted that these studies were obtained using *in vitro* imaging techniques and did not consider preoperative *in vivo* data.

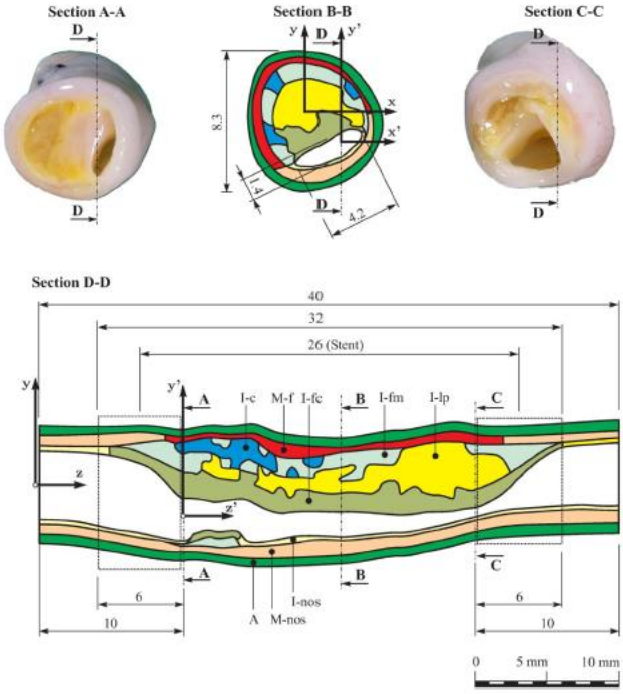

Figure 2.6: External iliac artery sections; with B-B section at the region with the smallest lumen diameter. The tissue components are: non-diseased intima (I-nos), non-diseased media (M-nos), adventitia (A), fibrous cap (I-fc), lipid pool (I-lp), calcifications (I-c), fibrotic intima at medial border (I-fm) and diseased media (M-f) [123].

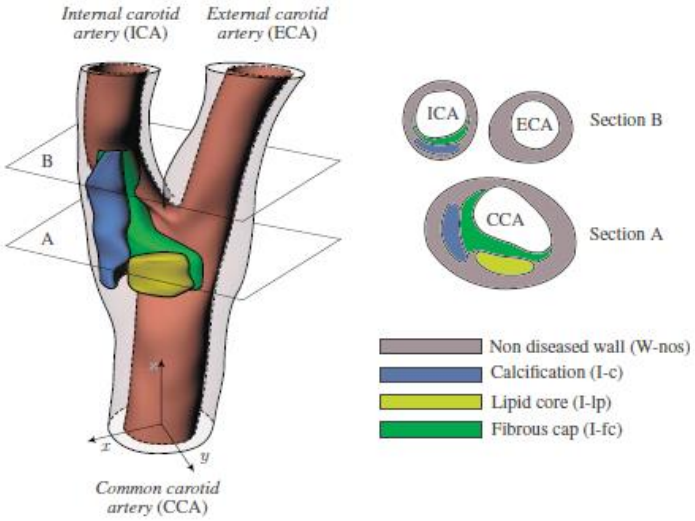

Figure 2.7: 3D patient-specific model of a stenotic human carotid bifurcation with the four tissues considered. The geometry was based on in vitro MRI and reconstructed using NURBS [124].

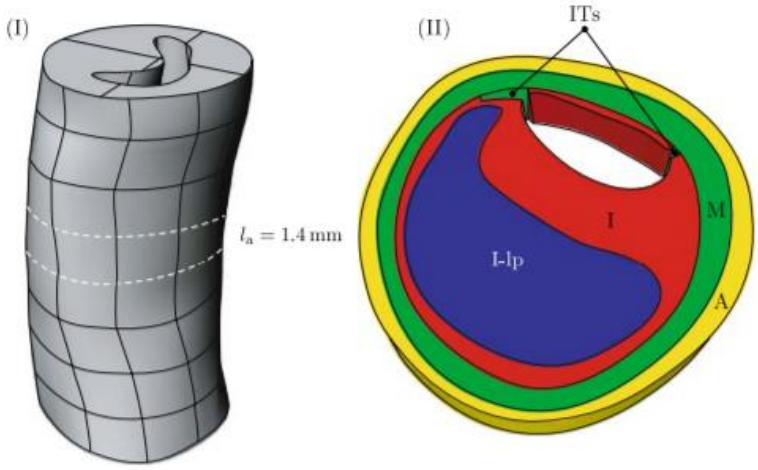

Figure 2.8: (I) 3D geometry of the reconstructed stenotic iliac artery. (II) An extracted arterial slice with the four arterial tissues: intima (I), media (M), adventitia (A), and lipid pool (l-lp) [125].

Differently, some other studies used the computed tomography angiography (CTA) for geometry creation. Auricchio et al. (2011, 2013), Decorato et al. (2014) and Conti et al. (2017) used CTA images from which 3D geometries for their carotid [127], [128], arteriovenous fistula [129], and popliteal [75] arteries were respectively generated, see [Figure 2.9]. It is clear that dimensions vary from one paper to another due to various patients and locations (coronary, carotid, peripheral arteries...). What we can see at the first sight is that the plaque is much less defined in these models compared to the ones generated with other modalities: plaque is mono-component or embedded within the arterial wall. However let us recall here that CTA is the only imaging modality present in the clinical routine so far.

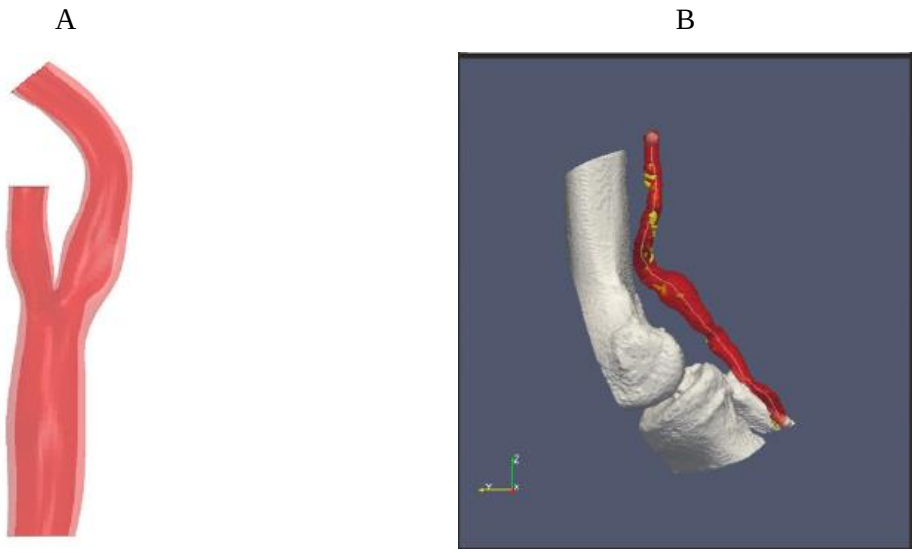

Figure 2.9: (A) 3D model of the carotid artery, with the dark red color corresponding to the lumen while the light color to the reconstructed outer vessel wall profile [127]. *(B) 3D geometry of the bone and the popliteal artery, with the lumen shown in red while the calcifications in yellow* [75].

2.1.2 Constitutive laws

In general, material models used by FEM studies of diseased arteries are usually developed by fitting to experimental data available in the literature. However, even *in vitro* based experimental studies considering arterial and plaque behaviors are relatively limited in numbers [90].

2.1.2.1 Artery

According to Holzapfel (2000) and Humphrey (2002), the artery is a nonlinearly elastic and anisotropic material [130][131]. Therefore it can be treated as a composite material: a matrix that is fiber-reinforced, with fibers corresponding to the collagen constituent within the artery, and modeled by an anisotropic strain energy function.

One example emphasizing anisotropy in arteries is the data reported by Holzapfel et al. (2004) on the (one cycle) quasistatic uniaxial tension tests in axial and circumferential directions showing experimentally the anisotropic behavior of tissues within diseased iliac arteries [132]. Experimental work also reported anisotropic behavior with an ideal dispersion of collagen fibers (i.e. perfect fibers alignment) within the material [133], [134]. Several FEM studies then implemented this material behavior (i.e. anisotropy with ideal dispersion of collagen fibers) within their arterial models [103], [123], [124], [135]. Afterwards, Gasser et al. (2006) considered the hyperelastic modeling of arterial layers with the corresponding dispersion of collagen fibers [136]. Some FEM studies then incorporated this behavior in their models accordingly [111], [128]. Since this model requires collagen fibers dispersion within the tissue, it requires *ex vivo* histological studies as seen in [136].

Besides, other studies considered incorporating the inelastic behavior of arteries. The inelastic effects commonly present in literature include softening behavior similar to the Mullins effect [112] and plastic deformations [137]. Balzani et al. (2012) developed an anisotropic damage model for describing the stress-softening (Mullins effect) phenomenon observed during cyclic tensile supra-physiological loadings applied on arterial walls. The constitutive law proposed in their work includes terms from the continuum damage mechanics and the concept of internal variables (e.g. the scalar-valued variable that was integrated to represent damage of collagen fibers); no plasticity was included in their work [112], see [Figure 2.10 (A)]. Maher et al. (2012) proposed a constitutive model that accounts for the inelastic effects including Mullins effect (stress softening) in addition to permanent set in a fiber reinforced tissue. Inelasticity evolution was governed by a set of internal variables as well [138], see [Figure 2.10 (B)]. Unlike the Mullins effect seen in Balzani et al. (2012) work, permanent deformation is observed at the end of each cycle in the arterial tissue presented in Maher et al. (2012).

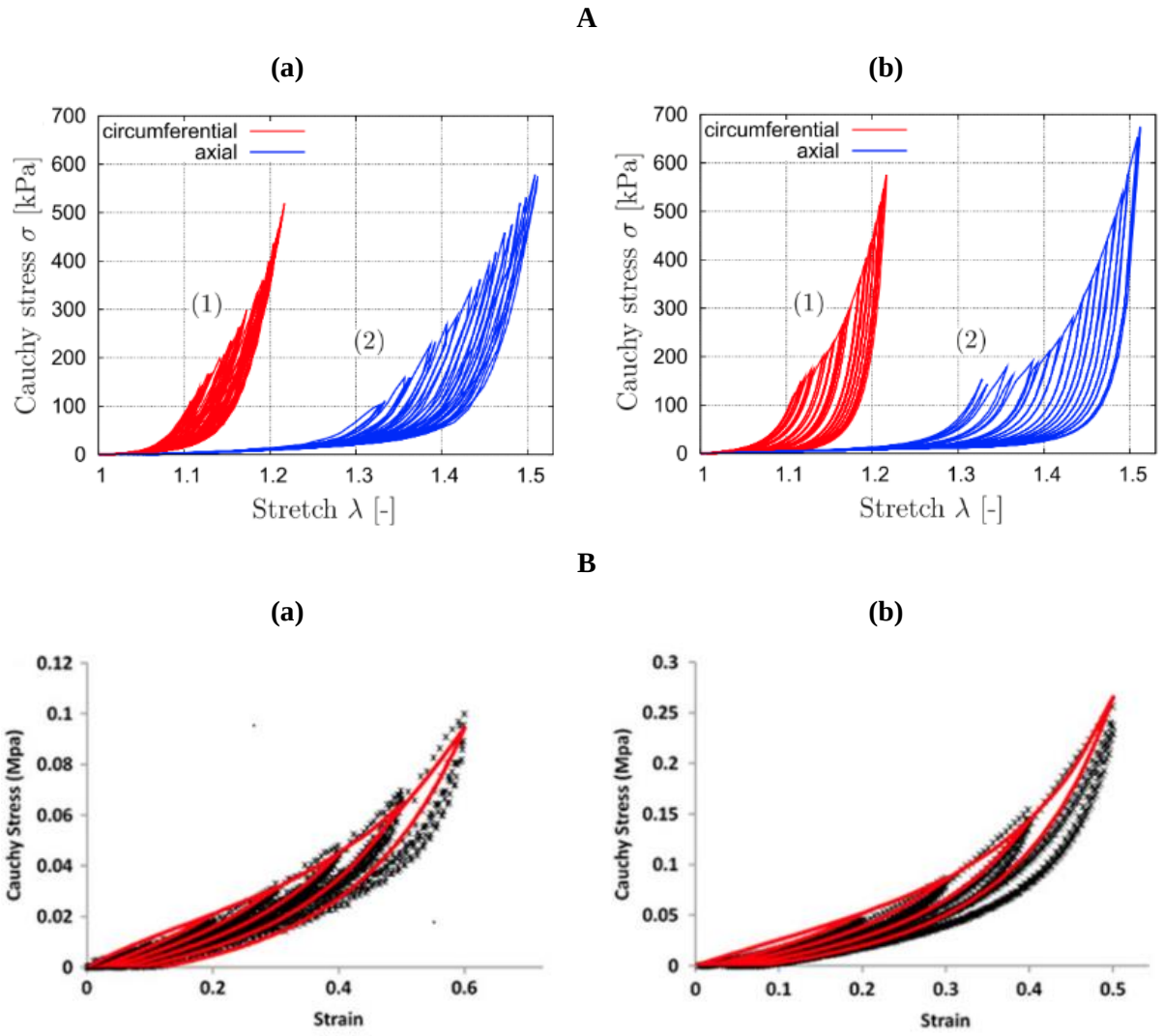

Figure 2.10: (A) Uniaxial cyclic tensile tests of the media from a human carotid artery in circumferential (1) and axial (2) directions: (a) experimental test data, and (b) results of (HGO) constitutive model used [112]. *(B) A comparison between experimental results and constitutive model fit for the stress-strain response in the (a) longitudinal and (b) circumferential directions of a carotid tissue sample* [138].

Differently, Gasser and Holzapfel (2002) suggested an elastoplastic constitutive model for fiber reinforced biological tissues. In their work, they used the multi-surface plasticity concept as the basis of their constitutive framework to induce plastic deformations within the tissue [137]. Then they used their model in order to describe the non-diseased medial behavior in a FEM analysis of balloon angioplasty in Gasser and Holzapfel (2007a). In this study, besides the plaque being modeled as a rigid body, the inelastic material parameters used for the non-diseased media were assumed presumably due to the lack of appropriate mechanical data on the inelastic behavior of vascular tissues [117]. In a similar way, Holzapfel et al. (2002) also used the concept of plasticity to model the inelasticity in non-diseased arterial components (intima and media) associated with tissue stretches beyond physiological domain [103]. No inelastic behavior was assumed for the modeled plaques in [103], [117].

Let us finally mention that isotropic hyperelasticity is still present within several of FEM studies simulating arterial walls behaviors: Neo-Hookean [94], [109], 5-parameter Mooney-Rivlin [116], [127], and Ogden [22], [100], [122] models.

2.1.2.2 Plaque

Some experimental studies considered testing human atherosclerotic plaques to assess their mechanical behavior. Plaque tissue mechanical characterization is frequently performed using uniaxial tensile tests: on aortic [139], carotid [4], coronary [140], or iliac plaques [132]. Walsh et al. (2014) presents a review on studies employing uniaxial testing to characterize plaques mechanical behaviors. They report the presence of a wide range of testing techniques among the reviewed studies which resulted in a large variance in their outcomes, making their comparison a challenging task. Walsh team then proposed a more standardized protocol for uniaxial testing in order to address this issue [141].

Even though *in vivo* plaque tissues experience some circumferential stretching during physiological (normal blood pressure pulsation) and supra-physiological loadings, the tissue is exposed more to radial compression. Thus some other studies considered performing compression tests in order to determine plaques mechanical behaviors. Chai (2015) presents a review on different techniques used to measure plaques mechanical properties under compression. They reported that similar to tensile studies, a wide variety in testing and loading protocols were also available for studies performing compressive tests on plaques, resulting in a large variation of stiffness outcomes [142]. Being interested in global stiffness of plaques, we will focus on studies performing the traditional unconfined compression test. In quasi-static experiments, the material stiffness can be identified, whereas cyclic compression at different rates helps determining frequency-dependent material characteristics [142]. The majority of compressive studies tested plaque tissues under static unconfined compression from different arterial locations: aorta [143], aortoiliac [144], and carotid [145]. Without dynamic effects, they could not characterize the inelastic behavior of the plaques. Differently, fewer other studies applied dynamic loading conditions during their tests, and therefore were able to obtain the recoverability and inelasticity parameters. They were also performed at plaques from different locations within the arterial tree: aorta [146], aortoiliac [147], and carotid [148].

Up to our knowledge, there exist only a limited number of experimental studies specifically reporting on the inelastic behavior of atherosclerotic plaques [147], [148]. In the work of Salunke and coworkers, the behavior of plaques under successive cyclic compressions and successive stress relaxations, in addition to ‘rest’ periods at unloading in each case, was examined. Different degrees of recovery and relaxation behaviors were observed depending on the plaque type with the calcified one reporting more elastic behavior than the other types [147]. Similarly, Maher et al. (2011) also reported the inelastic behavior of atherosclerotic plaques but at a wider range of applied strains. Human carotid plaques inelastic mechanical properties were investigated using a radial compressive cyclic loading

regime. This regime first allowed the observation of the changing stress-strain behavior resulting from loading history of the material; moreover it allowed the quantification of the remaining plastic deformation within the tissue. [Figure 2.11 (A and B)] shows the stress-strain curve representing a plaque of a typical mixed classification for the cyclic loading applied to the sample. The red dotted line represents the theoretical 'load envelope' of the tissue (i.e. a curve composed of the peak stress–strain values generated at each strain level). In rubbers, it has been observed that the monotonic loading behavior of a material is similar to this loading envelope. Since the varying nature of atherosclerotic plaque properties limits testing cyclic and monotonic behaviors separately, this loading envelope (corresponding to the cyclic testing) was assumed to be also indicative of the monotonic loading behavior of the plaque [148]. [Figure 2.12] illustrates the stress-strain curves of the atherosclerotic plaque tested with its different constituents: calcified (stiff), mixed, and echolucent (soft), during the initial loading and reloading cycles. [Figure 2.13] presents the plastic strain occurring on unloading for the increasing peak strain applied in the plaques.

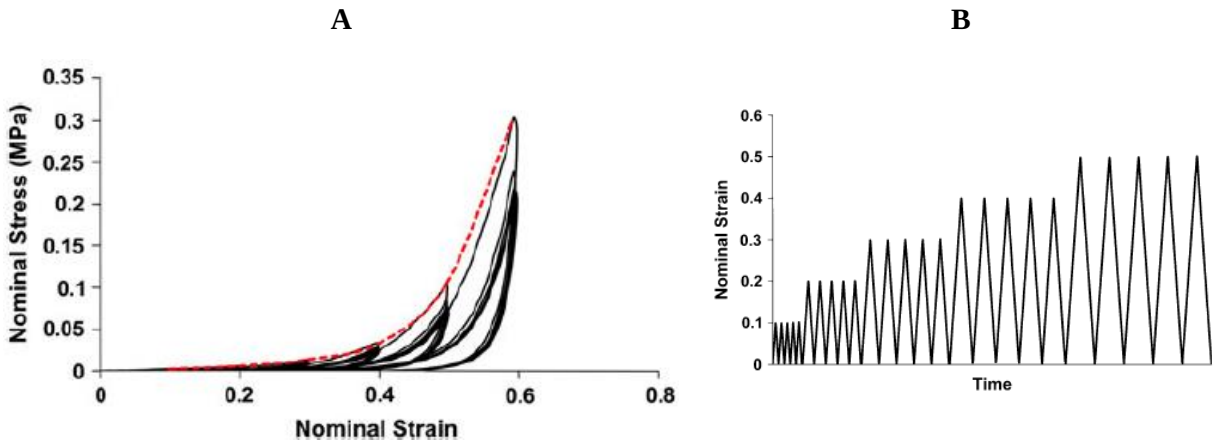

Figure 2.11: A typical response of an atherosclerotic plaque sample to the cyclic compressive loading applied [148].

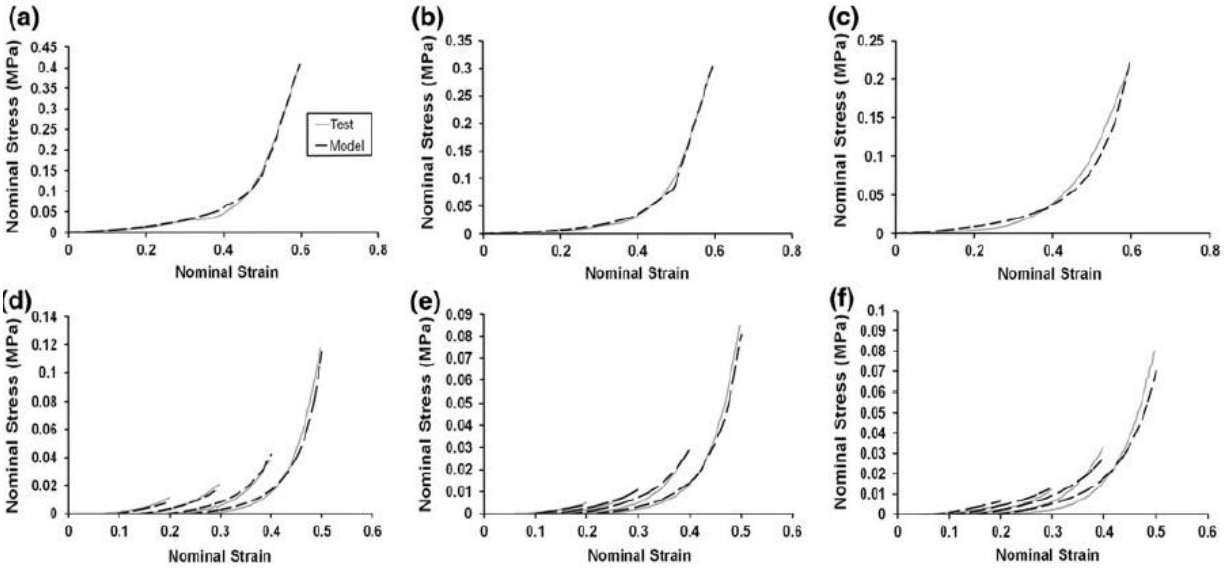

Figure 2.12: The experimental data (in grey), in addition to Maher's model fit (dashed black lines) for the initial loading behavior of the representative calcified (a), mixed (b), and echolucent (c) plaques; the second loading cycle of each strain level of the same representative plaques [(d), (e), and (f), respectively] [148].

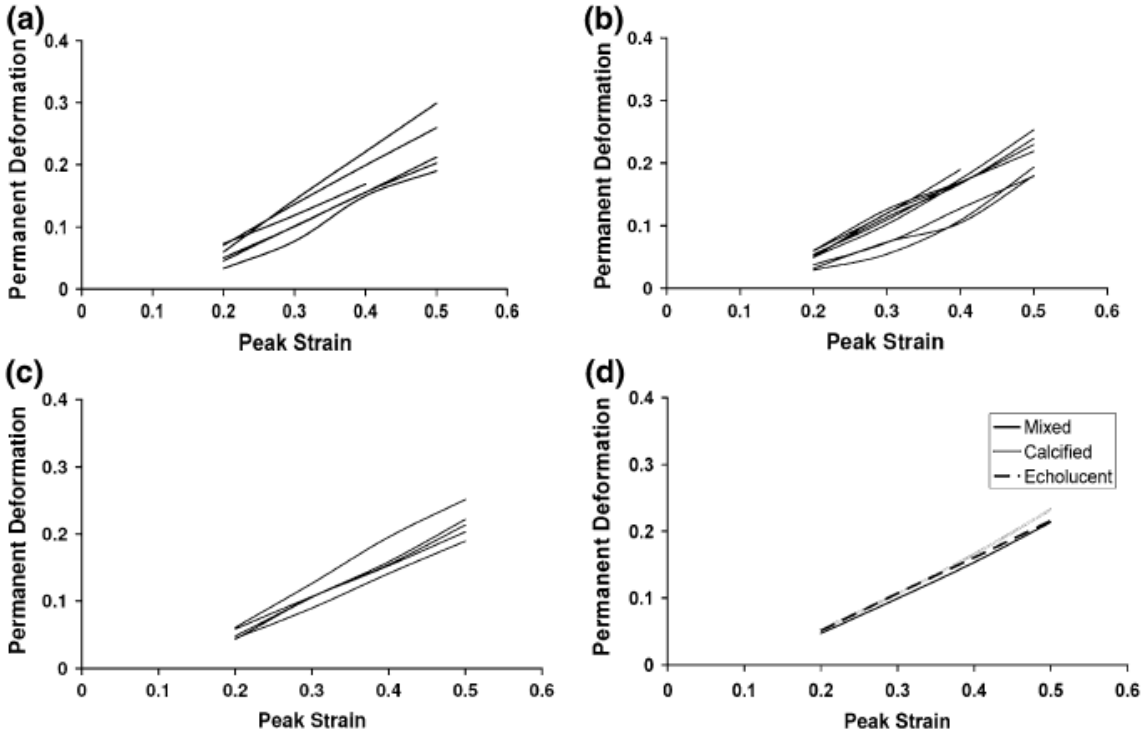

Figure 2.13: Plastic deformation at different applied peak strains for the three clinically classified plaque specimens: (a) calcified (stiff), (b) mixed, and (c) echolucent (soft); (d) presents for each classification the mean plastic (residual) strain for certain applied peak strains [148].

In the literature, most atherosclerotic tissues are usually modeled using the hyperelastic constitutive law [130]. Accordingly, several (2D and 3D) FE studies modeling diseased tissues used hyperelastic models [22], [109], [119], [123], [125], [127]. Moreover, it is interesting to mention, that the experimental data documented by Loree et al. (1994) (which reported the stress-strain behavior of 26

human aortic plaques classified as cellular, hypocellular and calcified [139]) was a common set used by several FE studies modeling hyperelasticity such as [5], [116], [127].

Besides, there exist also some FE studies which considered analyzing the rupture of soft diseased arterial tissues by incorporating different damage mechanisms: crack propagation, cohesive zone, or damage models. Yet since soft tissues usually experience heterogeneous, nonlinear, anisotropic, and viscoelastic behavior, modeling damage remains a complicated issue. Therefore physically describing in addition to modeling damage and failure in soft biological tissues is still limited and presents a challenging task [149]. Versluis et al. (2006) incorporated a crack propagation model into 2D idealized stenosed carotid artery and assessed the fatigue within the plaque over a number of pulse cycle [114]. Ferrara et al. (2008) integrated an anisotropic cohesive zone model within their 3D patient-specific geometry instead [126]. Differently, an isotropic cohesive zone model was developed by Gasser et al. (2007b) for simulating the atherosclerotic plaque fissuring and dissection during PTA [111]. Last but not least, Conway et al. in (2014) and (2017) incorporated models including the Mullins effect (stress softening and permanent set) within their FE simulations [121], [150]. This phenomenon, attributed to damage accumulation, was applied to the diseased tissues in their work using the compressive cyclic test data presented by Maher et al. (2011) [148].

Finally, few other FE studies considered including plasticity within their diseased tissues. With the experimental evidence of permanent deformation after load removal in plaques [148], Liang et al. (2005), Gastaldi et al. (2010) and Conway et al. (2014, 2017) incorporated plasticity in their plaque models [107], [121], [150], [151]. Up to our knowledge, very few FE studies such as Iannaccone et al. (2017) [122] considered including plasticity in both the plaque and arterial models together at the same time. For all the reported studies which included plasticity within their plaques, a perfect plasticity model was assumed. With the lack of sufficient experimental data representing plaque ruptures and its variabilities, different rupture stresses and strains were considered in the assumed perfect plastic models of FE studies: either based on the available monotonic tensile test data (such as Loree et al. 1994 [139]) [121], [151], or roughly chosen [107], [122].

2.2 MODELING OF PTA SURGERY

2.2.1 Devices modeling

PTA devices were modeled at different levels of complexity in the literature, from the absence of balloon (surface pressure instead) to the detailed unfolding of the balloon.

To start with, several studies considered modeling the physiological loadings (e.g. normal blood pressure) within diseased arteries, and therefore applied surface pressure on their geometry as loading condition such as Ohayon et al. (2008) in 2D [113] and Karimi et al. (2013) in 3D [115]. Similarly, at

supra-physiological loading, some other studies directly applied a uniform pressure on the luminal inner surface of the stent [152], [153].

Several other studies modeled the balloon as a cylindrical geometry within the stenosed artery and neglected the modeling of the unfolding process during its deployment:

- Holzapfel et al. (2002), Gervaso et al. (2008), Grogan et al. (2012) and Conway et al. (2017) used displacement loading to drive the inflation of their balloon [103], [121], [154], [155].
- Decorato et al. (2014) inflated a balloon using an internal pressure inside the balloon modeled as linear elastic [129].
- Liang et al. (2005) modeled a cylindrical balloon using a bilinear hyperelastic material driven by an internal pressure [107].
- Schiavone and Zhao (2015) modeled a polyurethane (rubber) cylindrical balloon using a hyperelastic Mooney-Rivlin material driven also by an internal pressure [156].
- Gasser and Holzapfel (2007a), Kiousis et al. (2009), Zahedmanesh et al. (2010), Li et al. (2012), and Iannaconne et al. (2017) modeled a pressure-driven cylindrical balloon using the theory of fiber-reinforced material, by assuming two families of fibers with different mechanical properties oriented in the longitudinal and circumferential directions, and embedded in an isotropic matrix-material [133]. The longitudinal fibers are assumed to be very stiff, whereas the circumferential-oriented ones are assumed to be very soft initially, and become stiffer at larger strains [117], [120], [122], [152], [157].

Last but not least, some other studies like Gervaso et al. (2008), De Beule et al. (2008), Gastaldi et al. (2010), Zahedmanesh et al. (2010), Conway et al. (2014), Schiavone and Zhao (2015), and Geith et al. (2019) modeled the foldings of a balloon before inflation based on its initial crimped geometry (i.e. modeled the unfolding process during the deployment) [150]–[152], [154], [156], [158], [159].

Most of the mentioned FE studies considered implementing stents within their simulations. Gervaso et al. (2008) compared three different approaches in modeling stent expansion, i.e., without balloon (pressure applied on the stent inner surface), free cylindrical rubber balloon inside the stent, and a folded balloon. They showed that the folded balloon method gave an inflation behavior of Cordis BX-Velocity stent closer to the manufacturer data [154]. Likewise, Schiavone and Zhao (2015) recommended using folded balloons in the simulation of stent deployment. They reported that the folded balloon produces sustained stent expansion under a lower pressure in comparison with a rubber balloon, leading to higher stress level and enhanced final inflation for the stent-artery system [156].

Differently, in comparison to applying pressure at the stent inner surface or to modeling detailed balloon folding, Zahedmanesh et al. (2010) reported that applying pressure to the inner surface of a stent and using restraining elements in connection to the stent as well (which would restrain further

stent expansion beyond its prescribed inflated diameter) may be used as an optimal alternative approach for numerically modeling stent PTA within complex arterial geometries. They stated that even though this method can be somehow limited in precisely predicting PTA device deformation (dog-boning and foreshortening) and vessel stresses occurring during the expansion, it can still accurately estimate these parameters at the final state of expansion and after full recoil [152]. In a similar way, De Beule et al. (2008) reported that an unconfined straight stent expanded using a rigid cylindrical shaped balloon would give an accurate prediction of the fully deployed stent geometry relative to that achieved in more computationally expensive wrapped balloon simulations [159]. Moreover, the appropriateness of using a cylindrical tube to simplify stent angioplasty simulations has been also verified by Grogan et al. (2012) [155].

2.2.2 Solver types

The majority of FEM studies used explicit solvers for modeling PTA (see for instance [122], [150]–[152]). This is generally to avoid convergence issues associated with high nonlinearities present in such systems resulting from nonlinear material behaviors, large deformations, and complex contact conditions. But since the explicit integration method is conditionally stable, specific attention should be paid to the selected time increment size which mainly depends on the material parameters, density, and characteristic element length (minimal nodal spacing). This time step size should not exceed a specific critical value. Therefore, besides the addition of non-physical dynamic inertia effects (mass scaling), simulation times can be very large.

With the drawbacks associated with explicit solutions, implicit time integration method seems to offer more benefits when possibly used (see for instance Geith et al. (2019) for more details [158]). Even though convergence criteria can sometimes be case-specific with an implicit solver, it still allows for larger time steps without adding nonphysical masses or changing the quasi-static character of converging simulations. Larger steps would accordingly significantly decrease the computational time of the performed FEA.

2.2.3 Modeling the procedure steps

PTA procedure steps varied among the different FEM studies modeling this treatment technique. In general they can be classified into five main categories:

- Holzapfel et al. (2002), Liang et al. (2005), Gasser and Holzapfel (2007a), Li et al. (2012), and Decorato et al. (2014) modeled the inflation and deflation (loading and unloading) of angioplasty balloons without stent implantation [103], [107], [117], [120], [129].
- Auricchio et al. (2011) and Conti et al. (2017) modeled the deployment of self-expandable stents with a superelastic material response (only loading) [75], [127]. Pericevic et al. (2009) modeled stent inflation by applying a surface pressure directly on the inner surface of the stent itself [5].

- Liang et al. (2005), Li et al. (2012), and Decorato et al. (2014), Zahedmanesh et al. (2010), and Conway et al. (2014) modeled the deployment of balloon-expandable stents (i.e. stent inflation driven by the balloon inflation, followed by balloon deflation while the stent remains deployed) [107], [120], [129], [150], [152].
- Conway et al. (2017) modeled pre-dilatation followed by the deployment of a balloon-expandable stent. Pre-dilatation is represented by first inflating and deflating an angioplasty balloon within the lesion (similar to the 1st category presented); and then pursued by deploying a balloon-expandable stent (as described in the 3rd category) [121].
- Gastaldi et al. (2010) and Iannaconne et al. (2017) modeled the deployment of a balloon-expandable stent followed by post-dilatation. A balloon-expandable stent is initially deployed (as described in the 3rd category); afterwards, another balloon is inflated and then deflated (similar to the 1st category) within the already deployed stent [122], [151].

2.3 MAIN SIMULATION OUTCOMES

As seen in the constitutive laws section, FE studies of diseased arteries use various elastic and inelastic material models, and these models are usually fitted to several sets of experimental data available in the literature. Accordingly generated outcomes usually vary among different simulated models.

Starting with ***elastic material*** models, some FE studies considered two-dimensional (2D) (plain strain) plaque biomechanical responses such as plaques' fibrous cap mechanical stress variation in relation to the disease histology and morphology, under physiological loadings [22], [109], [110] [113]. They mainly demonstrated that the cap peak stress, which is a known predictor for evaluating plaques instability and vulnerability to rupture, is to be viewed as a function of the combination of cap thickness, arterial remodeling index, and necrotic core thickness, rather than a consequence of the plaque fibrous cap thickness alone [113]. Furthermore, calcifications decrease the stress felt in the plaque unlike lipid pools that increase it [22], [110]; with higher stress concentrations observed at the shoulders, and at the thinnest fibrous caps sites within the plaques [22]. In addition, Speelman et al. (2011) reported that incorporating the initial stress into the atherosclerotic plaque model showed accuracy improvements in stress distribution within plaques towards better rupture risk analysis in the future [109].

Other studies highlighted the importance of 3D modeling (whether idealized or patient-specific) for further accuracy improvements in assessed data from simulated diseased arteries under different loadings (physiological and supra-physiological) [160], [161]. Most 3D FE studies were performed within idealized geometries; they evaluated 3D stress distributions within stenosed arteries to analyze their sensitivity to geometrical and material composition changes, or to design the deployed devices. Karimi et al. (2013) stated that soft plaques experience higher stress values and are thus more vulnerable to rupture compared to calcified plaques under normal physiological loading [115].

Schiavone and Zhao (2015) reported that the use of an anisotropic artery model reduced the expansions in the system at peak pressure compared to an isotropic one, but at the same time increased the final diameter due to the decrease in recoiling effect. They also stated that the stress distribution in the artery-plaque system was also dissimilar for different combinations of constitutive models for the artery and plaque [156]. Lally et al. (2005), Bedoya et al. (2006), Timmins et al. (2008), and Pericevic et al. (2009) reported that under supra-physiological loading, both final lumen radius and circumferential stresses were significantly influenced by stent design and plaque material composition [5], [116], [118], [119]. However as using idealized geometries showed that simulated results in diseased arterial models are highly sensitive to geometric and material parameters, lately patient-specific FE studies have become standard [103], [108]. Among these patient-specific FE studies, some focused on evaluating plaque vulnerability and risk to rupture at normal blood pressures (without any supra-physiological loading caused by a balloon or a stent…) [124]. Others (including Holzapfel et al. (2005), Kiousis et al. (2007), Auricchio et al. (2011) and Conti et al. (2017)) considered implanting stents within their simulations before any balloon deflation (using balloon-expandable or self-expanding stents), hence not assessing residual deformations obtained immediately after PTA alone [75], [123], [125], [127]. They focused mainly on stress distribution within stenosed arteries in relation to different stent designs (similar to what generic studies assessed), with results showing significant sensitivity as well. Conti et al. (2017) focused on assessing the mechanical response of a stent model virtually implanted inside a stenosed region when subjected to popliteal artery kinematic during leg flexion. Their study highlighted the importance of including non-linear and complex biomechanical loads for the design of popliteal stents [75].

On the other hand, some other studies considered incorporating ***inelasticity*** within their models of diseased arteries. Versluis et al. (2006) studied the crack propagation in the radial direction from the intimal layer (of their 2D model) by analyzing the rupture at numerous areas. They reported that crack propagation rate is highly dependent on both the lipid stiffness and the applied pressures [114]. Similar results were observed by Ferrara et al. (2008) within their 3D patient-specific geometry[126]. Gasser et al. (2007b) in a plain strain FE analysis reported that during PTA, atherosclerotic plaque fissures and dissections increase the risk of localized mechanical trauma, but prevent the stenosis main portion from experiencing high stresses [111]. Last but not least, damage distribution was computed by Balzani et al. (2012) within stenosed iliac arterial cross sections of previously identified components (also plain strain FE analysis), with results showing a major influence of axial residual strains on this distribution [112]. Their damage model described the stress-softening (Mullins effect) phenomenon without plasticity. No permanent deformation was modeled within the inelastic FE studies mentioned above.

Besides softening similar to Mullins effect alone, some FE studies investigated inelasticity by incorporating permanent deformation to the softening phenomenon [121], [150]; others by modeling

plasticity alone by itself [103], [107], [117], [120]–[122], [129], [150], [151]. Conway et al. (2014) explored the effects of variation of atherosclerotic tissue material models on tissue mechanical response during stent implantation. They reported that the underlying (elastic model) used for the atherosclerotic plaque is a dominant feature of the tissue representation for predicting its response in a stenting simulation. Moreover, they stated that Mullins effect does not have significant effect on the deformed shape, whereas the inclusion of plasticity (and in accordance with Conway et al. ([162])) do have significant influence on the deformed lumen size and shape in stenting simulations [150]. Similarly Conway et al. (2017) also studied the effect of varying atherosclerotic plaque compositions and constitutive representation on the response to arterial predilation. They reported that predilation impact on outcomes (stresses, lumen deformation) is dependent on the plaque constitutive representation, in particular in the presence of calcifications. Moreover, as was seen in Conway et al. (2014), permanent deformation is only significantly observed with the plasticity model [121]. Gastaldi et al. (2010) proposed a model for simulating provisional side-branch stenting (PSB) in stenosed coronary bifurcation, and studied the effect of performing the final re-dilatation utilizing one or two balloons in addition to those created by a different stent strut positioning around the side branch. They reported that the re-establishment of an optimal spatial stent configuration after PSB is achieved with both re-dilatation strategies; furthermore, stent positioning with one cell centrally placed should be favored [151]. Always with provisional side-branch stenting, Iannaccone et al. (2017) investigated the impact of plaque composition, bifurcation angle and procedure strategy on side branch compromise, and reported that plaque type had higher impact on side branch ostium shape compared to bifurcation angle. Their results showed ovalisation of the side branch lumen [122]. Holzapfel et al. (2002) investigated the arterial 3D stress states during PTA by developing a 3D model of a human diseased artery composed of different components, and studied the changes in the 3D state of stress caused by some model simplifications (neglecting *in situ* prestretch, assuming isotropic material responses, and plane strain states). They reported high sensitivities of such simplifications on resulting outcomes [103]. Gasser and Holzapfel (2007a) studied the states of deformations and stresses within stenosed artery before, during and after balloon angioplasty by considering the balloon-induced overstretch phenomenon in non-diseased arterial tissues. They reported that the 3D stress states significantly differ before and after balloon deflation, with the possibility of compressive normal stress to occur in the media after balloon angioplasty [117]. Li et al. (2012) extended and implemented a recently developed structural multi-mechanism damage model within a cerebral arterial tissue, and analyzed the resulting tissue damage, arterial deformation, and wall stress states during angioplasty. They stated that the constitutive model used in their work is robust in simulating complex tissue response generated by angioplasty balloons [120]. Decorato et al. (2014) simulated balloon angioplasty alone and then followed by stenting within an arteriovenous fistula, and compared the two endovascular treatments effects on outcomes and on simulated fluid-structural interactions (FSI). They reported that the stent is more likely to reduce restenosis by maintaining the vessel lumen shape over time. Furthermore, FSI

simulations indicated that similar hemodynamic conditions were induced by the two treatments [129]. Last, Liang et al. (2005) proposed a model for analyzing intracoronary stent implantation procedure using finite element methods. Besides reporting that high stress concentrates at contacting regions between the plaque and the stent, they showed that arterial wall injury might occur at the distal end of the stent which tilts during inflation. Moreover, they also presented recoil ratio values at single locations within the artery-plaque-balloon and artery-plaque-balloon-stent models after deflation [107].

2.4 AIM OF OUR WORK

The assessment of acute clinical outcome after balloon angioplasty is of pivotal importance for the treatment success evaluation. It has been even rising lately due to recent innovations in medical devices including catheters with "active" mode of actions such as drug-coated balloons. Limitations associated with stents, such as high restenosis rates at long terms [11], in addition to mechanical failure in small arteries and at complex kinematics regions (such as peripheral arteries) [75], also increased clinical interests in evaluating outcomes immediately after PTA alone. Despite its crucial potential in being useful for balloon manufacturers (device design and sizing) and clinicians (treatment planning), up to our knowledge only few FEM studies focused on assessing outcomes at short terms after PTA alone.

Several studies have reported the development of computational models for simulating PTA in diseased arteries using FEMs. Different combinations of geometries, constitutive laws and loading conditions were implemented, affecting accordingly the resulting outcomes. In general, one key factor permitting or not FEM studies from evaluating balloon angioplasty influences on outcomes immediately after the treatment is the material model selected for modeling the diseased artery. In the lack of *in vivo* material characterization methods presenting a clear advantage in extracting realistic material properties of atherosclerotic arteries, current FEM studies mainly focus on *in vitro* based experimental data in order to develop their constitutive laws [90]. Yet, even among the limited number of available experimental studies, very few considered quantifying permanent strains in human atherosclerotic tissues and assessing their inelastic behavior at supra-physiological loadings. Accordingly, the majority of FEM studies did not include any residual deformations within their diseased arterial material models, and thus were limited in modeling balloon angioplasty alone.

FEM studies that used the elastic (linear or not) constitutive laws for modeling arteries and plaques were restricted from evaluating outcomes directly after PTA alone. Without a stent implantation, elastic recoils after balloon deflation would have been theoretically equal to its gained deformation at max inflation (recoil of 100%), which contradicts clinical observations [87], [163]–[165]. According to clinical findings, elastic recoil immediately after PTA varies between 11% and 55% for different

stenosed regions, plaque compositions, and balloon/artery diameters ratios, the latter ratio (i.e. Balloon Sizing) showing highest influence on results [164].

Acute outcomes assessment after balloon angioplasty was also limited in FEM studies analyzing the rupture of arterial tissues by incorporating damage mechanisms such as crack propagation, cohesive zone, or damage models. Inelastic material models including damage such as the softening behavior on its own (Mullins effect) would result in no residual strains at unloading [112], contradicting clinical observations as well.

Differently, FE studies modeling inelastic constitutive laws within their models (either by incorporating Mullins effect together with permanent set or by including plasticity) are generally capable of assessing the outcomes of an angioplasty procedure in terms of residual deformations. However among these few FE studies, even though some presented detailed and interesting post-treatment assessments from their work, their focus was on outcomes after stent implantation and not after PTA alone [121], [122], [150], [151]. The remaining FE studies both modeling inelasticity and evaluating outcomes immediately after PTA alone (i.e. without stenting) are still limited in terms of presented results. They assessed either the elastic recoil ratio (ERR) at one location after deflation [107], [129], the lumen gain ratio (LGR) after deflation also at one location [117], or both ERR and LGR but qualitatively (no quantification presented) [103], [120]. Besides ERR and/or LGR, only Holzapfel et al. (2002) and Gasser and Holzapfel (2007a) respectively present also some data on state of deformation and/or state of stress within the artery during and after PTA alone [103], [117].

It is important to note that all these mentioned studies evaluating outcomes at short terms after PTA modeled the deployment of only one type of balloon inflated to a single sizing within a particular plaque composition. Up to our knowledge, no FE study explicitly evaluated the influence of varying procedure components (balloon type, balloon sizing or plaque composition) on treatment outcomes immediately after balloon angioplasty alone. Moreover, except for the generic model of Liang et al. (2005) [107], no FE study presents acute post-angioplasty simulated results in comparison with clinical outcomes.

According to manufacturers and clinicians, what remains challenging today is the adequate choice of balloon (design and sizing) for the corresponding patient that would minimize the ERRs, maximize lumen gain (LG), but at same time without damaging the arterial wall. **Consequently, the aim of this dissertation is to propose a patient-specific modeling strategy of PTA, using implicit FE analysis, to address outcomes at short term after PTA for different combinations of diseased arterial geometries, material compositions, balloon designs and specifically balloon sizing, in comparison to clinical outcomes. The majority of balloon angioplasties being clinically performed in femoropopliteal arteries, the work will be focused on femoral arteries.** Finally, towards a further

implementation within clinical routine, the proposed methodology will be based on routine medical images: CTA scans.

3 PROPOSED METHODOLOGY

The workflow illustrating our proposed modeling methodology towards a patient-specific finite element analysis of balloon angioplasty is presented in [Figure 3.1]. Each component within this workflow which will be detailed in subsequent chapters of this thesis is summarized in this section as well.

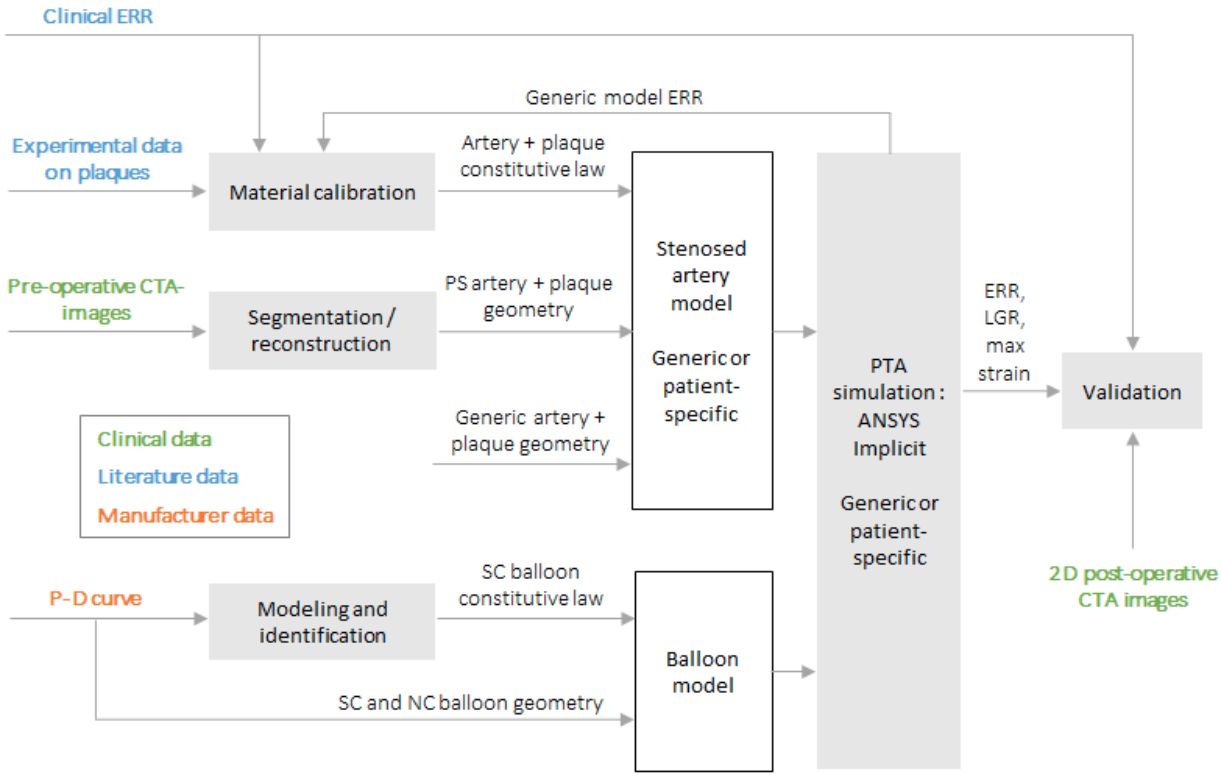

Figure 3.1: Overview of the thesis towards a patient-specific finite element analysis of balloon angioplasty. With (CTA), (ERR), (LGR), (SC), (NC), and (PTA) being respectively: computed tomography angiography, elastic recoil ratio, lumen gain ratio, semi-compliant, non-compliant and percutaneous transluminal angioplasty.

PTA BALLOON MODELING (CHAPTER 3)

One basic component within the workflow for simulating PTA treatment technique is modeling the angioplasty balloon itself. Based on its material and wall thickness, each balloon has an individual compliance chart that is provided by the manufacturer, describing its pressure-diameter evolution. Besides, PTA balloons are crimped onto the body of the catheter during manufacturing, so to facilitate insertion into the vasculature of the patient. Their deployment process can then be divided into two phases: unfolding and inflation phases. Therefore, in this work we first suggest a relation for categorizing these balloons based on their compliance data into two large families: semi-compliant

and non-compliant balloons. Then two different models are proposed based on each family characteristics. The models are rather simplified compared to a recently published one [158], but the aim of our work is to represent the balloon behavior using the implicit solver of Ansys with sufficient accuracy (specifically within its working range), yet at the same time with fast simulation times. Finally, for validating our semi-compliant balloon model, the resulting simulated pressure-diameter values are compared to their corresponding data provided by manufacturer.

SIMULATION OF BALLOON ANGIOPLASTY IN A GENERIC MODEL (CHAPTER 4)

Since PTA balloons have to deploy into occluded vessels, after being modeled and validated outside arteries, angioplasty balloons should be simulated within stenosed vessels. In this chapter we present the modeling methodology we suggest for generically simulating PTA within a stenosed artery. A generic model mimicking a diseased vessel was generated for that purpose. Several FE simulations were performed within this generic model for different combinations of arterial material constitutions, plaque material compositions (homogeneous lipid, homogeneous calcified, heterogeneous superimposed, heterogeneous randomly mixed), balloon designs (non-compliant, semi-compliant), and balloon sizings. Being interested in PTA outcomes at short terms, results are mainly assessed in terms of the elastic recoil ratios (ERR) and lumen gain ratios (LGR) obtained immediately after balloon deflation, in accordance with what clinicians evaluate. Maximum principal strains in the arterial walls interpreted as an indication for a risk of rupture at different balloon sizings are presented as well.

PLAQUE AND ARTERY MATERIAL MODELS CALIBRATION (CHAPTER 5)

An essential step towards generating a reliable model is to validate the constitutive laws being used. Therefore, in this chapter a calibration method for the plaque and the arterial material models is suggested. In the absence of a validated *in vivo* mechanical characterization of diseased arteries behavior, our proposed FE model first considers the *in vitro* experimental data obtained from Maher et al. (2011) study [148] on the inelastic behavior of plaques under compression in order to identify their constitutive laws. Then, the arterial material parameters were tuned in tension to satisfy averaged clinically attained ERR values after balloon deflation. The obtained material parameters are the ones implemented in both the generic and P-S simulations of PTA in Chapters 4 and 7 respectively.

PATIENT-SPECIFIC GEOMETRIC MODELING OF A DISEASED ARTERY (CHAPTER 6)

Another important step of a workflow towards proposing a patient-specific modeling strategy is the geometric model generation. As previously described in Section 1 of this chapter, computed tomography angiography (CTA) is the acquisition technique used in this work. The segmentation and surface model generation procedure we propose is presented in this technical chapter. It is first illustrated on an abdominal aortic artery stenosed by a plaque of mixed composition (lipid and

calcified). After that, being interested in peripheral cases, the process was applied on two other patients with superficial femoral stenosis: one with a lipidic atherosclerosis, while the other with a calcified plaque. Finally, 3D models corresponding to the segmented components were generated and prepared becoming geometrically ready for FEM simulations (presented in Chapter 7).

PATIENT-SPECIFIC FINITE ELEMENT ANALYSIS OF PTA IN FEMORAL ARTERIES (CHAPTER 7)

Now that the essential components towards a patient-specific simulation are determined, this chapter presents an assembled workflow for simulating patient-specific balloon angioplasty within peripheral arteries. PTA balloon models (seen in Chapter 3) were simulated within 3D P-S geometries of diseased femoral arteries (seen in Chapter 6) after incorporating their corresponding calibrated plaque and arterial material models (seen in Chapter 5). Two stenosed femoral arteries were studied: one with a dominant lipidic plaque, while the other with a calcified atherosclerosis. Several balloon sizings were tested. Being also interested in acute post-procedural outcomes (as for Chapter 4), besides analyzing arterial wall principal strains, results are mainly evaluated in terms of elastic recoil and lumen gain ratios obtained along the stenosed arterial centerlines by comparing the pre and post-treatment geometries for each balloon sizing. Finally, for the clinically performed balloon sizing within each stenosed patient individually, a comparison is presented between the clinical outcomes obtained from 2D post-operative medical images and its corresponding simulated results to evaluate the validity of the proposed framework.

CHAPTER 3

PTA BALLOON MODELING

In this chapter we introduce first the key characteristics of (high-pressure) PTA balloons used in the medical industry. After focusing on balloons compliance being their most significant feature, a brief recall on different techniques implemented by available FE studies for modeling PTA balloons is given. Afterwards, we suggest a relationship to categorize these high-pressure balloons based on their compliance data into two large families: semi-compliant and non-compliant balloons. Finally a modeling strategy is proposed for balloons from these two families.

OUTLINE

1 HIGH-PRESSURE MEDICAL BALLOON KEY CHARACTERISTICS

As stated in Chapter 1, the PTA delivery system is composed mainly of a guidewire, a guiding catheter (shaft), and a tipped balloon that has to be delivered towards the stenosed region passing through tortuous and small vessels. Accordingly the ability of the balloon catheter to bend as to easily advance through tortuous arterial segments (*trackability*), in addition a sufficient stiffness in the shaft to force it through the stenosis (*pushability*), are essential features of the delivery system. Guidewires act as rails for the progression of dilatation catheters towards diseased regions. They exist in various dimensions and are usually covered by a Teflon-coated stainless steel on their solid core bodies so to reduce friction between their surfaces and arterial tissues [88].

In this work, as interested in modeling the expansion of the dilatation catheter after being positioned within the stenosed region, we focus on characteristics of the balloon. Two main types of balloons exist in the medical industry: the high-pressure vs. the low pressure balloons. Low-pressure balloons are limited in terms of diameter and final shape accuracy, so they are more involved in applications such as fixation and occlusion. Conversely being able to keep their designed size and shape even at high pressures, high-pressure balloons are considered the suitable choice for angioplasty applications. For PTA, a balloon must have a repeatable or controlled size (pressure vs. diameter) ensuring that it will not continue expanding and damaging the artery after opening the blockage [166].

In order to characterize clinically used PTA balloons, two main aspects have to be taken into consideration: one related to the balloon geometry and dimension, and one to its material composition and compliance.

1.1 BALLOON GEOMETRY AND DIMENSION

An angioplasty balloon is initially tightly wrapped around a catheter shaft during manufacturing in order to decrease its *profile* and facilitate its insertion into patient vasculature. With different folding patterns designed, they all tend to ease the balloon advancement towards the diseased region by minimizing its crossing profile [Figure 1.1].

Folded balloon

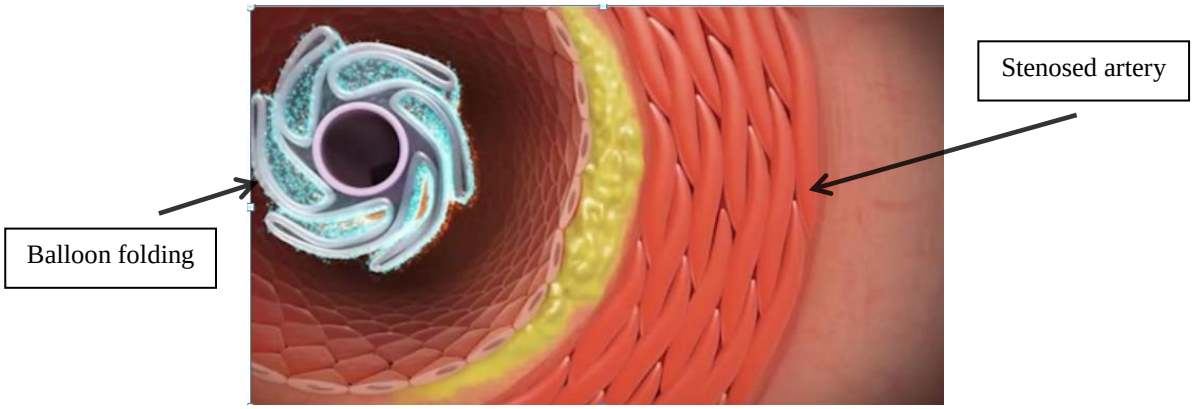

Figure 1.1: Front view showing a folded balloon prior to inflation within a stenosed artery [www.medtronic.com].

Moreover, thin walls in angioplasty balloons facilitate their folding and attaining smaller profiles. Even though their walls are thin, PTA balloons have considerably high strength that allows them to withstand high pressures without rupture during inflation, with relatively low elongations. Exhibiting high tensile strength is an essential criterion in such medical balloons towards achieving their desired goal to apply force whether to compress/damage the plaque or to post-dilate the stent [88], [89], [166].

A standard balloon consists mainly of a cylindrical body and two conical tapered ends which diameters decrease until reaching the diameter of the shaft from one side, and of the guide wire tube from the other. The guide wire tube connects the balloon tip at its end to the shaft on the other side passing inside the balloon. [Figure 1.2] depicts an angioplasty balloon when inflated.

Balloon dilatation catheter

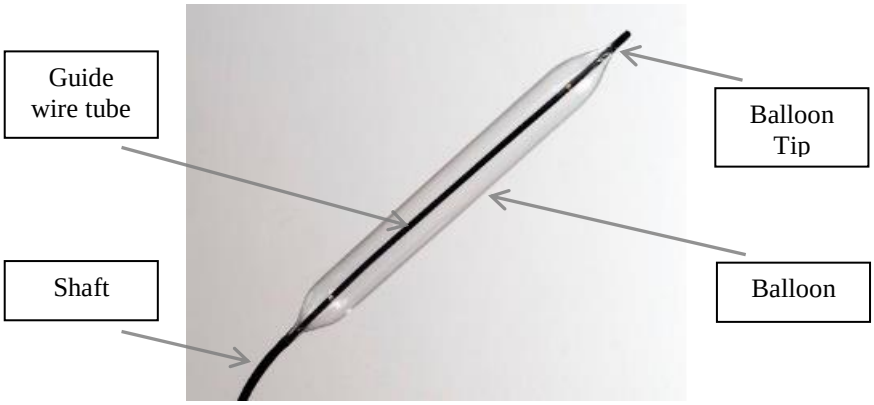

Figure 1.2: A standard high-pressure inflated PTA balloon [healthmanagement.org].

High-pressure balloons are produced in a large variety of lengths, diameters and shapes conforming to the wide range of minimally invasive procedures [167]. PTA balloons are accordingly manufactured in various dimensions corresponding to vessels of different sizes and locations susceptible to stenosis (coronary, carotid, femoral…). For instance, typical dimensions of angioplasty balloons used within femoral stenosis treatments at CHU of Rennes are 5 mm as nominal diameter, and 40 to 60 mm as

working length. Moreover, several angioplasty balloons manufacturing companies exist as well, each presenting their own products.

When discussing PTA balloon characteristics, it is essential to introduce some keywords definitions. Speaking about the nominal diameter and the working length, they correspond to the inflated balloon diameter at its nominal pressure and its straight body section length respectively. [Table 2] presents some basic terms definition for balloons.

Table 2: Balloon key definitions [166].

Desired Balloon Diameter (D_n)	Inflated balloon diameter measured at a particular pressure (P_n)
Nominal Balloon Diameter (D_N)	Nominal inflated balloon diameter measured at the nominal pressure (P_N)
Balloon Length	The working length of the balloon (its straight body part length)
Rated Burst Pressure (P_{RB})	Maximum statistically guaranteed pressure up to which a balloon can theoretically be inflated without failure (i.e. the inflation pressure below which 99.9% of balloons will not rupture)
Balloon Profile	Maximum diameter of the balloon when it is still deflated and wrapped on its catheter. In this work, this diameter is referred to by the *folded diameter (D_f)*
Balloon Compliance	The change in balloon diameter as a function of inflation pressure

More details on particular keywords involved in the balloons categorization and modeling will be presented in their respective Sections 3.1 and 3.2.

According to medical device manufacturers recommendations (e.g., Medtronic APV, Santa Rosa CA, USA), the balloon should exceed past the plaque from both sides. However, typically its length should not largely exceed that of the plaque to limit the risk of 'dogbone effect': small waist appearance in middle of balloon. With vascular injuries being associated with the dogboning effect [168], a compromise should be made on the selected balloon length that can properly exceed the plaque but without enhancing dogboning.

1.2 BALLOON MATERIALS AND COMPLIANCE

As reported in Chapter 1, the most significant feature of a PTA balloon is its capability to attain prescribed diameters precisely during inflation, even at high pressures. It is also the balloon ability in retaining its designed size and shape under such pressures. This characteristic is known as the balloon *compliance* and is associated with the material properties from which the balloon is made. Assessing

balloon compliance is thus essential to ensure that the inflating balloon will not continue its expansion randomly and damaging the arterial wall. Low-pressure elastomeric balloons which can diametrically stretch 100 to 600% during inflation (driven by volume instead of pressure) cannot be used in medical applications that require high pressures as the PTA endovascular treatment. Instead high-pressure balloons are the ones used for such applications. These balloons can be divided into three major families (compliant, semi-compliant, and non-compliant) based on their compliance property and their material. [Table 3] presents a brief comparison of some high-pressure balloons used in PTA treatments.

Table 3: High-pressure balloons of different material compositions [36], [88], [166].

Materials	**Tensile Strength**	**Compliance**	**Profile**	**Maximum Rated Burst Pressure (atm)**
Polyethylene terephthalate (PET)	High - Very High	Low	Low	≥ (20)
Nylons and High density polyethylene	Medium - High	Low-Medium	Low - Medium	~ (14-18)
Polyethylene (PE), other Polyolefin copolymers (i.e. POC), and Polyurethanes	Low - Medium	Medium-High	Medium - High	~ (10-14)
Polyvinyl chloride (PVC)	Low	High	High	~ (6-8)

The first fabricated PTA balloons were made from PVC material. In addition to their relatively low max rated burst pressures (which somehow limited inflations that required higher pressures), their thick walls resulted in rather larger profiles as well. Consequently, following the continuous innovations in manufactured angioplasty balloons, several materials replaced PVC in such balloons increasing their compliance and their rated burst pressure (see Table 3). Lately the majority of high-pressure angioplasty balloons are being produced from either nylon or PET, each material presenting its own advantages and disadvantages [166]. Besides showing very high tensile strengths and burst pressures, balloons formed from PET offer the advantage of having ultra-thin walls (5 to 50 microns) that result in a very low profile. Even though softer nylon balloons will generally have higher profiles (of thicker walls) compared to PET, their softer material can be more easily refolded and withdrawn

after the treatment. Further details regarding balloon compliance will be described in association with their categorization as presented in Section 3.1.

2 BRIEF RECALL ON ANGIOPLASTY BALLOON DEPLOYMENT MODELING

PTA devices were modeled at different levels of sophistication in the literature: from substituting the balloon by a surface pressure, to modeling the detailed folding pattern of the balloon. In general, four main strategies can be distinguished. To start with, several PTA studies neglected the balloon presence in their models replacing it by a pressure applied on the stent inner surface instead. Besides their various provided data, most of them have emphasized the non-uniformity of the stent deployment when the balloon is neglected [152], [159]. Other studies modeled the balloon as a rigid cylinder expanding using radial displacement loading [103], [121], [155]. Alternatively, others modeled their balloons as pressure-driven non-folded cylinders with linear elastic [129], bilinear hyperelastic [107], Mooney-Rivlin hyperelastic [156] or anisotropic (theory of fiber-reinforced) hyperelastic [117], [122], [157] material properties. The last modeling strategy reported by few other FE studies in the literature was simulating the folding patterns of the balloon and thus modeling its unfolding process in more details during inflation [152], [158], [159]. Refer to Chapter 2 for more details on PTA devices modeling.

As can be seen, the majority of studies simulating PTA considered modeling the stent as well within their work. Even though some studies recommended modeling folded balloons within simulations for better representing the stent deployment process [154], [156], others reported that applying pressure to the inner surface of a stent by using restraining elements in connection to the stent as well (which would restrain further stent expansion beyond its prescribed inflated diameter) [152] or using a rigid cylindrical shaped balloon [159] would give an accurate prediction of the stent geometry at its final state of expansion and after full recoil relative to those achieved in more computationally expensive wrapped balloon simulations. Furthermore the suitability of implementing a stiff cylindrical tube for simplifying (stent) angioplasty simulations has been also verified by Grogan et al. (2012) [155] and recently used accordingly by Conway et al. (2017) [121].

Since this work aims in evaluating simulation outcomes immediately after balloon angioplasty alone (without stent implantation), we are mainly interested in assessing the balloon and the stenosed artery behavior at three critical states during PTA: before inflation, at max balloon inflation and after its deflation. Less interest is thus required on predicting the PTA device deformation (dogboning and foreshortening) during its unfolding process. Therefore towards reducing significant computational expenses associated with modeling balloon foldings (see for example [158]), a non-folded cylinder is

considered here instead. Moreover, we will focus on the balloon as part of the clinical routine, which is a device that surgeons need to choose at the adequate sizing depending on the treated stenosis and available balloons. Therefore we propose a categorization strategy based on the balloon compliance chart (provided by the balloon manufacturer) associated to a modeling method depending on the balloon type, with an interest in optimizing both the simulation speed/cost and its accuracy at different balloons sizings within their working ranges.

3 BALLOONS MODELS: CATEGORIZATION AND MODELING

3.1 BALLOONS CATEGORIZATION

For PTA applications, a balloon must have a repeatable or controlled size (pressure vs. diameter) ensuring that it will not continue expanding and damaging the artery after opening the blockage. Knowing that there exist several high-pressure balloons in the medical industry of different pressure-diameter data, the aim of this section is to suggest a relation for categorizing available balloons into more general classes based on their compliance data, to be modeled after accordingly.

Based on its material and wall thickness, each high-pressure balloon has an individual compliance chart provided by the manufacturer reflecting the pressure at which the balloon reaches its nominal diameter, in addition to its diameter change per inflation pressures [88]. Compliance is determined by either the balloon diameter change per unit of inflation pressure step (*index of stretchability (IS)*), or by its diameter growth over a range of inflation pressures measured in % (*relative compliance (RC)*):

$$Index\ of\ stretchability = IS = \frac{D_{n+1} - D_n}{P_{n+1} - P_n} \tag{3-1}$$

$$Relative\ Compliance\ (\%) = RC = \frac{D_{RB} - D_N}{D_N} \times 100 \tag{3-2}$$

with D_{n+1} and D_n the balloon diameters at any two consecutive pressure levels P_{n+1} and P_n, ranging from the unfolded inflation pressure (P_{Unf}) to the rated burst pressure (P_{RB}). D_N and D_{RB} are the balloon diameters at the nominal and the rated burst pressures (P_N and P_{RB}) respectively [36], [89], [166]. The *working pressure range* provided by the manufacturer is $[P_N, P_{RB}]$. The *unfolded diameter* (D_{Unf}) corresponds to the diameter reached by the balloon when pressure starts being applied prior to any inflation (i.e. at P_{Unf}). It is different to the *folded diameter* (D_f) that corresponds to the inner diameter of the catheter in which the angioplasty balloon is crimped before insertion into the patient vasculature.

According to clinicians and manufacturers, there exist three general categories for characterizing available high-pressure balloons for PTA: compliant, semi-compliant, and noncompliant [36], [88]. Conforming to areas of least resistance during inflation, high-compliance balloons are typically used in presence of soft un-calcified lesions. Differently, keeping their defined diameters at high pressures, low-compliance balloons are typically inflated within highly calcified (stiff) lesions and/or for stents full expansion post-dilations [36], [88], [89], [166], [169]. Lately, there has been some debate on what type of balloon material is optimal for PTA. Some retrospective observational studies suggest differences in angiographic results and overall procedural outcomes for different balloon materials [170]; others do not [36], [171].

This work focuses first on modeling the main balloon families covering most balloon designs used by clinicians during PTA. In what follows, and because they would be applied the same modeling method, both compliant and semi-compliant balloons are considered belonging to the same category of semi-compliant balloons. Accordingly, two balloon families are studied: Semi-compliant vs. Non-compliant. In this work, all balloons data are provided by Medtronic APV, Santa Rosa CA, USA.

3.1.1 Semi-compliant balloons

Relative compliance of semi-compliant balloons made of high density polyethylene, nylon or polyolefin copolymer (POC) ranges between 10-20% [36], [88] or is greater than 8% [172]. Average index of stretchability (IS) is typically around 0.095 mm/atm for these balloons [36]. These balloons are rarely inflated within stiff stenosis to avoid the ‘dogbone effect’ that would occur around the lesion at high inflation pressures, see [Figure 3.1] [169]. Table 4 presents an example of Pressure-Diameter (P-D) compliance chart of a 2.8 mm semi-compliant balloon in addition to its average index of stretchability.

3.1.2 Non-compliant balloons

The relative compliance of highly non-compliant balloons is generally less than 7% [172] or 10% [36]. They are usually made of polyethylene terephthalate (PET) material. Their average index of stretchability (IS) fluctuates typically around 0.01 mm/atm [36]. These balloons impose their own geometry to the stenosis and hence experience negligible changes in profile during high-pressure inflation, see [Figure 3.1] [169]. For comparison with semi-compliant balloons, Table 4 also shows the P-D compliance chart for a 2.8 mm non-compliant balloon with its corresponding average index of stretchability.

Non-Compliant **Semi-Compliant**

Figure 3.1: Bench test showing the different profiles between a non-compliant balloon (A) and a semi-compliant balloon (B) during high-pressure inflation. The blue central cylinder represents the balloon-plaque contact region. A "dog bone" effect can be observed in the semi-compliant balloon case. (A) and (B) were reproduced from [169].

Table 4: P-D compliance charts with their calculated index of stretchability for two different families of 2.8 mm balloon designs (non-compliant vs. semi-compliant). Green and blue cells indicate diameters at nominal and rated burst pressures (P_N and P_{RB}) respectively.

Pressure $[P_n]$ **(atm)**	**Non-Compliant 2.8 mm balloon**		**Semi-Compliant 2.8 mm balloon**	
	Diameter $[D_n]$ **(mm)**	**Index of stretchability** $[IS]$ **(mm/atm)**	**Diameter** $[D_n]$ **(mm)**	**Index of stretchability** $[IS]$ **(mm/atm)**
8	2.80	-	2.60	-
9	2.82	2.00E-02	2.65	5.00E-02
10	2.84	2.00E-02	2.80	1 .50E-01
11	2.85	1.00E-02	2.91	1.10E-01
12	2.87	2.00E-02	3.02	1.10E-01
13	2.88	1.00E-02	3.10	8.00E-02
14	2.90	2.00E-02	3.20	1.00E-01
15	2.90	0.00E+00	3.27	7.00E-02
16	2.91	1.00E-02	3.32	5.00E-02
17	2.92	1.00E-02	3.43	1.10E-01
18	2.93	1.00E-02	3.53	1.00E-01
19	2.95	2.00E-02	3.60	7.00E-02
20	2.95	0.00E+00	3.70	1.00E-01
21	2.96	1.00E-02		
22	2.97	1.00E-02		
23	2.98	1.00E-02		
24	2.99	1.00E-02		
25	2.99	0.00E+00		
26	3.00	1.00E-02		
27	3.01	1.00E-02		
28	3.02	1.00E-02		
Averaged index of stretchability $[\overline{IS}]$ (mm/atm) ± Standard Deviation		**1.10E-02** ± 6.24E-03		**9.17E-02** ± 2.76E-02

By linearly fitting the P-D graphs plotted using balloons compliance charts, see [Figure 3.2], D_N and D_{RB} can be written respectively as:

$$D_N = \overline{IS} \times P_N + D_{Unf} \tag{3-3}$$

$$D_{RB} = \overline{IS} \times P_{RB} + D_{Unf} \tag{3-4}$$

where $\overline{IS}$ is the average value of IS.

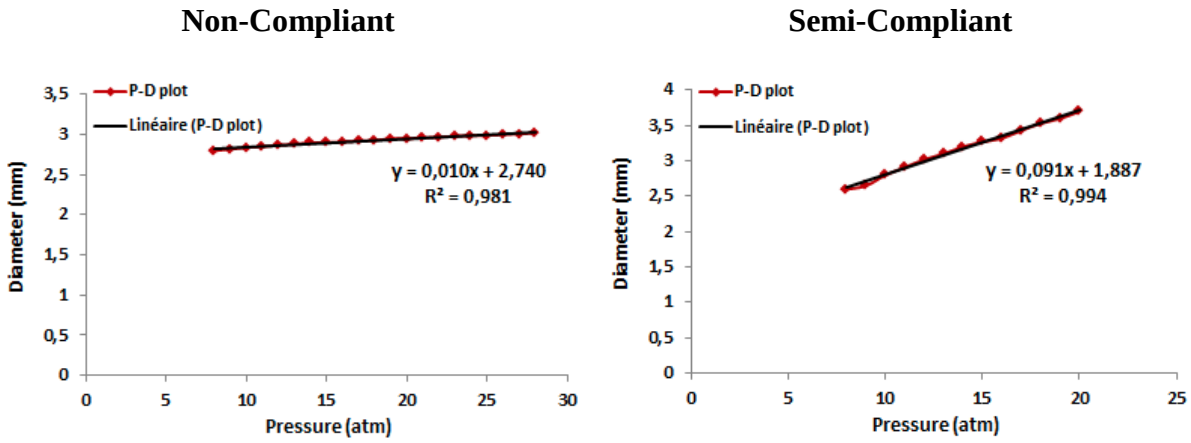

Figure 3.2: P-D plots with their respective linear curve fits and equations corresponding to each of the non-compliant vs. the semi-compliant balloons.

For a more consistent categorization, we propose to classify balloons based on *RC* values being related to their indices of stretchability, nominal diameters, in addition to nominal and rated burst pressures. *RC* can hence be expressed as:

$$RC = \frac{(P_{RB} - P_N) \times \overline{IS} \times 100}{D_N} \tag{3-5}$$

In this work we consider balloons with *RC* ranging below 8% belong to the non-compliant family, whereas balloons with *RC* above 8 % belong to the semi-compliant family.

3.2 BALLOONS MATERIAL MODELING

As mentioned, an angioplasty balloon is initially crimped into the catheter body during manufacturing so to facilitate its insertion into patient vasculature. Accordingly, it unfolds first with complex kinematics (see for instance Geith et al. (2019) for details [158]) during the initial phase of the inflation process reaching eventually its unfolded diameter (D_{Unf}). After that, any further increase in the applied inner pressure would start the balloon inflation until reaching the desired diameter with a typical behavior corresponding to its design. To limit the computational cost of our simulation, the modeling of the detailed unfolding process is neglected in this work; instead a cylindrical model is

used in order to mimic the overall balloon catheter mechanical response. The appropriateness of using a cylindrical tube to simplify angioplasty simulations has been verified by Grogan et al. [155].

Our modeling strategy therefore consists of considering first a realistic folded diameter (D_f) so that the balloon can be inserted into a highly stenosed artery, and then use the balloon compliance chart to build a constitutive law that can describe the balloon behavior mainly within its working range (between D_N and D_{RB}). In what follows, the modeling work is performed with the 2.8 mm nominal diameter balloons (seen in Table 4). This rather small diameter compared to those usually used for femoral arteries PTA, was chosen to limit the computational cost of simulations (seen in Chapter 4) at this stage of the study, that is developing the model and evaluate its validity.

Regardless of balloon type, D_f was fixed here to 1.15 mm. It is in accordance with balloon profile values found on commercially-available angioplasty balloon catheters designed by medical device manufacturers and used by clinicians.

D_{Unf} was determined from the plotted P-D diagrams seen in [Figure 3.2]. It is defined as the intercept with the diameter (ordinate) axis of the P-D graph: the diameter at approximately zero (very low) pressure. In this work, the estimated unfolded diameters of the semi-compliant and the non-compliant balloons were $D_{Unf} = 1.887\ mm$ and $D_{Unf} = 2.740\ mm$ respectively.

3.2.1 Semi-compliant balloon modeling

Having thin walls (0.035 mm) and a high index of stretchability, semi-compliant balloons were driven by pressure, to accurately simulate the plaque/balloon interaction, especially the dogbone effect [Figure 3.1]. Therefore, an accurate constitutive law for the balloon is required. The deployment of PTA balloons is divided into two phases: the unfolding phase (from D_f to D_{Unf}), followed by the inflating phase (from D_{Unf} to D_n). During the unfolding phase, the folded balloon deploys freely at very low pressures. Then, the unfolded balloon continues by an elastic deformation during the inflating phase until reaching the desired diameter (D_n) within its working range.

In order to simplify this 2-phase deployment process, an Ogden 1st order hyperelastic constitutive model was implemented in this work. This model is able to replace both phases by a continuous non-linear elastic expansion. From the manufacturer compliance charts (Table 4), a corresponding stress-strain (σ_n, ε_n) curve for the semi-compliant balloon was determined using equations (3-6) and (3-7) and considering it as a thin walled pressure vessel:

$$\sigma_n = \frac{P_n \times D_n}{2 \times t} \tag{3-6}$$

$$\varepsilon_n = \frac{D_n - D_f}{D_f} \tag{3-7}$$

where t is the balloon wall thickness, considered constant. Using these data-points and the values of D_f and D_{Unf}, the Ogden law could be identified.

3.2.2 Non-compliant balloon modeling

During inflation of these balloons, the initial unfolding process is usually followed by a very stiff (non-compliant) response at higher pressures [Figure 3.1]. Gasser and Holzapfel (2007a) reported that this irregular mechanical behavior cannot be attained using simple isotropic material models for representing the balloon [117]. Instead they suggested using the theory of fiber-reinforced materials for the design of these models.

However, having thicker walls (0.15 mm), negligible changes in their profiles during inflation [169] and low *IS*, another option for simulating non-compliant PTA balloons without losing fidelity is to drive them by radial displacement. This assumption is defendable by the fact that such balloons are stiff enough to impose their own shapes to the diseased region while inflating [103], [155]. Accordingly, the inflation and deflation of non-compliant balloons were driven by radial displacement in this work.

Displacement driven simulations allow of course a perfect control of the balloon diameter evolution as well as better simulation robustness. Being fully simulated by displacement boundary conditions, there is no need for an accurate constitutive law for this balloon family.

3.3 BALLOONS GEOMETRY, MESH AND BOUNDARY CONDITIONS

The balloon geometry is a 13 mm long hollow cylinder, with 2 symmetrically lofted caps at its ends for the semi-compliant family and without the caps for the non-compliant one. The balloon working length was chosen to exceed the plaque length according to manufacturers' recommendations. Balloons were meshed by 4-nodes shell elements, see [Figure 3.3].

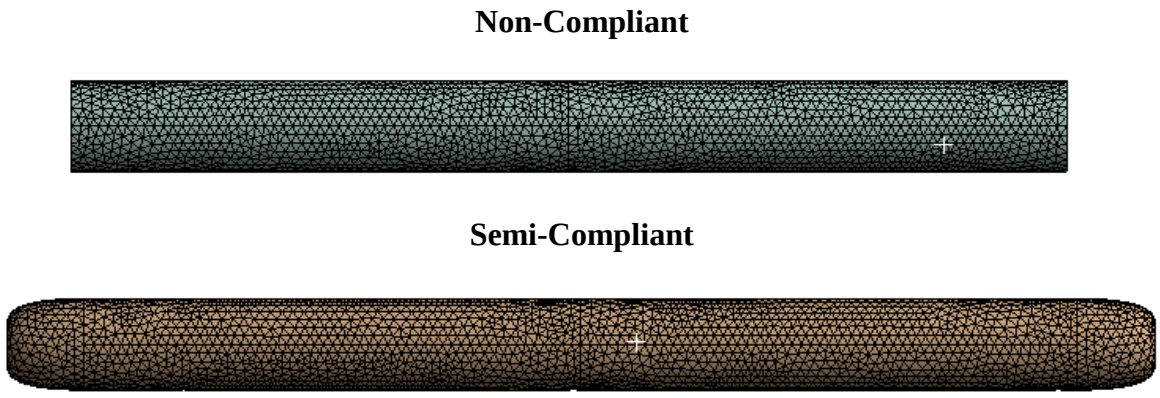

Figure 3.3: Non-compliant vs. semi-compliant balloons meshed geometries.

For semi compliant balloons, hydrostatic fluid elements were implemented to simulate the pressure driven inflation. Hydrostatic fluid elements are usually used to model fluids that are fully enclosed by solids [173]. An incompressible fluid with a negligible thermal expansion was defined for the fluid material model used. A uniform time dependent pressure was then applied at the pressure node, located at the center of the fluid volume. This pressure varied from zero to the desired inflation pressure and then back to zero.

Regarding loading conditions, both simulated balloon families were driven up to all their successive inflation pressures/diameters within their working ranges, and then deflated back to their initial positions.

Boundary conditions were defined to ensure free radial expansion of the balloons: fastened on one side (mimicking the bonding to the catheter shaft), while preventing only axial displacement at the other end (modeling the role of the tip on the balloon) for the semi-compliant balloon type [Figure 1.2], whereas clamped on both sides for the non-compliant one.

4 BALLOONS MODELS: RESULTS AND DISCUSSION

4.1 RESULTS

Prior to their inflation within the stenosed arteries, the two classified balloon families were independently tested.

Driven by radial displacement, the non-compliant balloon model always reaches required inflation diameters accurately. This model is robust and converges easily with a fast simulation time on a normal computer: less than one minute on an Intel(R) Xeon(R) workstation with 64 bit CPU dual core processors of 2.10 GHz clock speed. Maximum circumferential deformation simulated in this balloon model was around 165%.

Driven by pressure, the semi-compliant balloon model was tested for its accuracy before being inflated inside stenosed arteries. Curve-fitting computed the following parameters for the balloon Ogden law: $\mu = 1.72$ MPa, $A_1 = 4.55$ and $D_1 = 0$. This set of parameters reproduces very accurately manufacturers data in terms of pressure-diameter values (see working range on [Figure 4.1]) and ensures robustness, i.e. simulation convergence no matter the plaque stiffness, despite large deformations and contacts (seen in Chapter 4). The maximum circumferential deformation simulated with this balloon model was around 225% at its rated burst pressure.

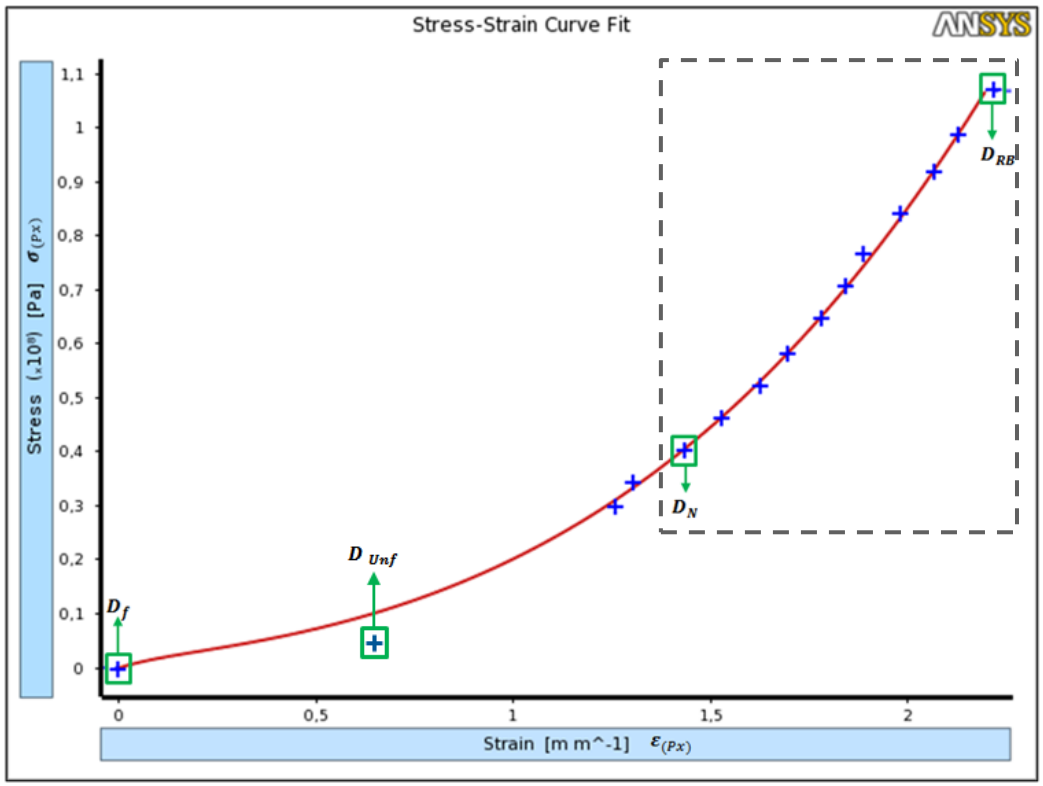

Figure 4.1: Stress-strain pairs (blue crosses) in addition to their fit (red solid line) by the hyperelastic constitutive model considered for the semi-compliant balloon of this study (Table 4). D_f, D_{Unf}, D_N and D_{RB} are the folded, unfolded, nominal and rated-burst diameters respectively with their corresponding stress-strain values. Balloon working range is shown within the grey dashed rectangle (between D_N and D_{RB}).

Table 5 presents a comparison between the diameter extracted from manufacturers P-D compliance charts and the FE simulated inflation diameter for the semi-compliant balloon. Diametric differences were then computed using the relative error general equation which showed negligible error values at respective inflation pressures. The simulation convergence time was around 2 minutes for this semi-compliant balloon type.

[Figure 4.2] shows the non-compliant and the semi-compliant balloons inflated to their nominal diameters (D_N = 2.8 mm). It illustrates their diametric evolution at their central planes along the inflation and deflation process. Both balloons virtually reached their expected nominal diameters when simulated alone, with negligible changes in their profiles at max inflation.

Table 5: Relative % error between experimental and FE simulations diameters obtained at respective pressures during inflation of the semi-compliant balloon described in Section 3.2.1. Green and blue cells indicate diameters at nominal and rated burst pressures (P_N and P_{RB}) respectively.

Pressure $[P_n]$ (atm)	**Semi-Compliant 2.8 mm balloon**		
	Diameter $[D_n]$ (mm)	**Simulated Diameter (mm)**	**% Error on Diameter**
8	2.60	2.569	1.18
9	2.65	2.691	1.55
10	2.80	2.805	0.17
11	2.91	2.912	0.07
12	3.02	3.013	0.22
13	3.10	3.110	0.32
14	3.20	3.202	0.06
15	3.27	3.290	0.61
16	3.32	3.374	1.64
17	3.43	3.456	0.75
18	3.53	3.534	0.12
19	3.60	3.610	0.28
20	3.70	3.684	0.44

(A-I): Inflated non-compliant balloon

(A-II): Inflated semi-compliant balloon

(B): Semi vs. Non-compliant balloons diametric evolution at their central planes simulated outside stenosed arteries

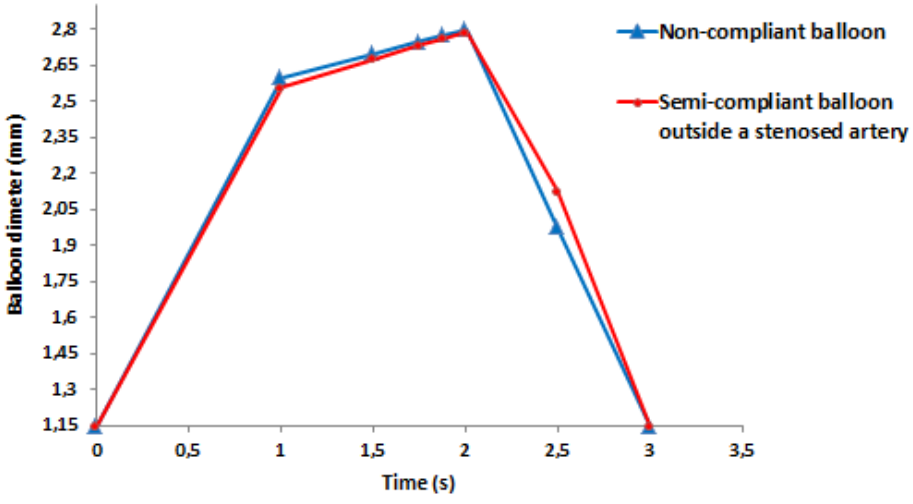

Figure 4.2: (A) Non-compliant and semi-compliant balloons inflated to their nominal diameters (D_N=2.8 mm) outside a stenosed artery, while (B) their diameter evolution at their central planes along the inflation and deflation process.

4.2 DISCUSSION

Based on their compliance characteristics, we categorized balloons into two families: non-compliant and semi-compliant, to be modeled accordingly. Classification can be performed using the relation we developed linking known relative compliance ranges [88], [172] to indices of stretchability, nominal diameters, in addition to nominal and rated burst pressures, which are extracted from the balloons compliance charts.

Each balloon type was first modeled independently. Based on the hypothesis that they are stiff enough to inflate within the stenosed region with minor changes in their profiles [103], [155], [169], non-compliant balloons inflation was driven by displacement; thus no accuracy verification was required. Differently, driven by pressure, semi-compliant balloons were tested first outside the stenosed artery for accuracy. Existing FE studies used isotropic elastic materials as well to model their cylindrical geometries in order to represent PTA semi-compliant balloon inflation. Decorato et al. (2014) for example used a linear elastic model [129], while Schiavone and Zhao (2015) used a hyper-elastic Mooney-Rivlin one [156], both inflating their balloons by internal pressure. However, material parameters were not estimated from specific balloons in clinical use and/or did not present any comparison with real balloon inflation (P-D) data to verify the accuracy of their balloon models alone. In this work, the implemented Ogden law did provide high accuracy in mimicking the semi-compliant balloon deployment process when compared to P-D manufacturer data, specifically within its working range (very low relative % errors as seen in Table 5). Moreover, convergence times are satisfyingly small, with inflations starting from realistic folded diameters (as manufactured), capable to be introduced and simulated inside large-enough stenosis for typical PTA treatments.

The methodology was also applied on different balloons (of different P-D charts) and resulted in similar small errors which validates our balloon model. Appendix A.1 presents an example for another semi-compliant PTA balloon of D_N = 5 mm modeled using our proposed approach, and showing a high accuracy as well. However it is important to note that for unfavorable cases such as large arteries and thick plaques leading to the use of long balloons with small diameter (D_f), the identified value of μ can be too small to ensure robustness due to insufficiently large tangent stiffness at the beginning of the inflation, between D_f and D_{Unf}. In that case, we suggest identifying Ogden law after removing the first points of the manufacturers data (below the nominal pressure when possible), to obtain a larger value of μ. The cost would be a poorer accuracy in the working range but it improves robustness. Another solution would be to start with a larger folded diameter (D_f) also when possible.

Moreover, it is important to recall that straight cylindrical geometries with particular boundary conditions were considered in this work for reducing computational costs. The suggested balloon models in their current states would be somehow limited in being driven in highly tortuous and much narrowed lumens. Different boundary conditions in addition to ad hoc strategies should thus be

applied to position the device when simulating specific arteries with very narrowed and curved/tortuous lumens.

Last but not least, with no resisting external forces being applied on the balloon when simulated alone, both balloon types have shown no profile changes at max inflation. These generated shapes will be compared with profiles resulting from similar balloons when inflated inside a stenosed artery (PTA treatment) in Chapter 4.

CHAPTER 4

SIMULATION OF BALLOON ANGIOPLASTY IN A GENERIC MODEL

This chapter presents the modeling strategy we propose for generically simulating PTA using implicit finite element analysis. The geometry, mesh, material models, and boundary conditions implemented within the stenosed artery are first described. Then the post-processing applied for analyzing simulation results at short terms after balloon angioplasty is detailed. Finally using the suggested model, we present a parametric study based on balloon type, plaque material composition, plaque material distribution, and balloon sizing, which quantifies their influence on lumen gain and elastic recoil ratios obtained right after PTA.

OUTLINE

1 MATERIAL AND METHODS

1.1 GEOMETRY

The artery was modeled as a 25 mm long hollow cylinder, a healthy lumen diameter of 3 mm and a thickness of 1 mm. With the boundary conditions used in this work (see Section 1.4), the arterial length choice did not show significant influence on results (see Appendix A.2 for more details). Accordingly, a 25 mm arterial length was considered here to exceed the plaque and balloon lengths from both sides, but simultaneously to reduce the simulation computational costs. Dimensions were obtained from measurements made by Karimi et al. [115]. The modeled plaque was designed non-axisymmetric to represent irregular shapes experienced in reality. Its length was 10 mm. Plaques are usually characterized by luminal stenosis which severity is expressed as a portion of the initial lumen [174]. Stenosis severities are commonly assessed either in terms of diameters or in terms of areas. In this work we use the diametric definition, corresponding to:

$$\%\ stenosis = \frac{D_{hl} - D_s}{D_{hl}} \times 100 \qquad (4\text{-}1)$$

where D_{hl} and D_s are the healthy lumen and stenosis diameters respectively. A plaque of maximum 60% stenosis was generated, see [Figure 1.1]. The shared topology feature was used between the artery and the plaque geometries. The balloon was modeled as described in Chapter 3.

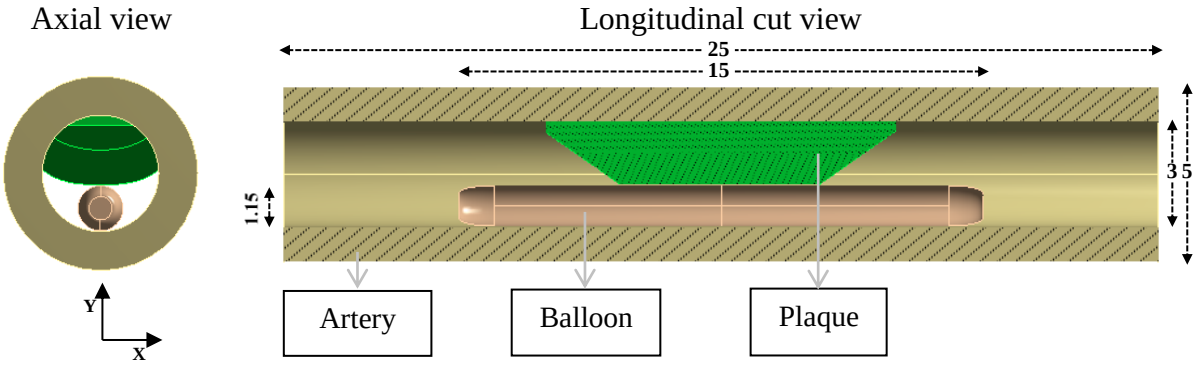

Figure 1.1: PTA system components: artery, plaque, and balloon geometries and dimensions.

1.2 MESH

After a mesh sensitivity analysis, both artery and plaque were meshed respectively by 178856 and 36692 4-node hybrid solid elements (of mixed u-P formulations), corresponding to typical element sizes of 0.25 mm and 0.2 mm in that order. The mesh convergence study is detailed in Appendix A.3. With shared topology being applied, meshes were connected between the two geometries at their

shared circumferential region. Shared topology ensures that a conformal mesh would be achieved where bodies meet, their intersection being meshed perfectly. The 3D FEM model of the complete PTA system is shown in [Figure 1.2].

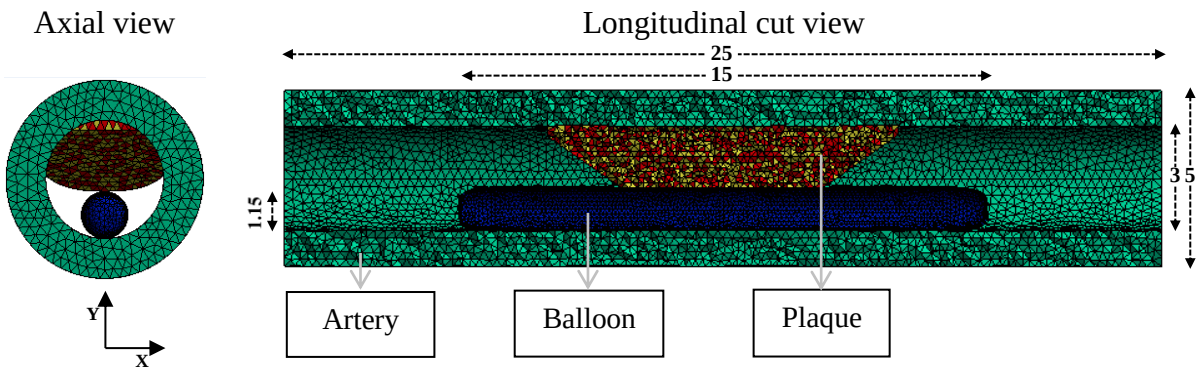

Figure 1.2: Finite element model of the complete percutaneous transluminal angioplasty system. The plaque represented here is heterogeneous with 50% randomly distributed calcifications.

1.3 CONSTITUTIVE LAWS

Elasto-plastic constitutive laws were used in our simulations for all the atherosclerotic components to model residual deformations, towards evaluating acute outcomes after balloon deflation. All details of the material calibration method used for identifying the constitutive laws of each of the artery and plaque within the stenosed region prior to performing PTA simulations are described in Chapter 5. We present here only the material parameters of the lipid and calcified plaque in addition to their corresponding artery in Table 6.

Table 6: Material parameters of the lipid and calcified plaque and their corresponding artery.

Plaque Type	Young Modulus of Elasticity E (MPa)	Poisson Ratio (ν)	Yield Strength (KPa)	Tangent Modulus (KPa)
Lipid Plaque	0.105	0.40	5	62.77
Calcified Plaque	0.189	0.40	15.79	111.88
Artery (Lipid plaque case)	0.677	0.44	7	256.5
Artery (Calcified plaque case)	0.677	0.44	7	330.75

Concerning plaque types simulated in this work, since a wide variability in plaque composition exists among patients, seven different combinations were modeled: a homogenous lipid plaque, a homogenous calcified plaque, two heterogeneous plaques of superimposed equal lipid and calcified parts (see [Figure 1.3]), and three heterogeneous plaques of diverse lipid-to-calcified plaque constitution ratios (30%, 50% and 70% randomly distributed calcifications, see [Figure 1.2]). All seven plaque combination cases were incorporated in the parametric studies of *plaque material*

constitution and *distribution* influence on angioplasty outcomes. Differently, the two homogenous plaques were simulated for the *balloon design* and *balloon sizing studies*.

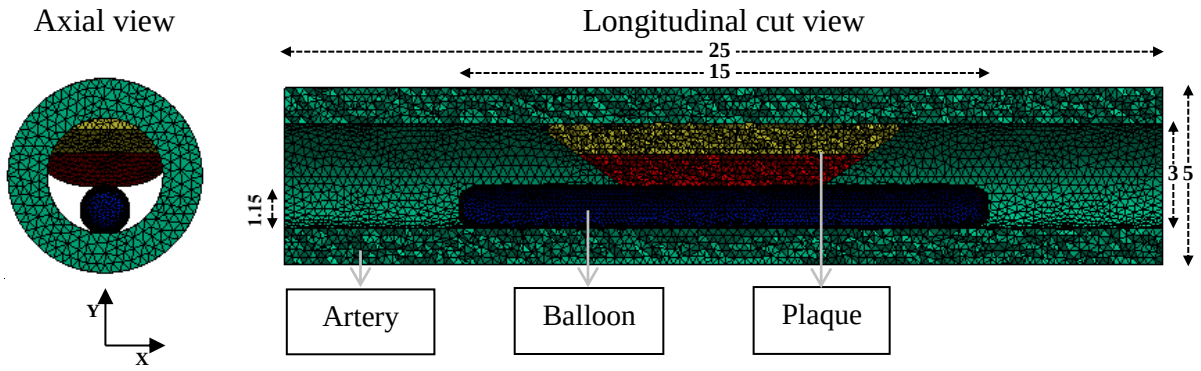

Figure 1.3: Stenosed artery showing a heterogeneous plaque of superimposed equal (in volume) lipid and calcified parts, in comparison to the heterogeneous case with the 50% randomly distributed calcifications seen in [Figure 1.2].

1.4 LOADING AND BOUNDARY CONDITIONS

As detailed in Chapter 3, the non-compliant and the semi-compliant balloons were driven by displacement and pressure respectively.

Regarding the *balloon design* test (semi-compliant vs. non-compliant), both balloon families were inflated up to their nominal diameter (D_N = 2.8 mm), and then deflated back to their initial position. In a similar way, the semi-compliant balloon was also driven up to D_N = 2.8 mm (at P_N = 10 atm) for the different *plaque material composition* and *distribution* simulation tests. Finally, and being also interested in the assessment of *balloon sizing* influence on acute PTA outcomes, three different inflating pressures were simulated using the semi-compliant balloon as well. The chosen balloon sizings with their corresponding rated diameters at each inflation pressure are depicted in Table 7. All simulated balloon diameters fall within the clinically recommended range of balloon sizings (inflated balloon diameter to healthy arterial lumen diameter ratio) of [0.9 to 1.1] for PTA treatments [36].

Table 7: Balloon sizing at each simulated inflation pressure

Inflation Pressure (atm)	**Corresponding Rated Diameter (mm)**	**Balloon Sizing (Balloon/Artery ratio)**
10	2.8	0.933
12	3.02	1.007
14	3.2	1.067

In-plane (x-y plane) arterial translations were allowed at both ends of the artery to allow its free adaptation to balloon inflation (preventing any unrealistic bending), the balloon being itself clamped as described in Section 3.3 of Chapter 3. Axial translation and all rotations were prevented in the

model. The non-linear contact between the balloon, the plaque, and the artery is frictionless and formulated by pure penalty. ANSYS implicit commercial finite element software (ANSYS® Academic Research Mechanical, Release 19.1.) was used to solve these large-deformation analyses, solved under the finite strain theory.

1.5 ANALYSIS OF RESULTS

Simulation results were analyzed in terms of elastic recoil ratio (ERR) and lumen gain ratio (LGR) obtained after PTA for the four studies: *balloon design*, *plaque material composition*, *plaque material distribution,* and *balloon sizing* influences on acute post-procedural outcomes. The elastic recoil ratio was assessed as the difference between the max-inscribed-sphere diameter that can be generated along the centerline at max balloon inflation vs. after balloon deflation (equation (4-2)). ERR is comparable to what clinicians usually measure after performing PTA as a control for their treatment outcomes. In a similar way, the lumen gain ratio was calculated as the difference between max-inscribed-spheres diameter after balloon deflation vs. before balloon inflation (equation (4-3)). Vascular Modeling Toolkit (VMTK) (www.vmtk.org) was used for centerlines and max-inscribed-spheres extractions.

VMTK is a collection of libraries and tools that are usually used for 3D reconstruction, mesh generation, and surface data analysis for image-based modeling of blood vessels. Since our simulations consisted of 3D solid models with volumetric mesh (and not surface mesh), the direct use of VMTK for the analysis and the extraction of the desired data in our work was not possible alone.

Accordingly, surface models representing the inner lumen geometries of the simulated stenosed arteries (at the required states during PTA) had to be generated prior to the usage of VMTK. To do so, a negligible surface pressure was first applied to the inner regions of the stenosed arteries. This allows the extraction of the connectivity data corresponding to the nodes and elements composing these inner surfaces. Besides, their nodes coordinates at three positions of interest during PTA (i.e. before balloon inflation, at its max inflation, and after its deflation) were also extracted from ANSYS® software using mechanical APDL commands (see Appendix A.4).

Once the elements connectivity data and their respective nodes coordinates were obtained, VTK files representing the diseased arterial inner surfaces at each required state during PTA were generated. The detailed C++ script applied for creating these VTK files from elements connectivity data and nodes coordinates is presented in Appendix A.5 (Part I). Afterwards, using VMTK, centerlines and max-inscribed-spheres data were extracted from the generated inner luminal geometries (VTK files) at the desired positions during the simulations. Finally ERR and LGR were computed from the max-inscribed-sphere diameters as can be seen respectively in equations (4-2) and (4-3). More details on the MATLAB script (MATLAB. (2013). 8.2.0.701 (R2013b). Natick, Massachusetts: The MathWorks Inc.) applied for extracting centerlines and max-inscribed-spheres using VMTK, and then computing

the ERR can be seen in Appendix A.5 (Part II). The same script can be applied for calculating the LGR after adjusting its formula to the one seen in equation (4-3).

$$Elastic\ Recoil\ Ratio\ in\ \% = ERR_{along\_centerline} = \frac{D_{\max\_inflation} - D_{after\_deflation}}{D_{\max\_inflation}} \times 100 \qquad (4\text{-}2)$$

$$Lumen\ Gain\ Ratio\ in\ \% = LGR_{along\_centerline} = \frac{D_{after\_deflation} - D_{before\_inflation}}{D_{before\_inflation}} \times 100 \qquad (4\text{-}3)$$

[Figure 1.4] presents an illustration of the inner luminal geometries showing their centerlines and the max-inscribed-spheres appearing in two different positions along the stenosed artery: (a) before inflating the balloon, (b) at its max inflation state and (c) after its deflation.

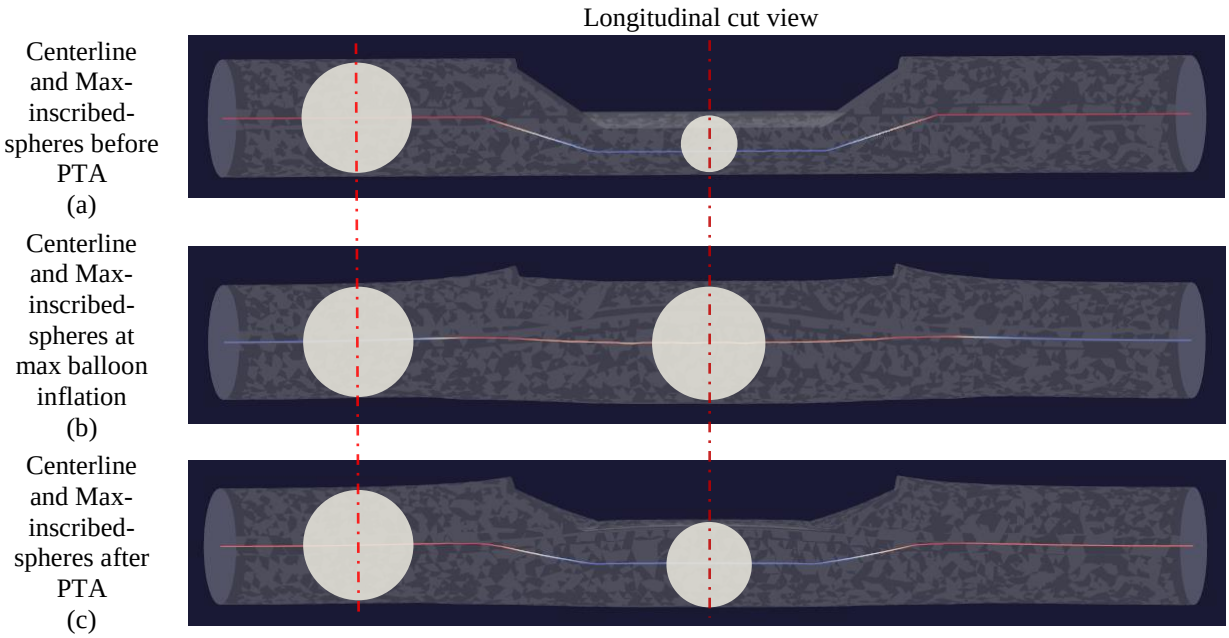

Figure 1.4: Reconstructed surface geometries that correspond to the stenosed artery inner lumen showing max-inscribed-spheres (in tan) at two random sections (in red) along their centerlines for the three states of interest during balloon angioplasty simulations.

2 RESULTS

Several combinations of balloon design, plaque material composition, plaque material distribution, and balloon sizing were simulated. Their convergence time did not exceed 2.5 hours when simulated on the same computer, with shorter times for displacement-driven non-compliant balloons.

2.1 BALLOON DESIGN INFLUENCE ON PTA OUTCOMES

Each balloon design was separately simulated to its nominal diameter (D_N = 2.8 mm) within the two homogeneous plaques (lipid and calcified). [Figure 2.1 (A)] illustrates the plastic deformations occurring in the calcified diseased artery model after balloon deflation in an axial and a longitudinal cut view. Residual deformations were observed in both the artery and the plaque, with more significant concentration within the stenosed region.

[Figure 2.1 (B-I) and (B-II)] respectively show the semi-compliant vs. the non-compliant balloon profiles at max inflation within the calcified plaque. It can be seen that only semi-compliant balloons experienced profile change during inflation, with more variations within calcified plaques (dog-bone effect). At the stenosed region, the semi-compliant balloon shifted more towards the opposite side of the plaque, causing more residual deformation in the artery opposing the stenosis. Differently, more permanent deformation was observed in the artery covering the plaque with the non-compliant balloon.

[Figure 2.1 (C)] presents the balloons diameter evolution at their central plane along the inflation/deflation phases for four different cases: a non-compliant balloon, a semi-compliant balloon outside a stenosed artery, and a semi-compliant balloon inside a stenosed artery with a lipid vs. a calcified plaque. The non-compliant balloon and the semi-compliant one simulated outside the stenosed artery virtually reached their anticipated nominal diameters (D_N) of 2.8 mm at max inflation (seen also in Chapter 3). Even though the semi-compliant balloons did not reach the exact desired diameter at nominal pressure when inflated within stenosed arteries, the differences were not significant.

[Figure 2.1 (D)] shows the lumen gain and the elastic recoil ratios attained along the artery axis after PTA using the two modeled balloon designs, within the lipid and calcified homogenous plaques. [Figure 2.1 (D-I)] also shows the initial lumen diameter evolution along the axis. LGR directly evaluates the lumen expansion caused by the balloon inflation, thus residual strains occurrence within the tissues. ERR appraises how much the diseased artery recoils after being expanded by the balloon; if the tissues were fully elastic, they would move back to their initial positions after balloon deflation. Both LGR and ERR were larger where there was large stenosis (small initial lumen diameter), while they reached 0 or even (slight) negative values where no plaque was present. Negative values were

probably caused by the surrounding elastic and plastic strains that can influence the arterial diameters locally even at healthy regions. As expected, in largely stenosed regions, ERR were higher within the calcified plaque cases, see [Figure 2.1 (D-II)]; consequently, lower LGR were observed within these calcified stenosis cases, see [Figure 2.1 (D-I)]. Finally, upon comparing the balloon-type influence on acute PTA post-procedural outcomes (LGR and ERR), no differences were observed within both simulated homogeneous plaques whether a semi-compliant or a non-compliant balloon model was used.

(A-I): Axial view

(A-II): Plastic deformations in stenosed artery (longitudinal cut view)

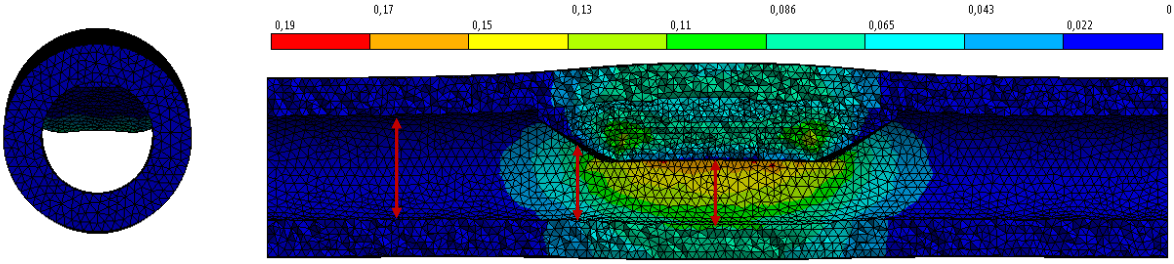

(B-I): Semi-compliant balloon profile at max inflation

(B-II): Non-compliant balloon profile at max inflation

(C): Semi vs. Non-compliant balloons diametric evolution at their central planes simulated outside and inside stenosed arteries

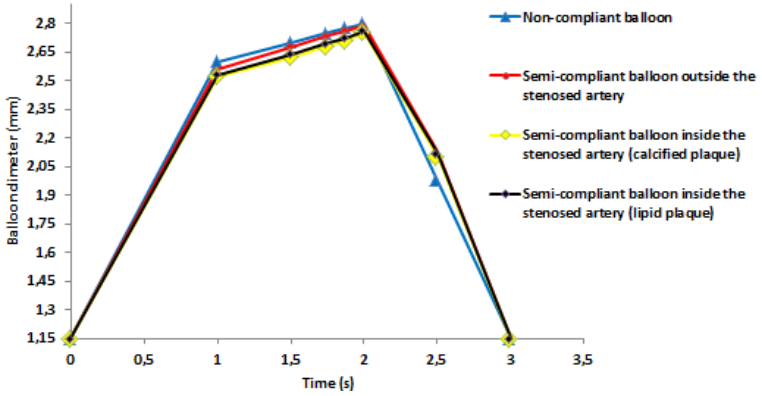

(D-I): Lumen gain ratio for different Balloon Designs, and the initial lumen diameter evolution along the axis

(D-II): Elastic recoil ratio for different Balloon Designs

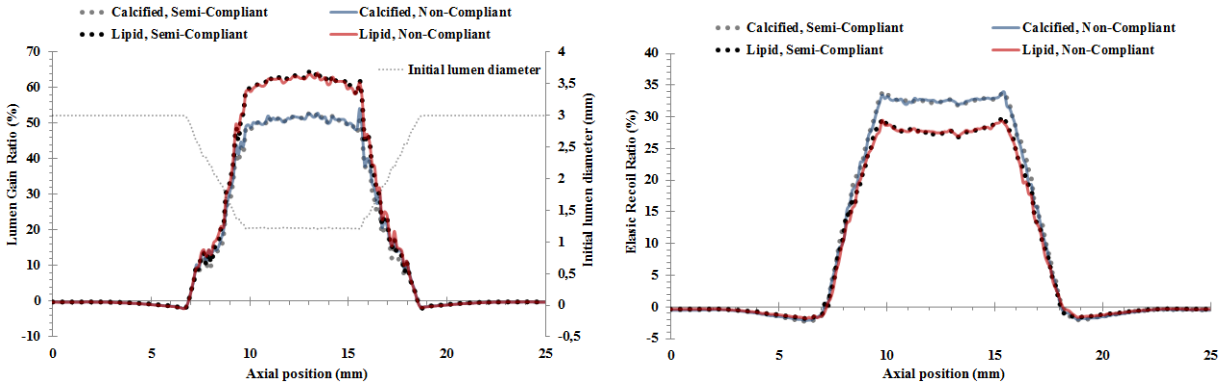

Figure 2.1: (A) Plastic deformations resulting after PTA in one simulation at 10 atm with red arrows representing the final lumen diameter ($D_{after\_deflation}$) attained after balloon deflation at 3 random positions. (B) The semi-compliant vs. the non-compliant balloons profiles at their max inflation states within a calcified stenosis. (C) Balloons diameter evolution at their central plane along the inflation and deflation process for 4 different cases: non-compliant balloon, semi-compliant balloon outside a stenosed artery, and semi-compliant balloon inside the stenosed artery by a calcified vs. a lipid plaque. (D) Lumen gain ratios (D-I) in addition to the elastic recoil ratios (D-II) obtained along the artery axis after PTA using the two different balloon designs, within the lipid and calcified homogenous plaque compositions.

2.2 PLAQUE MATERIAL COMPOSITION INFLUENCE ON PTA OUTCOMES

To evaluate the influence of the plaque material on the PTA outcomes, the semi-compliant balloon was inflated up to its nominal diameter into a stenosed artery for different plaque compositions.

Besides the two homogeneous (lipid and calcified) plaques, three heterogeneous cases of different lipid-to-calcified plaque ratios (30%, 50% and 70% randomly distributed calcifications) were also modeled for this parametric study. Upon analyzing the attained LGR and ERR values after PTA, see [Figure 2.2], it can be seen that they varied in the opposite direction with respect to the change in calcification concentration in the plaque. LGR reached its highest value (~62%) when the plaque contained 0% of calcifications (all lipidic); it decreased progressively with the growth of calcification proportion within the plaque, reaching (~51%) when the plaque was all calcified. Differently, the ERR had its lowest value (~29.5%) when the plaque had no calcifications; it gradually increased with the augmentation of calcification ratio within the plaque, reaching its highest value (~33.5%) when the plaque was totally calcified. Furthermore, the rate at which the LGR changed between the entirely calcified plaque and the completely lipidic one (51 to 62%) was larger than the rate at which the ERR changed between the same plaque compositions (33.5 to 29.5%).

Lumen gain ratio for different Plaque Material Compositions, and the initial lumen diameter evolution along the axis
(A)

Elastic recoil ratio for different Plaque Material Compositions
(B)

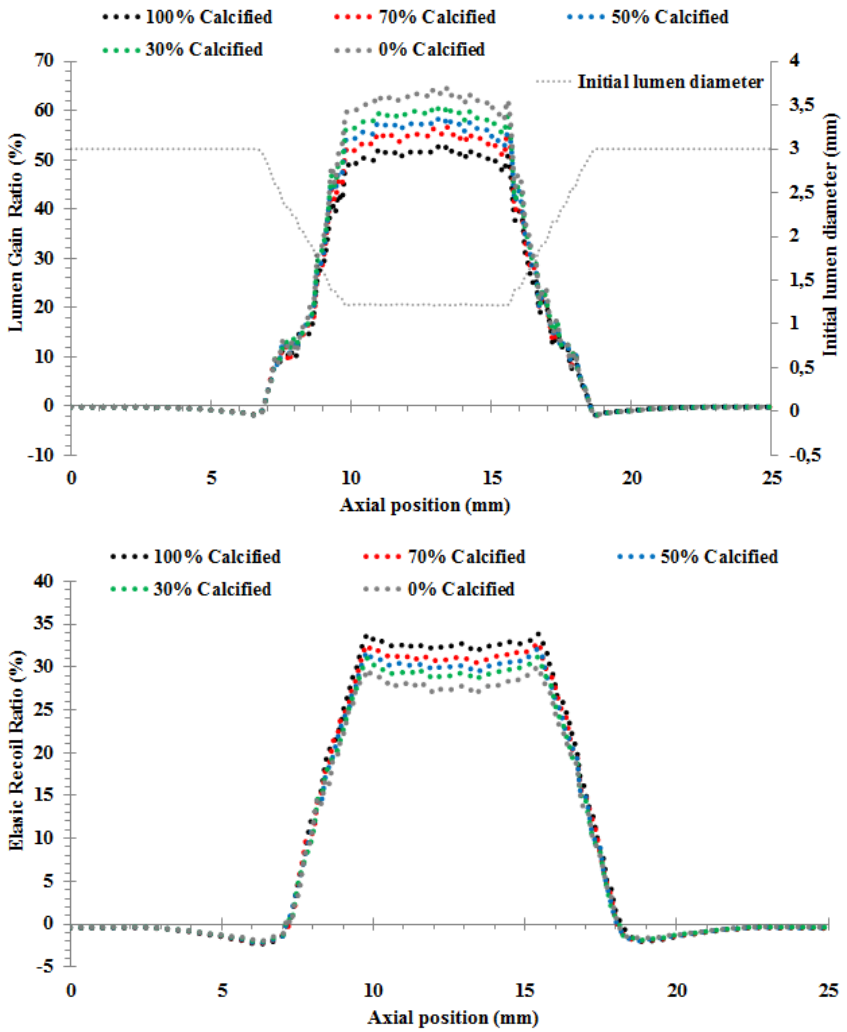

Figure 2.2: Lumen gain ratios (A) in addition to the elastic recoil ratios (B) attained along the artery axis after PTA for different plaque material compositions (lipid-to-calcified constitution ratios), using the semi-compliant balloon inflated at 10 atm. (A) also presents the initial lumen diameter progression along the stenosed artery prior to balloon angioplasty.

2.3 PLAQUE MATERIAL DISTRIBUTION INFLUENCE ON PTA OUTCOMES

To appraise the influence of the plaque material distribution on the PTA outcomes, the semi-compliant balloon was then simulated to its nominal diameter within three heterogeneous plaques of equal lipid-to-calcified constitution ratios, but of different distributions within the plaques. In addition to the heterogeneous plaque with 50% of randomly distributed calcifications, two other heterogeneous plaques of superimposed equal lipid and calcified parts were also modeled for this parametric study. [Figure 2.3 (A) and (B)] respectively present the LGRs and ERRs obtained along the artery axis after PTA within the three heterogeneous plaques. It can be seen that both of the LGR and ERR values showed negligible changes upon varying the distribution of the materials. Only a minor difference was observed between their curves showing a slightly higher LGR (while a slightly lower ERR) whenever the lipidic part of the heterogeneous plaque was closer to the balloon.

However upon analyzing plastic strains, significant differences can be observed in their distributions in accordance with the altered arrangements of materials in the plaques. Plastic strain values always showed higher magnitudes within the lipidic regions of the plaques in comparison to the calcified ones (see [Figure 2.3 (C)]). This was more clearly illustrated by the two superimposed heterogeneous plaque cases having their lipid and calcified components as two separate parts.

Lumen gain ratio for different Plaque Material Distributions, and the initial lumen diameter evolution along the axis
(A)

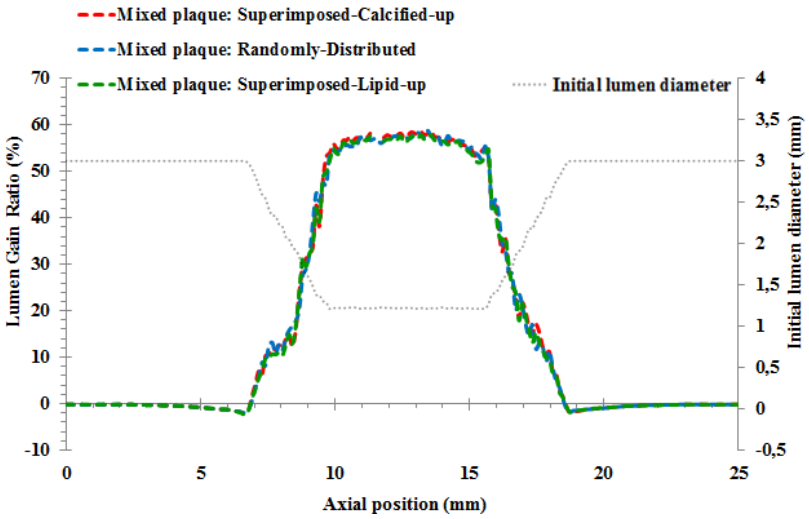

Elastic recoil ratio for different Plaque Material Distributions
(B)

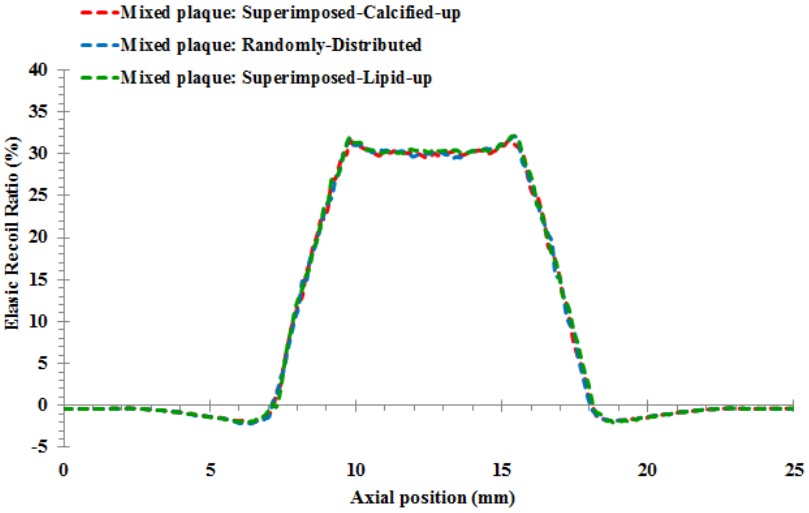

(C)

Mixed plaque: Superimposed-Calcified-up

Mixed plaque: Randomly-Distributed

Mixed plaque: Superimposed-Lipid-up

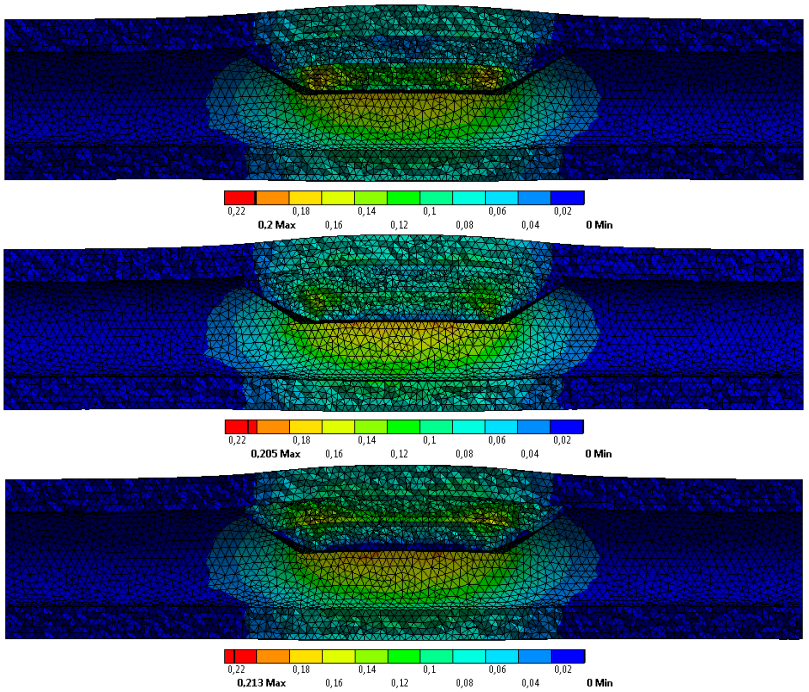

Figure 2.3: Lumen gain ratios (A) and the elastic recoil ratios (B) obtained along the artery axis after PTA within the three heterogeneous plaques of the same material composition (50%-to-50% lipid-to-calcified constitution ratios), but of different material arrangements, also using the semi-compliant balloon inflated at 10 atm. (C) Plastic strain distributions (in longitudinal cross-sectional views) within the stenosed arteries of the simulated heterogeneous plaque cases: superimposed calcified-up, randomly distributed, and superimposed lipid-up.

2.4 BALLOON SIZING INFLUENCE ON PTA OUTCOMES

Balloon sizing was evaluated by simulating the semi-compliant balloon within the two homogenous plaques for different balloon diameters falling within the clinically recommended range of balloon/artery diameters ratios. [Figure 2.4 (A) and (B)] respectively present the evolutions of LGR and ERR along the artery axis for the three balloon sizes. Unlike LGR that directly relates to the lumen expansion due to balloon inflation, the interpretation of ERR can be slightly more challenging when it comes to comparing balloon sizings. We can see on [Figure 2.4 (A) and (B)] that both LGR and ERR are in positive correlation with balloon sizing, with significantly larger rates of change for the LGR in comparison to the ERR from one sizing to another. This indicates that increasing the balloon sizing to a small extent increases the ERR, and to a larger extent increases the LGR. It also means that the stenosed vessel experiences more of both plastic and elastic strains with the increase of balloon sizing, with much larger potentials of residual deformations, i.e. lumen expansion.

[Figure 2.4 (C)] depicts in longitudinal cut views the max principal strains distributed in the arterial wall at max inflation for the three balloon sizings. Their peak value showed a significant increase at larger simulated inflation pressures: 0.25 at 14 atm vs. 0.19 at 10 atm. Besides, the peak values seem to occur at a similar location among the different sizings, within the max stenosed region.

Lumen gain ratio for different Balloon Sizings, and the initial lumen diameter evolution along the axis
(A)

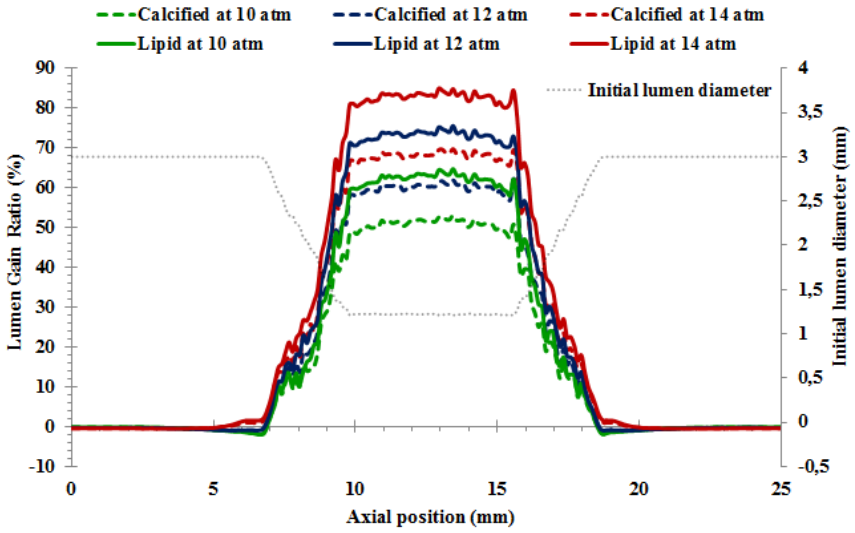

Elastic recoil ratio for different Balloon Sizings
(B)

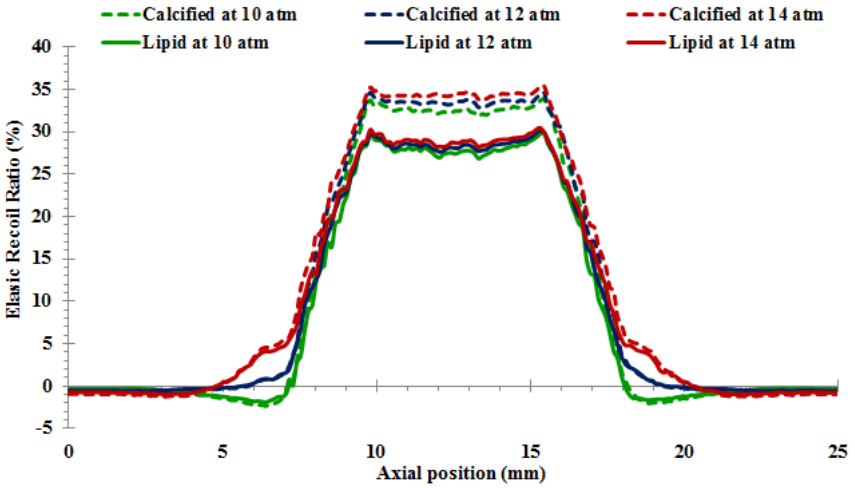

(C)

Balloon Sizing at 10 atm

Balloon Sizing at 12 atm

Balloon Sizing at 14 atm

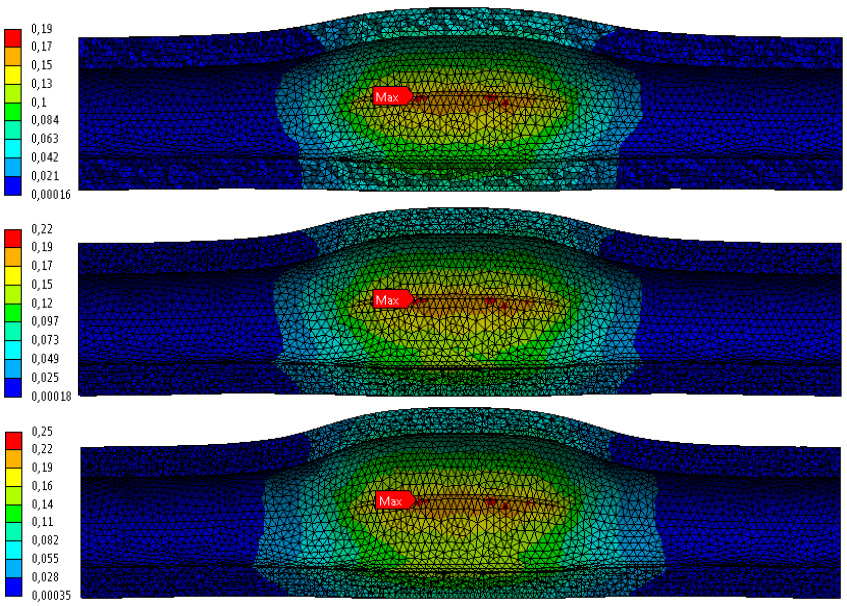

Figure 2.4: Lumen gain (A) and elastic recoil (B) ratios evolution after PTA along the artery axis for diverse sizings of the semi-compliant balloon at 10, 12 and 14 atm, within the two homogenous plaque compositions (lipid and calcified). (C) Max principal strain field in the arterial wall (in a cross sectional view) during PTA at max balloon inflation for the three different balloon sizings. Max value site is also shown for each sizing. The plaque is not shown.

3 DISCUSSION

The assessment of clinical outcomes after balloon angioplasty is important for the treatment success evaluation. The present chapter aims at proposing a generic modeling strategy for PTA using an implicit FEM solver, to evaluate the acute post-procedural outcomes for different balloon designs, plaque material compositions, plaque material distributions, and balloon sizings. Elasto-plastic material models were implemented within both the plaque and artery to promote permanent deformations. Besides appraising plastic strain distributions of some simulations, results were mainly assessed in terms of LGR and ERR. Maximal principal strains within the arterial walls were also evaluated for the different balloon sizings simulated.

In order to analyze balloon design influence on outcomes at short term after balloon angioplasty, the two modeled balloons (semi- and non-compliant, see Chapter 3) were simulated within stenosed arteries. As expected, only the semi-compliant balloon showed a change in its profile during inflation, with a larger alteration inside the calcified stenosis, see [Figure 2.1 (B)]. This phenomenon is known as the 'dogbone effect' (small waist appearance in middle of balloon), which usually occurs around stiff plaques when dilated with softer balloons [89], [169]. This uncontrolled over-expansion of the balloon outside the plaque may damage the artery or cause balloon rupture; therefore, clinicians usually suggests using the non-compliant balloons in the presence of calcified lesions for more effective dilations [88], [89], [169]. Because of the plaque resistance, semi-compliant balloons do not exactly reach their expected diameter when inflated into a stenosed artery, but this is not significant, see [Figure 2.1 (C)]. For both soft and stiff plaques, negligible differences were also observed in terms of the LGR and ERR obtained after PTA upon changing balloon design, see [Figure 2.1 (D)]. Therefore, in this work, balloon type showed no influence on acute post-procedural outcomes after PTA. This finding is in accordance with the retrospective nonrandomized studies that showed no difference between semi-compliant and non-compliant balloons with respect to the final procedural outcomes (e.g. final residual stenosis) [36], [171].

Independent from the balloon design, plaque composition, plaque material distribution or balloon inflation size used, LGR and ERR always showed a negative correlation to the initial lumen diametric evolution along the artery axis. This indicates that as expected, the most stenosed regions (smallest initial lumen diameters) are the most susceptible to balloon angioplasty treatments. It explains why clinicians usually assess PTA outcomes at such regions as well [88], [164], [165].

When interpreting the ERRs attained from our simulations in comparison to clinically reported values [164], [165], [175], it confirms that the assumption for the material models of the artery and plaque considered in this work is reasonable. Hanet et al. found mean clinical recoil ratios of 32% ± 12% of luminal diameter immediately after PTA in coronary arteries [165]. Similarly Isner et al. and Gardiner

et al. reported that elastic recoils in iliac peripheral arteries respectively averaged 28.6% ± 7.2% vs. 36% ± 11% [164], [175]. Clinicians generally compute their ERR at most stenosed regions. With our measured ERR values at similar locations ranging between 28% and 36% for the different balloon designs, plaque material compositions, plaque material distributions, and balloon sizings simulated, our results showed consistency with clinical findings. This 28-36% range of ERR can appear rather narrow, this is due to the fact that it is measured at locations with large stenosis (60%); a wider range would be obtained when considering different locations with different degrees of severity.

Unlike balloon types, plaque material composition showed an impact on simulated results obtained immediately after PTA (LGR and ERR). As expected, the calcified plaque experienced a higher ERR compared to the lipid one. This assumption was based on clinical findings that reported rather higher ERR values in the presence of calcified plaques with the hypothesis that these stiff plaques would experience less compression themselves while expanding more the elastic arterial wall during reasonably sized inflations, leading to higher recoils after balloon deflation, even if the differences were not major [164], [165]. On the other hand, LGR decreases while calcification proportion within the plaque increases. This indicates that plastic deformations would be higher when the plaque is less calcified. Both ERR and LGR were affected by the calcification ratio in the plaque but without a significant effect of the randomized distributions of components themselves.

The plaque material distribution parametric study highlights the negligible influence of the arrangements of materials within the plaque on the LGR and ERR obtained directly after PTA. However, a significant difference was observed in how the plastic strains were distributed among the three heterogeneous simulated plaque cases. Being softer, lipidic regions experience higher plastic deformations, making material distribution a possible cause for unequal vulnerability in different heterogeneous plaques.

Balloon sizing has also a significant influence on results attained shortly after balloon angioplasty. Both ERR and LGR showed a positive correlation to the augmentation in inflation pressure, independently from the plaque composition. This finding is in agreement with clinical observations stating that the elastic recoil is generally in direct association with the balloon/artery ratio [164], [165], [176]. However ERR and LGR do not evolve at the same rate with respect to sizing, which makes sense given their expression. Indeed, at the max stenosed region, for pressure growing from 10 to 14 atm, the ERR rose from 29.5% to 30.5% with the lipid plaque and from 33.5% to 35.5% with the calcified one, while the LGR rose from 62% to 83% with the lipid plaque and from 51% to 68% with the calcified one. This indicates that at higher sizings, the treated stenosed artery experiences significant plastic strain. In this work, we did not model the complex damage and flow mechanisms occurring at small scales in diseased arteries during PTA; plasticity was used instead to represent these phenomena. It is important to note that this damage can be always considered as a positive

phenomenon allowing a larger lumen after balloon angioplasty (as 'controlled vessel injuries' [77]), until the artery itself become vulnerable to dissections.

Max principal strains occurring in the arterial walls at max inflations for the three simulated sizings were interpreted as an indication for their risk of rupture. With strain peak values showing sharp increases from 0.19 to 0.25 for a sizing change from 10 to 14 atm, the artery vulnerability to rupture is influenced by the balloon sizing choice as well. This model seems to objectify clinical observations indicating that a compromise should be settled achieving the desired lumen gain after balloon angioplasty but without dissecting the healthy arterial tissues.

One should keep in mind that despite continuing to be the method that all other available endovascular treatment modalities are still compared against to date [40], the standard plain balloon angioplasty technique is clinically associated to some limitations as well. Treatment of complex lesions including heavily calcified long lesions and chronic total occlusions remains challenging for angioplasty balloons, even for drug-eluting ones [177]. Accordingly, several interventional approaches are being lately further investigated and applied either as stand-alone treatments or as lesions preparations prior to PTA to overcome its limitations. Numerous balloons of different mechanisms of action available nowadays on the market are devoted to preparing such complex lesions [178]. Focal force balloons and endovascular atherectomy devices are examples of treatment alternatives designed to prepare complicated lesions to enhance acute post-procedural outcomes. In this context, simulating angioplasty remains an issue of interest, either because PTA is part of the treatment process, or in order to evaluate and define the interventional strategy.

Limitations of this study concerning the artery and plaque models are described in details in the discussion and limitations section of Chapter 5 that focuses on the artery and plaque material models calibration.

Another important limitation of this work concerns the pressure-driven semi-compliant balloon models. Whenever convergence difficulties are encountered while simulating large diameters balloons outside a stenosed artery, our suggested way in Chapter 3 (which consists of identifying Ogden law after removing the first two or three points of the manufacturers data to obtain a larger value of μ) can be a good solution for the problem. However that is not always true for balloon models when simulated inside large stenosed arteries. In such cases convergence will be subject to several aspects including the balloon initial and nominal diameters, and the plaque thickness, shape and composition. As in our proposed modeling method for semi-compliant balloons (of Chapter 3) we do not model their foldings (for simplicity), a 7 mm nominal diameter balloon for example would have to inflate starting from its very small initial diameter (1.15 mm) until reaching its desired nominal diameter. Outside a stenosed artery, this might be solved by increasing the value of μ as mentioned previously; however within a stenosed artery, it would not be sufficient. Accordingly, in order to avoid divergence

issues resulting from the failure of the balloon model within the stenosed artery, we suggest increasing (D_f) (the initial folded diameter), and to start with larger values compared to usual values found from manufactured catheters (~ 1.15 mm for example). A recommended way would be to try to keep the inflation ratio between the final nominal diameter (D_N) and the initial one (D_f) less than ~2.25 when possible. In summary, the proposed pressure-driven balloon modelling method using Ansys implicit solver (seen in Chapter 3) is somehow limited for large diameter balloons within highly stenosed arteries; nevertheless it is still an ideal approach for arteries of small diameters (less than 3.5 or 4 mm), keeping the correct initial folded diameter of the modeled balloon (to avoid insertion issues), and ensuring robustness, accuracy and minimal simulation time as well. Besides, displacement driven non-compliant balloons can always be the possible substituting choice whenever very large arterial diameters of thick stenosis are to be simulated; it also ensures convergence with robustness. With no variations in ERR nor LGR values detected when the balloon design was changed, despite the differences observed in their profile at max inflation as seen in Section 2.1, replacing the pressure driven semi-compliant balloon by the non-compliant one when required should not affect the sought objective of this work. It is also important to state that up to our knowledge, all the available FEM studies in the literature which used an implicit solver to model balloon angioplasty considered arteries of small diameters as well [107], [120], [129]. Another possible solution for modeling PTA using pressure within highly stenosed large diameter arteries would definitely be to use an explicit solver instead, like was done by the majority of FEM studies. Explicit solvers are usually better for large deformation and sliding contact cases, but of course with the drawbacks of dynamic inertia effects (e.g. mass scaling) and large simulation times [158].

4 CONCLUSION

This work proposes a generic modeling strategy of PTA using an implicit FEM solver capable of assessing post-procedural outcomes at short terms after balloon deflation. After categorizing and modeling balloons (seen in Chapter 3), and developing and identifying consistent constitutive laws for both the plaque and artery (further detailed in Chapter 5), we present a parametric study based on balloon type, plaque composition, plaque material distribution and balloon sizing, which quantifies their influence on the ERR and the LGR. It shows that for a given plaque, balloon sizing is the key factor to obtain a satisfactory post-procedural lumen diameter, as it allows to control the amount of plastic strain stored in both the artery and the plaque.

Now that the framework of a relatively fast and accurate PTA modeling within a generic stenosed artery is set, the next step of our work is its application to patient-specific situations, of different arterial diameters, plaque material compositions and severities.

CHAPTER 5

PLAQUE AND ARTERY MATERIAL MODELS CALIBRATION

One key step towards obtaining reliable results from FEM simulations is the right choice of their material models and their parameters. In this chapter we present the calibration method used for defining the constitutive laws of the artery and the plaque prior to performing PTA simulations. With still no method of in vivo material characterization offering a clear advantage in determining realistic material properties of diseased arteries, the in vitro based experimental data on the inelastic behavior of plaques under compression obtained from Maher et al. (2011) [148] *were initially considered in our model in order to identify the plaques constitutive laws. Afterwards, the arterial material models were tuned in tension to satisfy averaged clinically obtained ERR values after balloon deflation. The artery and plaque material parameters are then presented to be implemented in the FEM simulations of PTA. The advantages and limitations of this calibration method are finally described.*

OUTLINE

1 INTRODUCTION

The success of balloon angioplasty at short term is evaluated by the permanent lumen gained directly after the endovascular treatment. Non-recoverable deformation usually occurs within both the plaque (compression/damage) and the artery (clinically known by "controlled vessel injury" [77]). The achieved lumen is usually assessed by either the patency rate or the elastic recoil ratio (ERR) measured at the maximum stenosed region after PTA. The ERR characterizes how much this atherosclerotic section recoils after balloon deflation. Therefore assessing acute clinical outcome (residual deformations, elastic recoils...) after balloon angioplasty is of fundamental importance for the evaluation of the treatment success.

In spite of its potential for clinicians (treatment planning) and balloon manufacturers (device design and sizing), up to our knowledge only few FEM studies focused on assessing outcomes at short terms after balloon angioplasty alone (i.e. without stent implantation). In general, one key factor allowing or not FEM studies from evaluating PTA influences on outcomes directly after the treatment is the constitutive laws selected for modeling the atherosclerotic artery.

Since there is still no method of *in vivo* material characterization presenting a clear advantage in extracting realistic material properties of atherosclerotic arteries, most FEM studies still currently mainly focus on *in vitro* experimental data in order to develop material models for their diseased arterial components. Yet, even these experimental studies are relatively limited in numbers [90].

Atherosclerotic arteries were differently modeled by diverse FEM studies simulating PTA. Some considered elastic material models while others inelastic ones, with their constitutive laws being usually fitted to sets of experimental data available in the literature. Chapter 2 presented a review of the various material models considered by different FE studies for each of the plaque and artery components distinctly: elastic (linear/non-linear; isotropic/anisotropic) and inelastic (damage mechanisms with/without permanent deformation). Accordingly, notable variations were also observed within their generated outcomes as was detailed in the same chapter. Results obtained from biomechanical studies strongly depend on the constitutive laws and the parameters used.

In what follows, we first summarized the different material models considered by FE studies modeling PTA in relation with their abilities in assessing outcomes at short terms after the treatment; afterwards we focused more on studies considering inelastic constitutive laws with residual deformations in their models, towards our material models choice in this work.

Even though hyperelasticity can be a good approximation for several soft tissues behaviors [90], this type of material model does not allow for differentiating loading and unloading paths. Neglecting inelasticity and modeling hyperelasticity alone would prevent PTA simulations from evaluating acute

treatment outcomes that usually show residual deformations observations. According to clinical findings, elastic recoil immediately after PTA varies between 11% and 55% for different stenosed regions, plaque compositions, and balloon/artery diameters ratios [87], [163]–[165], [175], [176]. Similarly, FEM studies analyzing the rupture of atherosclerotic arterial tissues by incorporating damage mechanisms such as cohesive zone, crack propagation, or damage models were also limited in terms of the acute outcomes assessment after balloon angioplasty. Inelastic material models including damage such as the softening behavior on its own (Mullins effect) would result in no residual strains at unloading [112], contradicting clinical observations as well. Therefore plasticity was incorporated in the materials constitutive laws of the present work for the purpose of assessing angioplasty procedure outcomes in terms of permanent deformations.

There are few FE studies available in the literature that considered describing the inelastic behavior of soft tissues (such as arteries [103], [117], [120] and plaques [107], [121], [122], [150], [151]) by using inelastic constitutive laws with residual deformations in their models.

Each of Holzapfel et al. (2002), Gasser and Holzapfel (2007a), and Li et al. (2012) modeled inelasticity in non-diseased arterial components (media alone [117], or intima and media [103], [120]) associated with tissue stretches beyond physiological domain. Li et al. (2012) used a multi-mechanism model where damage is introduced in the collagen and elastin separately, and a permanent strain results when the elastin fails [120]. Whereas Holzapfel et al. (2002) and Gasser and Holzapfel (2007a) used the concept of plasticity to model inelasticity in their arterial components. Holzapfel et al. (2002) [103] used inelastic constants for the non-diseased media obtained from their own experimental work in [179]. In this work they considered applying two supra-physiological loading cycles on the non-diseased media tissue only, thus computing its inelastic behavior. Whereas due to the lack of suitable mechanical data on the inelastic behavior of soft vascular tissues in [117], [120], inelastic constants for their non-diseased components modeled were assumed presumably. Moreover, among the mentioned studies, no inelastic behavior was hypothesized for the modeled plaques [103], [117], [120].

In a different way, Liang et al. (2005), Gastaldi et al. (2010) and Conway et al. (2014, 2017) included plasticity within their plaque models [107], [121], [150], [151]. All these reported studies (considering plasticity within the plaques) assumed a perfect plasticity model. But due to large variabilities in plaque composition from one side, in addition to limited experimental data available on their rupture, different rupture stress and strain values were considered in the assumed perfect plastic models of the mentioned FE studies: either based on the available monotonic tensile test data (such as Loree et al. 1994 [139]) [121], [151], or empirically chosen [107], [122]. Conway et al. (2014, 2017) also simulated plaque models including the Mullins effect with permanent set as well [121], [150]. Up to our knowledge, only Iannaccone et al. (2017) [122] considered incorporating plasticity in both the artery and the plaque material models at the same time. However, similar to the previously reported

studies, also here, perfect plasticity models were used in order to roughly emulate the behavior of the stenosed region after the treatment; no parameter calibration in comparison to clinical data was further performed.

Since it has been experimentally observed that neither the plaque nor the arterial tissues behave as elastic materials under supra-physiological loading conditions [148], [180], in this work plasticity was integrated within both the plaque and artery material models with the aim of evaluating PTA procedure outcomes in terms of residual deformations. Accordingly, the plaques constitutive laws were first tuned based on Maher et al. (2011) experimental data on the inelastic behavior of plaques [148], while the arterial models were then identified to satisfy averaged clinically obtained ERR values after PTA.

2 CALIBRATION OF THE PLAQUE MATERIAL MODEL

2.1 METHODS

Knowing that we aim in this work to evaluate acute outcome after PTA alone, one balloon inflation-deflation cycle was required to be simulated. Accordingly and for simplification, no stress-softening (Mullins effect) was included in the plaque material models. Moreover, even though atherosclerotic plaque tissues have been observed to exhibit non-linear behavior, in this simplified calibration work, bilinear isotropic hardening models [181] were considered. Plaque material constitutive laws were then tuned based on permanent deformations experimentally obtained in these atherosclerotic tissues as reported in the literature.

Among the reported experimental data on the mechanical properties of atherosclerotic plaques, Maher et al. (2011) work is one of the very few studies that evaluated the inelastic behavior of human plaques [148]. The global inelastic mechanical properties of carotid plaque tissues were investigated using dynamic unconfined cyclic radial compressive tests at room temperature. Tests were performed on 21 plaque samples that were classified using ultrasound imaging into calcified (stiffest plaque types), echolucent (least stiff), and mixed. The samples were loaded and then unloaded at a rate of 5% strain per second, with five successive loading-unloading cycles for each of the different levels of strain: 10, 20, 30, 40, and 50%. Other than allowing the observation of stress softening, this loading regime permitted the quantification of the permanent inelastic deformations in the tissues.

Besides Poisson's ratio, three material parameters should basically be set in order to determine the isotropic bilinear material model used in this work: Young's modulus (E), yield strength (YS), and tangent modulus (TM), the former one being an elastic material parameter while the latter two being the inelastic parameters, see [Figure 2.1].

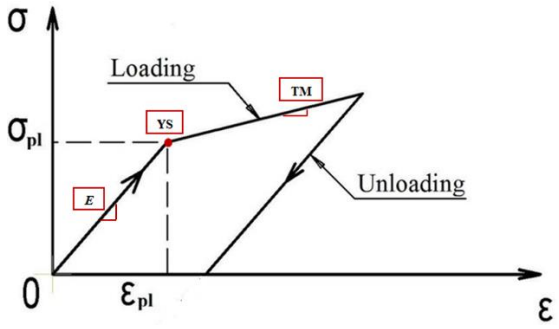

Figure 2.1: Bilinear model of elastoplastic loading-unloading curve.

In this work, the echolucent (lipid) and the calcified plaques were considered in the calibration. Material coefficients for the plaques elastic behavior (i.e. Young's modulus) were obtained from Maher's stress-strain experimental data corresponding to the maximal strain values after which permanent deformations start to be detected. According to Maher's data, plastic strains are observed from a level of strain around 20%; below this value, we assumed that the tissue behaved linearly. Therefore the Young's modulus was identified as the tangent modulus at 20% strain for both plaque types, see [Figure 2.2]. As expected, the calcified plaques are the stiffer type. Poisson's ratio was fixed to 0.4 for both plaque compositions.

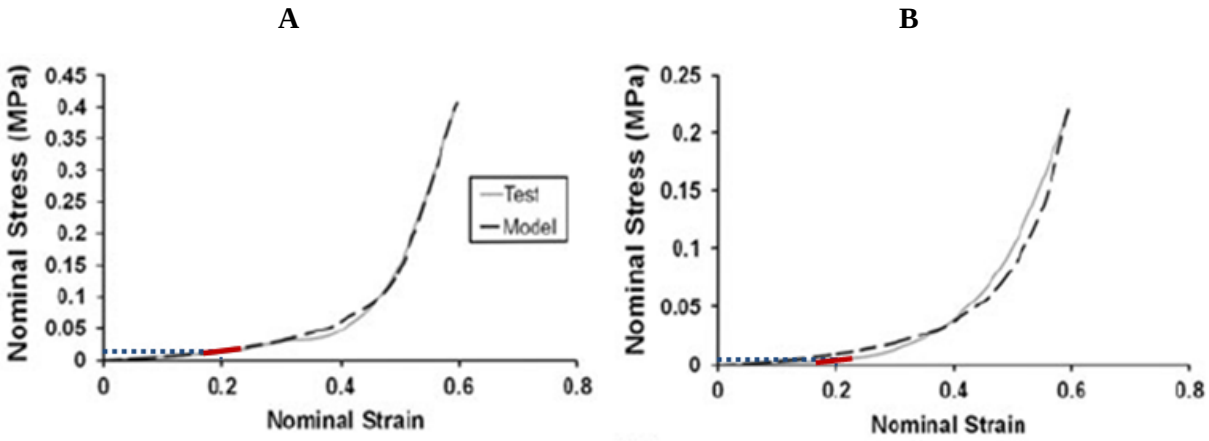

Figure 2.2: Stress-strain curves of the calcified (A) and the lipid (B) plaques during their initial loading cycles at the different strain levels. The experimental data for the load envelopes of both plaque types can be seen by the grey solid lines (Test) [148]. *The dynamic stiffness values used in our plaque material models correspond to the slopes of the tangents to the experimental curves (shown in red) at 0.2 nominal strains. The blue dotted lines indicate the yield strength values considered for each plaque type at the same nominal strain of 0.2 (i.e. where residual strains start to occur).*

Yield strength values were pulled out afterwards from the same stress-strain graphs for each plaque type. These yield stresses were identified corresponding to the 0.2 nominal strain value as well, where permanent strains start to form, see [Figure 2.2].

Subsequently, the remaining inelastic material parameters (tangent moduli), were empirically tuned to attain the experimentally observed residual strains for given peak strains for each plaque type. [Figure 2.3] presents the magnitude of permanent deformation occurring on unloading for given peak strains

applied to the plaques. At a peak strain value of 0.4 (assuming plaques would compress around 40% during inflation for instance), each of the calcified and lipid plaque exhibited a residual deformation of 0.16 and 0.17 respectively. Values were extracted from samples showing more repeatability in behavior among each tested plaque type, see [Figure 2.3].

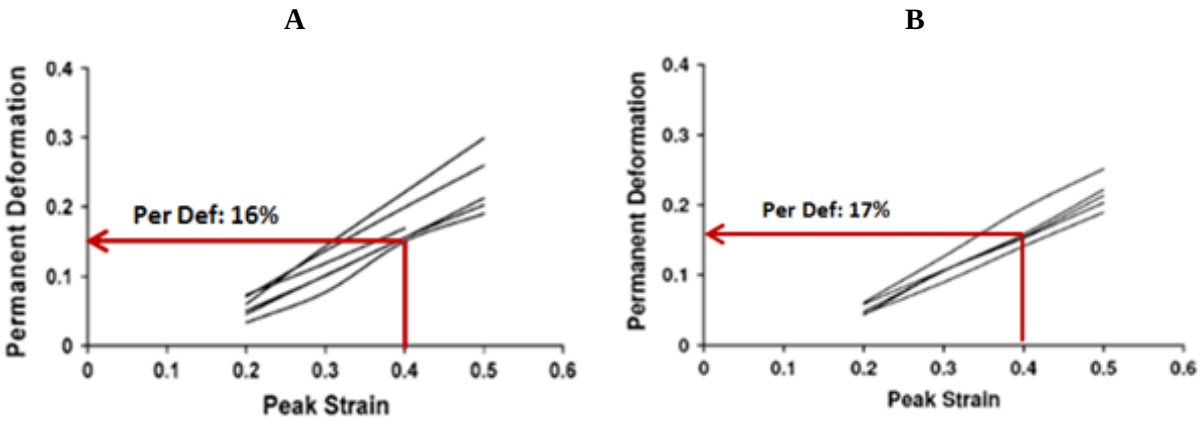

Figure 2.3: Magnitude of residual strains occurring on unloading at different peak strains applied to the calcified (A) and lipid (B) plaques, with the red arrows showing the plastic deformation in each plaque type at a peak strain of 0.4 [148].

The parameter tuning was performed on small cube samples as seen in [Figure 2.4], so to obtain the anticipated residual strain corresponding to the peak strain applied on each plaque type individually, see [Figure 2.3].

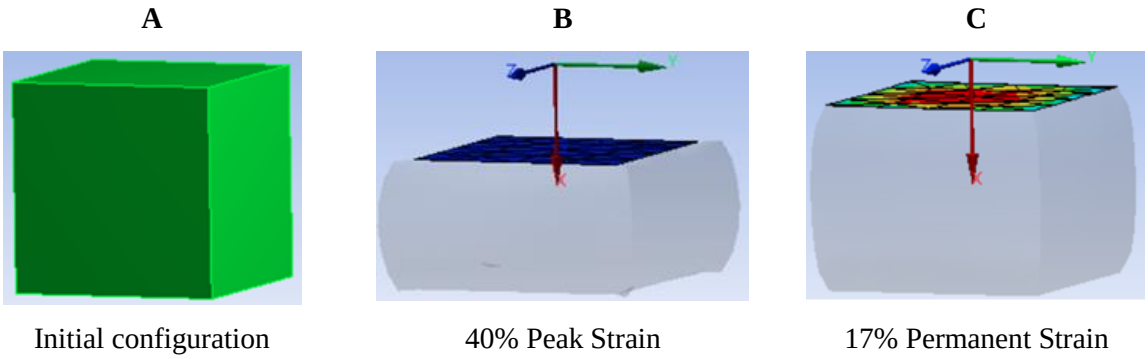

Figure 2.4: (1,1,1) mm cube used for identifying the tangent moduli parameters in our material models.

2.2 RESULTS

The lipid and the calcified plaques material parameters are presented in Table 8; their stress-strain plots are shown in [Figure 2.5].

Table 8: Material parameters of the lipid and calcified plaques.

Plaque Type	Young Modulus of Elasticity E (MPa)	Poisson Ratio (ν)	Yield Strength (KPa)	Tangent Modulus (KPa)
Lipid Plaque	0.105	0.40	5	62.77
Calcified Plaque	0.189	0.40	15.79	111.88

Lipid plaque

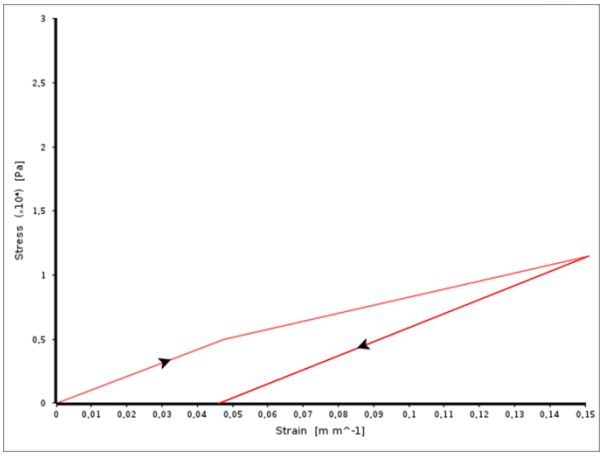

Calcified plaque

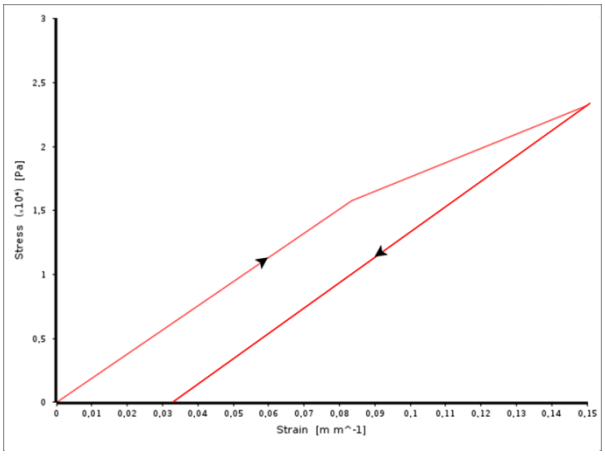

Figure 2.5: Lipid and calcified plaque materials stress-strain plots.

3 CALIBRATION OF THE ARTERY MATERIAL MODEL

3.1 METHODS

In this work, the artery behavior was first modeled using a Neo-Hookean model with initial shear modulus $\mu = 0.227\ MPa$ and incompressibility parameter $D = 0.177\ MPa^{-1}$ extracted from Paini et al. *in-vivo* study [182].

To check the validity of the identified parameters, a generic 3D stenosed artery with an un-symmetric plaque of 60% (assumed as an average value for diametric severity of clinically treated stenosed cases) [164] was modeled. The model used in an intermediate step for calibration is depicted on [Figure 3.1]. More details on its geometry, mesh and boundary conditions were presented in Chapter 4. This model was subjected to a virtual angioplasty using the semi-compliant balloon model detailed in Chapter 3, with a balloon sizing (balloon/artery ratio) of 1. It was simulated with each of the calcified and the

lipid plaque material parameters separately. Then the intermediate simulation outcomes were compared to clinically reported data to evaluate if the constitutive law for the artery required further development.

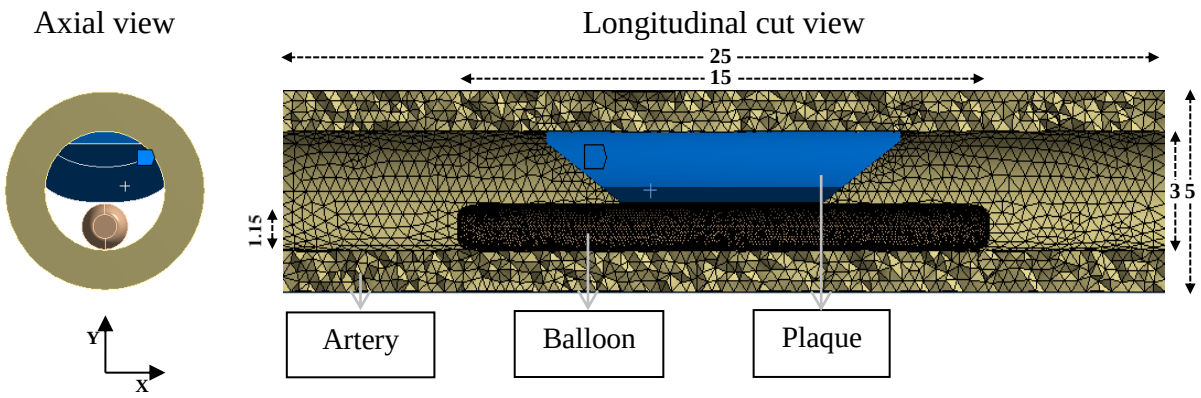

Figure 3.1: The 3D stenosed arterial geometry used in an intermediate step for the calibration of the material models.

The average luminal diameter loss after PTA, also referred to as the diametric elastic recoil ratio (ERR), is computed as the luminal diameter difference between the max balloon inflation state vs. after its deflation. It is calculated using equation (5-1) along the stenosed arteries. More details on elastic recoil ratio can be seen in the analysis of results section of Chapter 4.

$$Elastic\ Recoil\ Ratio\ in\ \% = ERR_{along\_centerline} = \frac{D_{\max\_inflation} - D_{after\_deflation}}{D_{\max\_inflation}} \times 100 \qquad (5\text{-}1)$$

Outcomes at short term (plastic strains [Figure 3.3] and ERRs [Figure 3.4]) generated from the intermediate simulations after PTA are presented in Section 3.2.1.

As previously mentioned in Section 1, for different stenosed regions, plaque compositions, and balloon sizings, clinically obtained elastic recoil ratios directly after PTA varied between 11% and 55% [87], [163]–[165], [175], [176]. The diametric ERR resulting from our intermediate simulations exceeding the clinically expected ones (30% and 35% respectively assumed for the lipid and calcified plaque cases as average values from clinical outcomes) indicates that the diseased artery in these intermediate simulations elastically recoiled more than what was observed clinically. This can also be seen in terms of the minimal lumen diameter (d_f) (i.e. at max recoiling stenosed regions) which displayed smaller values directly after balloon deflation in our intermediate simulations compared to the clinically observed ones.

Two possible corrective suggestions could be considered. The first option would be to modify the plaques material parameters calibrated according to Maher et al. experimental work as described in Section 2, and adapt their constitutive laws so that ERRs of 30% and 35% would be obtained with residual deformations occurring only in the plaques. However, as arterial tissues has also

experimentally shown an inelastic material behavior under supra-physiological loadings [179], [183], in this work a second option was chosen: it was hypothesized that the artery itself would also experience permanent deformations; consequently it was modeled as a bilinear isotropic hardening model as well. For the same reasons discussed for the plaques in Section 2.1, the arterial material models did not include the Mullins effect. Anisotropy was also neglected.

[Figure 3.2] presents a sectional view showing a graphical illustration of the stenosed artery at three key states during PTA: (a) before balloon inflation, (b) at its max inflation position, and (c) after its deflation.

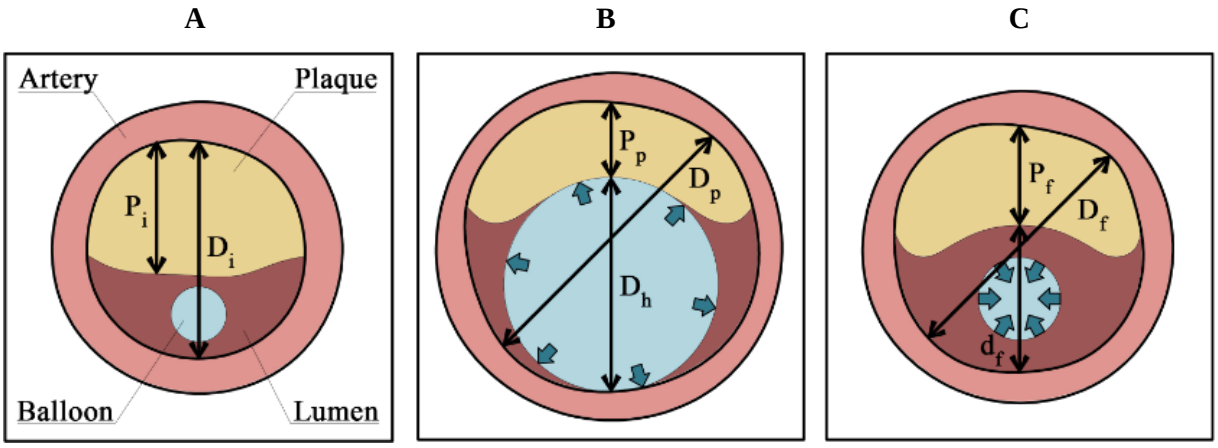

Figure 3.2: A cross-sectional view presenting the stenosed artery (A) before inflating the balloon, (B) at its max inflation state, and (C) after its deflation. P_i, P_p and P_f are the plaque thicknesses respectively before balloon inflation, at its max inflation, and after its deflation. D_i, D_p and D_f represent the inner arterial wall diameters successively for the three crucial states during balloon angioplasty as well. D_h is the balloon diameter at its max inflation, and in this work it is equivalent to D_i, the inner arterial wall diameter before any balloon inflation. (d_f) is the minimal lumen diameter after balloon deflation.

The elastic material parameters used for modeling the arterial behavior in the intermediate simulations (obtained from Paini et al. *in-vivo* study [182]) were kept the same in the new elastoplastic model. With the lack of data on their inelastic behavior, the arterial yield strength values were empirically chosen here.

Regarding the remaining inelastic material parameters (tangent moduli), the arterial wall peak circumferential strains reached at max inflation (see [Figure 3.2 (B)]) were first computed using equation (5-2):

$$\varepsilon_{\theta\theta_{peak}} = \frac{2\pi D_p - 2\pi D_i}{2\pi D_i} = \frac{D_p - D_i}{D_i} \qquad (5\text{-}2)$$

with D_i and D_p being respectively the initial and peak inner arterial wall diameters correspondingly before balloon inflation vs. at its max inflation; see [Figure 3.5] as an example illustrating D_p obtained in one of the intermediate simulations.

Their corresponding peak circumferential arterial wall lengths (L_p) were subsequently calculated using equation (5-3):

$$\varepsilon_{\theta\theta_{peak}} = \frac{L_p - L_0}{L_0} \tag{5-3}$$

with L_0 being the initial arterial wall circumferential length (before the inflation) calculated as πD_i.

The residual circumferential strains in the arterial wall after balloon deflation ($\varepsilon_{\theta\theta_{residual}}$) were next to be computed. However with the inner arterial wall diameters after the deflation (D_f) being also unknown, calculating $\varepsilon_{\theta\theta_{residual}}$ by simply replacing D_p by D_f in equation (5-2) was not feasible.

Instead, knowing that here we have a target to attain clinically expected minimal lumen diameters $d_{f_{(clinically\ expected)}}$ after the treatment, $\varepsilon_{\theta\theta_{residual}}$ was expressed in terms of $d_{f_{(clinically\ expected)}}$ and computed as:

$$\varepsilon_{\theta\theta_{residual}} = \frac{D_f - D_i}{D_i} = \frac{d_{f_{(clinically\ expected)}} - d_{f_{(intermediate\ simulation)}}}{D_i} \tag{5-4}$$

where $D_f - D_i$, the difference between the inner arterial wall diameters before balloon inflation vs. after its deflation (i.e. the diametric *arterial* permanent deformations), is supposed equivalent to $d_{f_{(clinically\ expected)}} - d_{f_{(intermediate\ simulation)}}$, which is the difference in minimal lumen diameters between outcomes obtained from our previous intermediate simulations after balloon deflation vs. the clinically expected ones, see [Figure 3.2 (B and C)].

Similarly, residual circumferential arterial wall lengths (L_f) were then calculated from their corresponding permanent strains using equation (5-5):

$$\varepsilon_{\theta\theta_{residual}} = \frac{L_f - L_0}{L_0} \tag{5-5}$$

Accordingly the arterial plastic material coefficients were tuned on rectangular specimens corresponding to the arterial wall initial circumferential length, to satisfy the anticipated residual strain after being tensioned to their peak circumferential deformations for each of the lipid and the calcified plaque cases respectively.

3.2 RESULTS

3.2.1 Intermediate simulations

In this section we present outcomes obtained at short terms from the two intermediate simulations in which plaques were modeled as elastoplastic while arteries as hyperelastic.

[Figure 3.3] illustrates the plastic deformations occurring in each plaque type after balloon deflation in an axial and a longitudinal cut view. As expected, no residual deformations were formed in the modeled hyperelastic arteries.

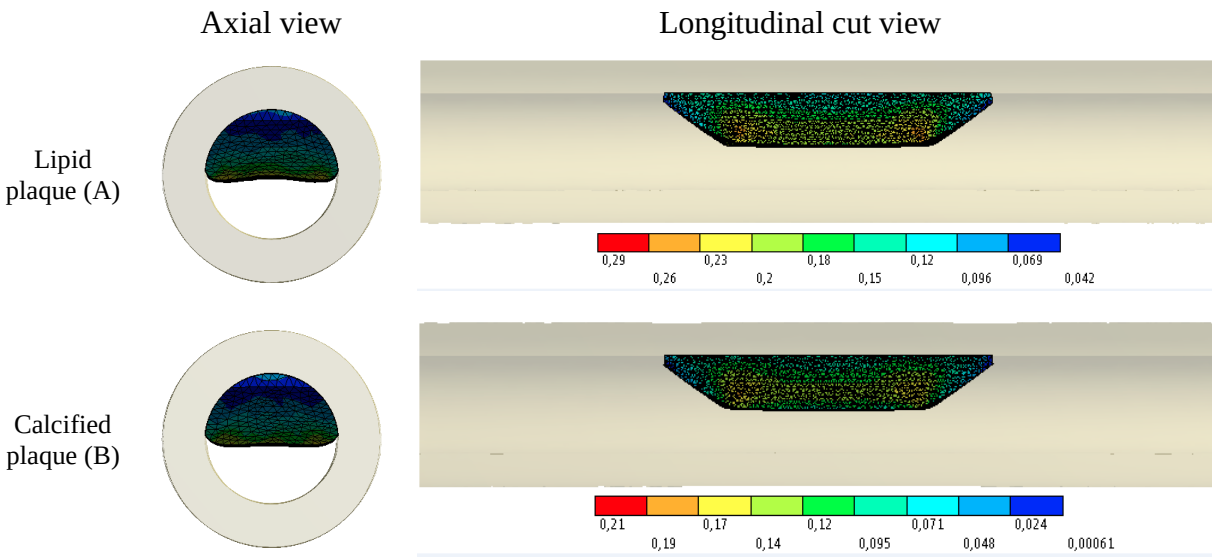

Figure 3.3: Plastic strains in the lipid and calcified plaques after the intermediate angioplasty simulations.

The average loss of luminal diameter at max stenosed region computed immediately after balloon deflation from these two simulations was 52% for the lipid plaque case while 54% for the calcified one, see [Figure 3.4].

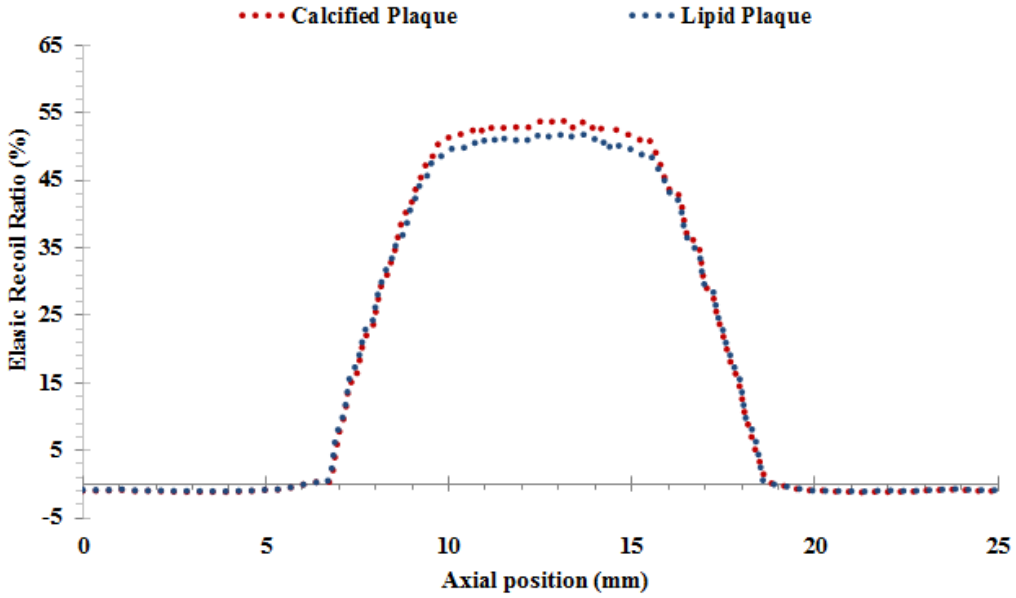

Figure 3.4: Elastic recoil ratios along the stenosed artery axis obtained from the intermediate simulations after virtual PTA within each of the lipid and calcified plaques.

[Figure 3.5] presents the peak inner arterial wall diameter D_p at max balloon inflation obtained from the intermediate simulation with the lipid plaque. The color-map illustrates the inner arterial wall radial displacements in mm at the max inflation state of the balloon.

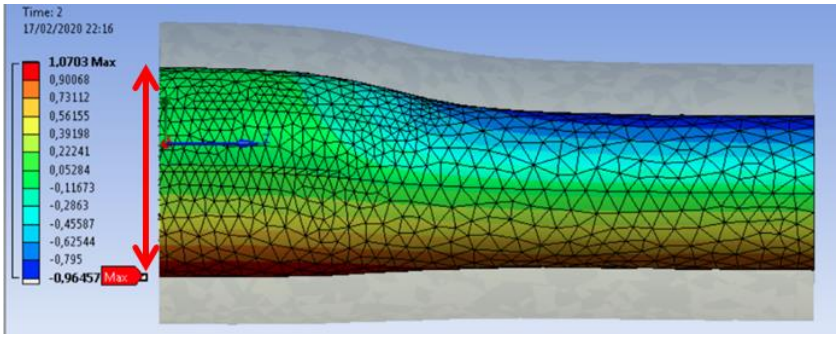

Figure 3.5: A cut view showing the inner arterial wall with its peak diameter reached at max balloon inflation (D_p) (red arrow). The color-map presents radial displacements in (mm) that should be added to the inner arterial wall diameter before balloon inflation ($D_i = 3\ mm$) in order to obtain (D_p).

3.2.2 Calibrated simulations

This section first presents the tuning of arterial material parameters, followed by the acute post-procedural outcomes attained from the final calibrated simulations (with both arteries and plaques material models as elastoplastic).

[Figure 3.6] shows the rectangular specimen used in the tuning of the arterial wall plastic material parameters. Different to the plaques that were tuned under compressive loading (see Section 2), the constitutive law of the arteries were calibrated in tension.

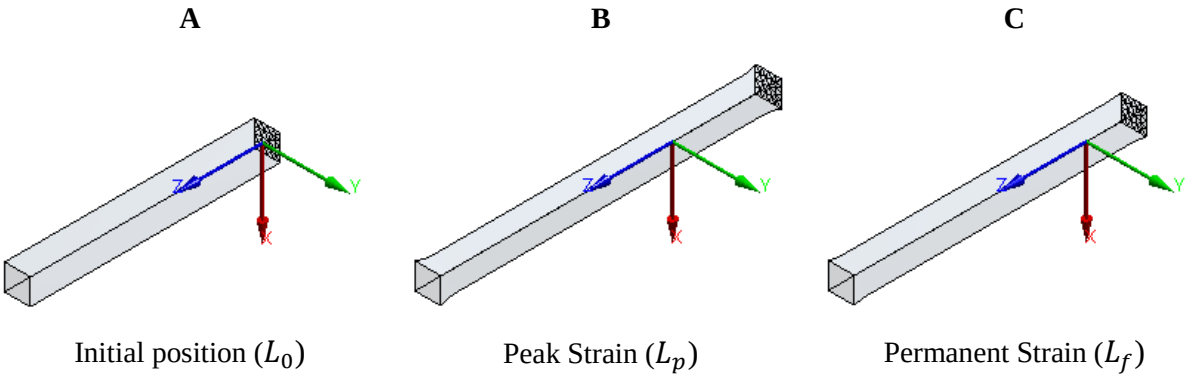

Figure 3.6: The rectangular specimen used for identifying the tangent moduli coefficients in our arterial material models.

The obtained arterial material parameters corresponding to each of the lipid and the calcified plaque cases are shown in Table 9. Their stress-strain plots are presented in [Figure 3.7].

Table 9: Material parameters of the arteries corresponding to the lipid and calcified plaque cases.

Plaque Type	Young Modulus of Elasticity E (MPa)	Poisson Ratio (v)	Yield Strength (KPa)	Tangent Modulus (KPa)
Artery (Lipid plaque case)	0.677	0.44	7	256.5
Artery (Calcified plaque case)	0.677	0.44	7	330.75

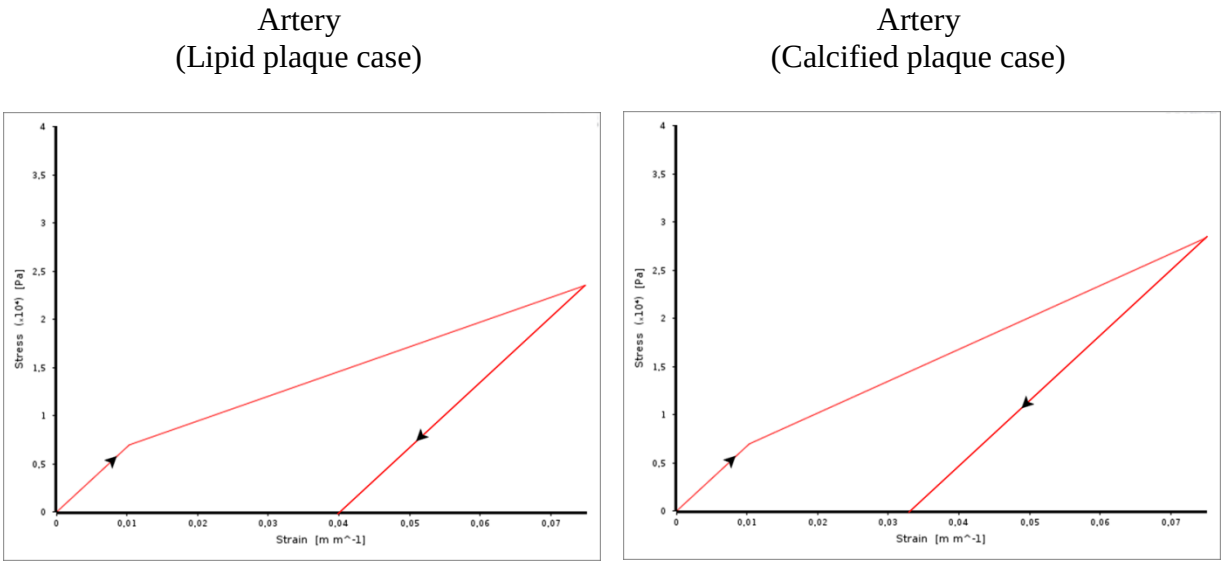

Figure 3.7: Arterial material stress-strain plot corresponding to each of the lipid and calcified plaques.

With the artery and the plaque modeled as elastoplastic materials, permanent deformations were expected in the two components. [Figure 3.8] illustrates the residual deformations forming in the stenosed regions of both plaque cases after balloon deflation in an axial and a longitudinal cut view.

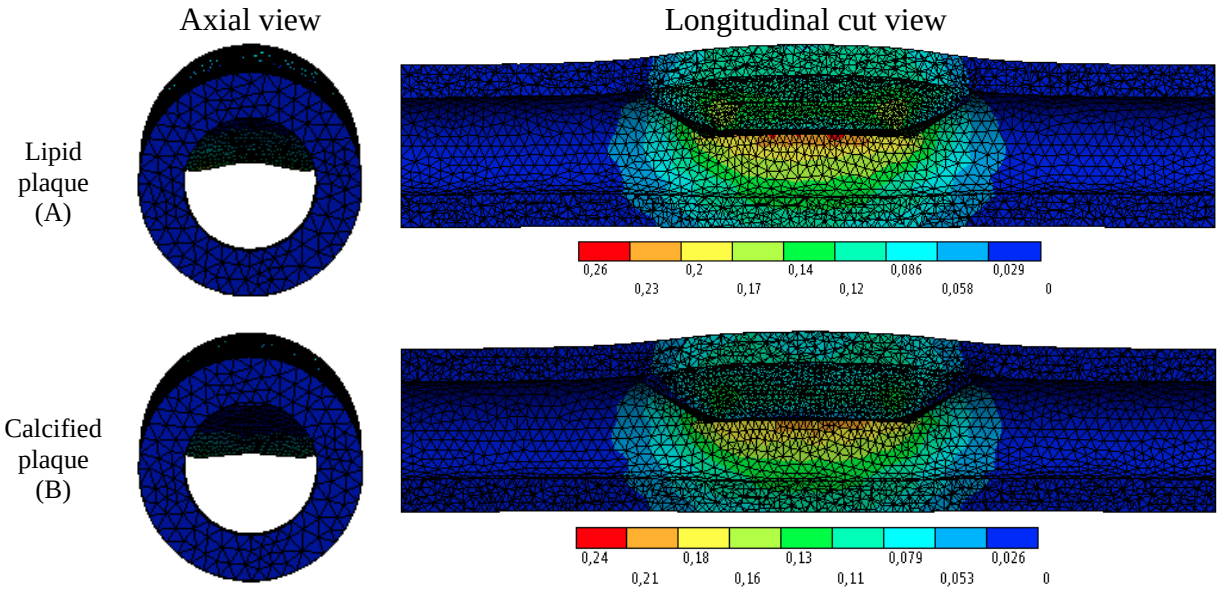

Figure 3.8: Plastic deformations in both arteries and plaques obtained from the final calibrated angioplasty simulations.

As aimed from our proposed calibration method, the max diametric elastic recoil ratio values obtained at max stenosed regions directly after PTA were around 30% and 35% for the lipid vs. the calcified plaque cases respectively, see [Figure 3.9].

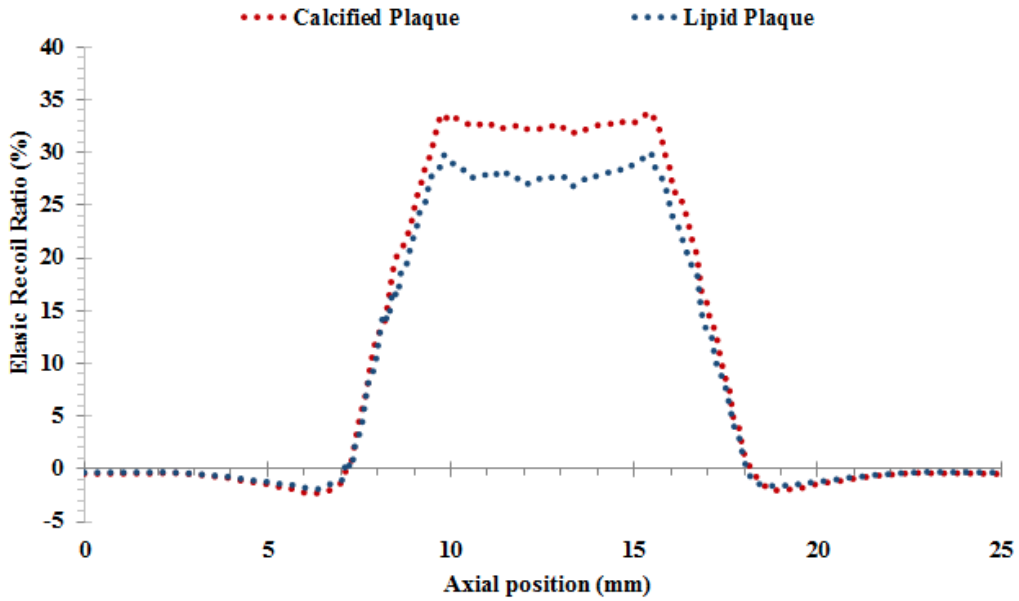

Figure 3.9: Elastic recoil ratios along the stenosed artery axis attained from the final calibrated simulations after PTA within the lipid and calcified plaque cases.

4 DISCUSSION

In this chapter we propose a calibration approach for identifying the suitable material models and parameters for the artery and the plaque before simulating the balloon angioplasty procedure. With our aim in evaluating acute post-PTA outcomes in this work (i.e. directly after balloon deflation), the suggested calibration methodology consists mainly in tuning the constitutive laws based on the permanent deformations resulting in materials under supra-physiological loadings.

With Maher et al. (2011) being among the very few experimental studies evaluating *at large strains the inelastic behavior of human atherosclerotic plaque tissues* [148], our modeled plaques were tuned in accordance with these experimental data so to attain similar residual deformations after load removal. Even though the calcified plaque type simulated in our work is relatively soft compared to the stiff micro calcifications reported by the experimental work of Ebenstein et al. [184], it still falls within the stiffness ranges reported by other experimental studies for calcified plaques as well, such as [143], [185] for example. It should be noted that a large variability of data was shown among different studies reporting plaque stiffness in the literature. Besides the natural variability of the plaque behavior, this might be caused by the different techniques used to measure the mechanical properties of plaques including unconfined compression, micro-indentation, and nano-indentation. However, in this work we focused on studies that applied dynamic loading conditions to present the inelastic and recoverability behavior of plaques, such as [148].

Regarding arteries, and human ones specifically, experimental studies assessing their inelastic behaviors (in terms of residual deformation) were very limited in numbers in the literature. Among these studies, Holzapfel et al. (2000) reported experimental inelastic behavior in the artery wall for example, but applied their protocol for the medial arterial layer only, and by applying relatively small peak strains (up to 20%) restricted to two cycles [179]. Different to plaques, with the lack of experimental data representing *human arterial wall tissues inelastic behavior at large strains* specifically, simulated arterial wall models were identified to satisfy averaged clinically obtained ERR values after PTA instead.

Also among these few studies focusing on the inelastic behavior of atherosclerotic tissues, Maher et al. (2012) characterized the inelasticity of arterial tissues at different sites through the arterial tree [183]. Even though in their work they quantify and report residual deformations obtained after load removal for different peak strains applied as well, the reason why we didn't use their data for calibrating our arterial model was that their cyclic experimental tests were performed on arteries harvested from 3-4 month old female pigs. Mechanical properties might vary among arteries obtained from young pigs vs. others corresponding to elderly human at the time when treatments are usually required. Accordingly

our choice was to calibrate the arteries based on clinically obtained average values of ERR obtained directly after balloon deflation as described in Section 3.

Upon comparing permanent deformations resulting from our calibrated arterial models with the ones corresponding to Maher et al. (2012) study, higher values were shown generally in our work, exceeding the values shown in the carotid, femoral and aorta pig arteries (experimentally tested). This might be related to the fact that younger arteries harvested from the pigs might be healthier, thus experiencing less residual deformations at unloading. Nevertheless, permanent deformation values resulting from our calibration are still realistic and fall within the inelastic residual strains range corresponding to the coronary arteries experimentally tested in [183]: ~21.5% residual deformation obtained when ~40% peak strain is applied on arteries for example as seen from both sources.

Since Maher's experimental tests were on stress-free tissues, it makes sense here to consider our generic geometry as a stress-free model as well to calibrate the parameters. The loading condition applied by blood pressure within the stenosed artery is much smaller than the one exerted by the balloon, so the stress-strain state corresponding to blood pressure would somehow be one of the intermediate states within our PTA simulation.

The calibration method presented in this work also had some limitations. They mainly concern the artery and plaque material models. To start with, here we do not claim to model the detailed phenomena of damage that might occur during PTA. Instead, plasticity is meant to average any complex damage and flow phenomena occurring at small scales within the diseased artery. The main reason for our choice is that we aim to present a tool that can then be easily applied on patient-specific geometries and be incorporated into the clinical routine, without the need of additional imaging. With computed tomography angiography (CTA) being a principal part of the clinical routine, it is generally known that these images resolution would not allow for a detailed differentiation of the plaque components within the diseased arteries, especially for small diameter arteries. Besides, the calibration of the proposed constitutive laws is mostly based on kinematic quantities, such as residual strains extracted from Maher's work and the clinical ERR provided by different papers; therefore, the proposed model might require further validation to assess a risk of rupture based on maximum stress.

Atherosclerotic tissues usually experience a stiffening behavior at higher loading conditions. However, constant stiffness values were considered instead in the bilinear isotropic hardening models used in this work. Even though this assumption might somehow underestimate the stress levels at high strains in the modeled components, it was still considered as valid in our work which aims to evaluate acute outcomes after PTA, specifically ERR and LGR at unloading.

In case higher dynamic stiffness values corresponding to higher peak strains were initially chosen for the plaques, the same calibration method presented in this chapter could always be applied to obtain the remaining material parameters of the plaques and arteries. Again, towards the aim of our current

work (i.e. mainly ERR and LGR assessments after balloon angioplasty), the focus of the applied calibration is more on representing the permanent deformations forming in the materials (i.e. their behavior at unloading), to be compared afterwards with clinical outcomes after PTA.

We are also aware that modeling the artery as an isotropic single-layer tissue is a limitation, as it is known to exhibit an anisotropic behavior. However, even though *in-vitro* experimental studies evaluating atherosclerotic tissues behaviors are generally available in the literature, only a few among them considered studying the inelastic behavior of such tissues. Up to our knowledge, no study presented the inelastic behavior of each arterial layer separately under supra-physiological loadings. Similarly, very limited data is available regarding the inelastic behavior (in terms of residual deformation) of human arterial tissues supra-physiologically loaded in different directions as well. Accordingly, with the lack of the necessary experimental data that represent the anisotropic and/or layer specific inelastic behaviors of arteries, in this work and as a first contribution, an inelastic single-layered isotropic artery was considered and was tuned correspondingly to model residual deformations obtained directly after PTA. Similarly, the model could also be improved by including the Mullins effect associated to a permanent set, as was done by Maher et al. [138], [148].

Experimental studies showed variations in mechanical properties between healthy and diseased arteries [186]. Even though there is still no clear evidence on how the artery itself could be affected by the type of the plaque forming on its inner wall, in this work we assumed that arteries with lipid plaques at their inner wall should have softer inner arterial layers as well, and would accordingly also experience slightly higher permanent deformations compared to arteries with calcified plaques after PTA.

With this calibration method, our model showed consistent results in comparison with clinical findings; it seems to be a promising tool towards outcomes evaluation at short terms (e.g. ERR and LGR) after PTA. Furthermore, the material parameters of the modeled stenosed arteries were tuned based on average ERR values of 30% and 35% for the lipid vs. calcified plaque cases respectively obtained from clinical studies. Nevertheless, a more precise assumption could be integrated later after applying our calibration procedure on various patient-specific geometries of different plaque compositions and severities. This can be performed in the presence of detailed pre- and post-operative clinical routine images for the simulated diseased region before vs. after balloon angioplasty.

CHAPTER 6

PATIENT SPECIFIC GEOMETRIC MODELING OF A DISEASED ARTERY

The objective of this chapter is to show the feasibility of generating 3D patient-specific geometries for stenosed peripheral arteries from pre-operative CTA scans, with a focus on the steps that ensure a good mesh quality. The segmentation and surface model generation process is described first. The method is illustrated with a case of abdominal aorta stenosis with a plaque of mixed composition. It is then applied on two superficial femoral diseased arteries each with a different plaque constitution: calcified vs. lipid plaque. Finally we present the steps followed for generating a 3D model from segmented components ready for simulation by finite element method.

OUTLINE

1 SEGMENTATION AND VOLUME RECONSTRUCTION

Towards our aim of developing a tool that can be integrated into the clinical routine without any additional imaging, computed tomography angiography (CTA) was considered as the source of patient images in this work. It is one of the very few imaging modalities generally present in most hospital protocols and being performed for the vast majority of patients prior to PTA treatment (specifically in peripheral arteries).

Preoperative CTA images of a stenosed abdominal aorta and two stenosed femoral arteries were obtained at CHU de Rennes in conformity with the ethical standards required. The scanner was configured for 80kV and 160mA with a slice (axial image) thickness of 1mm. Images were saved in the standard DICOM format.

Nowadays, imaging techniques, such as CTA or magnetic resonance angiography (MRA), can provide high-quality three-dimensional (3D) volume rendering of patients' vasculatures in real time. However, they are not adapted for numerical purposes as currently performed. Post-processing of angiography images (segmentation and reconstruction techniques) is therefore required and essential in order to obtain the 3D geometry of the patient-specific stenosed vessel of sufficient quality.

1.1 SEGMENTATION PROCESS AND SURFACE MODEL GENERATION

Segmentation and volume reconstruction is first presented and illustrated on a case of a stenosed abdominal aorta. This aorta is composed of an arterial wall and a mixed plaque with mostly lipidic constituent. The CTA dataset was processed using the open-source softwares ITK snap and 3D slicer. The segmentation process follows three steps described below: 1. isolating the lumen and calcifications, 2. generating the arterial wall volume, 3. generating the soft (lipid) plaque. This section also presents additional processing in surface model generation to ensure its quality for simulation purposes.

The segmentation procedure aims first at isolating the vessel lumen from the surrounding tissues and structures. After selecting the desired region of interest from the stack of images, the lumen was segmented using the 'snake active contour method' implemented in ITK-Snap [187], see [Figure 1.1 (A-I)]. One must note that even though the reconstructed geometry corresponding to the segmented lumen would not be part of the 3D stenosed artery geometry exported for FE simulations afterwards, it still serves in defining the interlining between the plaques and lumen boundaries, facilitating and/or verifying their differentiation/separation (prior to any surface model generation).

With relatively high capabilities in absorbing x-rays, calcifications were easily identified based on their high CT densities. Either manual segmentation or segmentation based on high greyscale

threshold levels (corresponding to calcifications densities) can be applied for segmenting calcified plaques [Figure 1.1 (A-II)].

As the vessel wall is not clearly visible on CTA images, a constant outer arterial diameter was assumed along the segmented region. According to the clinical experience in our hospital center, this hypothesis is valid knowing that the considered vessel segments are rather short in length. The vessel wall was modeled as a single layer of initially constant thickness in this work [Figure 1.1 (A-III)]. A subtraction Boolean operation is then applied to remove calcified regions and possibly enlarged lumen regions from the generated arterial wall itself, resulting in the segmentation of the healthy arterial wall and of the calcifications independently. Note that this leads to potential variation of the arterial wall thickness along its axis. This segmentation step was not required for this stenosed abdominal aorta case (as calcifications were not within the wall and the lumen diameter was rather constant); however it was essential for the two femoral stenosed cases, especially the highly calcified one which is presented in section 1.2.1.

Besides, with the limitation of CTA imaging in distinguishing between components such as lipid-rich and fibrous plaques, in this work all 'un-calcified' plaques were segmented together and referred to as the lipidic plaque. For this component, a subtraction Boolean operation was applied to remove the previously segmented lumen and calcified plaque parts from a new segment filling the inner region bounded by the generated arterial wall, resulting in the lipid plaque segmentation [Figure 1.1 (A-IV)]. This technique was performed in order to make sure that the segmented regions would be continuously connected to one another at the level of segments, without any gaps and/or overlapping which might generate convergence issues when transferred for FE simulations. Finally the four separate segments obtained from the stenosed artery (i.e. lumen, calcified plaque, lipid plaque and arterial wall) were combined together at the level of segments into a single label-map by an addition Boolean operation [Figure 1.1 (A-V)].

[Figure 1.1 (A)] presents the steps of the applied segmentation procedure illustrated on one axial cross-sectional slice located at a highly stenosed region within the abdominal aorta. [Figure 1.1 (B)] shows the four segments on a sagittal cross-section. At the end of the segmentation process, 3D surface models were generated from their corresponding 3D segments as depicted in [Figure 1.1 (C)]. The 'joint smoothing' feature was applied in 3D slicer while generating the 3D surface models from the segmented parts (within the label-map). Theoretically this function should ensure that all resulting models would fit together smoothly like jigsaw puzzle pieces. Otherwise the models would be smoothed independently, and may overlap. One must note that the reconstructed geometries depend on the segmentation process applied which still contains some manual or semi-automatic steps; it can therefore be affected to a certain extent by the operator and his experience. Moreover, there may be variabilities in the quality of the images being segmented depending on the resolution of the scanner

being used, the stenosis location, the time at which the images were taken during the cardiac cycle, and the operator experience; that might also affect the segmented parts and their generated surface models accordingly.

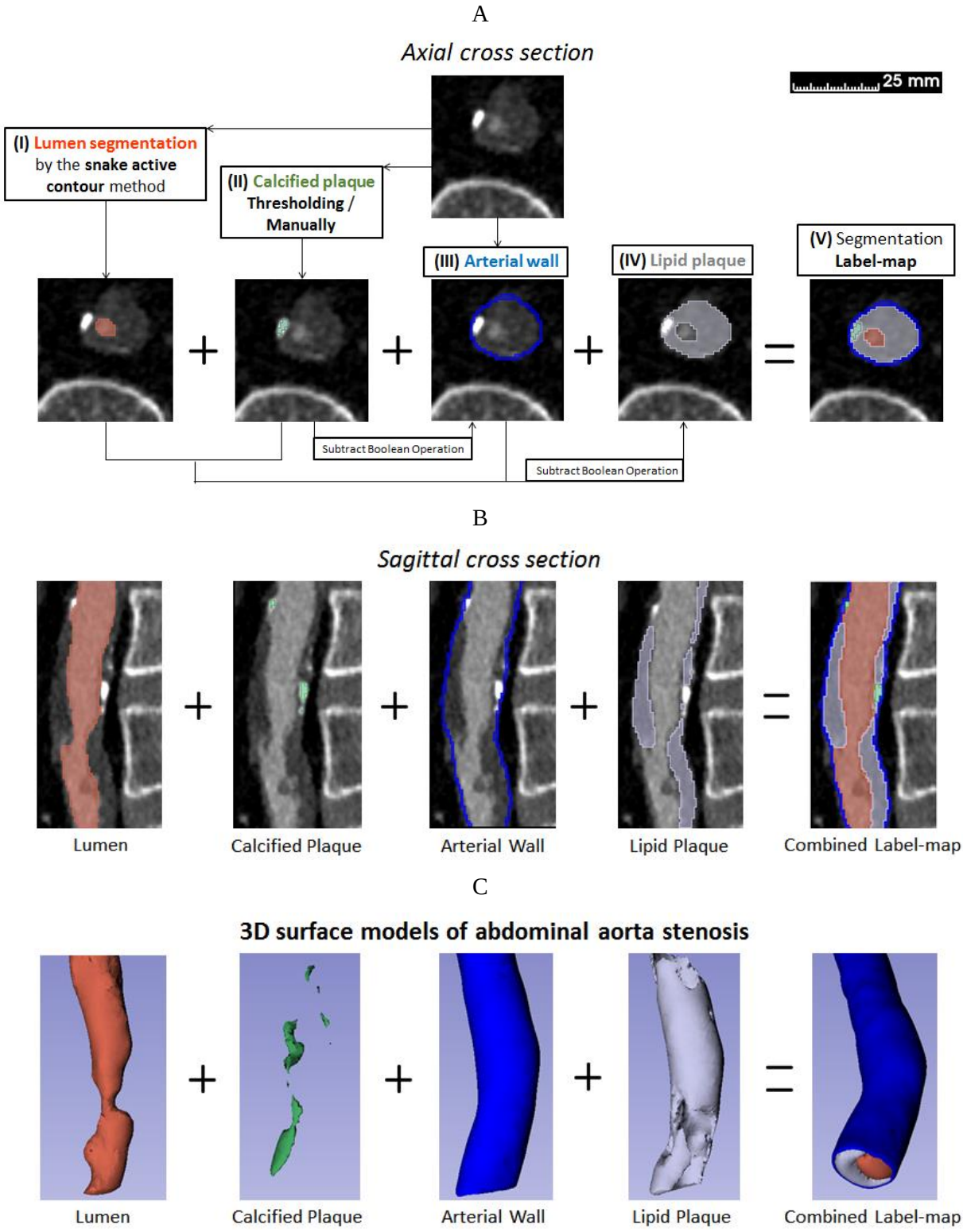

Figure 1.1: (A) Segmentation procedure presented on one axial slice located at a highly stenosed region within the diseased aorta; (B) segmented regions illustrated on a sagittal cross-section; and (C) their corresponding 3D surface models.

1.2 APPLICATION IN STENOSED FEMORAL ARTERIES

In this work, being interested in studying peripheral arterial disease (PAD) at lower extremities, the segmentation and surface model reconstruction procedure was applied on two stenosed superficial femoral arteries. According to the clinical experience in our hospital center, at the time they require treatment, most femoral plaques cases are rather homogeneous. They are often clinically evaluated as either stiff (calcified) or soft (lipidic). Besides, previous findings on femoral atherosclerotic plaque compositions showed fibrocalcific predomination in plaque sections [11], [188], [189]. Accordingly two femoral plaques representing these two extremity cases: totally calcified vs. totally lipidic, were considered in this section.

1.2.1 Calcified femoral stenosis case

Being usually one of the most frequently occurring atherosclerosis scenarios in femoral arteries, a calcified stenosis case was first considered in our work. Pre-operative CTA scans were obtained from a patient with a calcified superficial femoral stenosis of varying severity along the plaque, reaching ~41%.

A segmentation algorithm similar to the one described in Section 1.1 was applied on the CTA dataset corresponding to the highly calcified femoral stenosis case. The vessel lumen and calcified plaques were first segmented accordingly. Afterwards a vessel wall thickness of 0.7 mm was assumed and modeled along arterial length [190]. However, as the processed stenosed case was highly calcified, at some locations, calcifications developed also in the arterial wall itself. Consequently, unlike the abdominal aortic case, a subtraction Boolean operation was essential here to remove calcified regions from the generated arterial wall, resulting in the segmentation of the healthy arterial wall and of the calcifications separately [Figure 1.2 (A and B)]. Moreover, since no lipid material was detected within the treated plaque (confirmed by clinicians working with us), step IV of the suggested segmentation process presented in Section 1.1 was not required for this case. Finally surface geometries corresponding to each of the healthy arterial wall and calcifications were reconstructed as seen in [Figure 1.2 (C)].

A

B

C

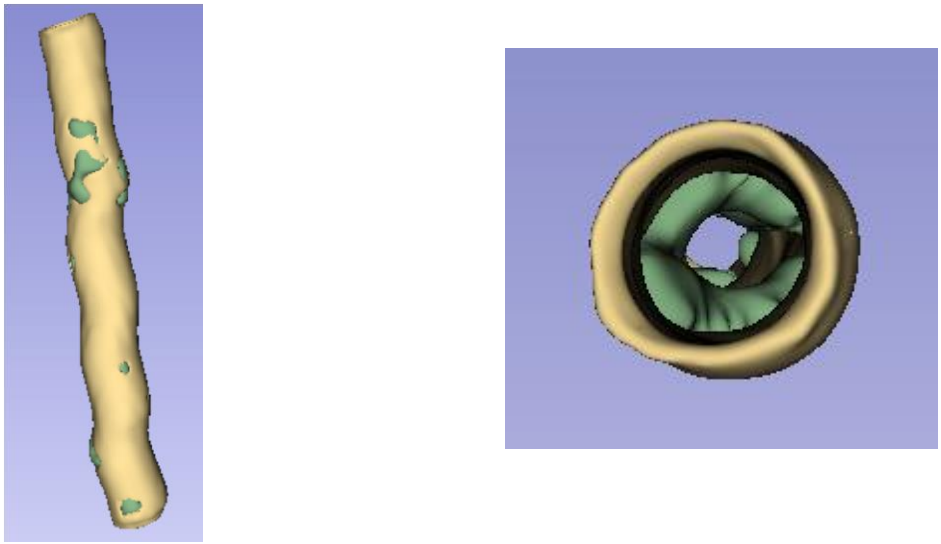

Figure 1.2: (A) and (B) are respectively axial and sagittal slices showing the stenosed artery before and after the segmentation (healthy artery in yellow while calcification in green). (C) presents their corresponding 3D surface models in longitudinal and axial views.

1.2.2 Lipid femoral stenosis case

A third set of pre-operative CTA scans were obtained from a patient with a lipidic superficial femoral stenosis of a varying severity along the plaque as well, reaching ~52% at its most stenosed region.

The same segmentation algorithm presented in Section 1.1 was applied to this highly lipidic femoral stenosis case with only few modifications. The vessel lumen was initially segmented in a similar way. Unlike the calcified case (seen in Section 1.2.1), segmenting the lumen was essential for this highly lipidic stenosis. As previously mentioned, even though its reconstructed geometry would not be part of the simulated 3D stenosed artery geometry later, the lumen segment serves in defining the inner boundaries of the lipid plaque and the arterial wall (at the stenosed and heathy regions respectively) that cannot be clearly seen on CT scans due to their low absorption levels of X-rays. Afterwards, a vessel wall thickness of 0.9 mm was assumed and modeled here along the arterial length [190]. The slightly enlarged luminal regions were then removed from the generated arterial wall correcting its thickness along its length. Besides, the lipid plaque was segmented without any modifications from what was previously described. [Figure 1.3 (A and B)] present the arterial wall and the lipidic plaque segmentations. For this case, since no calcifications were observed within the treated plaque, step II of the suggested segmentation was not required. Finally, 3D surface models corresponding to each of the lipid lesion and the arterial wall were generated as seen in [Figure 1.3 (C)].

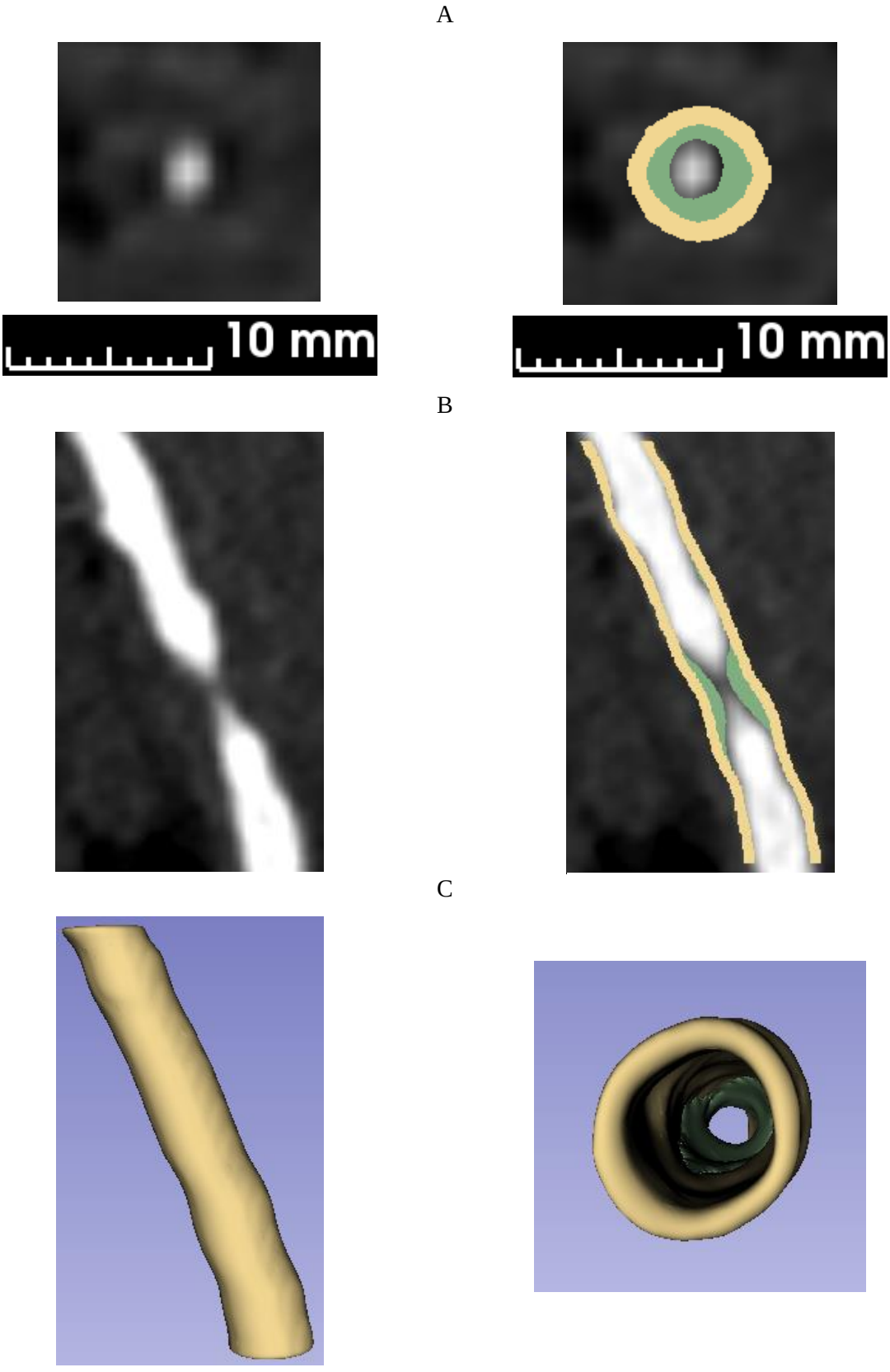

Figure 1.3: (A) and (B) are respectively axial and sagittal slices showing the stenosed artery before and after the segmentation (healthy artery in yellow while lipid plaque in green). (C) presents their corresponding 3D surface models in longitudinal and axial views.

2 PATIENT-SPECIFIC 3D MODELS IN ANSYS: SPACECLAIM AND MECHANICAL

Prior to any FE simulation, the model should be prepared and verified at the geometric level even before the creation of the mesh. First, surface geometries corresponding to independent segments (generated in 3D slicer as described in sections 1.2.1 and 1.2.2) were imported to Ansys SpaiceClaim (ANSYS® Academic Research Mechanical, Release 19.1) for validation before being meshed. Even though the 'joint smoothing' feature was applied in 3D slicer while generating the 3D surface models from their segmented parts (which theoretically should ensure that all resulting models would fit smoothly together), some gaps and/or overlapping were detected when opened in Ansys SpaiceClaim. One probable cause can be the presence of some automatic smoothing functions that might be applying on the segments separately during their 3D volumes reconstruction process (in Slicer) forming these gaps/overlappings. Exporting and importing the generated independent surface geometries among different CAD softwares can be another possible reason.

Regardless the cause, even though these gaps or overlappings might seem negligible with their small sizes, their effect might be crucial in terms of creating geometric divergence issues when simulated at large deformations. Therefore, in this work we decided to join the segments together again into a single one (at the level of segments), and generate a single geometry from 3D slicer incorporating all components of the stenosed region (arterial wall and plaques) combined together [Figure 2.1].

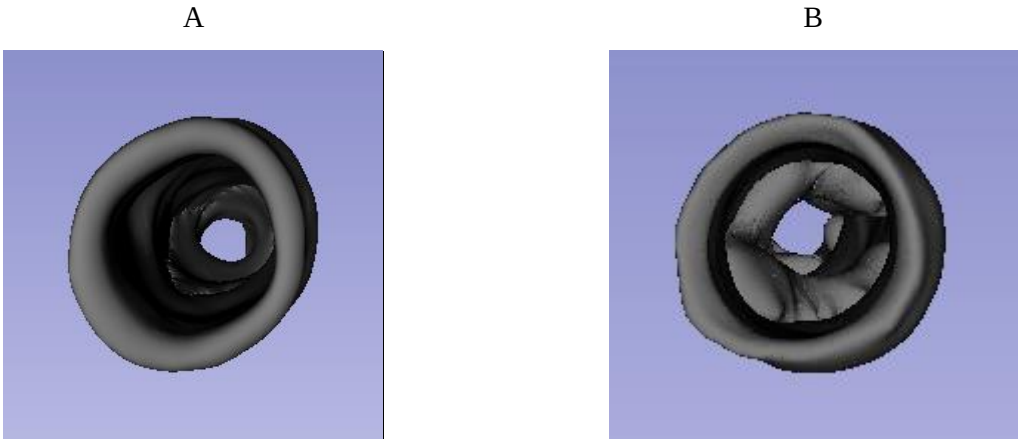

Figure 2.1: Axial views showing 3D geometries exported from 3D slicer including all components of the stenosed arteries as single models which correspond to each of the lipid and the calcified case in (A) and (B) respectively.

The combined 3D STL geometries (which contain all components as one part) were then imported into Ansys SpaceClaim where they were cleaned, shrink-wrapped, and verified. Shrink-wrap was applied to reduce the number of triangles and smooth the STL surface geometries in order to avoid

convergence difficulties due to geometric irregularities and sharp edges. Finally 3D solid models were generated from the surface mesh geometries as depicted in [Figure 2.2].

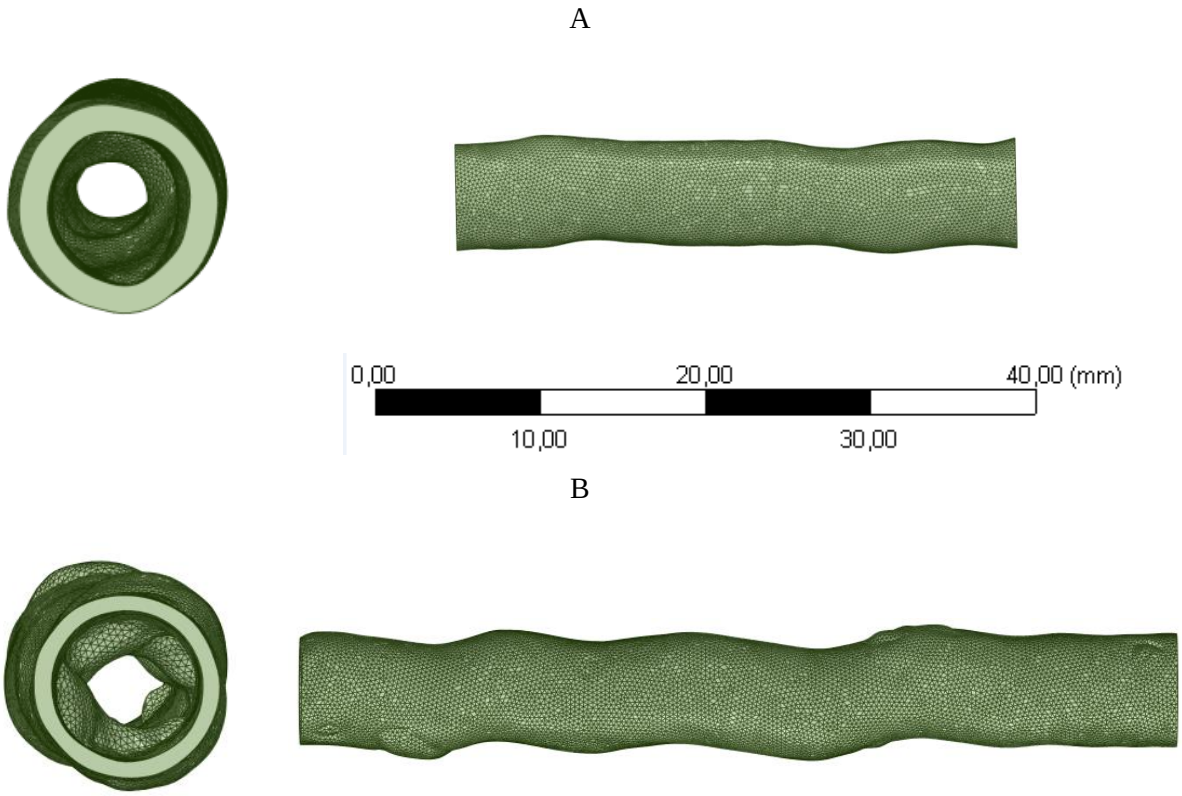

Figure 2.2: 3D solid models created from the (surface) STL geometries in axial and longitudinal views illustrating the lipid (A) and the calcified (B) stenosis cases.

[Figure 2.3] illustrates 3D reconstructions of both patients' stenosed arteries as can be seen using a clinical software [191] (EndoSize, Therenva, Rennes), and using the segmentation and volume reconstruction process we used to generated the P-S models simulated in this work.

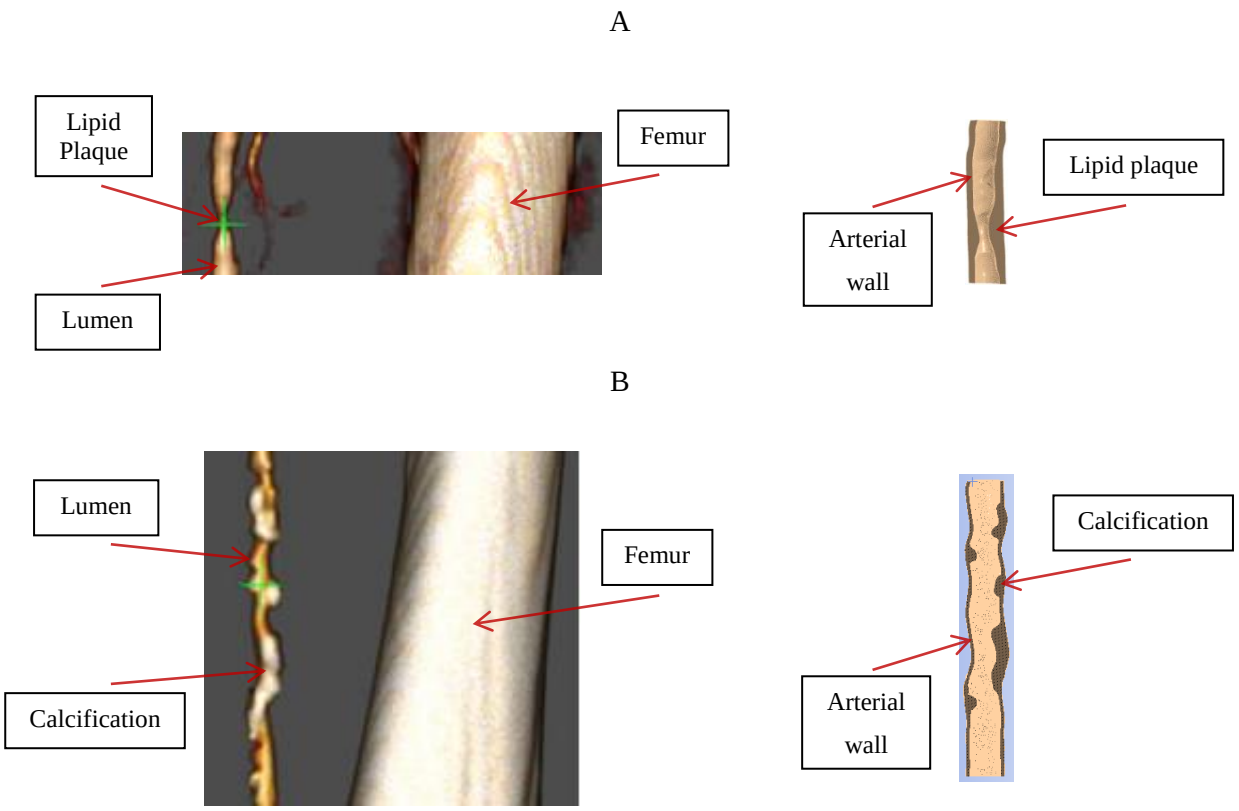

Figure 2.3: 3D reconstructions of the lipid (A) vs. the calcified (B) stenosed arteries as can be depicted using EndoSize (Therenva, Rennes) and using 3D slicer in addition to Ansys workbench for model generation prior to our FE simulations.

Finally the 3D solid geometries were meshed in Ansys Mechanical. The artery and plaque were meshed by 4-node hybrid solid elements ensuring u-P mixed formulation. With the P-S stenosed artery being processed as a single geometry including both arterial wall and the plaque, elements of different material models shared common nodes. Sufficient elements were assured along the thin arterial wall thickness. Moreover, finer mesh was generated at the stenosed artery inner surface where contact with the inflating balloon may occur.

Although it improves pre-processing for FE simulations (ensuring components connectivity, reducing geometric imperfections…), generating a single geometry from the segmentation step requires an additional step to assign the correct constitutive laws to the different components. A MATLAB function "INPOLYHEDRON" (MATLAB. (2013). 8.2.0.701 (R2013b). Natick, Massachusetts: The MathWorks Inc.) was first applied in order to assign the required material index for each element according to its location within the geometry (arterial wall vs. lipid/calcified plaque geometric coordinates for patients 1 and 2 respectively). [Figure 2.4] presents a graphical illustration showing elements from a combined stenosed arterial model falling within the calcified plaque spatial geometry seen in orange as an example. This function consists of testing whether the query points (elements centroids corresponding to the combined geometries) are inside a 3D triangulated (faces/vertices) surface: healthy artery or plaque, and assigning to them different indices accordingly. Therefore prior

to that, besides computing the centroid of the elements belonging in the combined geometry, the "STLREAD" function was required in order to import the triangular faces from the STL files (corresponding to the separate geometries: artery or plaque) into MATLAB, and returning their faces and vertices. More details on the functions used can be seen in Appendix A.6.

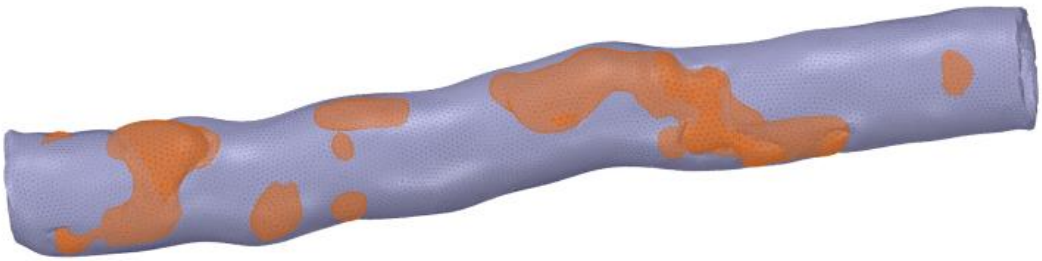

Figure 2.4: Combined stenosed artery with the elements which fall within the calcified plaque spatial geometry identified in orange.

Finally, the "mpchg" APDL command (Ansys mechanical) was used to modify each element material model based on its assigned index. The 3D FE models corresponding to the two patients' stenosed arteries are shown in [Figure 2.5].

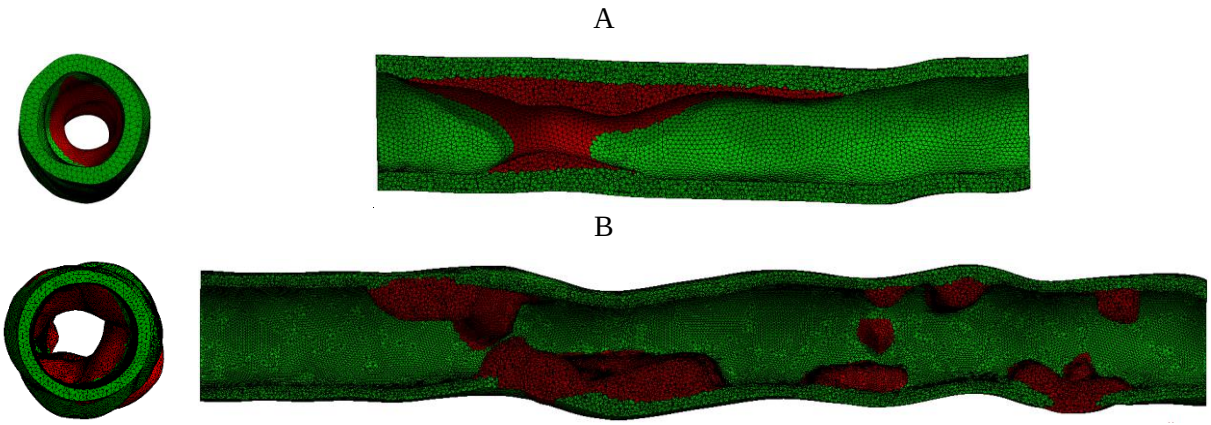

Figure 2.5: The 3D finite element models showing the diseased arteries in axial and longitudinal views for each of the lipid and the calcified stenosis cases in (A) and (B) respectively. The healthy artery is illustrated in green while the plaque in red.

CHAPTER 7

PATIENT-SPECIFIC FINITE ELEMENT ANALYSIS OF PTA IN FEMORAL ARTERIES

In this last chapter we present two patient-specific (P-S) models of PTA within a peripheral artery using implicit FE analysis, in order to evaluate the balloon sizing influence on the procedure outcomes. With the main components of the P-S simulation presented in details in previous chapters, geometries, mesh, material models, boundary conditions, and analysis of results are here briefly recalled in the first part of this chapter. The proposed modeling approach is then presented on two stenosed femoral arterial cases: one with a dominant calcified atherosclerosis, while the other with a lipidic plaque. Finally acute results obtained after balloon angioplasty for different sizings are reported for both P-S cases in the second part of this chapter. A qualitative comparison between the simulated PTA and the corresponding clinical outcomes obtained from 2D post-operative medical images is presented.

OUTLINE

1 INTRODUCTION

Peripheral arteries are one of the most vulnerable vascular locations for the occurrence of atherosclerosis. The development of this disease in femoral vessels is the main cause of claudication and critical limb ischemia (ischemic rest pain) [11].

Most studies were performed within idealized geometries. However, with simulations showing high sensitivity in results to small geometric and material properties changes [103], FE studies are shifting recently to patient-specific simulations. Among these patient-specific FE studies, some focused on evaluating plaque vulnerability and risk to rupture at normal blood pressures (without any supra-physiological loading caused by a balloon or a stent…) [22], [124]. Others considered implanting stents before balloon deflation (balloon-expandable or self-expanding stents), hence not assessing residual deformations obtained immediately after PTA alone [75], [123], [125], [127]. They focused mainly on stress distribution within stenosed arteries in relation to different stent designs, with results showing significant sensitivity. Furthermore, a recent generic study also highlighted the importance of modeling residual deformations (by modeling pre-dilations) towards endovascular treatment planning using FEMs [121].

However, very few patient-specific FE studies considered incorporating inelasticity with residual deformation within their models [103], [129]; moreover, up to our knowledge no clear FE study intended evaluating PTA outcomes (ERR, LGR…) at short terms within femoral arteries specifically, despite still being the initial revascularization approach practically considered by clinicians at such arterial locations. Holzapfel et al. (2002) was on an iliac artery [103]; Gasser and Holzapfel (2007a) was a generic model mimicking a coronary artery [117]; Decorato et al. (2014) was in an arteriovenous fistula [129]. Finally, except for the generic model of Liang et al. (2005) [107], no FE study presents acute post-angioplasty simulated results in comparison with clinical outcomes.

Now that the essential components towards a patient-specific (P-S) simulation have been developed in the previous chapters, the present chapter describes an assembled workflow for simulating P-S balloon angioplasty within femoral arteries, in order to evaluate the balloon sizing influence on their acute outcomes.

2 MATERIAL AND METHODS

2.1 GEOMETRY

Geometric models corresponding to stenosed femoral arteries were generated from preoperative computed tomography angiography (CTA) scans as was detailed in Chapter 6. [Figure 2.1 (A) and (B)] present the two patient-specific stenosed femoral arteries showing the lipidic and calcified plaque cases respectively. Both segmented patient geometries were of varying stenosis severities reaching ~52% within the lipid plaque case and ~41% in the calcified one, at the most stenosed region. The calcified case had a more elongated distribution, so a 53.7 mm arterial segment was modeled to include the entire stenosed region. A shorter arterial segment of 34 mm in length was considered for the lipidic plaque case.

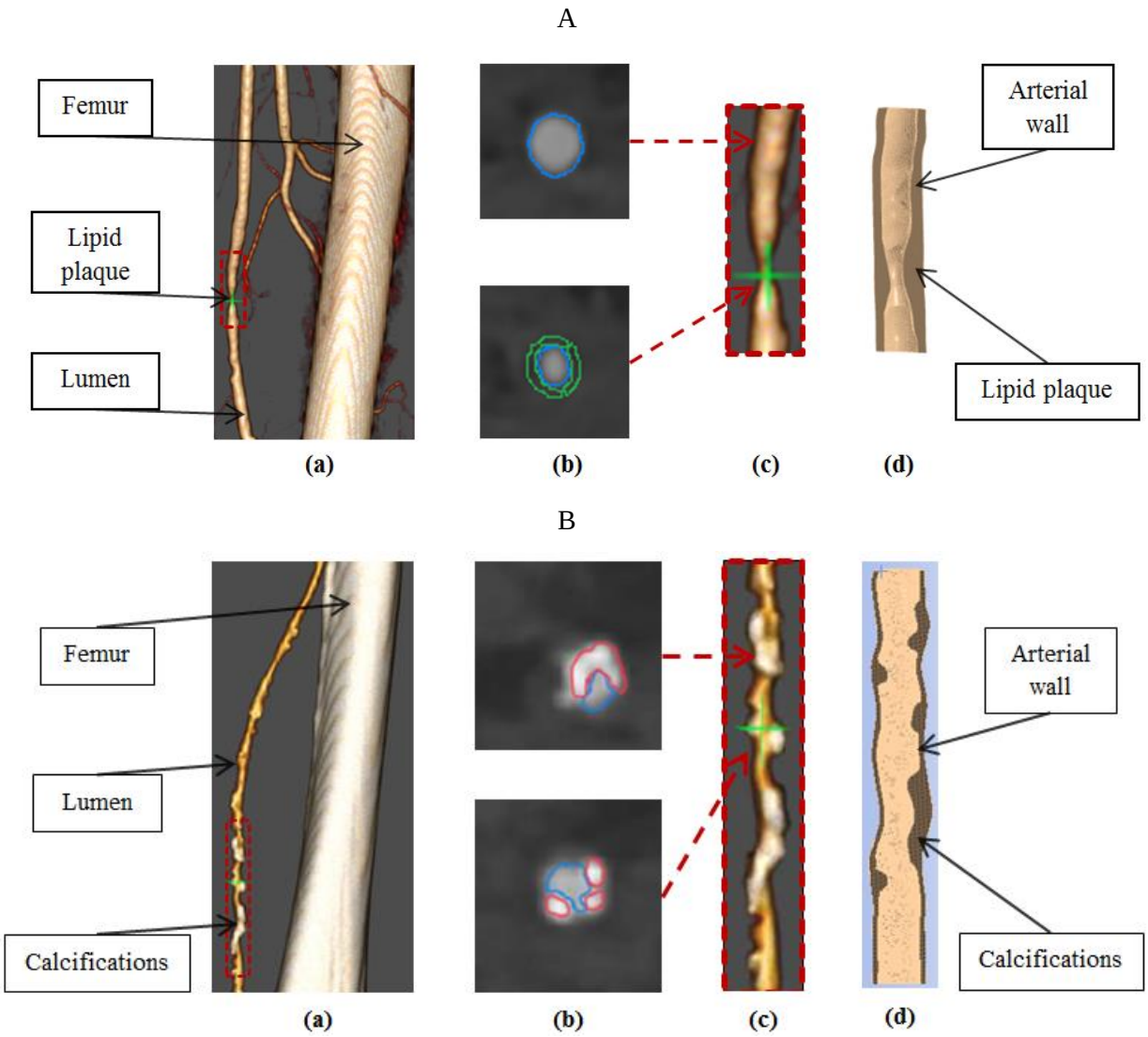

Figure 2.1: Patient-specific femoral stenosis arterial models corresponding to the lipid (A) and the calcified (B) plaque cases respectively: (a) 3D observation of each stenosed artery and femur bone from CTA. (b) Pre-operative CTA axial slices at two different locations along each diseased artery, with the lumen, the lipid plaque, and the calcifications shown in blue, green, and red respectively. (c) 3D observation of each atherosclerotic region in a zoomed view, with the lumen seen in yellow, the calcifications in white, while the lipid plaques not represented. (d) A cross-sectional view at a random plane showing the plaque and the arterial wall of each reconstructed 3D geometry.

2.2 MESH

As was also mentioned in Chapter 6, the artery and plaque of both patients were meshed using hybrid solid elements in Ansys mechanical ensuring u-P mixed formulation. Following the mesh sensitivity analysis performed with the generic model presented in Chapter 4, the P-S stenosed artery with the calcified plaque was meshed by 773230 4-node solid elements corresponding to typical element sizes of 0.24 mm for the entire geometry and 0.19 mm in the inner surface subjected to contact with the inflating balloon. Differently, in order to reduce the simulation time required for the calcified plaque simulations, another sensitivity analysis was performed on the mesh for the patient with the lipid plaque before executing the needed simulations for that case. Accordingly the stenosed artery of this

patient was meshed by 272991 4-node solid elements corresponding to 0.28 mm and 0.24 mm element sizes respectively for the whole model and in the stenosis inner surface in contact with the balloon. The new mesh convergence study (corresponding to the patient with the lipid plaque) is presented in Appendix A.7. In what follows, the patients with the lipidic and calcified stenosis would be referred to as Patient 1 and Patient 2 respectively. The 3D FEM models of the complete PTA system for both patients are shown in [Figure 2.2].

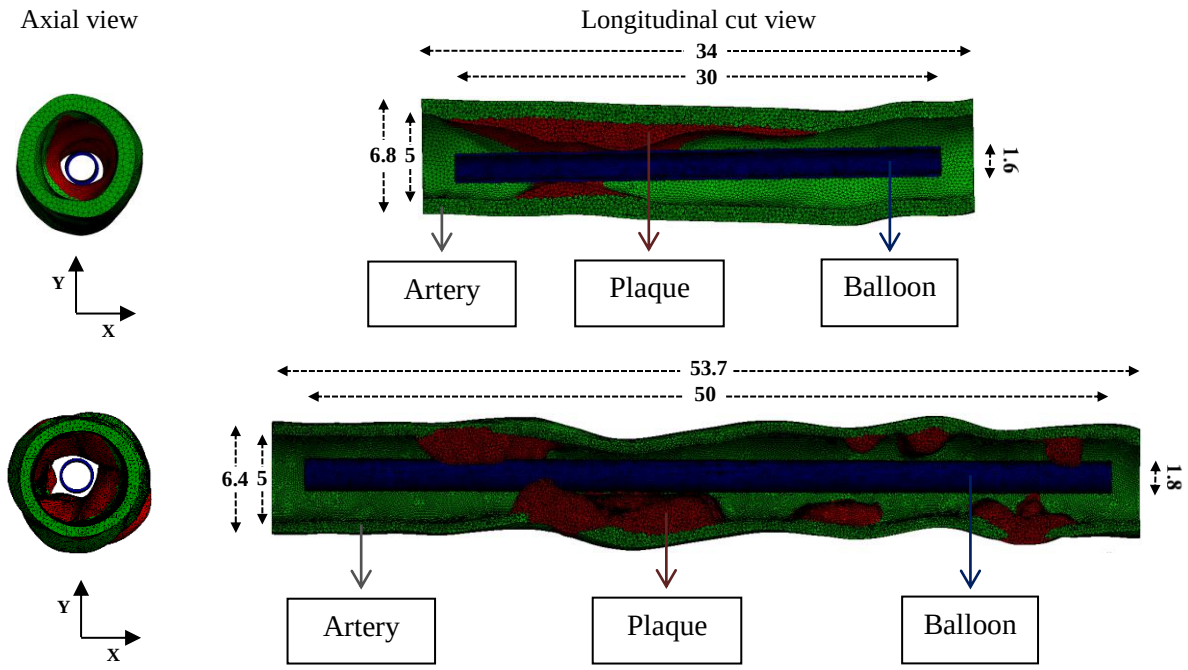

Figure 2.2: Finite element model of the complete balloon angioplasty system within the two P-S geometries at their initial state: the lipidic plaque case seen at the top, while the calcified one at the bottom. All dimensions are in mm.

2.3 CONSTITUTIVE LAWS

Similar to the generic model presented in Chapter 4, elasto-plastic constitutive laws were also used within the atherosclerotic components of our P-S simulations here to model residual deformations and evaluate acute outcomes after balloon deflation. All details of the material calibration method used for identifying the constitutive laws of the artery and the plaque were described in details in Chapter 5. Table 10 summarizes the material coefficients of the material models implemented in this work.

Table 10: Material parameters of the lipid and calcified plaque and their corresponding artery

Plaque Type	Young Modulus of Elasticity E (MPa)	Poisson Ratio (ν)	Yield Strength (KPa)	Tangent Modulus (KPa)
Lipid Plaque	0.105	0.40	5	62.77
Calcified Plaque	0.189	0.40	15.79	111.88
Artery (Lipid plaque case)	0.677	0.44	7	256.5
Artery (Calcified plaque case)	0.677	0.44	7	330.75

2.4 LOADING AND BOUNDARY CONDITIONS

The Medtronic Admiral Xtreme and the ULTRAVERSE 035 PTA balloon catheters were clinically deployed within patient 1 (with the lipidic plaque) and patient 2 (with the calcified atherosclerosis) respectively. Both balloons are of 5 mm nominal diameters. The balloon implemented in patient 1 was modeled with an initial diameter of 1.6 mm and a length of 30 mm, whereas the balloon of patient 2 was modeled with an initial diameter of 1.8 mm and a length of 50 mm. The modeled initial diameter was defined as the crimped balloon diameter onto its catheter, while the simulated length was chosen enough to extend past the lesions on both sides, according to manufacturers' recommendations.

With both balloons falling in between the semi and non-compliant balloon families following the relationship we proposed to categorize PTA balloons in Chapter 3, and most importantly with no significant variation observed in the results of interest of this work (ERR, LGR…) when the balloon design changed (as was seen in Chapter 4), being the more robust method, both balloons were modeled here as displacement-driven non-compliant balloons.

Being interested in balloon sizing influence analysis on acute PTA outcomes, six and ten balloons of different nominal diameters were simulated to their nominal values, and then deflated back to their initial position within patient 1 and 2 respectively. Table 11 and Table 12 present the balloon sizing corresponding to each simulated diameter for patient 1 and 2 respectively. All simulated balloon diameters fall within the clinically recommended balloon sizing range (balloon/artery ratio) of [0.9 to 1.1] for PTA treatments [36].

Table 11: Balloon sizing at each inflation diameter simulated within the lipidic patient 1

Nominal Diameter (mm)	Balloon Sizing (Balloon/Artery ratio)
4.5	0.9
4.75	0.95
5.00	1
5.12	1.024
5.25	1.05
5.42	1.084

Table 12: Balloon sizing at each inflation diameter simulated within the calcified patient 2

Nominal Diameter (mm)	Balloon Sizing (Balloon/Artery ratio)
4.5	0.9
4.625	0.925
4.75	0.95
4.875	0.975
5.00	1
5.06	1.012
5.12	1.024
5.23	1.046
5.33	1.066
5.42	1.084

Similar to the generic model presented in Chapter 4, in-plane arterial translations (in x-y plane) were allowed at both arterial ends to adapt to balloon radial inflation, with the balloon itself being clamped from both sides as described in Chapter 3. Axial translation and rotation were blocked in the model as well. Moreover, no internal pressure was further considered at the stenosed arterial inner wall under the hypothesis that the CTA data (from which the P-S geometries were generated) were obtained at normal blood pressure.

The non-linear contact between the balloon and stenosed artery is frictionless and formulated by pure penalty method. ANSYS implicit commercial finite element software (ANSYS® Academic Research Mechanical, Release 19.1.) was used to solve these large-deformation analyses.

2.5 ANALYSIS OF RESULTS

To analyze balloon sizing influence on PTA outcomes, results were mainly evaluated in terms of the elastic recoil ratio (ERR) and the lumen gain ratio (LGR) attained after balloon deflation. As a brief recall, elastic recoil is computed as the difference between the largest inscribed sphere diameter that can be generated along the centerline at max balloon inflation vs. after balloon deflation (see equation (7-1)), while lumen gain is similarly assessed but after balloon deflation vs. before balloon inflation (equation (7-2)). *ERR* is comparable to what surgeons usually evaluate as a control for their clinical outcomes. *LGR* would be useful in interpreting the obtained elastic recoils in comparison to the stenosed arterial initial configuration. Lumen centerlines and max-inscribed-spheres were computed using the Vascular Model Toolkit library (VMTK—www.vmtk.org). [Figure 2.3] presents an illustration of the inner luminal geometries of patient 1 showing the centerline and the max-inscribed-spheres appearing in two different positions along the stenosed artery, (a) before balloon inflation, (b) at its max inflation, and (c) after its deflation.

$$Elastic\ Recoil\ Ratio\ in\ \% = ERR_{along\_centerline} = \frac{D_{\max\_inflation} - D_{after\_deflation}}{D_{\max\_inflation}} \times 100 \qquad (7\text{-}1)$$

$$Lumen\ Gain\ Ratio\ in\ \% = LGR_{along\_centerline} = \frac{D_{after\_deflation} - D_{before\_inflation}}{D_{before\_inflation}} \times 100 \qquad (7\text{-}2)$$

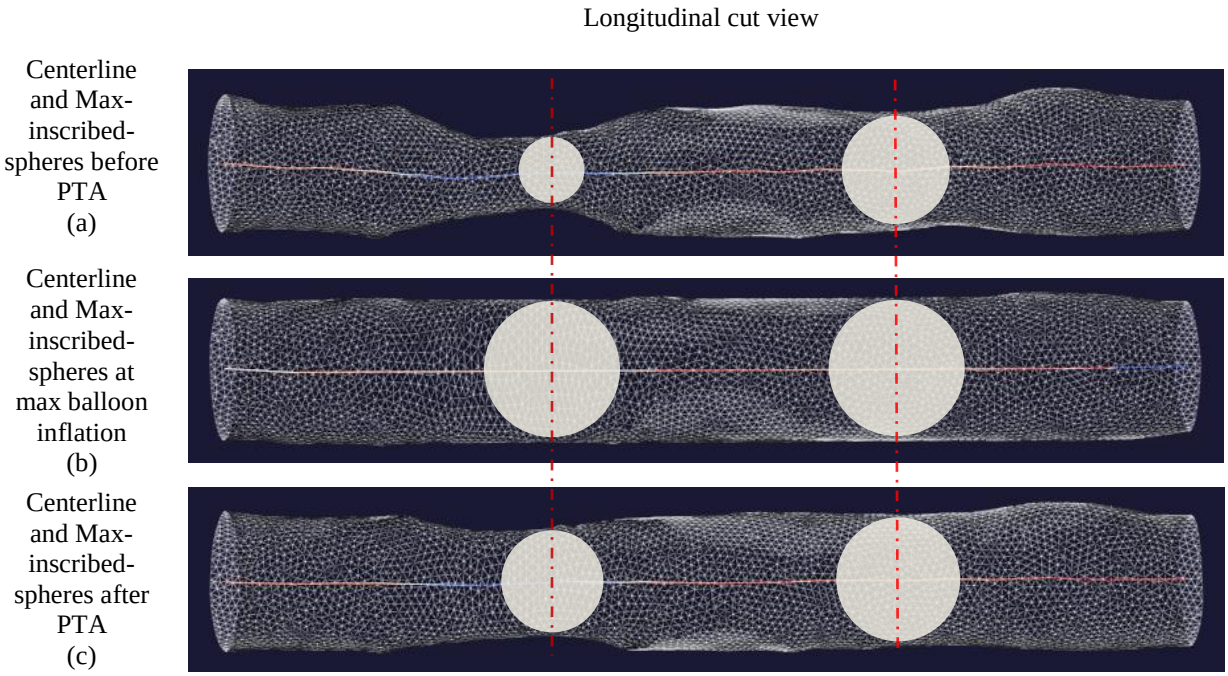

Figure 2.3: Reconstructed surface geometries that correspond to the stenosed artery inner lumen of Patient 1 showing max-inscribed-spheres (in beige) at two random sections (in red) along their centerlines for the three states of interest during balloon angioplasty simulations.

3 RESULTS

Several balloon sizings were simulated within each of the lipidic and calcified stenosed P-S geometries. Results associated to Patient 1 and Patient 2 are presented in Section 3.1 and Section 3.2 respectively.

3.1 PATIENT 1 WITH THE LIPID PLAQUE

3.1.1 Simulation vs. clinical outcomes: a qualitative comparison

This patient was clinically treated using a balloon catheter inflated up to 5 mm and then deflated. [Figure 3.1 (A-I)] presents a 2D projection view of the injected lumen before PTA with a blue elliptical shape around its main treated region. [Figure 3.1 (A-II)] shows another projection view of the lumen inner surface corresponding to the 3D stenosed femoral geometry generated from preoperative CTA of the same patient. The healthy arterial inner regions are seen in green, whereas the lipid plaque in red. [Figure 3.1 (B)] presents clinical and simulation outcomes obtained immediately after balloon deflation. Projection view of the injected lumen after PTA emphasizes the lumen gain along the treated region, see [Figure 3.1 (B-I)]. The deflated balloon catheter can still slightly be seen in white. [Figure 3.1 (B-II)] displays the plastic strains computed in the simulated stenosed arterial model after balloon deflation. Residual deformations can be clearly observed by comparing in axial view the arterial lumen before vs. after balloon angioplasty simulation.

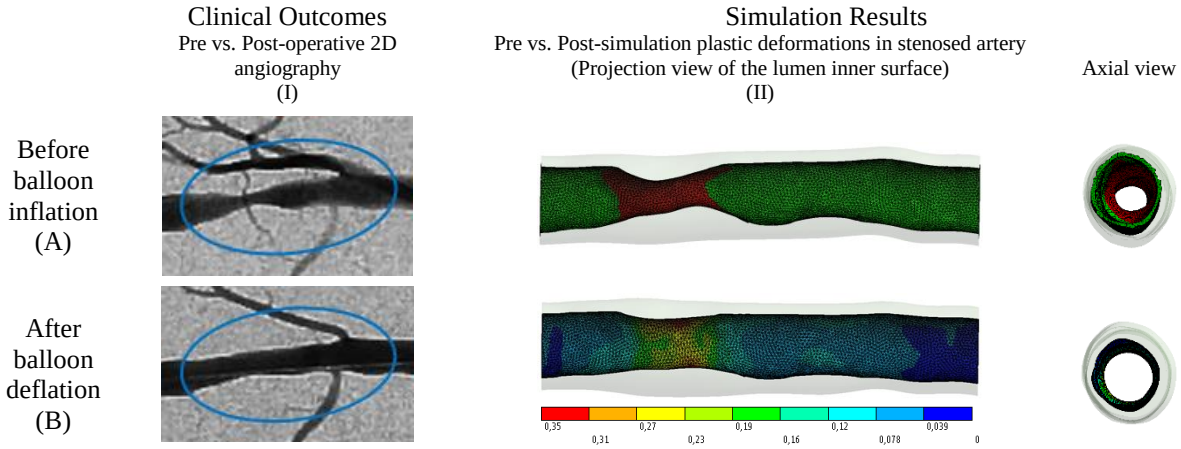

Figure 3.1: Clinical vs. simulation outcomes before (A) and after (B) balloon angioplasty. (A): Projection view of the injected femoral lumen before PTA (I) and another of its corresponding 3D geometric reconstruction (healthy arterial inner surface in green while the lipid plaque in red) (II). (B): Projection view of the same region after PTA illustrating its luminal gain (before catheter removal). Blue elliptical shape shows the main treated region (I). Simulation results also present the plastic strains resulting after balloon deflation with their effect on the final arterial lumen (II).

3.1.2 Balloon sizing influence on post-procedural outcomes: LGR and ERR

Balloon sizing was evaluated by simulating angioplasty for six different balloon diameters within the range of clinically recommended balloon/artery diameters ratio. [Figure 3.2 (A)] presents the evolution of LGR along the artery axis and the corresponding initial lumen diameter. LGR directly evaluates the lumen dilation due to balloon inflation, i.e. the presence of plastic strains within the tissues. As expected, LGR is noticeably larger where the initial lumen diameter is small (i.e. at main stenosis section) while it can reach 0 or even small negative values where there is no plaque. Negative values are probably due to surrounding plastic strains that can locally affect the artery diameter even in healthy sections. We can also see here that LGR is in positive correlation with balloon sizing, showing significant changes from one sizing to another. At the largest stenosed area for example, LGR locally reaches up to around 65% with the largest inflated balloon. [Figure 3.2 (B)] focuses more on the relationship between the LGR and the initial lumen diameter. For this patient, it can be seen that the dispersion of LGR is fairly small all along the treated region. This means that for such a patient, with a rather simple plaque geometry, the clinician can to a certain extent precisely control the attained LGR by driving the balloon expansion to the relevant sizing.

Unlike LGR that directly relates to the lumen expansion due to balloon inflation, ERR can be slightly more difficult to interpret when it comes to comparing sizings. ERR characterizes how much the stenosed artery recoils after being stretched by the inflated balloon; if the tissues were fully plastic, ERR would be 0. We can see on [Figure 3.3] that ERR is maximum at the most stenosed region. Moreover, ERR increases with balloon sizing as well, which means that the stenosed artery experiences more elastic strain when balloon sizing increases. ERR does not indicate how much plastic strain the tissues have stored. Also, as the denominator $D_{\max\_inflation}$ changes at each balloon sizing, it is not straightforward to explain the observed differences from one sizing to the other in terms of ERR, although it is typically the quantity that clinicians measure.

A

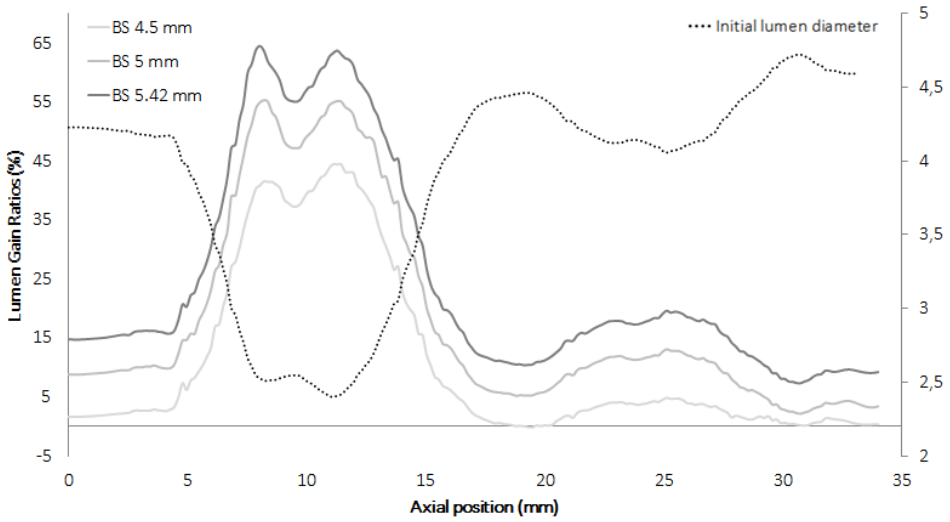

B

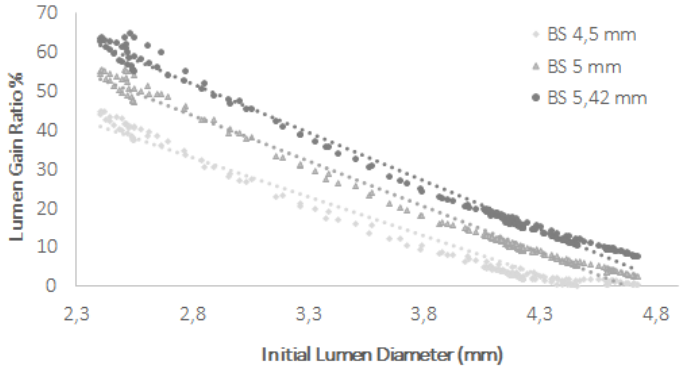

Figure 3.2: (A): Lumen gain ratio for different Balloon Sizings (BS) and initial lumen diameter along the artery axis. (B): Attained LGR values for various initial lumen diameters along the arterial length, for different balloon sizings.

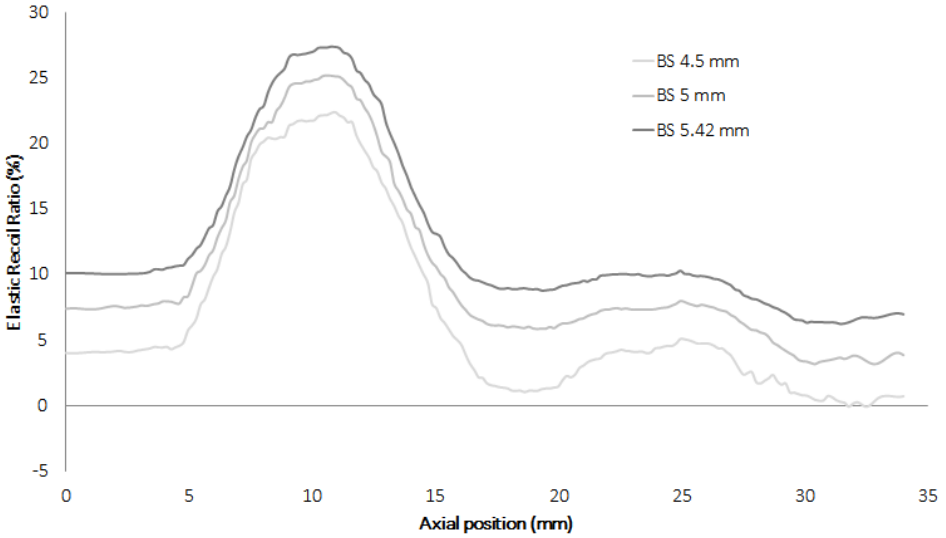

Figure 3.3: Elastic recoil ratio evolution after PTA along the artery axis for diverse balloon sizings within the lipidic plaque case.

To evaluate which of the lipidic plaque and arterial wall is the most involved in the lumen gain, we have calculated the plastic deformation in both tissues over 5mm-long portions of the model at 5 mm balloon sizing. [Figure 3.4] presents the residual strain distribution within the two components in each 5mm section along the arterial length. We can see that highest values of plastic strains forming within both components are attained at the most stenosed regions, i.e. in sections 5/10mm and 10/15mm. This confirms [Figure 3.2 (A)] which showed larger LGR values where the initial lumen diameter were small (i.e. within main stenosis segments as well). Moreover, as expected, the lipidic plaque stores larger amounts of plastic strain compared to the artery in similar sections; this is noticeably observed between 5 and 15 mm, always in the maximum stenosed region.

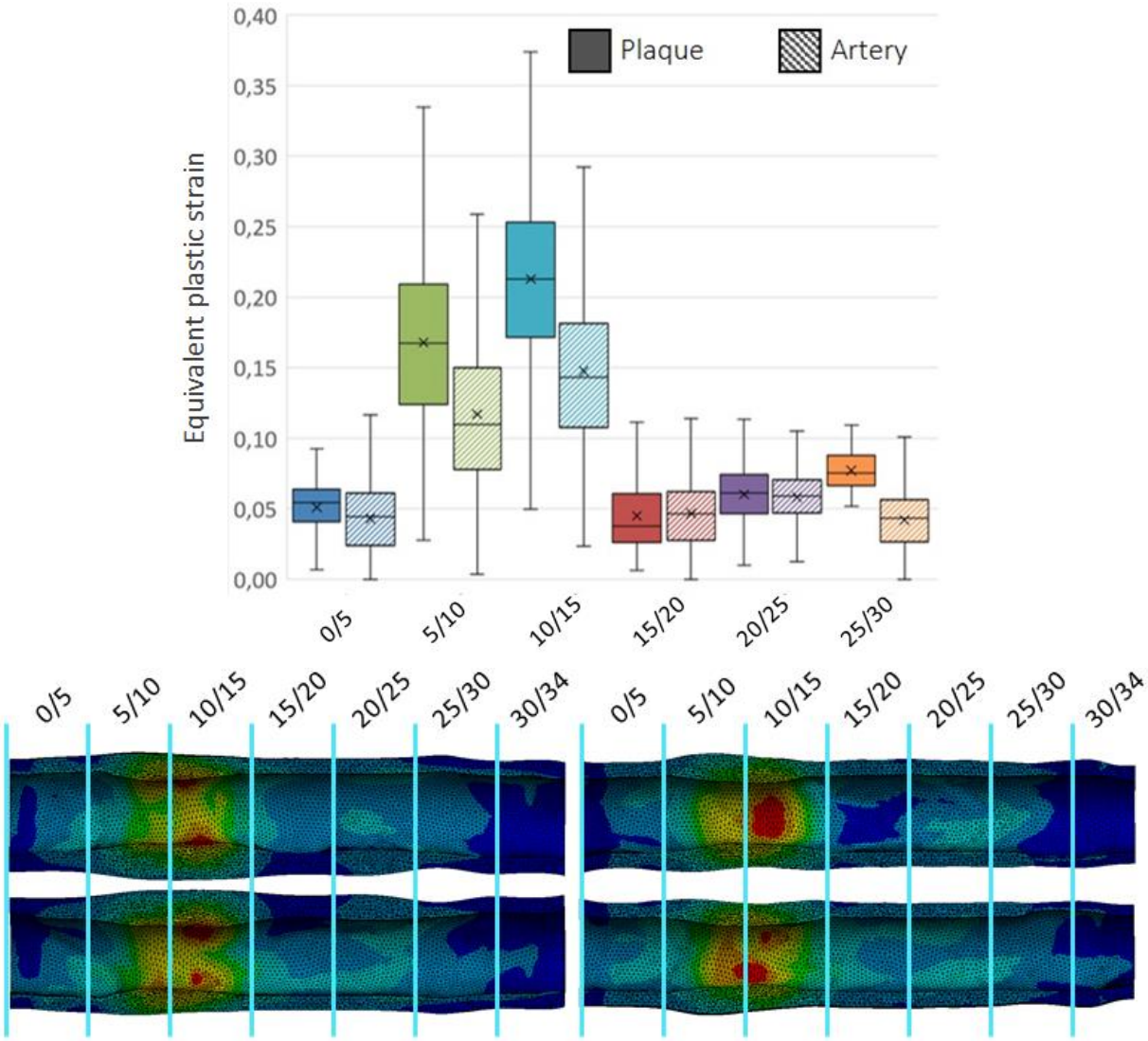

Figure 3.4: Distribution of the plastic strain stored in the lipid plaque and the arterial wall respectively. Each bar is calculated over a 5mm-long section which axial position is indicated in mm below each couple of bars.

Finally, [Figure 3.5] presents the evolution of the ERR and LGR together with balloon sizing, for three initial lumen diameters lying in moderately to largely stenosed areas within the patient with the lipid plaque. We can see on [Figure 3.5] that both ERR and LGR are in direct correlation with balloon sizing, with significantly larger rates of change for the LGR in comparison to the ERR from one sizing to another. This indicates that increasing the balloon sizing to a large extent increases the LGR, and to a smaller extent increases the ERR. It also means that the stenosed vessel experiences more of both plastic and elastic strains with the increase of balloon sizing, with larger potentials of permanent deformations, i.e. lumen expansion.

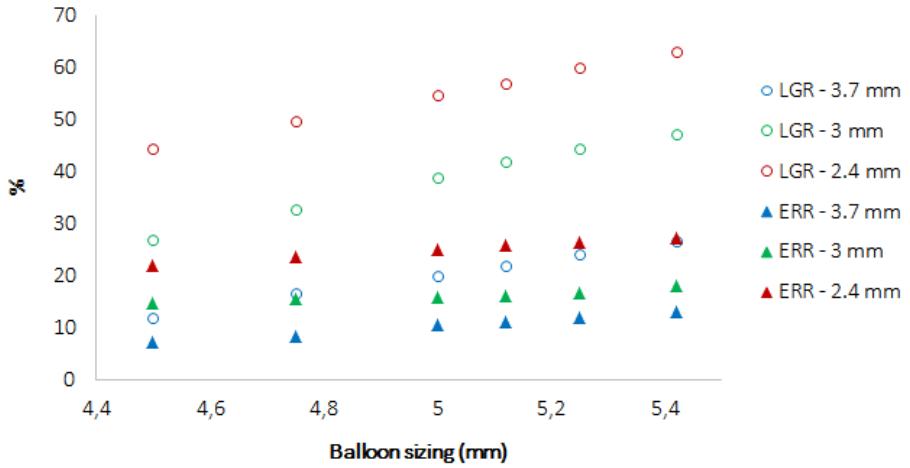

Figure 3.5: ERR and LGR evolution with balloon sizing for different initial diameters within patient 1.

3.1.3 Arterial wall max principal strain at max balloon inflation

Max principal strains forming in the external surface of the arterial walls at max inflations were compared for three different balloon sizing: 4.5, 5.12 and 5.42 mm. Results are depicted in [Figure 3.6]. In general their peak values showed a relatively gradual increase at larger simulated diameters. After increasing from 0.12 at 4.5 mm to 0.15 at 5.12 mm, peak strains only augmented to 0.16 when the balloon inflation reached 5.42 mm. Besides, the peak values occur at a similar location among the different sizings, within the max stenosed region.

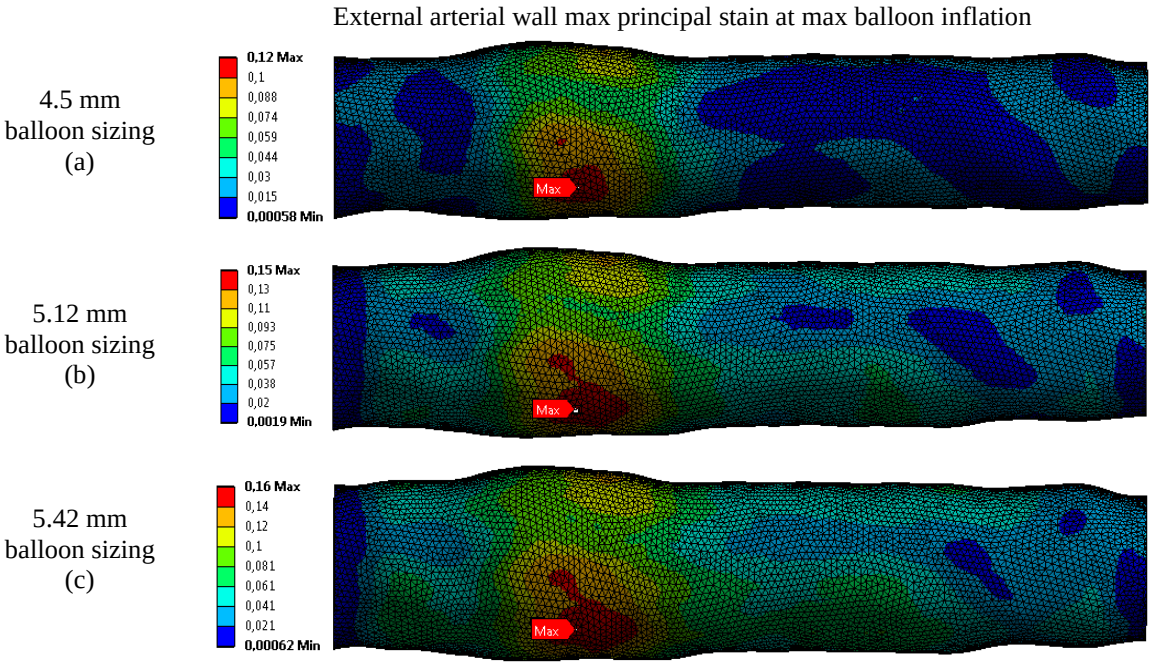

Figure 3.6: Max principal strain field in the outer arterial wall during PTA at max balloon inflation for three different balloon sizing: 4.5 mm (a) 5.12 mm (b) and 5.42 mm (c). Max value site is also shown for each sizing.

3.2 PATIENT 2 WITH THE CALCIFIED PLAQUE

3.2.1 Simulation vs. clinical outcomes: a qualitative comparison

Clinically, this calcified patient was treated using a balloon catheter inflated up to 5.12 mm and then deflated. Similar to what was presented for the lipidic patient in Section 3.1.1, [Figure 3.7 (A-I)] illustrates a 2D projection view of the injected lumen before the treatment, with a blue elliptical shape around its stenosed region. [Figure 3.7 (A-II)] here shows a longitudinal cut view of the lumen inner surface corresponding to the 3D femoral geometry generated from preoperative CTA of this patient. Healthy arterial inner regions are seen in green, while calcifications in red. As for Patient 1, [Figure 3.7 (B)] presents clinical and simulation outcomes obtained immediately after balloon deflation. Projection view of the injected lumen after PTA qualitatively illustrates the lumen gained along the treated region within this patient, see [Figure 3.7 (B-I)]. The deflated balloon catheter was still present and is more visibly seen in white here. [Figure 3.7 (B-II)] displays the plastic deformations occurring in the simulated stenosed artery model after balloon deflation. Permanent strains can also be clearly perceived by comparing in axial view the arterial lumen before vs. after balloon simulation, for this patient as well.

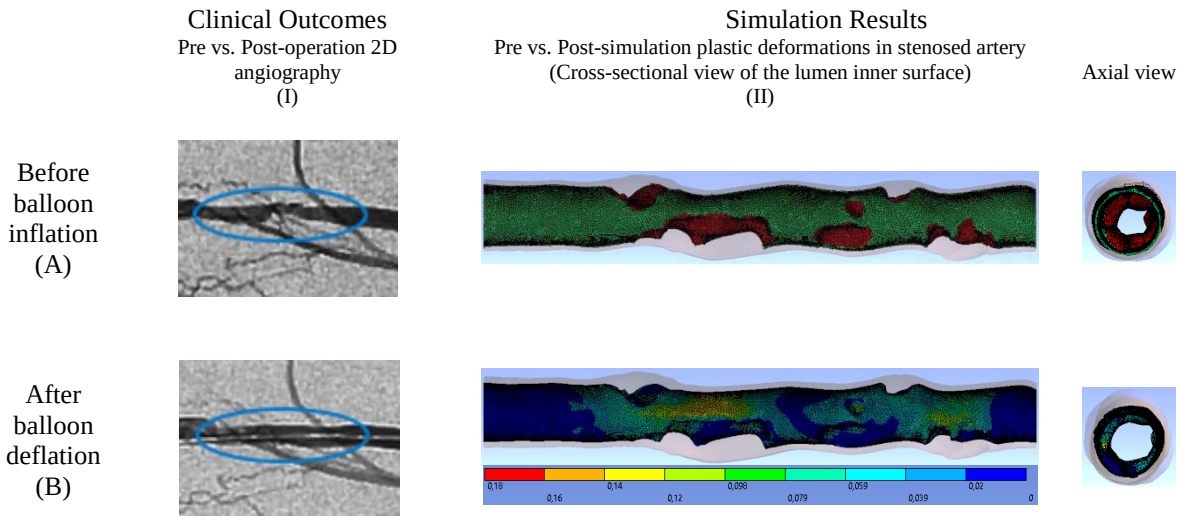

Figure 3.7: Clinical vs. simulation outcomes before (A) and after (B) balloon angioplasty. (A): Projection view of the injected femoral lumen before PTA (I) and a cross-sectional view of its corresponding 3D geometric reconstruction (healthy arterial inner surface in green while calcified plaques in red) (II). (B): Projection view of the same region after PTA illustrating its luminal gain (before catheter removal). Blue elliptical shape shows the treated region (I). Simulation results also present the residual deformations resulting after balloon deflation with their effect on the final arterial lumen (II).

3.2.2 Balloon sizing influence on post-procedural outcomes: LGR and ERR

Balloon sizing was evaluated by simulating PTA for ten different balloon diameters within this patient, also falling in the range of recommended balloon/artery diameters ratio. [Figure 3.8 (A)] shows the evolution of LGR and the initial lumen diameter along the artery axis corresponding to this calcified stenosis case. As expected, LGR was larger where the initial lumen diameter was small (large stenosis) while it reached 0 and even negative values where there was no plaque. Moreover, it can also be seen within this calcified patient that changing sizing in the recommended range significantly influences LGR as well. It more than doubled the LGR in largely stenosed areas, reaching locally around 30% with the largest balloon. [Figure 3.8 (B)] shows the relationship between the LGR and the initial lumen diameter within this patient. For highly stenosed areas (lumen diameter below 3.5 mm), the dispersion is small; it means that one can control more precisely the balloon sizing expansion to reach a targeted LGR. However this is less true here for larger initial lumen diameters; what happens in the mildly stenosed areas is usually clinically less crucial for the surgery success, but it is interesting to see that several locations of similar medium severity can experience, due to geometrical variations, dispersed outcomes in terms of LGR.

For the same reasons previously mentioned in Section 3.1.2, the interpretation of ERR can be slightly more challenging when it comes to comparing balloon sizings. [Figure 3.9] presents the evolution of ERR along the artery axis for different balloon sizes and shows that it is in positive correlation with balloon sizing.

A

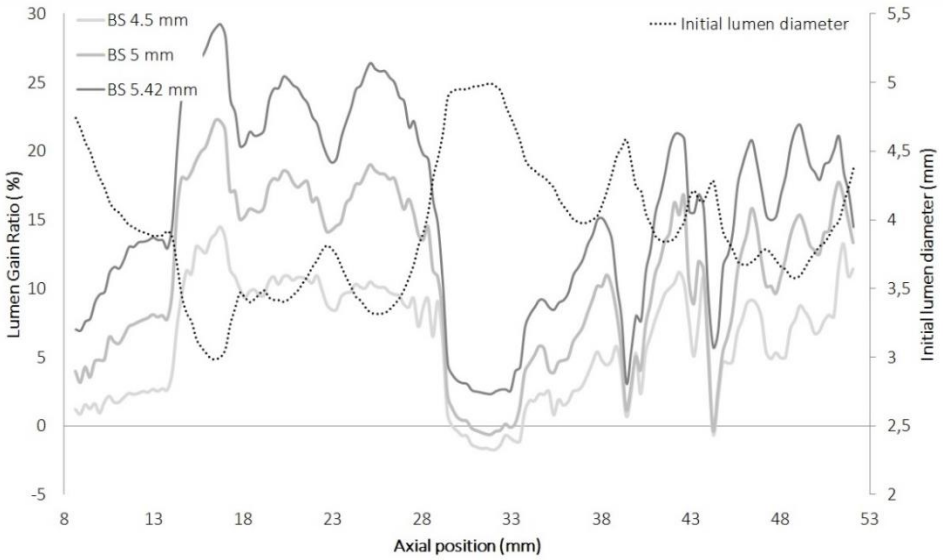

B

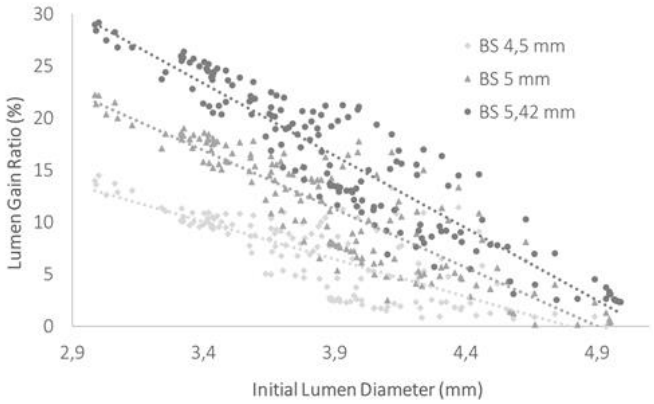

Figure 3.8: (A) LGR for different balloon sizings in addition to the initial lumen diameter along the artery axis. (B): Obtained LGR for various initial lumen diameters along the artery, for different balloon sizings.

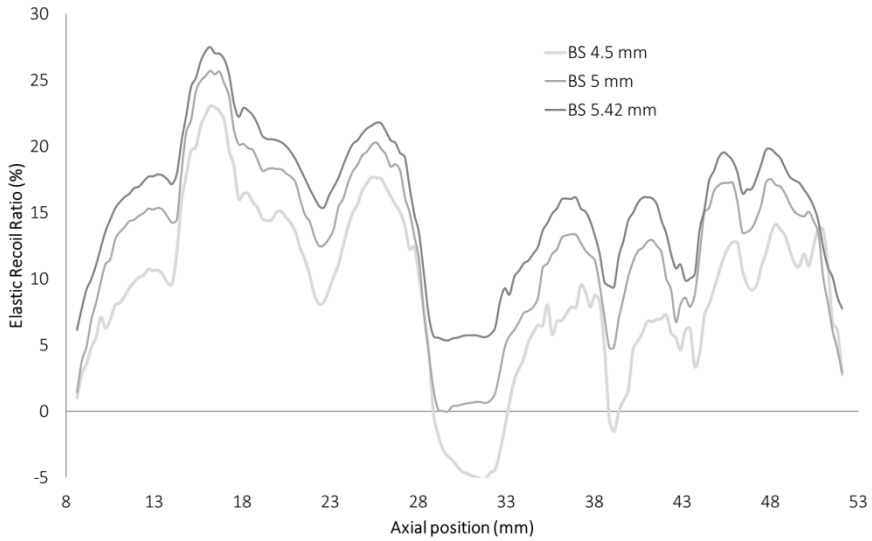

Figure 3.9: Elastic recoil ratio evolution after PTA along the artery axis for different balloon sizings within the calcified plaque case.

Also here, to evaluate which of the plaque and arterial wall is the most involved in the lumen gain, we have computed the plastic strain in both tissues over 5mm-long portions of this model at 5 mm balloon sizing as well. We obtain the graph on [Figure 3.10]: it shows a large disparity in the plastic strain distribution in both the artery and the calcifications, which is more difficult to analyze for this patient. We can however draw some tendencies: in general, the artery experiences as much or more plastic strain than the calcified plaque. From 14 to 29 mm, two large plaque volumes are present; the transition from one to the other is in the 19/24mm section, in which we observe a transfer of plasticity from the plaque to the artery. Also, in the 39/44mm, there is just one medium-size plaque which stores a large amount of plastic strain, while the rest of the artery circumference is healthy. Hence besides observing that in general the arterial wall experiences more residual deformations in comparison to the calcified plaque within the various sections, it also seems that the more calcifications are present at different locations on the periphery of the section, the more plasticity is transferred to the arterial wall itself as well.

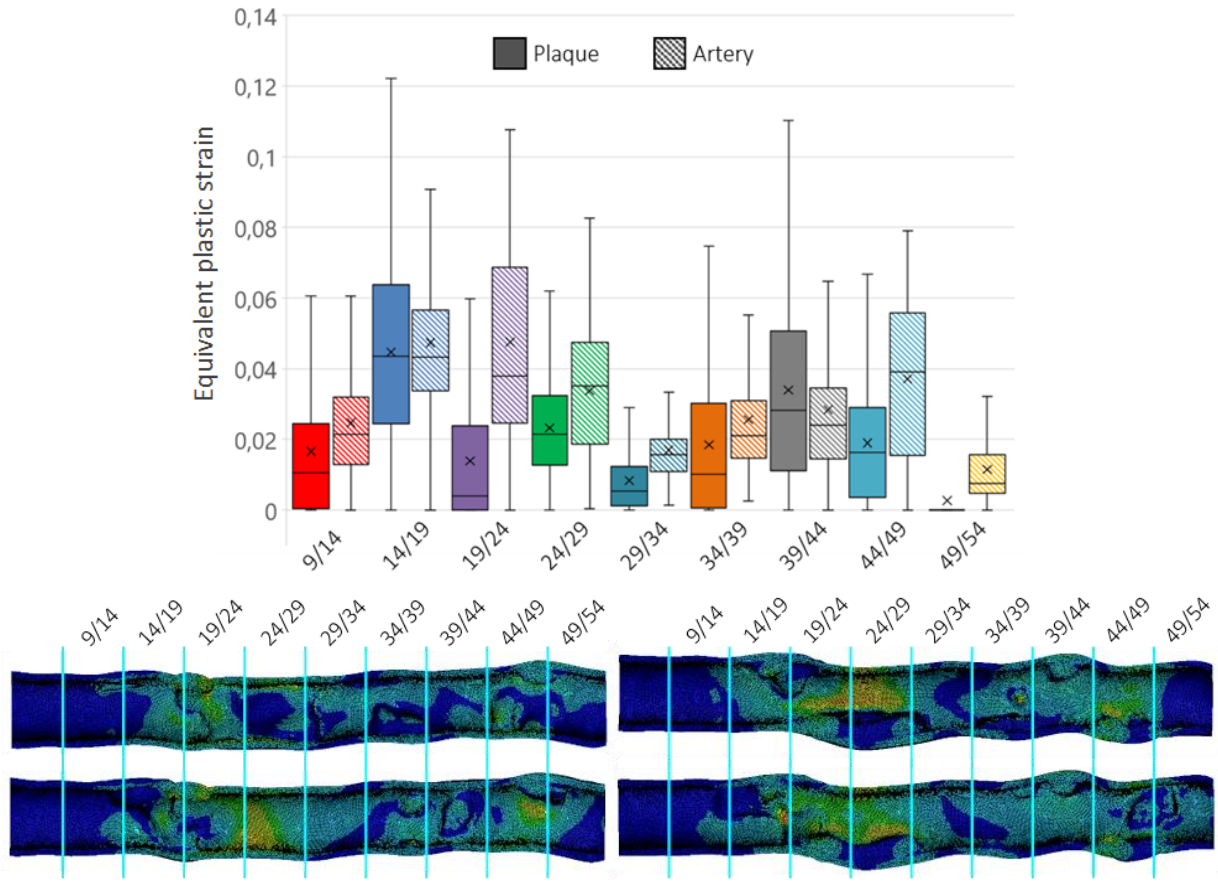

Figure 3.10: Distribution of the plastic strain stored in the calcified plaque and the arterial wall respectively. Each bar is calculated over a 5mm-long segment which axial position is indicated in mm below each couple of bars.

Finally, [Figure 3.11] shows the evolution of the LGR and ERR together with balloon sizing for three different initial lumen diameters lying in moderately to largely stenosed areas. Even though the LGR values obtained here are relatively smaller than those of the lipidic case (seen in [Figure 3.5]), the graph below confirms that increasing the balloon sizing would to a large extent increase the LGR and to a smaller extent increase the ERR.

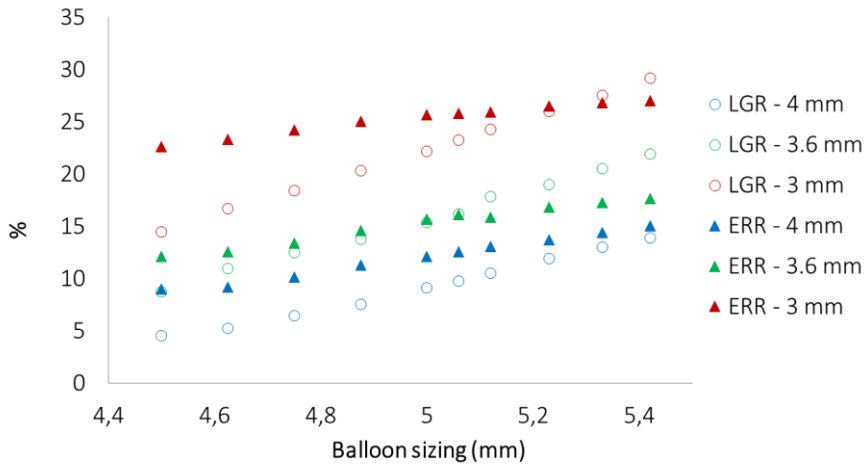

Figure 3.11: ERR and LGR evolution with balloon sizing for different initial diameters within patient 2.

3.2.3 Arterial wall max principal strain at max balloon inflation

[Figure 3.12] illustrates the max principal strains distributed within the outer arterial wall at max inflation, for the three balloon sizings: 4.5, 5.12 and 5.42 mm. In comparison to the lipid stenosis case presented in Section 3.1.3, max principal strains peak values here show a more significant increase at larger diameters simulated: (0.27 at 5.42 mm vs. 0.16 at 4.5 mm).

The peak value location (labeled in red) seems to change within this patient for different balloon diameters; however the three presented cases indicate that the peak value always occurs around the same axial cross-sectional area along the arterial length, i.e. also at max stenosed region.

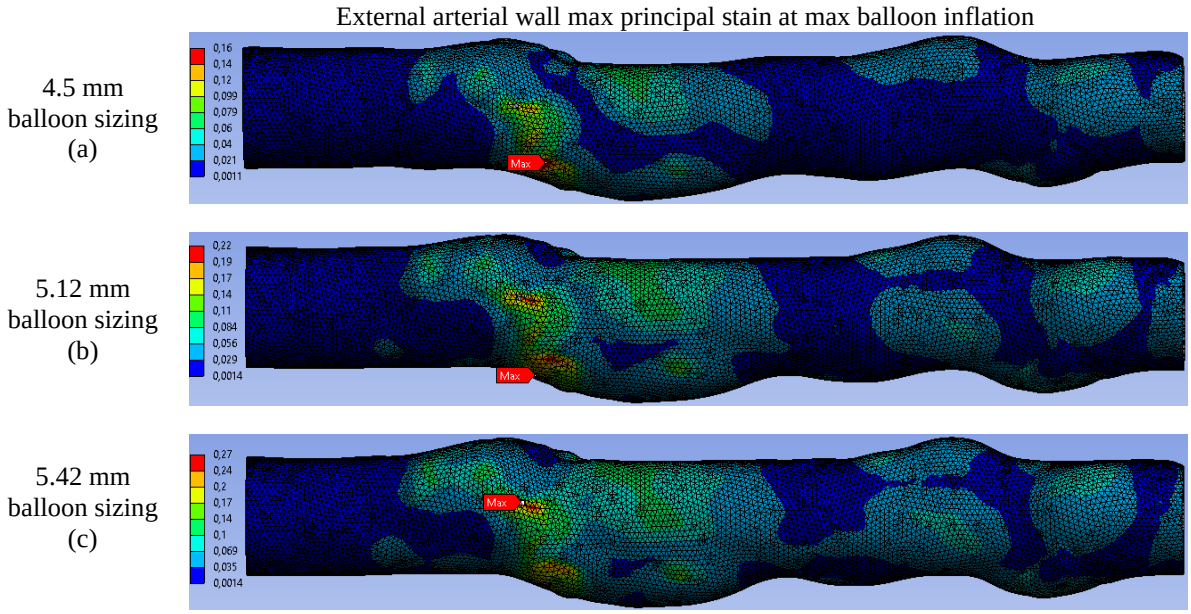

Figure 3.12: Max principal strain field in the outer arterial wall at max balloon inflation during PTA for the three different balloon sizing: 4.5 mm (a) 5.12 mm (b) and 5.42 mm (c). Max value location is marked for each sizing.

4 DISCUSSION

The present chapter aims at presenting a patient-specific modeling approach using implicit FEM for evaluating acute outcomes of a PTA procedure for different balloon sizings. Elasto-plastic constitutive laws were used for both the artery and plaque to model residual deformations. Results were mainly assessed in terms of ERR and LGR on two peripheral stenosis cases, one with a lipidic plaque while the other with calcifications; the distributions of plastic strains and maximal principal strains within the stenosed arteries and outer arterial walls were evaluated as well.

The balloon was initially driven up to 5 mm within the lipidic femoral geometry (patient 1), while to 5.12 mm within the calcified one (patient 2), and then deflated back to its original position in both cases. These inflation diameters were chosen in accordance with what was clinically performed for each patient separately. For both patients, a qualitative comparison between clinical vs. simulation outcomes before and after PTA shows residual deformation development in the stenosed regions after balloon deflation, see [Figure 3.1] and [Figure 3.7]. Permanent deformations can be clearly observed in the axial views of our simulations results. This observation is in accordance with FE studies that reported the presence of lumen gain within the vessel after PTA alone, even if these studies were not performed using *in-vivo* input imaging data [103], [117], [120]. Besides, straightening was observed in the lumen configuration of both patients after the treatment as well.

With the wide dispersion of calcifications within patient 2, both ERR and LGR curves showed several oscillations along the diseased artery accordingly with the plaque severity initial distribution. A similar behavior was observed on the corresponding curves of patient 1, but with noticeably fewer fluctuations throughout the arterial length being composed of a more concentrated plaque. However for both patients, ERR and LGR displayed a negative association to the initial lumen diameter variation along the stenosed region. This indicates that as expected, the most stenosed regions (smallest initial lumen diameters) are usually the most vulnerable to endovascular treatments; it corroborates the fact that treatment outcomes are usually clinically evaluated at such regions as well [88], [164], [165].

Both ERR and LGR attained shortly after balloon angioplasty showed direct correlations to the increase in balloon inflation diameters within the two patients. This finding is in accordance with clinical results reporting positive association between balloon sizing and degree of elastic recoil [164], [165], [176].

When analyzing clinically reported ERRs [163]–[165], [175] in association to values obtained from our P-S simulations, it confirms that the calibration for the material models of the plaque and artery considered in this work is reasonable. Isner et al. [175] reported an average ERR of 28.6% ± 7.2% after PTA in iliac arteries. At similar locations, Gardiner et al. [164] measured 36% ± 11% as loss in

luminal diameter after balloon deflation (ERR). Our ERR values computed at most stenosed sections after angioplasty, as usually measured by clinicians, ranged between 22% and 27.5% within both patients for the different balloon sizings simulated, thus showing consistency with clinical findings.

As a supplementary assessment for our simulation results, we also reported the LGR values attained by the two patients at similar sites (max stenosed regions). For the balloon diameters driven in this work, LGR ranged between 42% and 63% within the lipidic patient while between 14.5% and 29.2% within the calcified one. It is noticeably higher between the two simulated patients here when the plaque is lipidic in comparison to when it is calcified. This finding is qualitatively in accordance with the clinical experience observed in our hospital center. In addition, quantitative clinical findings stated in the literature showed a large variety in their reported LGR values as well: for example 28.5% with [87], while 110% with [192]. It is important to mention that from the way LGR is computed (seen in equation (7-2)), besides atherosclerotic tissue composition and balloon sizing effects, we expect it to be also directly dependent on the initial geometric features of the stenosis (i.e., shape, distribution, and mainly severity). Recall that the two patients here had plaques of different distributions, shapes and severities, with patient 1 having the more severe plaque. Their arterial dimensions were initially not the same as well. Accordingly a direct one-to-one LGR comparison between the two cases here would not be relevant.

To better understand the behavior of the stenosed artery subjected to PTA, a statistic evaluation of plastic strain distribution within both the artery and the plaque is proposed for each patient individually at 5 mm balloon sizing. Plastic strains were mostly stored within the main stenosed regions of both patients. At these locations, it can be observed that significantly higher residual deformations were formed in the plaque of the lipidic patient compared to its corresponding arterial wall; however, with more equally distributed plastic deformations within the components of the calcified case, it seems that large calcifications are rather more resistant to balloon pressure and promote more transfer of plastic strains to the artery. It can be seen that predicting which of the plaque or the artery would experience the more plastic deformation is not always straightforward; more patient data would be necessary to quantitatively confirm the hypothesis of the calcified case. Last, the noticeably larger magnitude ranges of plastic strains stored within the stenosed region of patient 1 confirms the significantly larger LGR values reported for the same patient as discussed in the previous paragraph.

Patient 1 showed higher LGR magnitudes compared to ERR at similar axial locations within the treated artery. Differently, patient 2 in general showed higher ERR values with respect to LGR instead. Nevertheless for both patients, with the balloon sizing growth, the increase in ERR became limited compared to the rise in LGR, particularly at highly stenosed regions; they do not evolve at the same rate with respect to sizing, which makes sense given their expression. Indeed, on the max

stenosed section, for an augmentation of balloon diameter from 4.5 mm to 5.42 mm, the ERR was increased from 22% to 27% with the lipidic patient and from 23% to 27.5% with the calcified one, while the LGR rose from 42% to 63% with the lipidic case and from 14.5% to 29.2% with the calcified one. First it seems rational that, given arterial elastic properties, any increase in arterial stretching would lead to a growth in elastic recoils [164]. However the small rise in elastic recoil compared to lumen gain indicates that the treated stenosed arteries evolve mostly in their plastic range of deformation at higher balloon sizing, showing more permanent deformations than elastic ones.

Damage assessment is a critical issue in the prediction of clinical outcomes. It can be considered as a positive observation by clinicians ('controlled vessel injury' enhancing resulting lumen after PTA) until it starts risking the artery itself from being injured. In this work we do not claim to model the detailed damage phenomenon that might occur during balloon angioplasty. Plasticity was considered instead to approximate complex damage and flow phenomena occurring in stenosed arteries at small scales. Showing reliable results in comparison with clinical outcomes, our implemented model seems to be promising for ERR and LGR assessments after PTA. In this work, any increase in plastic deformations (quantified by LGR augmentation), is an indication of the presence of more damage within treated region at higher balloon sizing.

Max principal strains at max inflations showed wider distributions along the outer arterial walls of both patients for higher balloon sizings. Here, max principal strains in the external surface of the arterial walls were considered for the assessment of their risk of rupture. It can be observed for the two patients as well, that the magnitude of their peak values also increased at higher inflation diameters, but with a sharper increase with the calcified plaque. Strain peak values increased from 0.16 to 0.22 to 0.27 when the plaque was calcified vs. from 0.12 to 0.15 to 0.16 when the plaque was lipidic, respectively for the three different evaluated sizings. It seems that augmenting balloon sizing during PTA would place the arterial wall at higher risks to rupture when the treated plaque is calcified than when it is lipidic soft. Increasing balloon sizing seems to be a safer option for clinicians towards enlarging the lumen gained within a lipidic stenosis compared to a calcified one.

Moreover, within the lipid plaque, strain peak values occurred at a similar location of maximum stenosis for the three sizings. For the calcified case, even though their locations seemed to vary among the different sizings, they all ended up occurring around the same axial position, where the stenosis severity was maximal initially. Therefore, despite showing the highest LGRs with balloon sizing increase for both plaque types, arterial walls at maximum stenosed regions were most likely to experience the highest max principal strain values during inflation as well. This indicates that a compromise should be considered for each stenosis type, maximizing the achieved lumen gain after PTA from one side, but at the same time without damaging the healthy arterial tissue. Hence selecting the max possible balloon sizing that would not put the treated region under the risk of rupture should

be the adequate sizing choice towards clinical outcomes optimization. Threshold values setting arterial risks of rupture should be further defined for an appropriate balloon sizing selection.

Limitations of the present work principally concern the plaque and artery models, as already stated in Chapter 5. Modeling the plaque as a single component is a simplification here as well. The reason for this choice was first, that according to the clinical experience in our hospital center, femoral artery plaque is generally homogeneous when it requires treatment, and it is usually evaluated as being either calcified (stiff) or lipidic (soft), rather than with multi-components as seen in other stenosed regions [94], [132]. The second reason is that we aim to develop a tool that can be integrated into the clinical routine without any additional imaging. We can clearly see on [Figure 2.1], [Figure 3.1] and [Figure 3.7] that the spatial resolution and contrast of routine images currently do not allow for a detailed multi-component plaque geometry.

Moreover, the initial state of stress without the physiological blood pressure is not considered in this work for the same reason described in Chapter 5. Another simplification here is neglecting also blood pressure effect on the P-S geometry by considering the imaged geometry (the one that we segmented) to be similar to the geometry without blood pressure. We consider here this assumption acceptable as our constitutive law is linear in its elastic phase, so the stiffness is rather larger starting from the 0-stress configuration. However, further validation of the effect of the physiological blood pressure on acute outcomes after PTA might still be required at this stage for more precision, as we expect plastic strains to possibly occur sooner if the simulation is run from a configuration pre-stressed by blood pressure.

Despite the mentioned simplifications, with consistency being shown between simulations results and clinical outcomes, our model seems to be promising towards ERR and LGR assessments after balloon angioplasty.

5 CONCLUSION

This work presents a new approach for the evaluation of angioplasty balloon sizing influence on outcomes immediately after the treatment of a patient-specific femoral artery. It is based on the combination of implicit structural finite element analysis, material law identification and medical image analysis. Higher plastic strains (and LGR accordingly) were shown within the stenosed region of the lipidic patient. Simulated results also showed a direct and quantified correlation between balloon sizing and each of the attained ERR and LGR after PTA for both patients, with a more significant influence on the lumen gain. The max principal strain values in the outer arterial wall augmented at higher balloon sizes during inflation as well. Their rates of increase were higher when the plaque was calcified. The maximal LGRs were attained at the same axial position where the peak

strain values were observed; they both coincided with the initial max stenosis severity location. Therefore, our model shows that despite enhancing the resulting lumen after PTA, excessive balloon sizing might place the treated artery at more injury risks, with higher ones when the plaque is calcified. Results also illustrate that increasing balloon sizing can be the better choice towards optimizing acute outcomes after PTA (more safely maximizing lumen gain) within a lipidic plaque compared to a calcified one. The proposed approach can thus serve as a step towards a clinical decision support system to improve angioplasty balloon selections, with respect to the patient stenosis, prior to the surgery.

CONCLUSION AND PERSPECTIVES

This work focused on the potential of developing a method based on numerical simulations capable of modeling PTA towards a better computer-assisted planning of this endovascular treatment of stenosis. Even though it is a regularly performed technique, according to manufacturers and clinicians, selecting the suitable balloon (design and sizing) for the corresponding stenosed patient is still challenging. This can significantly influence the treatment outcomes, affecting further treatment decisions as well. In the absence of adequate alternatives, clinical choices are mainly based on surgeons' experience. If numerical simulations manage to fit within the procedure of clinical application of PTA, it can serve as a decision support tool adapted to address this issue.

In this thesis we have proposed a patient-specific modeling methodology capable of simulating PTA and assessing post-procedural outcomes at short terms after balloon deflation. It is based on the combination of implicit structural finite element analysis, material law identification, and medical image processing.

The first component within the workflow for simulating PTA treatment technique was modeling the angioplasty balloon itself. After suggesting a relationship to categorize clinically-used PTA balloons based on their compliance data into two large families (semi-compliant and non-compliant balloons), a modeling strategy was proposed for each balloon family correspondingly. Material law identification was the subsequent essential component within the workflow. A calibration method for defining the constitutive laws of the plaque and the artery prior to performing PTA simulations was proposed (respectively based on experimental and clinical literature data). The majority of FEM studies modeling PTA did not include any residual deformations within their diseased arterial material models. Differently, in accordance with clinical observations, plasticity was considered in this work to model permanent deformations. After modeling balloons and identifying consistent constitutive laws for the plaque and artery, we proposed a generic modeling strategy of PTA using an implicit FEM solver to evaluate the acute post-procedural outcomes. Using this model, we then presented a parametric study based on balloon type, plaque material composition, plaque material distribution, and balloon sizing, which quantifies their influence on elastic recoil ratios (ERR) and lumen gain ratios (LGR) obtained right after PTA. No variations in ERR nor LGR values were detected when the balloon type changed, despite the differences observed in their profile at max inflation. Moreover, LGR and ERR inversely varied with the augmentation of calcification level within the plaque, with the largest LGR obtained when stenosis was entirely lipidic. In a different way, plaques with similar material compositions but of altered distributions showed minor influences on ERR and LGR, yet

strong variations in their plastic strains arrangements. Furthermore, results showed a direct correlation between balloon sizing and each of the LGR and ERR, with noticeably higher rates of change for LGR. Simulation results illustrate that unlike design, balloon sizing has a significant impact on the attained lumen gain after PTA, but might increase arterial injury risk as well. This proposed methodology opens the way for evaluation of angioplasty balloon selections towards clinical procedure optimization.

Headed for our aim in presenting a patient-specific simulation of PTA, another component within the workflow was the generation of the P-S geometric model. A segmentation and model generation procedure was proposed to generate 3D P-S geometries suitable for FE simulations, for stenosed peripheral arteries from pre-operative CTA images. With the objective of developing a tool that can be integrated into the clinical routine without any additional imaging, only CTA scans were considered in this work. The process was applied on two superficial femoral stenosed arteries cases: one with a dominant calcified atherosclerosis, while the other with a lipidic plaque. With all required components for a patient-specific simulation of PTA being determined, we finally presented two rather different P-S models of the treatment within a peripheral artery, in order to assess the balloon sizing influence on the procedure acute outcomes. In accordance with clinical observations, simulations results showed that there should be a compromise between maximizing lumen gain and preventing the arterial wall from rupturing; such a model can help quantifying this compromise and provide guidance to the surgeons in the pre-operative sizing phase.

Despite the limitations of our proposed model, mainly in the chosen material models, it generally showed consistent results in comparison with clinical findings reported in the literature. It seems to be a promising tool towards acute outcomes prediction after PTA. Moreover, a qualitative comparison between the simulated PTA and the corresponding clinical outcomes obtained from 2D post-operative medical images showed encouraging results within the P-S geometries as well. However towards being introduced in clinical routine as a tool to help surgeons in the decision-making process, further validation of our model parameters should be performed using pre- and post-operative clinical data on several cases of different arterial dimensions, plaque severities, plaque compositions. A more automatic segmentation and volume reconstruction technique for generating the P-S geometries might be required for this step. Moreover, arterial rupture threshold values can be further defined in the model as well for more precise selections (e.g. objectively selecting the balloon sizing that would maximize the lumen gain, but would not risk rupturing the treated region).

Besides, the modeling approaches and findings of this thesis can serve as a starting point for several other interesting perspectives:

- To begin with, although being a crucial component towards the accurate FE modeling of certain endovascular treatments (mainly including PTA), only a limited number of experimental studies

considered evaluating the inelastic behavior of atherosclerotic tissues. More mechanical tests at different strain levels (including supra-physiological loadings) should be performed to characterize the inelastic behavior of atherosclerotic materials. Different arteries within the arterial tree should also be taken into consideration.

- Another future aim of the work is to generate a reduced order model (ROM) from our presented model capable of performing similar parametric studies in even smaller times (in terms of minutes or seconds), to be integrated in clinical decision support systems as well. A preliminary ROM corresponding to the generic simulation model described in this thesis has already been developed thanks to the collaboration with Ansys.

- Last but not least, the proposed simulation of PTA in this work can be used as a basic component within other endovascular treatments as well. Our model could be further upgraded later to simulate other treatments such as: drug-coated balloons, balloon-expandable stenting, pre-dilatations (using a balloon prior to the implantation of a stent), or post-dilatations (using a balloon after the implantation of a stent) for example if required. Upgrading the material models accordingly to include stress-softening (Mullins effect) here would be recommended.

Perspectives are definitely not limited to the mentioned suggestions here. With each by itself being a starting point for further developments in this innovating field, together they can form the bridge introducing numerical simulations into clinical practice.

LIST OF PUBLICATIONS

B. Helou, A. Bel-Brunon, C. Dupont, W. Ye, C. Silvestro, M. Rochette, A. Lucas, A. Kaladji, and P. Haigron, "Patient-specific Finite Element simulation of peripheral artery Percutaneous Transluminal Angioplasty to evaluate the procedure outcome without stent implantation," 2021, (Manuscript submitted for publication).

B. Helou, A. Bel-Brunon, C. Dupont, W. Ye, C. Silvestro, M. Rochette, A. Lucas, A. Kaladji, and P. Haigron, "Influence of balloon design, plaque material composition, and balloon sizing on acute post angioplasty outcomes: an implicit Finite Element Analysis," *Int. J. Numer. Method. Biomed. Eng.*, vol. 37, no. 8, pp. e3499–e3522, 2021.

B. Helou, A. Bel-Brunon, C. Dupont, W. Ye, C. Silvestro, M. Rochette, A. Lucas, A. Kaladji, and P. Haigron, "The influence of angioplasty balloon sizing on acute post-procedural outcomes: a Finite Element Analysis," *2020 42nd Annual International Conference of the IEEE Engineering in Medicine & Biology Society (EMBC)*, Montreal, QC, Canada, pp. 2535-2539, 2020.

B. Helou, A. Bel-Brunon, W. Ye, C. Dupont, C. Silvestro, M. Rochette, A. Lucas, A. Kaladji, and P. Haigron, "Plaque composition influence on balloon angioplasty acute post-procedural outcomes: a Finite Element Analysis," *2020 Virtual Physiological Human (VPH)*, Paris, France, pp. 594-595, 2020.

B. Al-Helou, C. Dupont, A. Bel-Brunon, A. Kaladji, and P. Haigron, "Influence of plaque geometry and composition on numerically simulated balloon angioplasty outcomes," *2019 16th International Symposium on Computer Methods in Biomechanics and Biomedical Engineering (CMBBE)*, New York, United States, 2019.

B. Al-Helou, C. Dupont, A. Bel-Brunon, W. Ye, A. Kaladji, and P. Haigron, "Towards a patient-specific simulation of the balloon angioplasty treatment technique," *2019 Surgetica*, Rennes, France, pp. 87-89, 2019.

B. Al-Helou, C. Dupont, A. Bel-Brunon, W. Ye, C. Silvestro, A. Kaladji, and P. Haigron, "Développement d'une simulation numérique élastoplastique de la dilatation d'une artère sténosée," *2019 14ème Colloque National en Calcul des Structures (CSMA)*, Giens, France, pp. 1-8, 2019.

APPENDIXES

OUTLINE

A.1. ADDITIONAL SEMI-COMPLIANT BALLOON MODELING APPLICATION EXAMPLE

Driven by radial displacement, no confirmation is required for the modeling approach applied to non-compliant balloons. Conversely, for the validation of the modeling technique suggested for semi-compliant balloons inflation, another balloon of 5 mm nominal diameter was modeled as presented in this section.

The P-D compliance chart corresponding to this balloon is extracted from its manufacturer data as seen in Table A. 1.

Table A. 1: P-D chart extracted from the Medtronic Admiral Xtreme PTA Balloon Catheter data. NP and RBP correspond to the nominal and the rated burst pressures (P_N and P_{RB}) respectively.

IP (atm/bar)		BALLOON ∅ (mm)
8	NP	**5.00**
9		5.04
10		5.08
11		5.12
12		5.16
13		5.20
14		5.25
15		5.30
16		5.35
17	RBP	**5.40**

The balloon was modeled with a folded diameter (D_f) of 1.8 mm and a working length of 25 mm. It was meshed by 4-nodes shell elements. The loading and boundary conditions implemented here were similar to the ones presented in section 3.3 of Chapter 3.

Applying the same modeling approach described in section 3.2.1 (Chapter 3), the Ogden law was identified with the following parameters: $\mu = 5337$ Pa, $A_1 = 10.21$ and $D_1 = 0$. Upon examining Table A. 2, it can be seen that this set of parameters accurately reproduces the manufactures data in terms of pressure and diameter values. Yet as mentioned in the discussion section of the same chapter, with the relatively small initial shear stress (μ) value obtained by curve-fitting for this particular balloon, converge might not be direct when simulated within highly stenosed arteries or stiff plaques. Even though it might influence the balloon inflation accuracy, μ must be increased in such cases to ensure convergence. With this balloon (of $RC = 8$) fitting in both balloon families as classified in

Chapter 3, another possible solution is to model its inflation by displacement, preserving consequently higher accuracies in the reached diameters as would be seen in Chapter 7.

Table A. 2: Relative % error between experimental and FE simulations diameters obtained at respective pressures during inflation of the 5 mm nominal diameter balloon. Green and blue cells indicate diameters at nominal and rated burst pressures respectively.

Pressure $[P_n]$ (atm)	**Semi-Compliant 5 mm balloon**		
	Diameter $[D_n]$ (mm)	**Simulated Diameter (mm)**	**% Error on Diameter**
8	5.00	4.944	1.12
9	5.04	5.015	0.50
10	5.08	5.080	0.00
11	5.12	5.139	0.37
12	5.16	5.194	0.66
13	5.20	5.245	0.86
14	5.25	5.292	0.80
15	5.30	5.336	0.68
16	5.35	5.378	0.52
17	5.40	5.419	0.35

A.2. ARTERIAL LENGTH SENSITIVITY STUDY

The same stenosed arterial geometric dimensions as described in Section 1.1 of Chapter 4 were used in the following sensitivity analysis. The artery and the plaque were meshed by 4-node hybrid solid elements corresponding to typical element sizes of 0.35 mm vs. 0.25 mm respectively. Moreover, similar constitutive laws and boundary conditions as detailed in Sections 1.3 and 1.4 were implemented here as well. Simulations were driven by a non-compliant balloon inflated up to a diameter of 3.8 mm within the stenosed region and then deflated back to its initial position. The inflation here was higher than what is usually clinically recommended within a 3 mm healthy inner arterial diameter, ensuring the occurrence of any arterial length effect on outcomes in case it exists. [Figure A. 1] presents the influence of varying the simulated arterial length on each of the total strain energy at max inflation, and on the resulting simulation file size. The total strain energy was evaluated within the same stenosed arterial region among the different simulations. A 25 mm was considered as a good compromise for the simulated arterial length: showing small influences on the stored strain energy within the diseased artery from one side, and reducing the simulation computational costs from another.

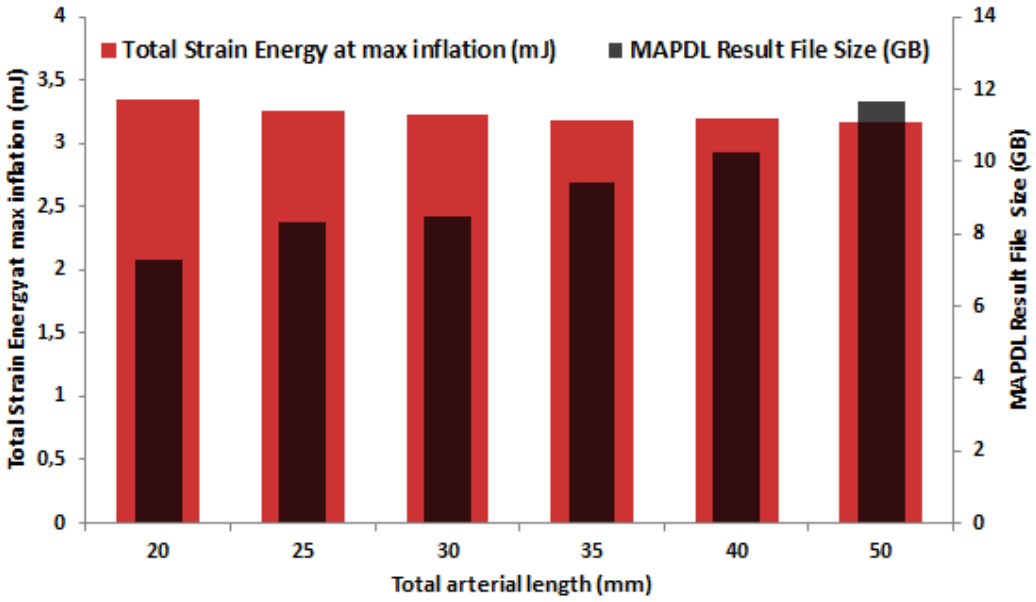

Figure A. 1: The simulated arterial length influence on the total strain energy (stored within the same stenosed arterial region among the different simulations), and on their resulting files sizes.

[Figure A. 2] shows the plastic strain distribution on longitudinal cross-sections corresponding to the different arterial lengths tested. Similar color maps can be observed within their common stenosed region for the various simulations independent from the modeled arterial length.

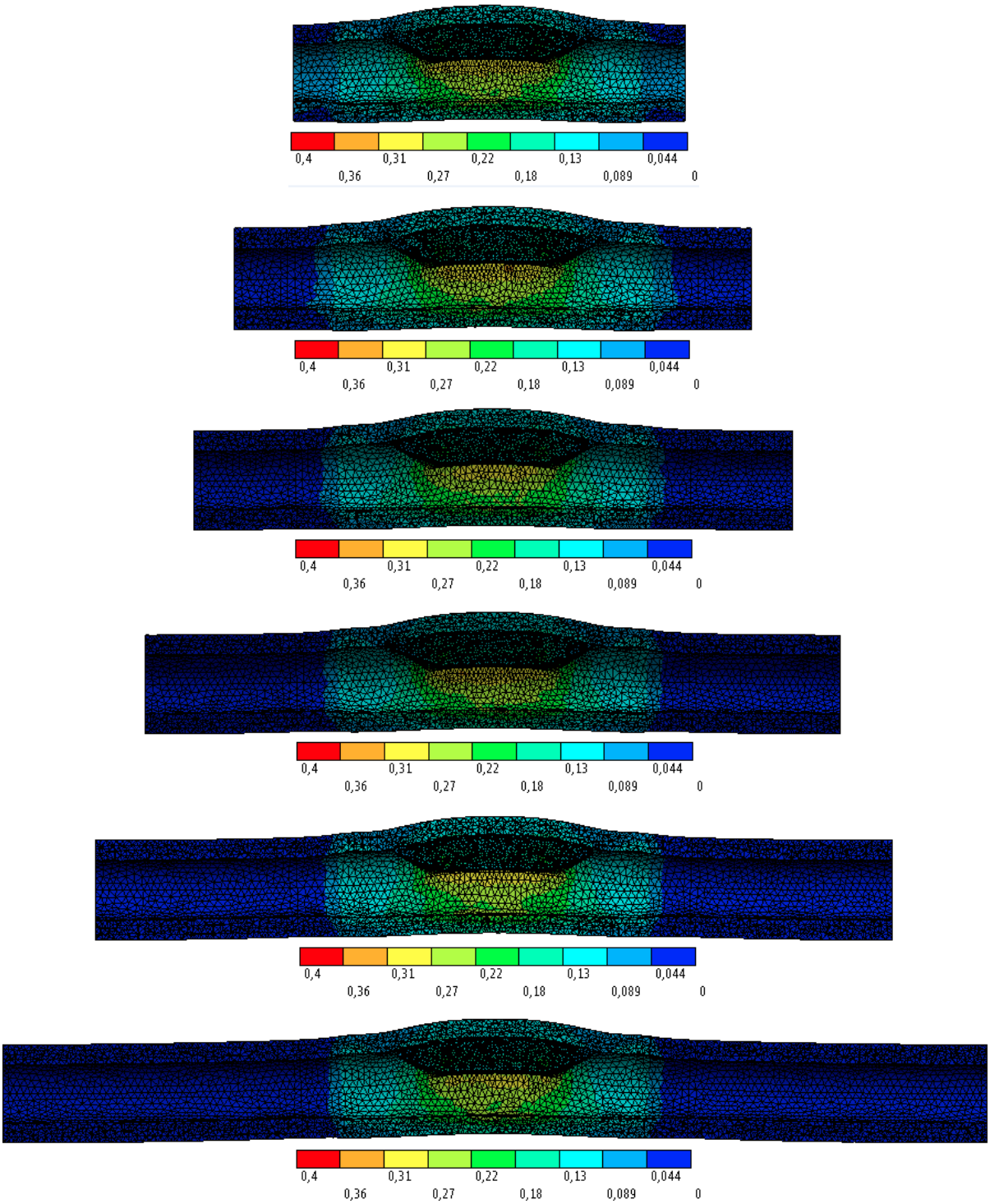

Figure A. 2: Plastic strain distribution along cross-sections of stenosed arteries modeled of different lengths: 20, 25, 30, 35, 40 and 50 mm.

A.3. MESH SENSITIVITY STUDY (GENERIC GEOMETRY)

The artery and the plaque were meshed by 4-node hybrid solid elements in Ansys workbench. These elements have a linear displacement and a hydrostatic pressure behavior. To avoid volumetric locking, elements with mixed u-P formulations were implemented to enhance accuracy within our simulations.

[Figure A. 3] presents the variation of the total strain energy at max balloon inflation and the result file size with respect to different element sizes for the artery and the plaque separately. Towards limiting the simulation computational costs while keeping a satisfying accuracy, element sizes of 0.25 mm and 0.2 mm were chosen for meshing the artery and the plaque respectively. Sizes were selected in a way to ensure enough elements in the arterial wall thickness and to avoid convergence issues associated to contacts with the balloon. [Figure A. 4] shows the plastic strain distribution along stenosed arteries with different mesh size combinations; their color-maps emphasize the minor impact of mesh density on the results and justify our elements sizes choice in this work.

A

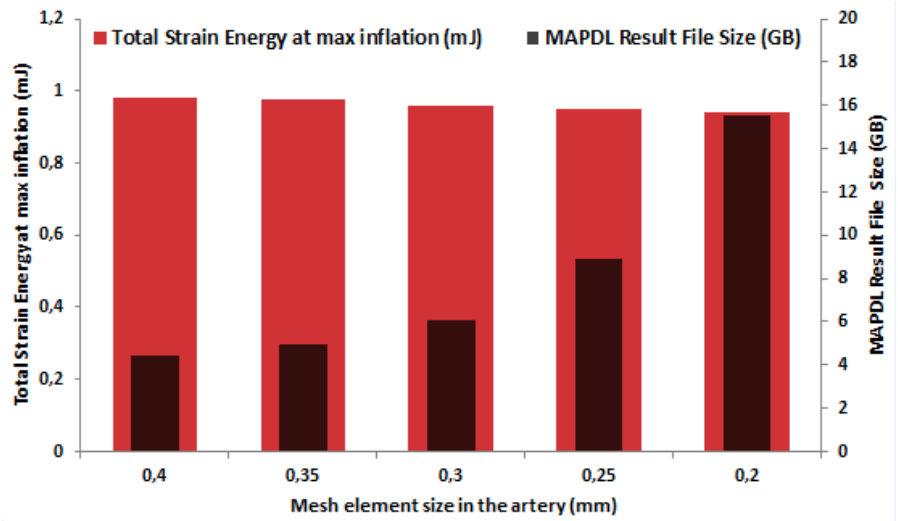

B

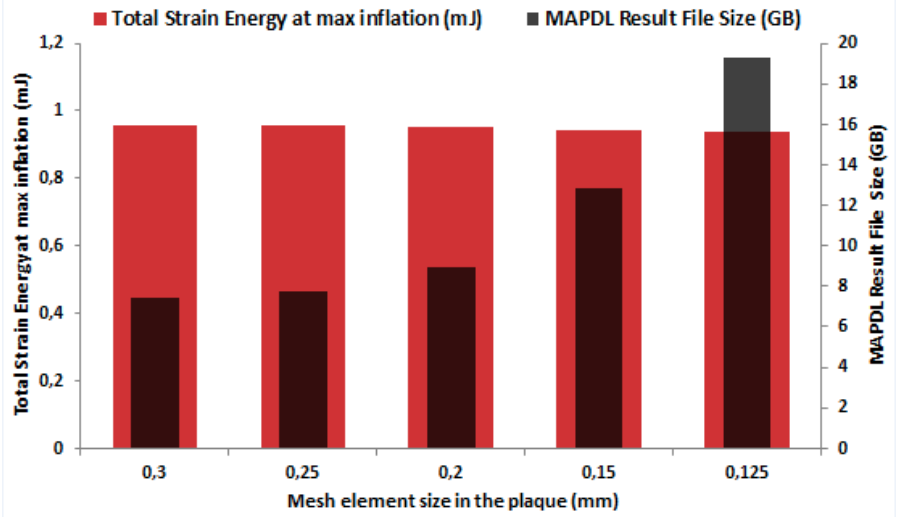

Figure A. 3: Artery (A) and plaque (B) mesh-sizes influences on the total strain energy stored in the diseased arteries at max inflation (diameter of 3 mm), and on their resulting files sizes.

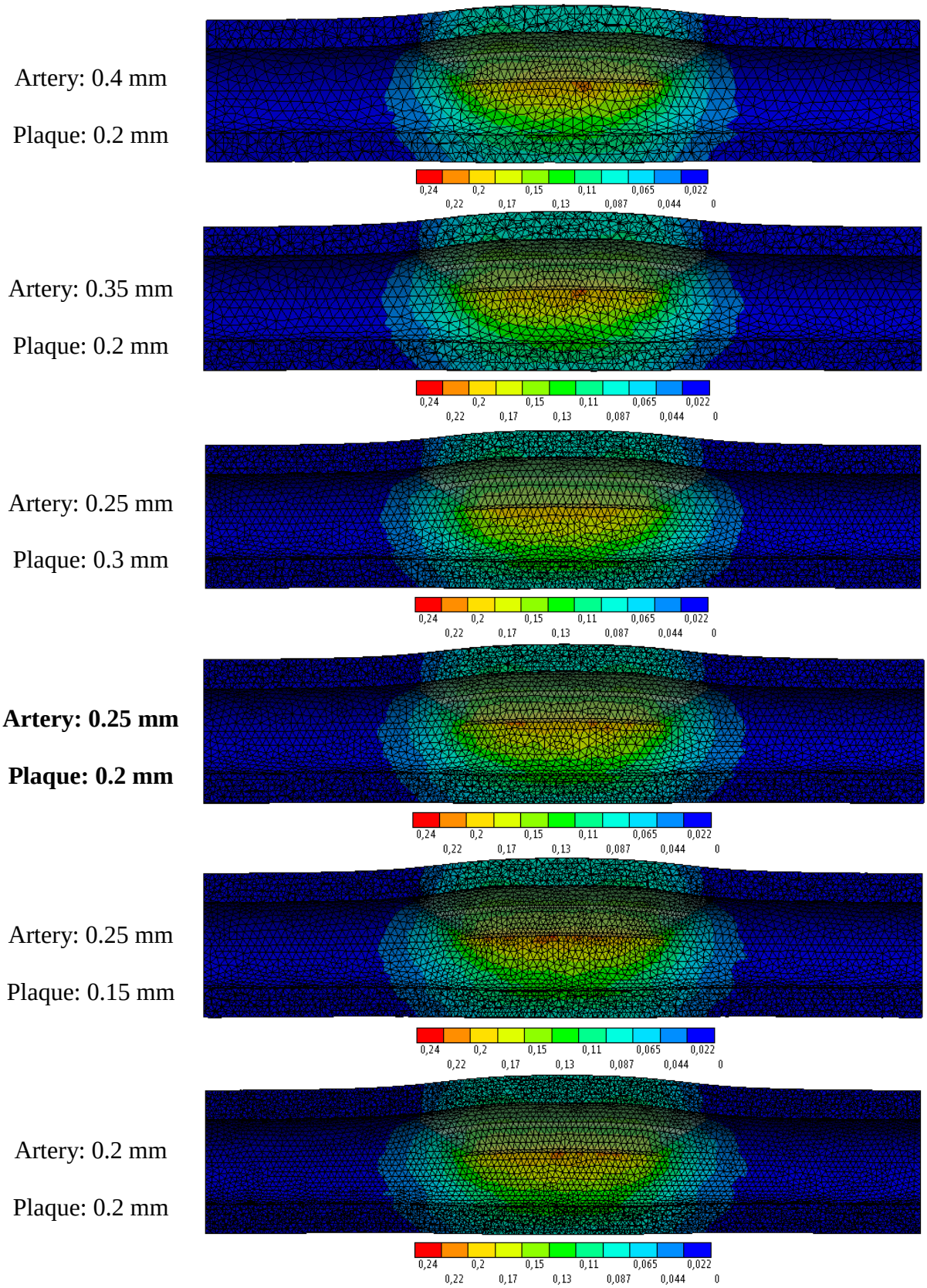

Figure A. 4: Plastic strain distribution along a longitudinal cross-section of the stenosed artery corresponding to different combinations of element sizes used for respectively meshing the artery and the plaque in each simulated case.

A.4. ANSYS MECHANICAL APDL COMMANDS FOR THE EXTRACTION OF INNER SURFACE NODES COORDINATES AT THE THREE POSITIONS OF INTEREST DURING PTA

```
!   Commands inserted into this file will be executed immediately after the
ANSYS /POST1 command.

!    Active UNIT system in Workbench when this object was created:  Metric
(mm, kg, N, s, mV, mA)
!    NOTE:  Any data that requires units (such as mass) is assumed to be in
the consistent solver unit system.
!                See Solving Units in the help system for more information.


/POST1
SET,2       ! Step at max balloon inflation
UPCOORD, 1   ! Update coordinates of the active set of nodes based on the
current displacements; full displacement value will be added to each node

! At max balloon inflation

! ALLSEL
CMSEL,S,inner
*GET,num_nodes,NODE,0,COUNT  !Get the number of nodes
/com, num_nodes=%num_nodes%
*GET,node_,NODE,0,NUM,MIN    !Get label of the first node
*CFOPEN,NewCoordMax,txt
*DO,i,1,num_nodes,1
! Define some parameters
*GET,nx_,NODE,node_,LOC,X
*GET,ny_,NODE,node_,LOC,Y
*GET,nz_,NODE,node_,LOC,Z
! Write line
*VWRITE,node_,nx_,ny_,nz_
(F8.0,',',E14.6,',',E14.6,',',E14.6)
! Select the next node
*GET,node_,NODE,node_,NXTH
*ENDDO
*CFCLOSE

/POST1
SET,2        ! Step at max balloon inflation
UPCOORD, -1   ! Update coordinates of the active set of nodes based on the
current displacements; full displacement value will be subtracted from each
node

! Before balloon inflation

! ALLSEL
CMSEL,S,inner
*GET,num_nodes,NODE,0,COUNT  !Get the number of nodes
/com, num_nodes=%num_nodes%
*GET,node_,NODE,0,NUM,MIN    !Get label of the first node
*CFOPEN,NewCoordInitial,txt
*DO,i,1,num_nodes,1
```

```
! Define some parameters
*GET,nx_,NODE,node_,LOC,X
*GET,ny_,NODE,node_,LOC,Y
*GET,nz_,NODE,node_,LOC,Z
! Write line
*VWRITE,node_,nx_,ny_,nz_
(F8.0,',',E14.6,',',E14.6,',',E14.6)
! Select the next node
*GET,node_,NODE,node_,NXTH
*ENDDO
*CFCLOSE

/POST1
SET,LAST        ! Step after balloon deflation
UPCOORD, 1

! After balloon deflation

! ALLSEL
CMSEL,S,inner
*GET,num_nodes,NODE,0,COUNT  !Get the number of nodes
/com, num_nodes=%num_nodes%
*GET,node_,NODE,0,NUM,MIN    !Get label of the first node
*CFOPEN,NewCoordLast,txt
*DO,i,1,num_nodes,1
! Define some parameters
*GET,nx_,NODE,node_,LOC,X
*GET,ny_,NODE,node_,LOC,Y
*GET,nz_,NODE,node_,LOC,Z
! Write line
*VWRITE,node_,nx_,ny_,nz_
(F8.0,',',E14.6,',',E14.6,',',E14.6)
! Select the next node
*GET,node_,NODE,node_,NXTH
*ENDDO
*CFCLOSE
```

A.5. POST-PROCESSING OF SIMULATION RESULTS

PART I

C++ script applied for creating VTK files (corresponding to stenosed arteries inner surfaces at different states during the PTA simulation) from their respective elements connectivity data and nodes coordinates. We thank Nicolas Courtial from LTSI lab for his support on VTK files format.

```
#include <iostream>
#include <fstream>

#include <vector>
#include <map>
#include <set>

#include <boost/algorithm/string.hpp>

int nbColumnsInCellFile = 9;
int startColumnInCellFile = 5;
int endColumnInCellFile = 7;

void extractConnectivityData(const std::string path_,
std::vector<std::vector<int>>& cells_, std::set<int>& usedIdx_);
void extractPointDatas(const std::string path_, std::map<int,
std::vector<float>>& points_, std::map<int, int>& idxTable_, const
std::set<int>& usedIdx_);

void initOutputFile(std::ofstream& ofs);
void addPointsToOutputFile(std::ofstream& ofs, const std::map<int,
std::vector<float>>& points_);
void addCellsToOutputFile(std::ofstream& ofs, const
std::vector<std::vector<int>>& cells_, const std::map<int, int>&
idxTable_);
void addColourToFile(std::ofstream& ofs, int points_);
void addNormalsToFile(std::ofstream& ofs, int points_);

namespace ltsi {
      namespace StringUtils {
            void splitString(const std::string& str_,
std::vector<std::string> &res_, const std::string& separator, bool
noEmptyVals_ = false);
            void removeSpaces(std::vector<std::string> &input_);
            void removeSpaces(std::string &str_);
      }
}


int main(int argc, char **argv)
{
      if (argc != 4) {
            std::cout << "Wrong usage:\n"
                  << argv[0] << "\n"
                  << "\t - CoordsFile.txt \n"
                  << "\t - ConnectivityTable.txt \n"
                  << "\t - OutputFileName \n";
            return -1;
      }
```

```
	std::string CoordsFile = argv[1];
	std::string ConnectivityTable = argv[2];
	std::string outputPath = argv[3];

	std::ofstream ofs;
	ofs.open(outputPath);

	std::set<int> usedIdx;
	std::vector<std::vector<int>> cells;
	std::map<int, std::vector<float>> points;
	std::map<int, int> pointTables;

	std::cout << "Extracting connectivity Data ";
	extractConnectivityData(ConnectivityTable, cells, usedIdx); std::cout
<<"\tDone! " << std::endl;

	std::cout << "Extracting Point Data ";
	extractPointDatas(CoordsFile, points, pointTables, usedIdx);
std::cout << "\tDone! " << std::endl;

	std::cout << pointTables.size() << std::endl;

	initOutputFile(ofs);
	std::cout << "Adding Points to output ";
	addPointsToOutputFile(ofs, points); std::cout << "\tDone! " <<
std::endl;

	std::cout << "Adding Cells to output ";
	addCellsToOutputFile(ofs, cells, pointTables); std::cout << "\tDone!
" << std::endl;

	//These two functions could be removed
	addColourToFile(ofs, points.size());
	addNormalsToFile(ofs, points.size());

	ofs.close();
	return 0;
}

void initOutputFile(std::ofstream& ofs) {
	ofs << "# vtk DataFile Version 4.1" << std::endl;
	ofs << "vtk output" << std::endl;
	ofs << "ASCII" << std::endl;
	ofs << "DATASET POLYDATA" << std::endl;

}

void addPointsToOutputFile(std::ofstream & ofs, const std::map<int,
std::vector<float>>& points_)
{
	ofs << "POINTS " << points_.size() << " float" << std::endl;

	int count(0);
	for (auto item : points_) {
		for (int i(0); i < 3; i++)
			ofs << item.second.at(i) << " ";

		count = (count + 1) % 3;
		if (count == 0)
			ofs << std::endl;
```

```
	}
	ofs << std::endl;
}

void addCellsToOutputFile(std::ofstream & ofs, const
std::vector<std::vector<int>>& cells_, const std::map<int, int>& idxTable_)
{
	ofs << "POLYGONS " << cells_.size() << " " << 4 * cells_.size() <<
std::endl;
	for (auto cell : cells_) {
		ofs << 3 << " ";
		for (auto item : cell) {
			if (idxTable_.count(item))
				ofs << idxTable_.at(item) << " ";
			else
				std::cout << "Can't find pt " << item << std::endl;
		}
		ofs << std::endl;
	}
}

void addColourToFile(std::ofstream & ofs, int nbPoints_)
{
	ofs << "POINT_DATA " << nbPoints_ << std::endl;
	ofs << "COLOR_SCALARS scalars 3 " << std::endl;

	for (int idx(0); idx < nbPoints_; idx++) {
		ofs << "0.235294 0.588235 0.901961 ";
		if (idx % 2 == 1)
			ofs << std::endl;
	}
	ofs << std::endl;
}

void addNormalsToFile(std::ofstream & ofs, int nbPoints_)
{
	ofs << "NORMALS Normals float" << std::endl;
	for (int idx(0); idx < nbPoints_; idx++) {
		ofs << "1 0 0 ";
		if (idx % 3 == 2)
			ofs << std::endl;
	}
	ofs << std::endl;
}

void extractConnectivityData(const std::string path_,
std::vector<std::vector<int>>& cells_, std::set<int>& usedIdx_)
{
	std::ifstream ifs;
	ifs.open(path_);
	if (!ifs.good())
		return;

	std::string buffer;
	std::vector<std::string> splitString;

	while (ifs.good()) {
		std::getline(ifs, buffer);
		ltsi::StringUtils::splitString(buffer, splitString, " ", true);
		if (splitString.size() != nbColumnsInCellFile)
			continue;
```

```
            std::vector<int> currcell(3);
            for (int i(startColumnInCellFile); i < endColumnInCellFile + 1;
i++) {
                  auto currIdx = std::stoi(splitString.at(i));

                  currcell[i - startColumnInCellFile] = currIdx;
                  usedIdx_.insert(currIdx);
            }
            cells_.push_back(currcell);
      }
}

void extractPointDatas(const std::string path_, std::map<int,
std::vector<float>>& points_, std::map<int, int>& idxTable_, const
std::set<int>& usedIdx_)
{
      std::ifstream ifs;
      ifs.open(path_);
      if (!ifs.good())
            return;

      std::string buffer;
      std::vector<std::string> splitString;


      while (ifs.good()) {
            std::getline(ifs, buffer);
            ltsi::StringUtils::splitString(buffer, splitString, ",", true);
            if (splitString.empty() || splitString.size() % 4 != 0)
                  continue;

            int idx = std::stoi(splitString.at(0));
            if (usedIdx_.count(idx)) {
                  std::vector<float> currPoint(3);
                  for (int i(0); i < 3; i++)
                        currPoint[i] = std::stof(splitString.at(i + 1));

                  points_[idx] = currPoint;
                  idxTable_[idx] = idxTable_.size();
            }
      }
}

//Copied functions from personal dependancy
namespace ltsi {
      namespace StringUtils {
            void splitString(const std::string& str_,
std::vector<std::string> &res_, const std::string& separator, bool
noEmptyVals_) {
                  res_.clear();
                  boost::split(res_, str_, boost::is_any_of(separator));
                  if (res_.back() == "")
                        res_.pop_back();

                  if (noEmptyVals_) {
                        auto copy = res_;
                        res_.clear();
                        removeSpaces(copy);
                        for (auto item : copy)
                              if (!item.empty())
```

```
                                    res_.push_back(item);
                        }
                }

                void removeSpaces(std::vector<std::string> &input_) {
                        for (auto &item : input_)
                                removeSpaces(item);
                }

                void removeSpaces(std::string &str_) {
                        while (!str_.empty() && str_.front() == ' ')
                                str_ = str_.substr(1, str_.length());
                        while (!str_.empty() && str_.back() == ' ')
                                str_ = str_.substr(0, str_.length() - 1);
                }
        }
}
```

PART II

MATLAB script applied for extracting centerlines and max-inscribed-spheres from the reconstructed inner luminal geometries using VMTK, and then computing their ERR values.

```
%% ---------------------------- Read files ---------------------------------
----------

DataDir = ['C:\Users\Bernard\Desktop\DemoW\matlab\input_files\'];

filename_Last = 'Last'; % without vtk extension
filename_Max = 'Max'; % without vtk extension

nb_pt = 200;
vessel_length = 25;

%% ----------------------------Extract Centerline -------------------------
------------

[centerlines_Last]=Extract_CL(DataDir, filename_Last);
centerlines_Last = sortrows(centerlines_Last,3);
write_vtk_points(centerlines_Last(:,1:3),[DataDir,'CL_Last.vtk']);

[centerlines_Max]=Extract_CL(DataDir, filename_Max);
centerlines_Max = sortrows(centerlines_Max,3);
write_vtk_points(centerlines_Max(:,1:3),[DataDir,'CL_Max.vtk']);

%% ---------------------------- Same CL discretization --------------------
-------------

[ curv0 ] = Define_curv_intep(nb_pt, vessel_length  );

[AbsCurvRadius_Max ] = Interpolation_CL( centerlines_Max,
curv0,[DataDir,'AbsCurvRadius_Max.txt']);

[AbsCurvRadius_Last ] = Interpolation_CL( centerlines_Last, curv0,
[DataDir,'AbsCurvRadius_Last.txt']);
```

```
%plot(AbsCurvRadius_Max(:,1),AbsCurvRadius_Max(:,2),'+',AbsCurvRadius_Last(
:,1),AbsCurvRadius_Last(:,2),'o' );

for i=1:1:nb_pt
       Recoil_ratio(i)= (AbsCurvRadius_Max(i,2)-
AbsCurvRadius_Last(i,2))/AbsCurvRadius_Max(i,2);
end

% Sauvegarde
fid = fopen([DataDir,'RecoilRatio.txt'],'wt');
fprintf(fid,'Curvilinear abscissa    Recoil ratio  \n');
for i=1:1:size(AbsCurvRadius_Max,1)
   fprintf(fid,'%f %f \n', AbsCurvRadius_Max(i,1), Recoil_ratio(i) );
end
fclose(fid);


plot(AbsCurvRadius_Max(:,1),Recoil_ratio,'-')

Max_recoil_ratio = max(Recoil_ratio)

localisation_max_recoil = AbsCurvRadius_Last(find(Recoil_ratio ==
Max_recoil_ratio),1)/vessel_length

fid = fopen([DataDir,'Info_RecoilRatio.txt'],'wt');
fprintf(fid,'Last value of the recoil ratio: %f \n', Max_recoil_ratio );
fprintf(fid,'Position of Last value of the recoil ratio : %f of the vessel
total lenght \n', localisation_max_recoil );
```

A.6. SCRIPT FOR ASSIGNING SPECIFIC MATERIAL INDICES FOR ELEMENTS WITHIN A SINGLE STENOSED ARTERY MODEL ACCORDING TO THEIR RESPECTIVE GEOMETRIC POSITIONS

```
clear;
%%
% % read point coords
 p
=loadtxt('ds.dat','skipline',32,'convert','force','nlines',179196,'verbose'
,'off');
 coord = reshape(p,[179196,4]);
% % read ele connectivity
 e
=loadtxt('ds.dat','skipline',219983,'convert','force','nlines',773230,'verb
ose','off');
 ele = reshape(e,[773230,15]);
%
% % computer centeroid of each element
% % tetra : node iD  is 12 13 14 15
 ele_c =
[(coord(ele(:,12),2)+coord(ele(:,13),2)+coord(ele(:,14),2)+coord(ele(:,15),
2))/4, ...

(coord(ele(:,12),3)+coord(ele(:,13),3)+coord(ele(:,14),3)+coord(ele(:,15),3
))/4, ...

(coord(ele(:,12),4)+coord(ele(:,13),4)+coord(ele(:,14),4)+coord(ele(:,15),4
))/4];
%
 save ele_c ele_c
%%
 load('ele_c.mat')
[F,V] = stlread('BinaryArtery.stl');
IN = inpolyhedron(F,V,ele_c,'TOL',1);
save IN IN
% % % % fileID = fopen('o.txt','w');
% % % % for i = 1:length(ele_c(:,1))
    % % % % if IN(i)==0
        % % % % fprintf(fileID,'%f, %f,
%f\n',ele_c(i,1),ele_c(i,2),ele_c(i,3));
    % % % % end
% % % % end
% % % % fclose(fileID);
% %%
% write apdl command to change material ID
fileID = fopen('matchange.inp','w');
for i = 1:length(ele_c(:,1))
    if IN(i)==0
        fprintf(fileID,'mpchg, %d, %d\n',8,i);
    else
        fprintf(fileID,'mpchg, %d, %d\n',2,i);
    end
end

fclose(fileID);
```

A.7. MESH SENSITIVITY STUDY (PATIENT-SPECIFIC GEOMETRY)

The stenosed artery was meshed by the same element type previously implemented within the generic model with mixed u-P formulations as well, for the same reason of avoiding volumetric locking and thus enhancing accuracy within the simulations. In the following mesh size sensitivity analysis, the balloon was simulated to a sizing of 5 mm within the patient-specific lipidic stenosis case.

[Figure A. 5] presents the variation of the total strain energy at max balloon inflation and the simulation result file size with respect to different element sizes within the stenosed artery. Towards minimizing the simulation computational costs while keeping a satisfying accuracy, element sizes of 0.28 mm and 0.24 mm were respectively chosen to mesh the entire geometry and the stenosed inner surface in contact with the balloon during inflation. Enough elements in the arterial wall thickness were ensured with the selected mesh sizes. [Figure A. 6] shows the plastic strain distribution along the stenosed artery with the different mesh sizes; their color-maps emphasize the minor impact of mesh density on the results and also justify our elements sizes choice for the simulations of this patient.

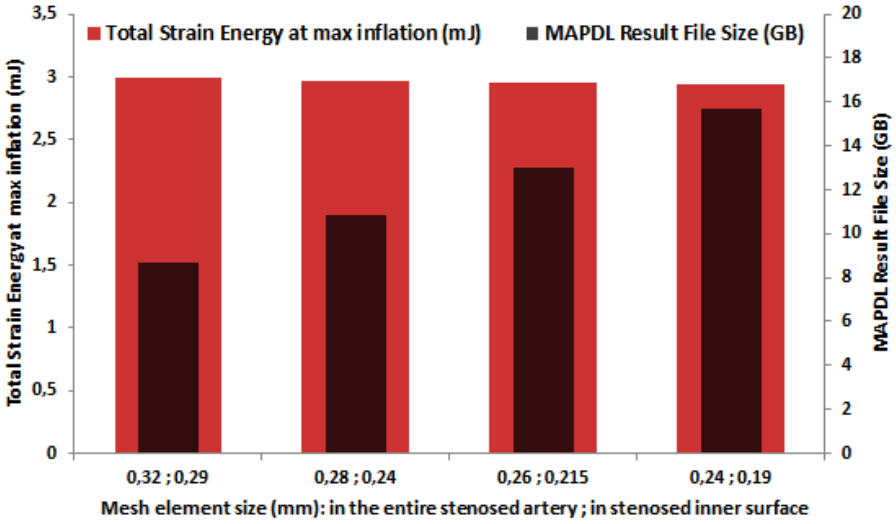

Figure A. 5: Mesh-sizes influence on the total strain energy stored in the diseased arteries at max inflation (diameter of 5 mm), and on their resulting files sizes.

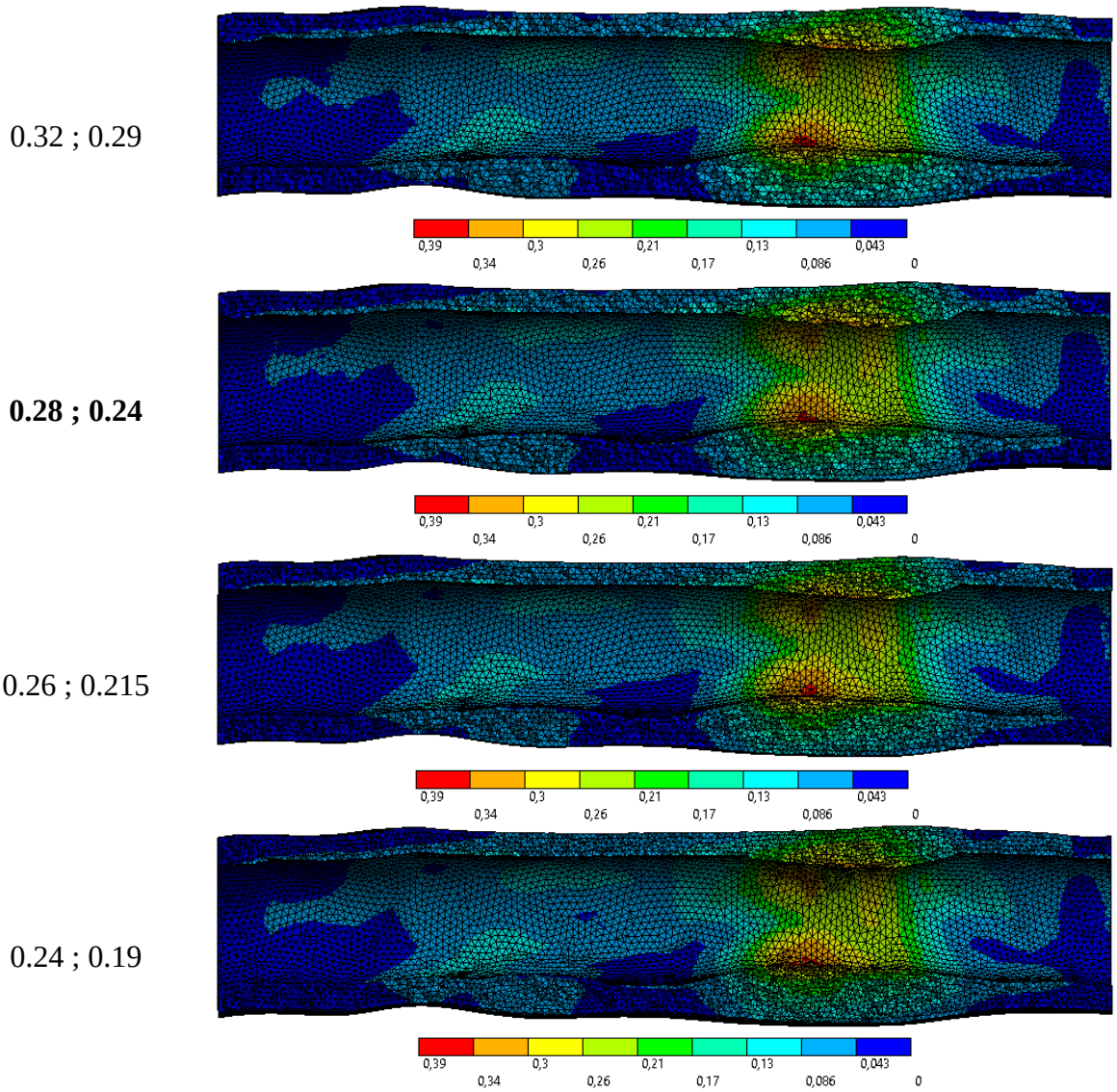

Figure A. 6: Plastic strain distribution along a longitudinal cross-section of the patient-specific geometry corresponding to different element sizes used for meshing the stenosed artery in each simulated case.

BIBLIOGRAPHY

[1] P. J. Kumar and M. Clark, *Textbook of clinical medicine*. Saunders (London), 2002.

[2] R. M. Berne, S. R. Geiger, and et al., "Handbook of physiology: a critical, comprehensive presentation of physiological knowledge and concepts. The cardiovascular system. Formerly Section 2: Circulation. The heart.," *American Physiological Society*, 1979.

[3] T. C. Gasser, R. W. Ogden, and G. A. Holzapfel, "Hyperelastic modelling of arterial layers with distributed collagen fibre orientations," *J. R. Soc. interface*, vol. 3, no. 6, pp. 15–35, 2006.

[4] Z. Teng, D. Tang, J. Zheng, P. K. Woodard, and A. H. Hoffman, "An experimental study on the ultimate strength of the adventitia and media of human atherosclerotic carotid arteries in circumferential and axial directions," *J. Biomech.*, vol. 42, no. 15, pp. 2535–2539, 2009.

[5] I. Pericevic, C. Lally, D. Toner, and D. J. Kelly, "The influence of plaque composition on underlying arterial wall stress during stent expansion: The case for lesion-specific stents," *Med. Eng. Phys.*, vol. 31, no. 4, pp. 428–433, 2009.

[6] S. Z. Zhao *et al.*, "Blood flow and vessel mechanics in a physiologically realistic model of a human carotid arterial bifurcation," *J. Biomech.*, vol. 33, p. 975_984, 2000.

[7] P. Constantinides, "Plaque fissures in human coronary thrombosis," *J. Atheroscler. Res.*, vol. 6, no. 1, pp. 1–17, 1966.

[8] A. C. Newby, "Dual Role of Matrix Metalloproteinases (Matrixins) in Intimal Thickening and Atherosclerotic Plaque Rupture," *Physiol. Rev.*, vol. 85, pp. 1–31, 2005.

[9] M. J. Davies, "The pathophysiology of acute coronary syndromes," *Heart*, vol. 83, pp. 361–366, 2000.

[10] J. R. Laird, "Limitations of percutaneous transluminal angioplasty and stenting for the treatment of disease of the superficial femoral and popliteal arteries," *J. Endovasc. Ther.*, vol. 13, no. 2, pp. 1130–1140, 2006.

[11] E. M. Cunnane, H. E. Barrett, E. G. Kavanagh, R. Mongrain, and M. T. Walsh, "The influence of composition and location on the toughness of human atherosclerotic femoral plaque tissue," *Acta Biomater.*, vol. 31, pp. 264–275, 2016.

[12] "The top 10 causes of death," 2018. [Online]. Available: https://www.who.int/en/news-room/fact-sheets/detail/the-top-10-causes-of-death/ on 29-08-2020.

[13] W. Insull, "The Pathology of atherosclerosis: Plaque development and plaque responses to medical treatment," *Am. J. Med.*, vol. 122, no. 1, pp. S3–S14, 2009.

[14] Z. Xia, F. Ju, and K. Sasaki, "A general finite element analysis method for balloon expandable stents based on repeated unit cell (RUC) model," *Finite Elem. Anal. Des.*, vol. 43, pp. 649–658, 2007.

[15] S. N. D. Chua, B. J. Macdonald, and M. S. J. Hashmi, "Finite element simulation of slotted tube (stent) with the presence of plaque and artery by balloon expansion," *J. Mater. Process. Technol.*, vol. 155–156, pp. 1772–1779, 2004.

[16] M. H. Kural, M. Cai, D. Tang, T. Gwyther, J. Zheng, and K. L. Billiar, "Planar biaxial characterization of diseased human coronary and carotid arteries for computational modeling,"

J. Biomech., vol. 45, no. 5, pp. 790–798, 2012.

[17] A. Nagaraj *et al.*, "Porcine carotid arterial material property alterations with induced atheroma : an in vivo study," *Med. Eng. Phys.*, vol. 27, pp. 147–156, 2005.

[18] T. Shoji *et al.*, "Arterial stiffness predicts cardiovascular death independent of arterial thickness in a cohort of hemodialysis patients," *Atherosclerosis*, vol. 210, no. 1, pp. 145–149, 2010.

[19] M. W. Claridge, G. R. Bate, P. R. Hoskins, D. J. Adam, A. W. Bradbury, and A. B. Wilmink, "Measurement of arterial stiffness in subjects with vascular disease: Are vessel wall changes more sensitive than increase in intima – media thickness?," *Atherosclerosis*, vol. 205, pp. 477–480, 2009.

[20] Y. S. Chatzizisis and G. D. Giannoglou, "Coronary hemodynamics and atherosclerotic wall stiffness: A vicious cycle," *Med. Hypotheses*, vol. 69, pp. 349–355, 2007.

[21] S. J. George and J. Johnson, "Atherosclerosis: Molecular and Cellular Mechanisms," in *Wiley-VCH Verlag GmbH & Co. KGaA, Weinheim*, 2010.

[22] Z. Y. Li, S. Howarth, R. A. Trivedi, J. M. U-King-Im, and et al, "Stress analysis of carotid plaque rupture based on in vivo high resolution MRI," *J. Biomech.*, vol. 39, no. 14, pp. 2611–2622, 2006.

[23] D. Tang *et al.*, "Sites of Rupture in Human Atherosclerotic Carotid Plaques Are Associated With High Structural Stresses An In Vivo MRI-Based 3D Fluid-Structure Interaction Study," *Stroke*, vol. 40, pp. 3258–3263, 2009.

[24] P. Libby, "Molecular bases of the acute coronary syndromes," *Circulation*, vol. 91, pp. 2844–2850, 1995.

[25] G. Sommer, "Mechanical Properties of Healthy and Diseased Human Arteries and Related Material Modeling," PhD thesis, TU Graz, Graz, Austria, 2008.

[26] M. R. Jaff, B. D. MacNeill, and K. Rosenfield, "Angiography of the Aorta and Peripheral Arteries," in *Grossman's Cardiac Catheterization, Angiography, and Intervention*, 7th ed., D. S. Baim, Ed. 2005, pp. 254–280.

[27] J. Grimm, S. Müller-hülsbeck, T. Jahnke, C. Hilbert, J. Brossmann, and M. Heller, "Randomized Study to Compare PTA Alone versus PTA with Palmaz Stent Placement for Femoropopliteal Lesions," *J. Vasc. Interv. Radiol.*, vol. 12, pp. 935–941, 2001.

[28] "U.S. Department of Heath & Human Services," in *Chartbook on Cardiovascular, Lung and Blood Diseases.*, Bethesda, MD: NIH, NHLBI, 1994.

[29] R. D. Abbott, F. N. Brand, and W. B. Kannel, "Epidemiology of some peripheral arterial findings in diabetic men and women: experiences from the Framingham Study," *Am. J. Med.*, vol. 88, pp. 376–381, 1990.

[30] C. M. Gross, J. Kramer, J. Waigand, F. C. Luft, and R. Dietz, "Relation between arteriosclerosis in the coronary and renal arteries," *Am. J. Cardiol.*, vol. 80, pp. 1478–1481, 1997.

[31] J. I. Weitz, J. Byrne, G. P. Clagett, and et al., "Diagnosis and treatment of chronic arterial insufficiency of the lower extremities: a critical review," *Circulation*, vol. 94, pp. 3026–3049, 1996.

[32] M. Kornitzer, M. Dramaix, J. Sobolski, S. Degre, and G. De Backer, "Ankle/arm pressure index in asymptomatic middle-aged males: an independent predictor of ten-year coronary heart disease mortality," *Angiology*, vol. 46, pp. 211–219, 1995.

[33] T. W. Rooke and P. W. Wennberg, "Diagnosis and management of diseases of the peripheral

arteries and veins," in *V. Fuster, R. A. O'Rourke, R. A. Walsh, P. Poole-Wilson, Eds. Hurst's The Heart*, 12th ed., New York, NY: McGraw-Hill, 2007.

[34] M. M. Brown, J. Rogers, and J. M. Bland, "Endovascular versus surgical treatment in patients with carotid stenosis in the Carotid and Vertebral Artery Transluminal Angioplasty Study (CAVATAS): A randomised trial," *Lancet*, vol. 357, no. 9270, pp. 1729–1737, 2001.

[35] M. Roffi, D. Mukherjee, and D. G. Clair, "Carotid artery stenting vs . endarterectomy," *Eur. Hear. J.*, vol. 30, pp. 2693–2704, 2009.

[36] R. D. Safian *et al.*, "Comparison of coronary angioplasty with compliant and noncompliant balloons (the angioplasty compliance trial)," *Am. J. Cardiol.*, vol. 76, no. 7, pp. 518–520, 1995.

[37] F. Y. Tsai *et al.*, "Percutaneous transluminal angioplasty of the carotid artery," *Am. J. Neuroradiol.*, vol. 7, no. 2, pp. 349–358, 1986.

[38] T. Zeller, S. Schmitmeier, G. Tepe, and A. Rastan, "Drug- coated balloons in the lower limb," *J. Cardiovasc. Surg. (Torino).*, no. 52, pp. 235–243, 2011.

[39] L. A. Garcia and S. P. Lyden, "Atherectomy for infrainguinal peripheral artery disease," *J. Endovasc. Ther.*, vol. 16, pp. 105–115, 2009.

[40] A. Kansal, C. A. Long, M. R. Patel, and W. S. Jones, "Endovascular treatment of femoro-popliteal lesions," *Clin. Cardiol.*, vol. 42, no. 1, pp. 175–183, 2019.

[41] J. L. Kang, V. I. Patel, M. F. Conrad, G. M. Lamuraglia, T. K. Chung, and R. P. Cambria, "Common femoral artery occlusive disease : Contemporary results following surgical endarterectomy," *J. Vasc. Surg.*, vol. 48, no. 4, pp. 872–878, 2008.

[42] D. Mukherjee and T. Inahara, "Endarterectomy as the procedure of choice for atherosclerotic occlusive lesions of the common femoral-artery," *Am. J. Surg.*, vol. 157, pp. 498–500, 1989.

[43] A. Kechagias, K. Ylonen, and F. Biancari, "Long-term outcome after isolated endarterectomy of the femoral bifurcation," *World J. Surg.*, vol. 32, pp. 51–54, 2008.

[44] M. E. Springhorn, M. Kinney, F. N. Littooy, C. Saletta, and H. P. Greisler, "Inflow atherosclerotic disease localized to the common femoral artery: treatment and outcome," *Ann. Vasc. Surg.*, vol. 5, pp. 234–240, 1991.

[45] L. Norgren, W. R. Hiatt, J. A. Dormandy, M. R. Nehler, K. A. Harris, and F. G. Fowkes, "Group TIW, Inter-society consensus for the management of peripheral arterial disease (TASC II)," *J. Vasc. Surg.*, vol. 45, no. Suppl S, pp. S5–S67, 2007.

[46] B. . Nguyen, R. L. Amdur, M. Abugideiri, and et al, "Postoperative complications after common femoral endarterectomy," *J. Vasc. Surg.*, vol. 61, pp. 1489–1494, 2015.

[47] S. Kuy, A. Dua, S. Desai, and et al, "Surgical site infections after lower extremity revascularization procedures involving groin incisions.," *Ann. Vasc. Surg.*, vol. 28, no. 53–58, 2014.

[48] H. Krankenberg, M. Schluter, H. . Steinkamp, and et al, "Nitinol stent implantation versus percutaneous transluminal angioplasty in superficial femoral artery lesions up to 10 cm in length: the femoral artery stenting trial (FAST).," *Circulation*, vol. 116, pp. 285–292, 2007.

[49] R. R. Saxon, M. D. Dake, R. L. Volgelzang, and et al, "Randomized, multicenter study comparing expanded polytetrafluoroethylene-covered endoprosthesis placement with percutaneous transluminal angioplasty in the treatment of superficial femoral artery occlusive disease.," *J. Vasc. Interv. Radiol.*, vol. 19, pp. 823–832, 2008.

[50] P. P. Goodney, A. W. Beck, J. Nagle, and et al, "National trends in lower extremity bypass surgery, endovascular interventions, and major amputations.," *J. Vasc. Surg.*, vol. 50, pp. 54–

60, 2009.

[51] M. R. Jaff *et al.*, “An Update on Methods for Revascularization and Expansion of the TASC Lesion Classification to Include Below-the-Knee Arteries: A Supplement to the Inter-Society Consensus for the Management of Peripheral Arterial Disease (TASC II),” *Vasc. Med.*, vol. 20, no. 5, pp. 465–478, 2015.

[52] D. Halpin, Y. Erben, S. Jayasuriya, B. Cua, S. Jhamnani, and C. Mena-Hurtado, “Management of Isolated Atherosclerotic Stenosis of the Common Femoral Artery: A Review of the Literature,” *Vasc. Endovascular Surg.*, vol. 51, no. 4, pp. 220–227, 2017.

[53] G. Wong, S. Lahsaei, J. Aoun, and L. A. Garcia, “Management of common femoral artery occlusive disease: A review of endovascular treatment strategies and outcomes,” *Catheter. Cardiovasc. Interv.*, vol. 93, no. 3, pp. 514–521, 2019.

[54] J. A. Dormandy and R. B. Rutherford, “Management of peripheral arterial disease (PAD). TASC working group. Trans Atlantic inter society consensus (TASC).,” *J. Vasc. Surg.*, vol. 31, pp. S1–S296, 2000.

[55] M. Mehta, Y. Zhou, P. S. Paty, and et al, “Percutaneous common femoral artery interventions using angioplasty, atherectomy, and stenting.,” *J. Vasc. Surg.*, vol. 64, pp. 369–379, 2016.

[56] F. R. Bonvini, A. Rastan, S. Sixt, and et al, “Endovascular treatment of common femoral artery disease: Medium-term outcomes of 360 consecutive procedures.,” *J. Am. Coll. Cardiol.*, vol. 58, pp. 792–798, 2011.

[57] R. F. Bonvini, A. Rastan, S. Sixt, and et al, “Angioplasty and provisional stent treatment of common femoral artery lesions,” *J. Am. Coll. Cardiol. amer*, vol. 24, pp. 175–183, 2013.

[58] J. J. Siracuse, K. Van Orden, J. A. Kalish, and et al, “Endovascular treatment of the common femoral artery in the vascular quality initiative.,” *J. Vasc. Surg.*, vol. 65, pp. 1039–1046, 2017.

[59] R. Davies, W. Adair, A. Bolia, and et al, “Endovascular treatment of the common femoral artery for limb ischemia.,” *Vasc. Endovascular Surg.*, vol. 47, pp. 639–644, 2013.

[60] J. Guo, L. Guo, Z. Tong, X. Gao, Z. Wang, and Y. Gu, “Directional atherectomy is associated with better long term efficiency compared to angioplasty for common femoral artery occlusive disease in Rutherford 2 to 4 patients.,” *Ann. Vasc. Surg.*, vol. 51, pp. 65–71, 2018.

[61] P. B. Dattilo, T. T. Tsai, R. Kevin Rogers, and I. P. Casserly, “Acute and mediumterm outcomes of endovascular therapy of obstructive disease of diverse etiology of the common femoral artery.,” *Catheter. Cardiovasc. Interv.*, vol. 81, pp. 1013–1022, 2013.

[62] L. Azéma, J. M. Davaine, B. Guyomarch, and et al, “Endovascular repair of common femoral artery and concomitant arterial lesions,” *Eur. J. Vasc. Endovasc. Surg.*, vol. 41, no. 787–793, 2011.

[63] C. L. Paris, C. J. White, T. J. Collins, and et al, “Catheter-based therapy of common femoral artery atherosclerotic disease.,” *Vasc. Med.*, vol. 16, pp. 109–112, 2011.

[64] P. O. Thiney, A. Millon, T. Boudjelit, N. Della Schiava, P. Feugier, and P. Lermusiaux, “Angioplasty of the common femoral artery and its bifurcation.,” *Ann. Vasc. Surg.*, vol. 29, pp. 960–967, 2015.

[65] B. Nasr, A. Kaladji, P. A. Vent, and et al., “Long-term results of common femoral artery stenting.,” *Ann. Vasc. Surg.*, vol. 40, pp. 10–12, 2017.

[66] M. Cejna *et al.*, “PTA versus Palmaz stent placement in femoropopliteal artery obstructions: a multicenter prospective randomized study,” *J. Vasc. Interv. Radiol.*, vol. 12, pp. 23–31, 2001.

[67] D. Vroegindeweij, L. D. Vos, A. V. Tielbeek, J. Buth, and H. C. vd Bosch, “Balloon

angioplasty combined with primary stenting versus balloon angioplasty alone in femoropopliteal obstructions: A comparative randomized study," *Cardiovasc. Intervent. Radiol.*, vol. 20, pp. 420–425, 1997.

[68] M. Schillinger *et al.*, "Sustained benefit at 2 years of primary femoropopliteal stenting compared with balloon angioplasty with optional stenting," *Circulation*, vol. 115, pp. 2745–2749, 2007.

[69] S. H. Duda *et al.*, "Drug-eluting and bare nitinol stents for the treatment of atherosclerotic lesions in the superficial femoral artery: long-term results from the SIROCCO trial," *J. Endovasc. Ther.*, vol. 13, pp. 701–710, 2006.

[70] T. Htay and W. Ming Liu, "Drug-eluting stents: a review and update," *Vasc. Health Risk Manag.*, vol. 1, pp. 263–276, 2005.

[71] M. Schier, P. Erne, and T. Resink, "The road to bioabsorbable stents: Reaching clinical reality?," *Cardiovasc. Intervent. Radiol.*, vol. 29, pp. 11–16, 2006.

[72] M. R. Bennett, "In-stent stenosis: Pathology and implications for the development of drug eluting stents," *Heart*, vol. 89, pp. 218–224, 2003.

[73] T. C. Woods and A. R. Marks, "Drug-eluting stents," *Annu. Rev. Med.*, vol. 55, pp. 169–178, 2004.

[74] R. Beyar, "Novel approaches to reduce restenosis," *Ann. N. Y. Acad. Sci.*, vol. 1015, pp. 367–378, 2004.

[75] M. Conti *et al.*, "Patient-specific finite element analysis of popliteal stenting," *Meccanica*, vol. 52, no. 3, pp. 633–644, 2017.

[76] K. Diamantopoulos, A. Katsanos, "Treating Femoropopliteal Disease: Established and Emerging Technologies," *Semin. Intervent. Radiol.*, vol. 31, no. 4, pp. 345–352, 2014.

[77] W. R. Castaneda-zuniga, "Pathophysiology of transluminal angioplasty. In: Improvement of Myocardial Perfusion, edited by J. Meyer, R. Erberl, and H. J. Rupprecht. Boston, MA: Martinus Nijhoff," pp. 138–141, 1985.

[78] C. T. Dotter and M. P. Judkins, "Transluminal treatment of arteriosclerotic obstruction.," *Circulation*, vol. 30, p. 654, 1964.

[79] A. Gruentzig, "Die perkutane Rekanalisation chronischer arterieller Verschlusse (Dotter-Prinzip) mit einem neuen doppellumigen Dilatationskatheter," *ROFO*, vol. 124, pp. 80–86, 1976.

[80] A. Gruentzig, "Perkutane Rekanalisation chronischer arterieller Verschliisse mit einem neuen Dilatationskatheter: Modifikation der Dotter-Technik.," *Dtsch. Medizinische Wochenschrift*, vol. 99, p. 2502, 1974.

[81] A. Gruentzig, A. Senning, and W. Siegenthaler, "Non-operative dilatation of coronary artery stenosis: percutaneous transluminal coronary angioplasty," *N. Engl. J. Med.*, vol. 301, pp. 61–68, 1979.

[82] A. Gruentzig, W. Vetter, B. Meier, U. Kuhlmann, U. Luetolf, and W. Siegenthaler, "Treatment of renovascular hypertension with percutaneous transluminal dilatation of a renal-artery stenosis.," *Lancet*, vol. 1, pp. 801–802, 1978.

[83] F. Mahler, P. Probst, M. Haertel, P. Weidmann, and A. Krneta, "Lasting improvement of renovascular hypertension by transluminal dilatation of atherosclerotic and nonatherosclerotic renal artery stenoses: a follow-up study," *Circulation*, vol. 65, pp. 611–617, 1982.

[84] J. M. Isner and R. V. Fortrin, "Frequency in nonangioplasty patients of morphologic findings

reported in coronary arteries treated with transluminal angioplasty.," *Am. J. Cardiol.*, vol. 51, pp. 689–693, 1983.

[85] R. T. Lyon, V. K. Zarins, C. T. Lu, C. F. Yang, and S. Glagov, "Vessel, plaque and lumen morphology after transluminal balloon angioplasty: Quantitative study in distended human arteries.," *Atherosclerosis*, vol. 7, pp. 306–314, 1987.

[86] P. C. Block, K. L. Baughmnan, R. C. Pasternak, and J. T. Fallon, "Transluminal angioplasty: Correlation of morphological and angiographical findings in an experimental model.," *Circulation*, vol. 61, pp. 778–785, 1980.

[87] H. K. Salem *et al.*, "Effect of Balloon Angioplasty on Femoral Artery Evaluated With Intravascular Ultrasound Imaging," *Circulation*, vol. 86, no. 2, pp. 483–493, 1992.

[88] D. S. Baim, "Percutaneous Balloon Angioplasty and General Coronary Intervention," in *Grossman's Cardiac Catheterization, Angiography, and Intervention*, 7th ed., D. Baim, Ed. 2005, pp. 433–466.

[89] S. Gupta, "Overview of Balloon Catheter, Accessed November 2019, <http://www.scai.org/Assets/31e9f931-160b-459c-9d7b-b6771621b642/635742456224670000/gupta-guidecatheters-and-guidewire-pdf>." .

[90] G. A. Holzapfel, J. J. Mulvihill, E. M. Cunnane, and M. T. Walsh, "Computational approaches for analyzing the mechanics of atherosclerotic plaques: A review," *J. Biomech.*, vol. 47, no. 4, pp. 859–869, 2014.

[91] Y. Honda, P. J. Fitzgerald, and P. G. Yock, "Intravascular Imaging Techniques," in *Grossman's Cardiac Catheterization, Angiography, and Intervention*, 7th ed., D. Baim, Ed. 2005, pp. 371–394.

[92] A. H. Chau, R. C. Chan, M. Shishkov, and et al., "Mechanical Analysis of Atherosclerotic Plaques Based on Optical Coherence Tomography," *Ann. Biomed. Eng.*, vol. 32, pp. 1494–1503, 2004.

[93] S. Voros, S. Rinehart, Z. Qian, and et al., "Coronary Atherosclerosis Imaging by Coronary CT Angiography: Current Status, Correlation With Intravascular Interrogation and Meta Analysis," *J. Am. Coll. Cardiol.*, vol. 4, no. 5, pp. 537–548, 2011.

[94] J. Ohayon, O. Dubreuil, P. Tracqui, and et al, "Influence of residual stress/strain on the biomechanical stability of vulnerable coronary plaques: potential impact for evaluating the risk of plaque rupture.," *Am. J. Physiol. Hear. Circ. Physiol.*, vol. 293, pp. H1987–H1996, 2007.

[95] R. Maurice, G. Soulez, M.-F. Giroux, and et al., "Noninvasive vascular elastography for carotid artery characterization on subjects without previous history of atherosclerosis," *Int. J. Med. Phys. Res. Pract.*, vol. 35, no. 8, pp. 3436–3443, 2008.

[96] K. Yamashita, M. H. Yamamoto, S. Ebara, T. Okabe, and et al, "Association between increased epicardial adipose tissue volume and coronary plaque composition.," *Heart Vessels*, 2013.

[97] J. Tanigawa, P. Barlis, and C. Di Mario, "Heavily calcified coronary lesions preclude strut apposition despite high pressure balloon dilatation and rotational atherectomy: in-vivo demonstration with optical coherence tomography.," *Circulation*, vol. 72, pp. 157–160, 2008.

[98] H. M. Garcia-Garcia, N. Gonzalo, E. Regar, and P. W. Serruys, "Virtual histology and optical coherence tomography: from research to a broad clinical application," *Heart*, vol. 95, pp. 1362–1374, 2009.

[99] O. Manfrini, E. Mont, O. Leone, E. Arbustini, and et al, "Sources of error and interpretation of plaque morphology by optical coherence tomography.," *Am. J. Cardiol.*, vol. 98, pp. 156–159, 2006.

[100] U. Sadat *et al.*, "Finite element analysis of vulnerable atherosclerotic plaques: A comparison of mechanical stresses within carotid plaques of acute and recently symptomatic patients with carotid artery disease," *J. Neurol. Neurosurg. Psychiatry*, vol. 81, no. 3, pp. 286–289, 2010.

[101] H. A. Nieuwstadt, T. R. Geraedts, M. T. B. Truijman, M. E. Kooi, and et al, "Numerical simulations of carotid MRI quantify the accuracy in measuring atherosclerotic plaque components in vivo.," *Magn. Reson. Med.*, 2013.

[102] D. Stucht, K. A. Danishad, P. Schulze, and et al, "Highest Resolution In Vivo Human Brain MRI Using Prospective Motion Correction," *PLoS One*, vol. 10, no. 7, 2015.

[103] G. A. Holzapfel, M. Stadler, and C. A. Schulze-Bauer, "A Layer-Specific Three-Dimensional Model for the Simulation of Balloon Angioplasty using Magnetic Resonance Imaging and Mechanical Testing," *Ann. Biomed. Eng.*, vol. 30, no. 6, pp. 753–767, 2002.

[104] G. A. Holzapfel, M. Stadler, and T. C. Gasser, "Towards a Computational Methodology for Optimizing Angioplasty Treatments with Stenting," in *Holzapfel, G.A., Ogden, R.W (Eds.), Mechanics of Biological Tissue. Springer-Verlag, Heidelberg*, 2006, pp. 225–240.

[105] A. Kelly-Arnold, N. Maldonado, D. Laudier, E. Aikawa, and et al, "Revised microcalcification hypothesis for fibrous cap rupture in human coronary arteries," *Proc. Natl. Acad. Sci. USA*, vol. 110, pp. 10741–10746, 2013.

[106] N. Maldonado, A. Kelly-Arnold, Y. Vengrenyuk, and et al, "A mechanistic analysis of the role of micro-calcifications in atherosclerotic plaque stability: potential implications for plaque rupture.," *Am. J. Physiol. Hear. Circ. Physiol.*, vol. 303, pp. H619–H628, 2012.

[107] D. K. Liang, D. Z. Yang, M. Qi, and W. Q. Wang, "Finite element analysis of the implantation of a balloon-expandable stent in a stenosed artery," *Int. J. Cardiol.*, vol. 104, no. 3, pp. 314–318, 2005.

[108] A. C. Akyildiz *et al.*, "Effect of intima stiffness and plaque morphology on peak cap stress," *Biomed. Eng. Online*, vol. 10, p. 25, 2011.

[109] L. Speelman, A. C. Akyildiz, B. DenAdel, J. J. Wentzel, and et al, "Initial stress in biomechanical models of atherosclerotic plaques.," *J. Biomech.*, vol. 44, pp. 2376–2382, 2011.

[110] S. Y. Patel, M. R. Kaazempur-Mofrad, A. G. Isasi, and R. D. Kamm, "Diseased artery wall mechanics: correlation to histology.," in *Proceedings of the 2003 Summer Bioengineering Conference, Key Biscayne, Florida*, 2003.

[111] T. C. Gasser and G. A. Holzapfel, "Modeling plaque fissuring and dissection during balloon angioplasty intervention.," *Ann. Biomed. Eng.*, vol. 35, pp. 711–723, 2007.

[112] D. Balzani, S. Brinkhues, and G. A. Holzapfel, "Constitutive framework for the modeling of damage in collagenous soft tissues with application to arterial walls.," *Comput. Methods Appl. Mech. Eng.*, vol. 213–216, pp. 139–151, 2012.

[113] J. Ohayon, G. Finet, A. M. Gharib, D. A. Herzka, and et al, "Necrotic core thickness and positive arterial remodeling index: emergent biomechanical factors for evaluating the risk of plaque rupture," *Am. J. Physiol. Hear. Circ. Physiol.*, vol. 295, no. 2, pp. H717–H727, 2008.

[114] A. Versluis, A. J. Bank, and W. H. Douglas, "Fatigue and plaque rupture in myocardial infarction," *J. Biomech.*, vol. 39, pp. 339–347, 2006.

[115] A. Karimi, M. Navidbakhsh, S. Faghihi, A. Shojaei, and K. Hassani, "A finite element investigation on plaque vulnerability in realistic healthy and atherosclerotic human coronary arteries," *Proc. Inst. Mech. Eng. Part H J. Eng. Med.*, vol. 227, no. 2, pp. 148–161, 2013.

[116] C. Lally, F. Dolan, and P. J. Prendergast, "Cardiovascular stent design and vessel stresses: A finite element analysis," *J. Biomech.*, vol. 38, no. 8, pp. 1574–1581, 2005.

[117] T. C. Gasser and G. A. Holzapfel, "Finite element modeling of balloon angioplasty by considering overstretch of remnant non-diseased tissues in lesions.," *Comput. Mech.*, vol. 40, pp. 47–60, 2007.

[118] J. Bedoya, C. A. Meyer, L. H. Timmins, M. R. Moreno, and J. E. Moore, "Effects of Stent Design Parameters on Normal Artery Wall Mechanics," *J. Biomech. Eng.*, vol. 128, no. 5, pp. 757–765, 2006.

[119] L. H. Timmins, C. A. Meyer, M. R. Moreno, and J. E. Moore, "Effects of Stent Design and Atherosclerotic Plaque Composition on Arterial Wall Biomechanics," *J. Endovasc. Ther.*, vol. 15, no. 6, pp. 643–654, 2008.

[120] Dalong Li; Anne M. Robertson; Guoyu Lin; and Michael Lovell;, "Finite element modeling of cerebral angioplasty using a structural multi-mechanism anisotropic damage model," *Int. J. Numer. METHODS Eng. 92*, no. June, pp. 457–474, 2012.

[121] C. Conway, J. P. McGarry, E. R. Edelman, and E. Al., "Numerical Simulation of Stent Angioplasty with Predilation: An Investigation into Lesion Constitutive Representation and Calcification Influence.," *Ann. Biomed. Eng.*, vol. 45, pp. 2244–2252, 2017.

[122] F. Iannaccone, C. Chiastra, A. Karanasos, and et al, "Impact of plaque type and side branch geometry on side branch compromise after provisional stent implantation: a simulation study.," *EuroIntervention*, vol. 13, pp. e236–e245, 2017.

[123] G. A. Holzapfel, M. Stadler, and T. C. Gasser, "Changes in the mechanical environment of stenotic arteries during interaction with stents : computational assessment of parametric stent designs," *J. Biomech. Eng.*, vol. 127, pp. 166–180, 2005.

[124] D. E. Kiousis, S. F. Rubinigg, M. Auer, and G. A. Holzapfel, "A Methodology to Analyze Changes in Lipid Core and Calcification Onto Fibrous Cap Vulnerability: The Human Atherosclerotic Carotid Bifurcation as an Illustratory Example," *J. Biomech. Eng.*, vol. 131, no. 12, p. 121002, 2009.

[125] D. E. Kiousis, T. C. Gasser, and G. A. Holzapfel, "A numerical model to study the interaction of vascular stents with human atherosclerotic lesions," *Ann. Biomed. Eng.*, vol. 35, no. 11, pp. 1857–1869, 2007.

[126] A. Ferrara and A. Pandolfi, "Numerical modelling of fracture in human arteries.," *Comput. Methods Biomech. Biomed. Engin.*, vol. 11, pp. 553–567, 2008.

[127] F. Auricchio, M. Conti, M. De Beule, G. De Santis, and B. Verhegghe, "Carotid artery stenting simulation : From patient-specific images to finite element analysis," *Med. Eng. Phys.*, vol. 33, no. 3, pp. 281–289, 2011.

[128] F. Auricchio, M. Conti, A. Ferrara, and et al, "Patient-specific finite element analysis of carotid artery stenting: a focus on vessel modeling," *Int. j. numer. method. biomed. eng.*, vol. 29, pp. 645–664, 2013.

[129] I. Decorato, Z. Kharboutly, C. Legallais, and A. V. Salsac, "Comparison of two endovascular treatments of a stenosed arteriovenous fistula: Balloon-angioplasty with and without stenting," *Int. J. Artif. Organs*, vol. 37, no. 10, pp. 763–772, 2014.

[130] G. A. Holzapfel, "Nonlinear Solid Mechanics. A Continuum Approach for Engineering," John Wiley & Sons, Chichester, 2000.

[131] J. D. Humphrey, "Cardiovascular Solid Mechanics. Cells, Tissues, and Organs.," *Springer-Verlag*, New York, 2002.

[132] G. A. Holzapfel, G. Sommer, and P. Regitnig, "Anisotropic mechanical properties of tissue components in human atherosclerotic plaques," *J. Biomech. Eng.*, vol. 126, pp. 657–665, 2004.

[133] G. A. Holzapfel, T. C. Gasser, and R. W. Ogden, "A new constitutive framework for arterial wall mechanics and a comparative study of material models," *J. Elast.*, vol. 61, pp. 1–48, 2000.

[134] G. A. Holzapfel, G. Sommer, T. C. Gasser, and et al, "Determination of layer-specific mechanical properties of human coronary arteries with non-atherosclerotic intimal thickening, and related constitutive modeling.," *Am. J. Physiol. Hear. Circ. Physiol.*, vol. 289, pp. H2048–H2058, 2005.

[135] P. Mortier, G. A. Holzapfel, M. DeBeule, and et al, "A novel simulation strategy for stent insertion and deployment in curved coronary bifurcations: comparison of three drug-eluting stents," *Ann. Biomed. Eng.*, vol. 38, pp. 88–99, 2010.

[136] A. J. Schriefl, G. Zeindlinger, and D. M. Pierce, "Determination of the layer-specific distributed collagen fiber orientations in human thoracic and abdominal aortas and common iliac arteries.," *J. R. Soc. Interface*, vol. 9, pp. 1275–1286, 2012.

[137] T. C. Gasser and G. A. Holzapfel, "A rate-independent elastoplastic model for biological fiber-reinforced composites at finite strains: continuum basis, algorithmic formulation and finite element implementation.," *Comput. Mech.*, vol. 29, pp. 340–360, 2002.

[138] E. Maher, A. Creane, C. Lally, and D. Kelly, "An anisotropic inelastic constitutive model to describe stress softening and permanent deformation in arterial tissue," *J. Mech. Behav. Biomed. Mater.*, vol. 12, pp. 9–19, 2012.

[139] H. M. Loree, A. J. Grodzinsky, and S. Y. Park, "Static circumferential tangential modulus of human atherosclerotic tissue," *J. Biomech.*, vol. 27, pp. 195–204, 1994.

[140] G. V. R. Born and P. D. Richardson, "Mechanical properties of human atherosclerotic lesions," in *Glagov S., Newman W.P., Schaffer S.A. (eds) Pathobiology of the Human Atherosclerotic Plaque.*, Springer-Verlag, New York, Inc., 1990, pp. 413–423.

[141] M. T. Walsh, E. M. Cunnanea, J. J. Mulvihilla, and et al, "Uniaxial tensile testing approaches for characterisation of atherosclerotic plaques," *J. Biomech.*, vol. 47, no. 4, pp. 793–804, 2014.

[142] C. K. Chai, "Biomechanical properties of atherosclerotic plaques," Eindhoven: Technische Universiteit Eindhoven, 2015.

[143] R. T. Lee, S. G. Richardson, H. M. Loree, and et al, "Prediction of mechanical properties of human atherosclerotic tissue by high-frequency intravascular ultrasound imaging an in vitro study.," *Arterioscler. Vasc. Biol.*, vol. 12, pp. 1–5, 1992.

[144] L. D. T. Topoleski, N. V. Salunke, J. D. Humphrey, and et al, "Composition and history-dependent radial compressive behavior of human atherosclerotic plaque.," *J. Biomed. Mater. Res.*, vol. 35, no. 1, pp. 117–127, 1997.

[145] E. Maher, A. Creane, S. Sultan, N. Hynes, C. Lally, and D. J. Kelly, "Tensile and compressive properties of fresh human carotid atherosclerotic plaques," *J. Biomech.*, vol. 42, no. 16, pp. 2760–2767, 2009.

[146] R. T. Lee, A. J. Grodzinsky, E. H. Frank, and et al, "Structure-dependent dynamic mechanical behavior of _brous caps from human atherosclerotic plaques.," *Circulation*, vol. 83, no. 5, pp. 1764–1770, 1991.

[147] N. V. Salunke, L. D. T. Topoleski, J. D. Humphrey, and et al, "Compressive stress-relaxation of human atherosclerotic plaque," *J. Biomed. Mater. Res.*, vol. 55, no. 2, pp. 236–241, 2001.

[148] E. Maher, A. Creane, S. Sultan, N. Hynes, C. Lally, and D. J. Kelly, "Inelasticity of Human Carotid Atherosclerotic Plaque," *Ann. Biomed. Eng.*, vol. 39, no. 9, pp. 2445–2455, 2011.

[149] W. Li, "Damage Models for Soft Tissues: A Survey," *J. Med. Biol. Eng.*, vol. 36, pp. 285–307, 2016.

[150] C. Conway, J. P. Mcgarry, and P. E. MchugCHUGH, "Modelling of Atherosclerotic Plaque for Use in a Computational Test-Bed for Stent Angioplasty," *Ann. Biomed. Eng.*, vol. 42, no. 12, pp. 2425–2439, 2014.

[151] D. Gastaldi, S. Morlacchi, R. Nichetti, and et al, "Modelling of the provisional side-branch stenting approach for the treatment of atherosclerotic coronary bifurcations: effects of stent positioning," *Biomech. Model. Mechanobiol.*, vol. 9, pp. 551–561, 2010.

[152] H. Zahedmanesh, D. J. Kelly, and C. Lally, "Simulation of a balloon expandable stent in a realistic coronary artery—Determination of the optimum modelling strategy," *J. Biomech.*, vol. 43, pp. 2126–2132, 2010.

[153] H. Zahedmanesh and C. Lally, "Determination of the influence of stent strut thickness using the finite element method: implications for vascular injury and in-stent restenosis," *Med. Biol. Eng. Comput.*, vol. 47, pp. 385–393, 2009.

[154] F. Gervaso, C. Capelli, L. Petrini, and et al., "On the effects of different strategies in modelling balloon-expandable stenting by means of finite element method," *J. Biomech.*, vol. 41, pp. 1206–1212, 2008.

[155] J. A. Grogan, S. B. Leen, and P. E. McHugh, "Comparing coronary stent material performance on a common geometric platform through simulated bench testing.," *J. Mech. Behav. Biomed. Mater.*, vol. 12, pp. 129–38, 2012.

[156] A. Schiavone and L. G. Zhao, "A study of balloon type, system constraint and artery constitutive model used in finite element simulation of stent deployment," *Mech. Adv. Mater. Mod. Process.*, vol. 1, pp. 1–15, 2015.

[157] D. E. Kiousis, A. R. Wulff, and G. . Holzapfel, "Experimental Studies and Numerical Analysis of the Inflation and Interaction of Vascular Balloon Catheter Stent Systems," *Ann. Biomed. Eng.*, vol. 37, no. 2, pp. 315–330, 2009.

[158] M. A. Geith, K. Swidergal, and B. Hochholdinger, "On the importance of modeling balloon folding, pleating, and stent crimping: An FE study comparing experimental inflation tests," *Int. j. numer. method. biomed. eng.*, vol. 35, p. e3249, 2019.

[159] M. De Beule, P. Mortier, G. Carlier, and et al., "Realistic finite element-based stent design: the impact of balloon folding," *J. Biomech.*, vol. 41, pp. 383–389, 2008.

[160] D. Tang, C. Yang, S. Kobayashi, and D. N. Ku, "Effect of a lipid pool on stress/strain distributions in stenotic arteries: 3-D fluid–structure interactions (FSI) models," *J. Biomech. Eng.*, vol. 126, pp. 363–370, 2004.

[161] H. A. Nieuwstadt *et al.*, "The influence of axial image resolution on atherosclerotic plaque stress computations," *J. Biomech.*, vol. 46, no. 4, pp. 689–695, 2013.

[162] C. Conway, F. Sharif, and J. McGarry, "A computational test-bed to assess coronary stent implantation mechanics using a population-specific approach.," *Cardiovasc. Eng. Technol.*, vol. 3, pp. 1–14, 2012.

[163] B. J. Rensing, W. R. Hermans, B. H. Strauss, and P. W. Serruys, "Regional differences in elastic recoil after percutaneous transluminal coronary angioplasty: A quantitative angiographic study," *J. Am. Coll. Cardiol.*, vol. 17, no. 6 SUPPL. 2, pp. 34–38, 1991.

[164] J. Gardiner, J. Bonn, and K. L. Sullivan, "Quantification of elastic recoil after balloon angioplasty in the iliac arteries," *J. Vasc. Interv. Radiol.*, vol. 12, no. 12, pp. 1389–1393, 2001.

[165] C. Hanet, W. Wijns, X. Michel, and E. Schroeder, "Influence of balloon size and stenosis morphology on immediate and delayed elastic recoil after percutaneous transluminal coronary angioplasty," *J. Am. Coll. Cardiol.*, vol. 18, no. 2, pp. 506–511, 1991.

[166] M. A. Saab, "Applications of High-Pressure Balloons in the Medical Device Industry; 2000. Accessed September 20, 2020, <https://www.mddionline.com/applications-high-pressure-balloons-medical-device-industry>."

[167] F. Fogarotto, "Finite Element Analysis of Coronary Artery Stenting," PhD Thesis, University of Pavia, Italy, 2011.

[168] M. De Beule, "Finite Element Stent Design," PhD Thesis, Ghent University, Belgium, 2008.

[169] E. Romagnoli, G. M. Sangiorgi, J. Cosgrave, E. Guillet, and A. Colombo, "Drug-Eluting Stenting. The Case for Post-Dilation," *JACC Cardiovasc. Interv.*, vol. 1, no. 1, pp. 22–31, 2008.

[170] S. G. Ellis and E. J. Topol, "Results of percutaneous transluminal coronary angioplasty of high-risk angulated stenoses," *Am. J. Cardiol.*, vol. 66, no. 12, pp. 932–937, 1990.

[171] R. G. Bach, M. J. Kern, F. V. Aguirre, T. J. Donohue, C. Bell, and D. Penick, "Effects of percutaneous transluminal coronary angioplasty balloon compliance on angiographic and clinical outcomes," *Am. J. Cardiol.*, vol. 72, no. 12, pp. 904–907, 1993.

[172] N. MEDICAL, "Medical Balloons, accessed 11 July 2020, <https://www.nordsonmedical.com/Resources/Download?title=Medical%20Balloons&category=Sell%20Sheets>."

[173] D. Roche, "ANSYS: ACT Hydrostatic Fluid." pp. 1–31, 2017.

[174] U. Sadat *et al.*, "Association between biomechanical structural stresses of atherosclerotic carotid plaques and subsequent ischaemic cerebrovascular events - A longitudinal in vivo magnetic resonance imaging-based finite element study," *Eur. J. Vasc. Endovasc. Surg.*, vol. 40, no. 4, pp. 485–491, 2010.

[175] J. Isner, K. Rosenfield, D. Losordo, L. Rose, R.E. Langevin, S. Razvi, and B. Kosowsky, "Combination Balloon-Ultrasound Imaging Catheter for Percutaneous Transluminal Angioplasty Validation of Imaging, Analysis of Recoil, and Identification of Plaque Fracture," pp. 739–754, 1991.

[176] B. P. Kimball, S. Bui, E. A. Cohen, R. G. Carere, and A. G. Adelman, "Comparison of acute elastic recoil after directional coronary atherectomy versus standard balloon angioplasty," *Am. Heart J.*, vol. 124, no. 6, pp. 1459–1466, 1992.

[177] E. Blessing, I. Lugenbiel, and A. Holden, "The evidence to support the use of focal force balloon technology to improve outcomes in the treatment of lower extremity arterial occlusive disease," *J. Cardiovasc. Surg. (Torino).*, vol. 60, no. 1, pp. 14–20, 2019.

[178] L. Ettorre, G. Prouse, L. Giovannacci, and et al., "Vessel Preparation: What is the Evidence in the BTK Segment?," *Vasc. Dis. Manag.*, vol. 17, no. 7, pp. E142–E149, 2020.

[179] G. Holzapfel, C. A. J. Schulze–Bauer, and M. Stadler, "Mechanics of angioplasty: wall, balloon and stent," in *Mechanics in Biology, AMD-Vol. 242, BED-Vol. 46, New York*, J. Casey and G. Bao, Eds. 2000, pp. 141–156.

[180] B. Calvo, E. Pena, and et al, "An uncoupled directional damage model for fibred biological soft tissues. Formulation and computational aspects.," *Int. J. Numer. Methods Eng.*, vol. 69, pp. 2037–2057, 2007.

[181] E. L. Gaertner and M. G. D. de Bortoli, "Some Aspects for the Simulation of a Non-Linear Problem with Plasticity and Contact," *2006 Int. ANSYS Conf.*, pp. 1–15, 2006.

[182] A. Paini, P. Boutouyrie, D. Calvet, M. Zidi, E. Agabiti-Rosei, and S. Laurent, "Multiaxial mechanical characteristics of carotid plaque: Analysis by multiarray echotracking system," *Stroke*, vol. 38, no. 1, pp. 117–123, 2007.

[183] E. Maher, M. Early, A. Creane, D. J. Lally, and C. Kelly, "Site specific inelasticity of arterial tissue," *J. Biomech.*, vol. 45, no. 8, pp. 1393–1399, 2012.

[184] D. M. Ebenstein, D. Coughlin, J. Chapman, and et al., "Nanomechanical properties of calcification, fibrous tissue, and hematoma from atherosclerotic plaques," *J. Biomed. Mater. Res.*, vol. 91, no. 4, pp. 1028–1037, 2009.

[185] J. Walraevens, B. Willaert, G. De Win, and et al., "Correlation between compression, tensile and tearing tests on healthy and calcified aortic tissues," *Med. Eng. Phys. Phys.*, vol. 30, no. 9, pp. 1098–1104, 2008.

[186] A. Karimi, M. Navidbakhsh, A. Shojaei, and S. Faghihi, "Measurement of the uniaxial mechanical properties of healthy and atherosclerotic human coronary arteries," *Mater. Sci. Eng. C*, vol. 33, no. 5, pp. 2550–2554, 2013.

[187] P. A. Yushkevich *et al.*, "User-guided 3D active contour segmentation of anatomical structures : Significantly improved efficiency and reliability," vol. 31, pp. 1116–1128, 2006.

[188] F. Herisson, M. F. Heymann, M. Chetiveaux, and E. Al., "Carotid and femoral atherosclerotic plaques show different morphology," *Atherosclerosis*, vol. 216, pp. 348–354, 2011.

[189] S. Dalager, W. P. Paaske, I. B. Kristensen, and et al., "Artery-related differences in atherosclerosis expression: implications for atherogenesis and dynamics in intima-media thickness," *Stroke*, vol. 38, pp. 2698–2705, 2007.

[190] K. W. et al Beach, "An ultrasonic measurement of superficial femoral artery wall thickness," *Ultrasound Med. Biol.*, vol. 15, no. 8, pp. 723–728, 1989.

[191] A. Kaladji, A. Lucas, G. Kervio, and et al., "Sizing for endovascular aneurysm repair: clinical evaluation of a new automated three-dimensional software.," *Ann. Vasc. Surg.*, vol. 24, no. 7, pp. 912–20, 2010.

[192] M. Haude, R. Erbel, H. Issa, and et al., "Quantitative analysis of elastic recoil after balloon angioplasty and after intracoronary implantation of balloon expandable Palmaz-Schatz stents.," *J. Am. Coll. Cardiol.*, vol. 21, pp. 26–34, 1993.

UNIVERSITÉ DE RENNES 1

Titre : Modélisation et simulation numérique pour la planification de l'angioplastie transluminale percutanée

Mots clés : Angioplastie transluminale percutanée, Modèle spécifique au patient, Analyse par éléments finis implicite, Prédiction des résultats post-opératoires, Choix de ballon

Résumé : Plusieurs techniques de traitement de l'athérosclérose sont cliniquement pratiquées. En tant qu'option moins invasive, l'angioplastie transluminale percutanée (ATP) est généralement une alternative privilégiée aux traitements invasifs, notamment afin d'éviter les complications rencontrées avec les chirurgies conventionnelles. Bien qu'il s'agisse d'une technique fréquemment utilisée, le choix clinique du ballon approprié (type et taille) qui permettrait d'optimiser les résultats post-opératoires pour un patient spécifique sténosé reste un défi à ce jour. Cela peut influencer de manière significative les résultats du traitement, et donc les décisions thérapeutiques ultérieures.

Dans ce contexte, cette thèse présente la méthodologie de modélisation que nous proposons pour simuler l'ATP (d'abord dans un modèle générique, puis pour des cas spécifiques de patients), et évaluer l'influence de différentes combinaisons de caractéristiques du ballon et de la plaque (type de ballon, composition de la plaque, taille du ballon) sur les résultats post-opératoires à court terme après le dégonflement du ballon, sans implantation de stent. Elle est basée sur la combinaison d'une analyse par éléments finis structurels implicite, de l'identification de la loi matériau et du traitement d'images médicales. L'approche originale proposée est une étape vers un système d'aide à la décision clinique pour améliorer la sélection, avant la chirurgie, du ballon d'angioplastie optimal, en fonction de la sténose du patient considéré.

Title : Modeling and numerical simulation for the planning of percutaneous transluminal angioplasty

Keywords : Percutaneous transluminal angioplasty, Patient-specific model, Implicit finite element analysis, Post-procedural outcomes prediction, Balloon sizing

Abstract: Several treatment techniques are clinically available for atherosclerosis. Being a minimally-invasive option, percutaneous transluminal angioplasty (PTA) is usually a favored alternative to invasive treatments, notably in order to avoid complications experienced with conventional surgeries. Although it is a frequently performed technique, the clinical choice of the appropriate balloon (type and sizing) that would optimize the acute post-treatment outcomes for the specific stenosed patient is still challenging nowadays. This can significantly influence the treatment outcomes, affecting further treatment decisions as well.

In this context, this thesis presents the modeling methodology we propose for simulating PTA (first within a generic model, then for patient-specific cases), and assessing the influence of different combinations of balloon-plaque features (balloon type, plaque composition, balloon sizing) on post-procedural outcomes at short terms after balloon deflation, without stent implantation. It is based on the combination of implicit structural finite element analysis, material law identification, and medical image processing. The proposed approach is a step towards a clinical decision support system to improve angioplasty balloon selections, with respect to the patient stenosis, prior to the surgery.